This electronic thesis or dissertation has been downloaded from Explore Bristol Research, http://research-information.bristol.ac.uk

Author:
Ayres, Jake D S

Title:
Correlated Electron Systems Under Extreme Conditions

High Fields, High Pressures, Low Temperatures

General rights
Access to the thesis is subject to the Creative Commons Attribution - NonCommercial-No Derivatives 4.0 International Public License. A copy of this may be found at https://creativecommons.org/licenses/by-nc-nd/4.0/legalcode This license sets out your rights and the restrictions that apply to your access to the thesis so it is important you read this before proceeding.

Take down policy
Some pages of this thesis may have been removed for copyright restrictions prior to having it been deposited in Explore Bristol Research. However, if you have discovered material within the thesis that you consider to be unlawful e.g. breaches of copyright (either yours or that of a third party) or any other law, including but not limited to those relating to patent, trademark, confidentiality, data protection, obscenity, defamation, libel, then please contact collections-metadata@bristol.ac.uk and include the following information in your message:

- Your contact details
- Bibliographic details for the item, including a URL
- An outline nature of the complaint

Your claim will be investigated and, where appropriate, the item in question will be removed from public view as soon as possible.

Correlated Electron Systems Under Extreme Conditions

High Fields, High Pressures, Low Temperatures

Jake Ayres

University of Bristol

March 2020

A thesis submitted to the University of Bristol in accordance with the requirements for award of the degree of Doctor of Philosophy in the Faculty of Science, Department of Physics

Word count: 44175

Abstract

In this thesis, the results of four electronic transport studies of correlated electron systems performed under hydrostatic pressure, at low temperatures and in the presence of high magnetic fields are presented. Firstly, magnetoresistance and Hall effect measurements in $\mathrm{Tl_2Ba_2CuO_{6+\delta}}$, an overdoped cuprate, are presented. At low magnetic fields, a comparison between the evolution of the in-plane transport properties with a suppression of the superconducting transition temperature tuned by both chemical doping and the application of hydrostatic pressure. At high magnetic fields and in a region of doping-temperature phase-space in which conventional transport theory has previously been deployed to accurately describe the transport properties of highly overdoped cuprates, a highly unconventional magnetoresistance has been revealed. Definitive evidence of two charge sectors is presented where the first is orbital in nature whilst the second is highly unconventional and likely incoherent.

Secondly, a high-field Hall effect study of $\mathrm{YBa_2Cu_3O_{7-x}}$, an underdoped cuprate, is presented. The evolution of the superconducting transition temperature and the temperature at which the Hall coefficient changes sign, an indicator of a Fermi surface reconstruction due to the onset of charge order, are tracked as a function of hydrostatic pressure. The first is used as a measure of the strength of superconductivity whilst the second is used as a proxy for the strength of charge order. The implications with regard to the interplay or competition between the two phases are discussed.

Thirdly, a comprehensive study is presented of the in-plane magnetoresistance under pressure of $\mathrm{FeSe_{1-x}S_x}$ with sulphur concentrations that span the nematic phase. Nematicity is suppressed with pressure. At the critical pressure P_c at which the nematic transition is suppressed to zero temperature (at the nematic QCP), the in-plane resistivity measured at 35 T exhibits hallmarks of quantum criticality. Specifically, the high-field resistivity is highly linear down to lowest temperatures and a growing region of T^2 behaviour is observed at lowest temperatures as P is increased beyond P_c.

Finally, a quantum oscillation study of the nodal-line semi-metal ZrSiS has been performed under hydrostatic pressure. At ambient pressure, unconventional breakdown phenomena have been observed. Analysis of the Shubnikov de-Haas oscillations at both ambient and elevated pressures has been performed to elucidate the nature of the Fermi surface and the origin of the aforementioned breakdown phenomena.

Author's Declaration

I declare that the work in this dissertation was carried out in accordance with the requirements of the University's *Regulations and Code of Practice for Research Degree Programmes* and that it has not been submitted for any other academic award. Except where indicated by specific reference in the text, the work is the candidate's own work. Work done in collaboration with, or with the assistance of, others, is indicated as such. Any views expressed in the dissertation are those of the author.

Signed: Date:

Acknowledgements

As with all theses, there is only one author but the final product could not have been achieved without the support, guidance and effort of many others. It goes without saying that Tony, Sven and Nigel were all integral to the success of this project. I was certainly well equipped with supervisors. Their support throughout my PhD is hugely appreciated.

Much of my practical expertise (if I dare claim to have any) have been learned from Carsten Putzke. I would like to especially thank him for his guidance and patience early on in my PhD. Of course, I would like to thank the other past and current members of the CES group and the CDT-CMP for both their help and great company over the four years. Fortunately (for me), I'll be here a little longer.

I was very fortunate to spend a substantial amount of time at the High Field Magnet Laboratory, Nijmegen where a large proportion of the data presented in this thesis was performed. There (although now at Bristol), I am hugely grateful to Jonathan Buhot for the sheer number of measurement hours he spent with me. Your help was tireless. I am also very thankful the rest of the HFML team for their assistance and friendship. I look forward to our future scientific (and non scientific) endeavours.

Additional thanks go out to the workshop technicians, cryogenic technicians and administrative staff at both the University of Bristol and the HFML for their continuous hard work. You were all always very kind and helpful.

I would like to thank both my parents and sister for their encouragement and support. Finally, I thank Amy for her love, support and infinite tolerance. I wouldn't have completed this thesis without her.

Contents

Chapter 1

Introduction

1.1 Strongly Correlated Electron Systems

At room temperature, the crystalline solids that we commonly interact with can be broadly categorised by their electronic properties into one of two categories. There are those that are metallic, and those that are insulators. In insulators, electrons are restrained and are not mobile. In metals, they travel freely within the confines of the material much as air molecules are confined to a room. Thus, when an electric field is applied across the material, the electrons are able to 'flow'. The physical properties of metals are qualitatively captured by considering electrons to be non-interacting entities that are truly free. At high temperatures, the kinetic energy of the electrons is substantially larger than their interaction (Coulomb) energy. The approximation that they are independent charge-carrying entities remains valid. A statistical description of materials suffices to explain the properties of electrons in the aggregate. Insulating behaviour can be captured by considering an interaction between electrons and the crystal lattice but does not require that electrons interact with each other.

Another notable category of materials that are familiar to all of us are magnets (ferromagnets). In ferromagnets, the intrinsic magnetic moments of the electrons are aligned such that the net magnetic moment of the material is non-zero. Their orientations are linked such that the orientation of one is *correlated* with the orientation of another. Ferromagnetism is an example of a correlation effect that is able to persist up to room temperature in a number of materials, notably iron.

At low temperatures, thermal energy is reduced, Coulomb interactions become increasingly relevant and a plethora of additional electronic phases are able to reveal themselves. These electronic phases are a consequence of interactions between the electrons. They can no longer be considered independent of one another. Materials for which this is the case are said to be *correlated electron systems* and are the subject matter of this thesis. It has proved to be very difficult to predict how these correlations manifest themselves in the physical properties of the system concerned. As is summarised by the 'More is Different' maxim from Anderson [1], it is not necessarily the case that an understanding of the collective behaviour of a system can be found from an understanding of the properties of individual electrons.

A notable example of a correlated electronic phase is superconductivity. Discovered by Onnes [2], conventional superconductivity is an electronic state in which correlations between electrons are mediated by their interaction with vibrations of the atomic lattice [3, 4]. The result is the dissipationless flow of electrical current at temperatures below a critical temperature T_c. Superconductors are used to generate large magnetic fields in MRI scanners, low-volume and high-efficiency motors and are the basis of many quantum computing technologies. Superconducting technologies are somewhat restricted in their widespread use by the need to cool them, often by hundreds of degrees, to below their T_c.

The advent of high temperature superconductivity in cuprates [5] proved to be a landmark discovery. Cuprates both stimulated huge scientific interest for exhibiting superconductivity at temperatures far higher than conventional theory would suggest is possible and dramatically increased the practical utility of superconductors by virtue of T_c being above the boiling point of liquid nitrogen. Both $Tl_2Ba_2CuO_{6+\delta}$ and $YBa_2Cu_3O_{7-x}$, the subjects of Chapters 4 and 5, are members of the cuprate family of superconductors. $FeSe_{1-x}S_x$, a member of the iron-based family of high temperature superconductors, is studied in Chapter 6.

The cuprates also exhibit multiple other correlated electronic phases including charge order [6–8] (a periodic modulation of charge density) and magnetic order [9, 10] (a periodic alignment of spins). The practical utility of these phases has yet to be realised. Their understanding is principally motivated by a desire for an understanding of the microscopic origin of high temperature superconductivity. Despite more than 30 years of intensive investigation and a fine understanding of many peripheral aspects of these materials, high temperature superconductivity itself is not fundamentally understood. Nevertheless, it is widely believed that answers to this outstanding challenge lie in the study of their normal state (non-superconducting) properties. In this thesis, materials have been subjected to extreme conditions of temperature, magnetic field and hydrostatic pressure in order to study the evolution of their normal state transport properties with the aim of understanding the nature of their anomalous behaviour.

Another more recent field of interest is topological materials. In topological materials, the electronic properties are governed by particular symmetries or topological features of the system. Their properties are in many cases ‘protected’ and are more robust against temperature, deformations or other external influences that would otherwise adversely affect the system. One such example is ZrSiS, the subject of the final chapter (Chapter 7) of this thesis. These materials have garnered substantial scientific interest as well as practical interest. An inherent robustness to their electronic properties naturally makes them attractive to those seeking correlation effects beyond where they are more usually found.

1.2 Outline Of Thesis

The remainder of this theses is divided into six chapters. In the first, a synopsis of charge transport theories, their assumptions and predictions is presented followed by discussions of their respective flaws and successes. This is proceeded by short descriptions of various transport and magnetotransport phenomena and how each can be used to elucidate something about a material-of-interest.

Details of the experimental methods deployed throughout thesis are then presented. These correspond to the three ‘extreme conditions’, namely low temperatures, high magnetic fields and hydrostatic pressures that the correlated electron systems studied in this thesis have been exposed to.

The final four chapters comprise the body of experimental work. The material of interest and the subject matter of each chapter are distinct. An introduction to each material, motivation for the proceeding experiments and a discussion of the results and conclusions are presented in each chapter.

Chapter 2

Magnetotransport

Both transport and magnetotransport studies are powerful, practically simple and capable of elucidating much about a condensed matter system. The resistivity in zero magnetic field and the magnetoresistance, Hall effect and Shubnikov-de Haas oscillations in the presence of an applied magnetic field are examples of measurements from which many electronic properties of a material-of-interest can be extracted. Early models such as the Drude and Sommerfeld models consider the electrons in a metal to be free and non-interacting whilst more sophisticated models are required when this simple case is insufficient to capture the relevant physics. In this chapter, overviews of the aforementioned models of transport in metals are given. Each of the mentioned transport phenomena are also discussed alongside explanations of how the analysis of each yields different material properties.

2.1 Electronic Transport Theory

2.1.1 The Drude Model

The Drude model considers electrons to be classical, non-interacting particles that move freely amongst a lattice of stationary ions. Despite the fact that the core assumptions are simplistic, it provides a microscopic description of the behaviour of electrons in metals from which both the resistivity and Hall coefficient can be derived and provides a starting point from which more sophisticated theories are based.

In the Drude model, under the influence of an applied electric field E, electrons (with mass m and charge e) accelerate according to Newton's law of motion. Their acceleration is interrupted by random scattering events (with phonons or defects for example) which occur after a mean time τ. These scattering events result in the flow of electrons being inhibited or a resistance to the flow of current. That is, the differential equation that describes the electrons' motion becomes:

$$m\frac{d\mathbf{v}}{dt} = e\mathbf{E} - \frac{m}{\tau}\mathbf{v} \tag{2.1}$$

and the solution can be found to be proportional to the electric field:

$$\mathbf{v} = \frac{e\tau}{m}\mathbf{E}. \tag{2.2}$$

By relating the velocity to the current density

$$\mathbf{j} = ne\mathbf{v} = \sigma\mathbf{E} \tag{2.3}$$

within the Drude model, the conductivity is therefore found to be related to the aforementioned scattering time τ, the mass of the electron m, the charge of the electron e and the carrier density n by the Drude formula:

$$\sigma = \frac{ne^2\tau}{m} \tag{2.4}$$

In the presence of a magnetic field that is perpendicular to the applied electric field, the electrons experience a Lorentz force that deflects the electrons in a direction that is perpendicular to both the current and magnetic field. An opposing Hall field E_H is generated of a magnitude sufficient to achieve a steady state in which the total electric field is rotated by the Hall angle θ_H. The Hall coefficient is then defined as

$$R_H = \frac{E_H}{\mathbf{j}B} = -\frac{1}{ne} \tag{2.5}$$

and the Hall angle is:

$$\tan(\theta_H) = \frac{eB\tau}{m} = \omega_c\tau \tag{2.6}$$

where ω_c is the cyclotron frequency. The Hall angle is therefore equal to the mean number of cyclotron orbits completed by an electron in a scattering time (or mean carrier lifetime).

2.1.2 The Sommerfeld Model

The Sommerfeld model uses Drude theory as its basis but incorporates some of the quantum mechanical properties that the Drude model neglects. Specifically, the adherence to Fermi statistics due to the obeying of the Pauli exclusion principle that states that no two electrons can occupy the same quantum state (as opposed to Maxwell-Boltzmann statistics) was considered. The resultant ground state is then a filled 'sea' of occupied states that abruptly end at the Fermi energy. Excited states are created by exciting electrons from energies just below the Fermi energy to unoccupied states just above the Fermi energy. The *Fermi surface* that separates occupied from unoccupied states at $T = 0\,\mathrm{K}$ can be defined in **k**-space. If the system is assumed to be completely isotropic and non-interacting, one would expect that the energy dispersion is parabolic:

$$\epsilon(\mathbf{k}) = \hbar^2\mathbf{k}^2/2m \tag{2.7}$$

and that given an electron density of n, the Fermi surface would be a sphere of radius k_F where:

$$k_F = (3\pi^2 n)^{1/3} \tag{2.8}$$

as illustrated in Figure 2.1A.

In this picture, it is clear that only electrons with an energy within $\sim k_BT$ of the Fermi energy are able to contribute to the specific heat and only electrons with an energy within $\sim \mu_B B$ of the Fermi energy can magnetise, for example. Electrons with lower energies are 'buried' in that there is insufficient available energy for them to be excited into the next available (unoccupied) state. The density of states at the Fermi energy becomes a relevant quantity. As a result, at low temperatures, the specific heat is expected to be small and linear-in-temperature whilst the Pauli susceptibility is expected to be independent of temperature. These are experimental observations that the Drude model fails to correctly explain.

2.1.3 Nearly Free Electrons

A picture which more naturally resembles that of a crystalline solid is one in which electrons are moving in a periodic potential $V(\mathbf{r})$ with which they interact. A condition of periodicity, $V(\mathbf{r}) = V(\mathbf{r}+\mathbf{R})$, follows directly from the translational periodicity of the lattice in question: $\mathbf{R} = n_1\hat{a} + n_2\hat{b} + n_3\hat{c}$ where $\hat{a}$, $\hat{b}$ and $\hat{c}$ are the lattice vectors and n_1, n_2 and n_3 are integers. It follows that the solutions of the time-independent Schrödinger equation given a one-electron Hamiltonian are Bloch waves. Bloch waves are plane-waves that are modulated by a function that has the same periodicity as the lattice:

$$\psi_k(\mathbf{r}) = u_k(\mathbf{r})e^{ik\mathbf{r}}. \tag{2.9}$$

If the potential is set to zero, the non-interacting result of a parabolic dispersion is returned as expected.

The real-space periodicity is mirrored by a periodicity in momentum-space. That is, $\psi_{\mathbf{k}} = \psi_{\mathbf{k}+\mathbf{K}}$. Analogously to how we need only consider a single unit cell to understand a crystalline solid in real-space, it is sufficient to only consider a single repeating cell, a Brillouin-zone (BZ), in momentum-space to capture the entire dispersion $E(\mathbf{k})$. This is illustrated in Figure 2.1C in which bands from neighbouring Brillouin-zones have been back-folded into a single BZ in accordance with the ‘repeating zone scheme’.

The introduction of a finite potential results in the opening of a gap at the BZ boundary (Figure 2.1D). If electronic states are filled in accordance with the Pauli exclusion principle and the highest energy occupied states fall within a band, a Fermi surface can be defined. At finite but low temperatures, there are states immediately above (within k_BT) the Fermi surface into which electrons can be thermally excited. In the case where the chemical potential falls between bands (or within a band gap), it is possible that there are no states within k_BT of the chemical potential at low temperatures. This model therefore clearly captures the origin of both metallic and insulating behaviour. The presence of a Fermi surface is one reasonable defining characteristic of a metal.

2.1.4 Fermi Liquid Theory

Thus far, the discussed theories have all featured the core assumption that the electrons are non-interacting with each other. Although they are clearly successful in many instances, when the strength of electron-electron interactions becomes less insignificant, they are unlikely to remain

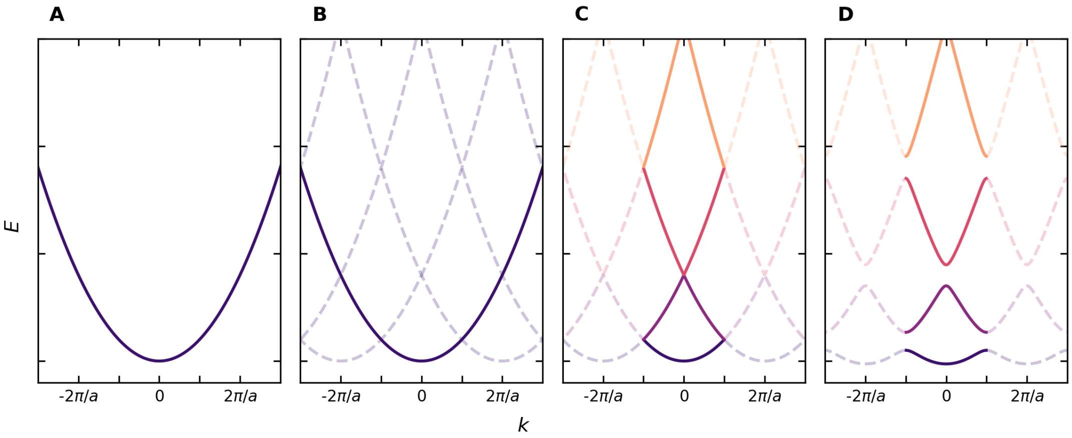

Figure 2.1: The energy-momentum dispersion relation for a free electron both with (a) and without (b) periodicity arising from the underlying crystal lattice. (c) shows the same dispersion as in (b) with back-folding into a reduced zone scheme. (d) The dispersion relation for a nearly free electron with a finite potential such that gaps open at the zone boundaries and discrete bands are formed.

valid. Fermi liquid theory generalises the non-interacting Fermi gas and introduces the interactions that have been ignored thus far. Although originally developed to explain the liquid state of He-3 [11], Fermi liquid theory has found success in describing the behaviour of electrons in metals where previous theories have failed.

The principal idea is that there is a one-to-one mapping between the eigenstates of the non-interacting system (a Fermi gas) and a system in which an interaction is turned on (a Fermi liquid). As the interaction is slowly (adiabatically) turned on, it is convenient to no longer consider true electrons but *quasiparticles* that are distinct from electrons in that their energies (and properties more generally) are different from those of the corresponding true electrons in the non-interacting case. That is, it is useful to reflect the effect of the interaction in the properties of the charge carriers as opposed to considering how true electrons behave in a modified system. More specifically, the eigenstates of the interacting system are superpositions of the eigenstates of the non-interacting system. The occupation function of the quasiparticles in the interacting case is the same as that of the electrons in the non-interacting case.

Importantly however, the introduction of an interaction does modify the occupation function of the true electrons in the interacting case (see Fig 2.2). The size of the discontinuous jump at k_F is reduced in size even at zero temperature in the interacting picture. The size of the jump, Z, is commonly termed the quasiparticle weight and is loosely speaking similar to an order parameter.

The equilibrium properties of the system retain their non-interacting form but are renormalised. Perhaps the most significant modification is that the quasiparticle mass is no longer that of the

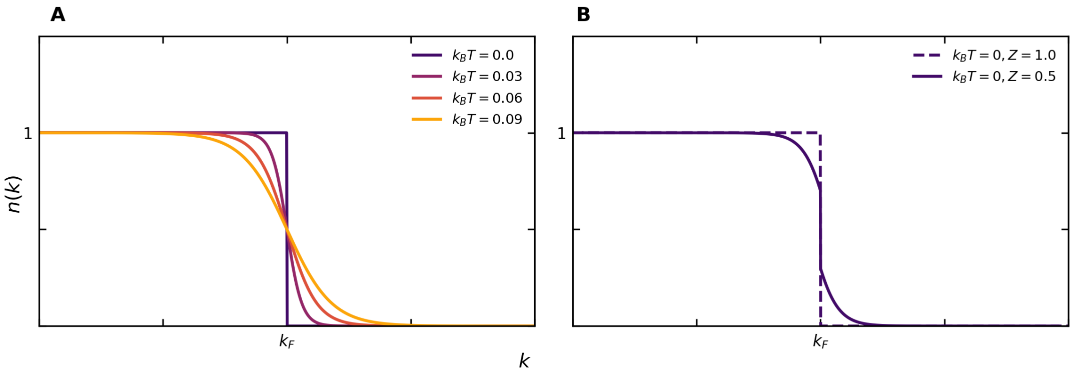

Figure 2.2: (a) The occupation function of both a non-interacting electron gas and that of quasi-particles in a Fermi liquid. (b) The occupation function of interacting electrons in a Fermi liquid at $T = 0$.

non-interacting electron. (It should be noted that this is an additional renormalisation to that of a free-electron with the introduction of a crystal lattice). That is, $m_b \to m^*$. As a consequence, the form of the specific heat, for example, is expected to retain it's free-electron form with a modified magnitude, in agreement with experimental observations. Another particular success of Fermi liquid theory is the prediction of a quadratic-in-temperature resistivity at low temperatures. This finding is discussed later.

2.1.5 Boltzmann Transport Theory

Boltzmann transport theory was developed to describe the out-of-equilibrium properties of an electron gas, e.g., the properties under the influence of external fields and/or temperature gradients. At its root, it seeks an answer by describing the evolution with time of $f_\mathbf{k}(\mathbf{r})$, the concentration of electrons in the vicinity of $\mathbf{r}$ that are in state $\mathbf{k}$, by considering diffusion, scattering and the influence of external fields. It follows that when in a steady state:

$$\frac{df}{dt} = \left(\frac{\partial f}{\partial t}\right)_{diff} + \left(\frac{\partial f}{\partial t}\right)_{scatt} + \left(\frac{\partial f}{\partial t}\right)_{ext} = 0 \tag{2.10}$$

First, the diffusion term is considered. If an electron in state $\mathbf{k}$ has a velocity $\mathbf{v_k}$, it will travel a distance $\delta t \mathbf{v_k}$ in time δt. It follows that the number of electrons in the vicinity of $\mathbf{r} + \delta t \mathbf{v}$, will increase by the same amount that the number at $\mathbf{r}$ will decrease:

$$f_\mathbf{k}(\mathbf{r}, \delta t) = f_\mathbf{k}(\mathbf{r} - \delta t \mathbf{v}, 0) \tag{2.11}$$

or equivalently:

$$\frac{\partial f_{\mathbf{k}}}{\partial t}|_{diff} = -\frac{\partial f_{\mathbf{k}}}{\partial \mathbf{r}} \cdot \mathbf{v}_{\mathbf{k}} \tag{2.12}$$

The term due to external fields can be similarly considered. In the presence of external electric and magnetic fields **E** and **B**:

$$\frac{d\mathbf{k}}{dt} = \frac{e}{\hbar}(\mathbf{E} + \mathbf{v}_{\mathbf{k}} \times B) \tag{2.13}$$

After a time interval δt, electrons will have increased their momentum by $(d\mathbf{k}/dt)\delta t$:

$$f_{\mathbf{k}}(\mathbf{r}, \delta \mathbf{t}) = f_{\mathbf{k}-(d\mathbf{k}/dt)\delta t}(\mathbf{r}, 0) \tag{2.14}$$

or equivalently:

$$\frac{\partial f_{\mathbf{k}}}{\partial t}|_{ext} = -\frac{e}{\hbar}\left(\mathbf{E} + \mathbf{v} \times \mathbf{B}\right) \cdot \frac{\partial f_{\mathbf{k}}}{\partial \mathbf{k}} \tag{2.15}$$

If an applied field (force) is suddenly turned off, it is expected that the electrons will return to their zero-field states and they achieve this via scattering mechanisms. The scattering term is simplified by using the ‘relaxation time approximation’. Within this approximation, there is an exponential relaxation back to equilibrium. Alternatively put, when in equilibrium (no fields are present) the system is perturbed from its equilibrium $f^0_{\mathbf{k}}$ to a steady state $f_{\mathbf{k}}$. We can define the perturbation $g_{\mathbf{k}}$ as the difference between the steady-state and equilibrium distributions $g_{\mathbf{k}} = f_{\mathbf{k}} - f^0_{\mathbf{k}}$ and this perturbation is assumed to exponentially decay to zero:

$$g_{\mathbf{k}}(t) = g_{\mathbf{k}}(0)^{-t/\tau} \tag{2.16}$$

where τ is a characteristic relaxation time associated with the scattering mechanisms at play. Within the relaxation time approximation, it follows that:

$$\frac{\partial f_{\mathbf{k}}}{\partial t}|_{scatt} = -\frac{g_{\mathbf{k}}}{\tau} = \frac{\partial f_{\mathbf{k}}}{\partial \epsilon_{\mathbf{k}}}\frac{e}{\hbar}\left(\mathbf{E} + \mathbf{v} \times \mathbf{B}\right) \tag{2.17}$$

Using the definition of $g_{\mathbf{k}}$ and the above equation we find that:

$$\frac{g_{\mathbf{k}}}{\tau} = -\frac{e}{\hbar}\left(\mathbf{E} + \mathbf{v} \times \mathbf{B}\right)\left(\frac{\partial g_{\mathbf{k}}}{\partial \mathbf{k}} + \frac{\partial f^0_{\mathbf{k}}}{\partial \mathbf{k}}\right) \tag{2.18}$$

from which the linearised Boltzmann equation can be derived:

$$\frac{g_{\mathbf{k}}}{\tau} + \frac{e}{\hbar}\left(\mathbf{v} \times \mathbf{B}\right)\frac{\partial g_{\mathbf{k}}}{\partial \mathbf{k}} = e\mathbf{E} \cdot \mathbf{v}\left(-\frac{\partial f^0_{\mathbf{k}}}{\partial \epsilon}\right) \tag{2.19}$$

Many out-of-equilibrium properties can be derived from the Boltzmann transport equation. If the zero-field conductivity is considered, for example, we need to consider an equilibrium function $f^0_{\mathbf{k}}$ that is perturbed by an electric field $\mathbf{E}$. This perturbation will cause a displacement of k-states in the direction of $\mathbf{E}$. The displacement $\delta k = e\tau\mathbf{E}/\hbar$. It therefore follows from $\mathbf{p} = \hbar\mathbf{k}$ and $\mathbf{v} = dE/d\mathbf{k}$ that for a charge carrier with mass m^*, the change in its velocity is given by:

$$\delta\mathbf{v} = -\frac{e\tau\mathbf{E}}{m^*} \tag{2.20}$$

If the carrier concentration is given by n, the current density $\mathbf{J} = ne\delta\mathbf{v} = ne^2\tau\mathbf{E}/m^*$ and the conductivity is given by:

$$\sigma = \frac{ne^2\tau}{m^*} \tag{2.21}$$

in accordance with the Drude model.

2.2 Resistivity

As has been explained, a resistance to the flow of electrical current is the result of various scattering processes between electrons and phonons, lattice defects, impurities and other electrons. If, for example, an ideal spherical Fermi surface is considered (as one would expect from isotropically dispersing bands), the resistivity tensor is given by:

$$\rho = \begin{pmatrix} \frac{m^*}{ne^2\tau} & 0 & 0 \\ 0 & \frac{m^*}{ne^2\tau} & 0 \\ 0 & 0 & \frac{m^*}{ne^2\tau} \end{pmatrix} \tag{2.22}$$

Each of the aforementioned scattering processes will be characterised by their own scattering time τ and will therefore each have an affect upon the zero-field resistivity. If the scattering mechanisms are sufficiently independent, it is often a good approximation to combine their effects using Matthiessen's rule in which scattering times are added in parallel:

$$\frac{1}{\tau} = \sum_i \frac{1}{\tau_i} \tag{2.23}$$

or alternatively, scattering rates $\Gamma(=1/\tau)$ are added in series:

$$\Gamma = \sum_i \Gamma_i \tag{2.24}$$

Some common scattering mechanisms that are relevant to this work are discussed further in this section.

2.2.1 Electron-Phonon

The predominant contribution to the resistivity at high temperatures is that from electron-phonon scattering. The Debye temperature $k_B\Theta_D = \hbar\omega_{max}$ is fixed by the energy of the highest frequency phonons and itself sets a temperature scale above and below which the temperature dependence of electron-phonon scattering is expected to be different. At high temperatures such that $T \gg \Theta_D$, all phonons are thermally excited with energies that are necessarily small compared with k_BT, the energy range over which the Fermi distribution is smeared. In this scenario, electron-phonon scattering is approximately elastic and scattering is simply proportional to the phonon population [12]. Phonons are governed by Bose-Einstein statistics. The occupation number $\bar{n}(\omega)$ of a phonon with frequency ω is therefore given by

$$\bar{n}(\omega) = \frac{1}{e^{\hbar\omega/k_BT} - 1} \tag{2.25}$$

In the $T \gg \Theta_D$ limit, $\bar{n} \sim k_BT/\hbar\omega$. It therefore follows that $\rho_{e-p} \propto T$ at high temperatures.

At low temperatures, the typical phonon energy $\hbar\omega \ll k_B\Theta_D$. Electrons can therefore only scatter into states with momenta that are in close proximity of their initial wavevector (due to the low phonon momentum transfer) and within a small shell of energies (within $\sim k_BT$) from E_F. Scattering can only occur in small steps around the Fermi surface. Following [12], an estimate of ρ_{e-p} can be made by considering the diffusional motion along the Fermi surface and it can be shown that

$$\rho_{e-p} \sim \frac{m*}{\hbar e^2 n} T^5. \tag{2.26}$$

2.2.2 Impurities and Defects

At the lowest temperatures, it might be anticipated that the resistivity would fall to zero as temperature also approaches zero. Experimentally, this is not found to be the case. A finite zero-temperature value ρ_0, termed a *residual resistivity*, is observed that arises from the presence of lattice defects and impurities that break translational symmetry. At the lowest temperatures, impurity and defect scattering is the dominant scattering mechanism. As Matthiessen's rule suggests (Equation 2.23), the following form is often found to be a good approximation for the observed low-temperature form of the total resistivity:

$$\rho = \rho_0 + \rho_{e-p}(T) \tag{2.27}$$

An estimate of the residual resistivity can be found using:

$$\rho_0 \sim \frac{\hbar k_f}{e^2 n \ell} \tag{2.28}$$

where ℓ, the mean-free-path, is inversely proportional to the impurity or defect density and proportional to the scattering rate [12].

Using the residual resistivity to determine impurity densities and scattering rates in absolute terms is difficult and not always possible. However, the high-temperature resistivity that is dominated by electron-phonon scattering is dependent upon material properties that are likely to be mostly sample-independent. Consequently, it is often the case that the high-temperature resistivity does not vary between samples of a given material whilst the residual resistivity varies depending on the purity and defect-density of the individual sample. For this reason, the residual resistivity ratio (RRR), commonly defined as $\rho(T = 300\text{K})/\rho(T = 0\text{K})$, is often used as a indicator of sample quality when comparing multiple samples of the same material. It should be noted that because the high-temperature resistivity is dominated by material specific properties, a comparison of the RRR between samples of different materials is not necessarily helpful.

2.2.3 Electron-Electron

As has been mentioned, a key feat of Fermi liquid theory is the prediction of a quadratic low-temperature contribution to the resistivity. This component is often found to be small in simple uncorrelated systems in which the electron-electron interaction is small. In those systems that are highly correlated, however, this quadratic term is expected to be large. As a result, the observation of a T^2 resistivity is often taken to be a signature of a material in which strong electron correlations play an important role. Examples of such families of materials are unconventional superconductors and heavy fermion systems.

Electron-electron scattering mechanisms involves the scattering of two quasiparticles from occupied states into unoccupied states. One must be excited whilst the other must decay in order for energy to be conserved. Thermal excitation will limit the availability of unoccupied states for higher-energy quasiparticles to decay into to within k_BT of the Fermi surface. As a result, the corresponding excitation will remain within k_BT of the Fermi surface as well. In a single scattering event, the final states of both quasiparticles will remain within a shell of the Fermi surface with a thickness $\sim k_BT$. It follows that the electron-electron scattering rate τ_{e-e} is proportional to the square of the volume of this shell. For low temperatures (small thicknesses), a spherical shell with a mean radius k_F has a volume $\sim \frac{4}{3}\pi k_F^2 k_BT$. τ_{e-e} and ρ_{e-e} are therefore $\propto T^2$ at low temperatures [13].

To conclude, different scattering mechanisms are expected to have different temperature-dependent scattering times that depend on the microscopic details of the mechanisms themselves. Each of these manifest themselves differently in the zero-field resistivity. Careful study of the resistivity of a material is therefore a useful probe of the microscopic origin of these mechanisms.

2.3 Magnetotransport

The two principle phenomena discussed in this section are the Hall effect and magnetoresistance. Short discussions of each are presented in this section.

2.3.1 The Hall Effect

As has been briefly discussed in the context of the Drude model in Section 2.1.1, with the application of a magnetic field, the Lorentz force experienced by charge carriers will result in the generation of a transverse Hall voltage perpendicular to both current and the applied field. Again, if isotropically dispersing bands are considered and the magnetic field is applied $B \parallel c$, the resistivity tensor becomes:

$$\rho = \begin{pmatrix} \frac{1}{\sigma_0} & \frac{\omega_c\tau}{\sigma_0} & 0 \\ \frac{\omega_c\tau}{\sigma_0} & \frac{1}{\sigma_0} & 0 \\ 0 & 0 & \frac{1}{\sigma_0} \end{pmatrix} \tag{2.29}$$

where $\sigma_0 = ne^2\tau/m^*$ (the Drude result). The magnetic field dependence is introduced in the off-diagonal terms. In this simple case, the Drude result for the Hall coefficient is also returned:

$$R_H = \frac{\rho_{xy}}{B} = -\frac{1}{ne} \tag{2.30}$$

In this simple scenario, the Hall coefficient can be used to probe the sign of the charge carriers (whether they are electrons or holes) as well as the carrier density.

If the resistivity tensor is considered more generally by inverting the conductivity tensor:

$$\rho = \sigma^{-1} = \begin{pmatrix} \frac{\sigma_{yy}}{\sigma_{xx}\sigma_{yy}-\sigma_{xy}\sigma_{yx}} & -\frac{\sigma_{xy}}{\sigma_{xx}\sigma_{yy}-\sigma_{xy}\sigma_{yx}} & 0 \\ -\frac{\sigma_{yx}}{\sigma_{xx}\sigma_{yy}-\sigma_{xy}\sigma_{yx}} & \frac{\sigma_{xx}}{\sigma_{xx}\sigma_{yy}-\sigma_{xy}\sigma_{yx}} & 0 \\ 0 & 0 & \frac{1}{\sigma_{zz}} \end{pmatrix} \tag{2.31}$$

the more general form of the Hall coefficient is given by:

$$R_H = \frac{\rho_{xy}}{B} = -\frac{\sigma_{xy}}{\sigma_{xx}\sigma_{yy} - \sigma_{xy}\sigma_{yx}}\frac{1}{B} \tag{2.32}$$

Simplifications can be made based on the symmetry arguments that are relevant to the system in question.

2.3.2 Magnetoresistance

As was shown in Section 2.2, in a strictly isotropic system in which the Fermi surface is expected to be spherical, the field-dependent terms in the resistivity tensor are all off-diagonal. The magnetoresistance (MR), $\Delta\rho/\rho_0$ defined as $(\rho(B,T) - \rho(B=0,T)/\rho(B=0,T)$, is zero. Again, if the generalised resistivity tensor (Equation 2.31) is considered, it can be seen that in general

$$\rho_{xx} = \frac{\sigma_{yy}}{\sigma_{xx}\sigma_{yy} - \sigma_{xy}\sigma_{yx}} \tag{2.33}$$

As before, simplifications based upon crystal symmetry can be made. However, in general, if an anisotropic system is considered, the longitudinal resistance will be dependent upon field-dependent off-diagonal terms in the conductivity tensor and the magnetoresistance will no longer be zero.

So far the scattering rate τ has been assumed to be isotropic. That is, it is the same everywhere on the Fermi surface. Also, only a single carrier species has been considered. In this case $\rho_0 (= \rho(B=0,T))$ is proportional to the scattering rate and the magnitude of the field dependence of ρ is determined by $\omega_c\tau$. It then follows that the temperature dependence of the MR is proportional to ρ_0. Therefore:

$$MR = \frac{\Delta\rho}{\rho_0} = f(\frac{B}{\rho_0}) \tag{2.34}$$

and plots of $\Delta\rho/\rho_0$ against $f(B/\rho_0)$ will collapse onto a universal curve. This is known as Kohler's rule and the corresponding collapse of the MR is known as Kohler's scaling and should, in principle, occur for all Fermi surface geometries if the scattering that introduces a finite MR is the same as that which determines the zero-field resistivity. Violation of Kohler's scaling may be indicative of the presence of more than one species of carrier. Alternatively, it can be caused by a temperature dependence to the electronic structure (T-dependent n, m^* for example) or the presence of a T-dependent anisotropy of the scattering rate. Finally, violation will occur if the origin of scattering that generates the MR and that which is responsible for $\rho(T)$ are different such that they have their own (different) temperature dependencies.

In summary, both the Hall effect and magnetoresistance serve as additional tools from which the details of the nature of charge carriers in metals and their associated scattering processes can be revealed.

2.4 Quantum Oscillations

In the presence of a magnetic field, quasiparticle orbital motion is quantised with allowed states residing on concentric tubular surfaces of constant energy oriented along the axis of the applied field. These cylinders, termed *Landau tubes*, increase in radius with increasing field strength. As only Landau tubes that reside below the chemical potential are populated, the expansion of Landau tubes from below to above the Fermi surface results in a periodic depopulation of quasiparticle states at the Fermi level and a corresponding oscillatory behaviour in the free energy. Consequently, oscillatory behaviour, *quantum oscillations*, will be seen in any properties that are coupled to the density of states at the Fermi-level, for example. Perhaps the most widely-studied quantum oscillations are de Haas-van Alphen and Shubnikov-de Haas oscillations, oscillations in magnetisation and resistivity respectively.

An understanding of the interactions that give rise to renormalised properties of a Fermi liquid, for example, can be gained through measurements of the renormalised values themselves. Quantum oscillations serve as one tool for achieving exactly this. Relevant to this work, they serve as perhaps the least ambiguous experimental tool for verifying the geometry of a computed Fermi surface. As will be seen, although quantum oscillations are insensitive to the k-space location of an orbit, the frequencies themselves strongly constrain which geometries agree with experiment in a manner than other probes do not.

Following this summary are descriptions of the origin and properties of quantum oscillations from which details of the Fermi surface and quasiparticle properties can be derived. A far more comprehensive exploration is found in the book, *Magnetic Oscillations in Metals*, by Shoenberg [14]. Much of what follows can be found in more mathematical detail in this book.

2.4.1 Quantum Oscillations at Zero Temperature

In a magnetic field, charged particles with non-zero momentum will experience a transverse Lorentz force. The Hamiltonian for an electron with $\mathbf{p} = (p_x, 0, 0)$ in a magnetic field $\mathbf{B} = (0, 0, B)$ is:

$$\hat{H} = \frac{\hat{p}_x^2}{2m} + \frac{(\hat{p_y} + eB\hat{x})^2}{2m}. \tag{2.35}$$

Substituting in the cyclotron frequency $\omega_c = eB/m$ and noting that $\hat{p} = \hbar k$ gives:

$$\hat{H} = \frac{\hat{p}_x^2}{2m} + \frac{m\omega_c^2}{2}\left(\hat{x} + \frac{\hbar k_y}{eB}\right)^2 \tag{2.36}$$

which is exactly that of a harmonic oscillator shifted in x by $\hbar k_y/eB$. Thus, energy is analogously quantised and is given by:

$$E_n = \hbar\omega_c(n + 1/2) \tag{2.37}$$

We can therefore conclude that a magnetic field $\mathbf{B} \perp \mathbf{p}$ will turn straight-line trajectories of electrons into helices in the plane perpendicular to the applied field and this in-plane helical motion is quantised. Motion in the z direction (parallel to B) remains unchanged. The quantisation is therefore such that states are confined in to concentric cylinders, *Landau levels*, in k-space that grow with increasing magnetic field.

As magnetic field is swept, Landau levels will increase in radius and periodically pass through the Fermi energy. As they do, there will be a periodic increase and subsequent decrease in the density of states at the Fermi energy. Quantities that are coupled to the density of states will oscillate in field accordingly. The area of a Landau tube is given by:

$$S(E, k) = (n + \gamma)\frac{2\pi eB}{\hbar} \tag{2.38}$$

where γ is a fixed phase. The spacing between adjacent tubes is

$$\Delta S = \frac{2\pi eB}{\hbar} \tag{2.39}$$

Quantities that are sensitive to this periodicity will therefore exhibit oscillatory behaviour that is periodic in $1/B$ with a frequency given by

$$F = \frac{\hbar}{2\pi e} S \tag{2.40}$$

For a cylindrical Fermi surface and with a magnetic field oriented along it's long axis, it is clear that population and depopulation will occur at all points of the Fermi surface at once. For complex Fermi surfaces, population and depopulation of states will occur at different k-space locations at different field strengths depending on the form of $k_F(\theta, z)$. Destructive interference of all of these oscillatory signals occurs for all points on the Fermi surface except those where the area in the plane perpendicular to B is extremal. Quantum oscillations will therefore contain only those frequencies that are related via Equation 2.40 to extremal cross-sectional areas of the Fermi surface. The oscillatory frequencies and their angle-dependence therefore reveal the geometry of the Fermi surface.

2.4.2 Damping Factors

There are numerous possible reasons for the measured oscillation amplitudes to be lower than in the idealised scenario previously described. Temperature is perhaps the most obvious extrinsic parameter whilst the electron relaxation time and sample inhomogeneity will also result in a decrease in the observed amplitude of oscillations.

Although there are numerous factors, it is the case that they are all manifestations of the same basic premise. Each mechanism has the effect of 'phase smearing' in which the frequency or phase is broadened continuously, or becomes distributed, over a finite range. A superposition of oscillations now needs to be considered. If the distribution function of the smearing is given by $D(z)$ where $z = \phi/\lambda$ and ϕ is the difference between the phase and its unsmeared value ψ, the effect of the smearing is simply to reduce the amplitude by a multiplicative factor

$$R = \frac{\mid \int_{-\infty}^{\infty} e^{i\lambda z} D(z) dz \mid}{\int_{-\infty}^{\infty} D(z) dz} = \frac{\mid f(\lambda) \mid}{f(0)} \tag{2.41}$$

where the numerator is the Fourier transform of the smeared distribution $D(z)$ with respect to λ, a parameter that is characteristic of the smearing mechanism being considered [14]. An important consequence of this observation is that the damping factor for each smearing mechanism can be calculated in isolation and their effects multiplied together.

Although they are hindrance in that they make the observation of quantum oscillations somewhat more challenging (necessitating low temperatures and clean, homogeneous samples), an understanding of the form of each damping factor makes the extraction of important material properties possible. The most common damping factors and how the relevant material properties can be extracted from their measurement will now follow.

2.4.3 Temperature Damping Factor

At a finite temperature T, the occupation of states becomes distributed in energy and is determined by the Fermi function

$$f(\epsilon) = 1/(1 + e^{(\epsilon - E_F)/k_B T}) \tag{2.42}$$

where the Fermi energy E_F remains the midpoint around which the probability of occupation becomes smeared. The periodic population and depopulation of Landau tubes in increasing magnetic field will consequently become a smoothed process. Intuitively, this can be understood by considering the distribution of extremal orbits that a distribution of energies around the Fermi energy would lead to. Alternatively yet equivalently, one could consider a weighted distribution of metals each at $T = 0$ with their own Fermi energies μ. It is necessary that the weight of the contribution for $\mu > \epsilon$ is given by

$$-\frac{df(\mu)}{d\mu} \tag{2.43}$$

as the integral of this distribution between ϵ and ∞ correctly yields the Fermi distribution. This distribution can be rewritten as:

$$-\frac{df(\mu)}{d\mu} = \frac{1}{2k_B T(1 + \cosh(\mu - E_F)/k_B T)}. \tag{2.44}$$

As was previously noted, the Fourier transform of the smearing distribution is required in order to determine the multiplicative damping factor. The form of the damping factor in this instance is therefore:

$$R = \frac{\mid f(\lambda) \mid}{f(0)} = \frac{\pi\lambda}{\sinh\pi\lambda} = \frac{2\pi^2 p k_B T/\beta H}{\sinh(2\pi^2 p k_B T/\beta H)} \tag{2.45}$$

where p is an integer corresponding to harmonic order. That is:

$$R_T(m_c, T) = \frac{x}{\sinh(x)}, x = \frac{2\pi^2 k_B m_c T}{\hbar e B} \tag{2.46}$$

The Lifshitz-Kosevich form of the temperature damping factor above only contains a single material-dependent property, the cyclotron mass m_c. It is therefore possible for the cyclotron mass to be determined from a fit of the measurement of the temperature dependence of the oscillation amplitude to a curve of the form given in Equation 2.46. The temperature dependence of the amplitude of quantum oscillations for different values of magnetic field and quasiparticle mass are illustrated in Figure 2.3.

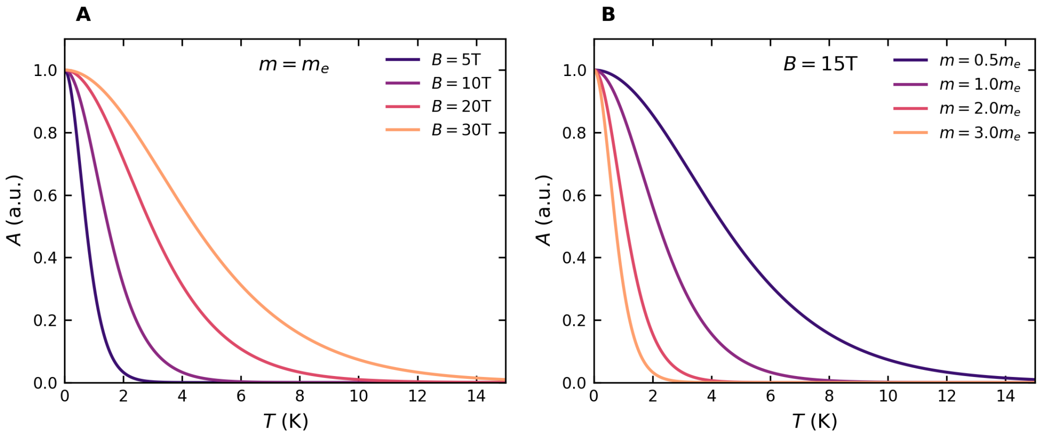

Figure 2.3: The temperature dependence of quantum oscillation amplitudes for (a) different magnetic field strengths and (b) different quasiparticle effective masses. Oscillation amplitude decays more slowly with temperature at higher magnetic fields and with lower effective masses.

It is clear that higher-fields and lower masses allow for the observation of oscillations at higher temperatures. This can be intuitively understood from the dispersion of heavy and light bands. The area of orbits associated with highly dispersive (light) bands (large $d\epsilon/dk$) will change little within k_BT of the Fermi energy. Conversely, the area of orbits associated with non-dispersive (heavy) bands (large $d\epsilon/dk$) will vary a lot within k_BT of the Fermi energy. It is therefore expected that the phase smearing associated with temperature will be exacerbated as the quasiparticle mass increases. The mass in question throughout this discussion has been denoted m_c, the cyclotron mass. The mass as measured by quantum oscillations is sensitive to both lattice and Fermi-liquid renormalisation. It is therefore a means of determining m^*.

2.4.4 Dingle Damping Factor

Broadly speaking, the Dingle damping factor is a measure of the scattering rate. Scattering broadens what would otherwise be sharp energy levels leading to phase smearing that is, again, equivalent to the presence of a distribution of Fermi energies. As was the case for the temperature damping factor, the Fourier transform of the smearing distribution determines the form of the damping factor. In this instance, the broadening is described by a Lorentzian and it therefore follows that the form of the Dingle damping factor is given by:

$$R_D(m_c, \tau) = e^{-\frac{\pi p}{\omega_c \tau}} = e^{-\frac{\pi p}{\omega_c \tau}} \tag{2.47}$$

It is useful to note that, at low temperatures, the form of the Dingle damping factor is similar to that of the temperature damping factor. It is therefore possible to equate the reduction in amplitude due to scattering to an equivalent rise in temperature, the Dingle temperature T_D:

$$\tau = \hbar/(2\pi k_B T_D) \tag{2.48}$$

The Dingle temperature is the quantity most usually quoted when expressing the magnitude of the Dingle damping term.

The Dingle damping factor is dependent upon both the cyclotron mass and the quasiparticle lifetime due to impurities and disorder. If the mass is known (for example through analysis of the temperature dependence of oscillation amplitudes), the scattering time (and rate) can be determined.

2.4.5 Zeeman Damping Factor

The final damping term addressed here, primarily for completeness, is that which arises from spin splitting. In the presence of a magnetic field, it might be expected that Zeeman splitting will cause the Landau levels to become split. That is, there is a field-dependent energy separation of spin-up and spin-down states. The form of R_S, the spin splitting damping factor has the following form:

$$R_S = \cos(\frac{\pi^g m_b(1+S)}{2m_e}) \tag{2.49}$$

where $1+S$ is the Stoner enhancement factor, g is the g-factor and m_b, m_e are the band and electron masses respectively.

Information relating to the normalised spin susceptibility χ^* is contained within the Zeeman damping factor. In order to extract this information, it is convenient to use a ‘crossed-field technique’ [15] in which a second solenoid is used such that two perpendicular components of the applied magnetic are independently tunable. It might be chosen, for example, that the components are oriented parallel and perpendicular to a particular crystallographic axis ($B_{\parallel}$, $B_{\perp}$). Then, in the absence of $B_{\parallel}$, $B_{\perp}$ can be swept and a constant damping factor given by 2.49 will be present. However, in the presence of a fixed $B_{\parallel}$, the rates at which the Landau tubes associated with spin-up

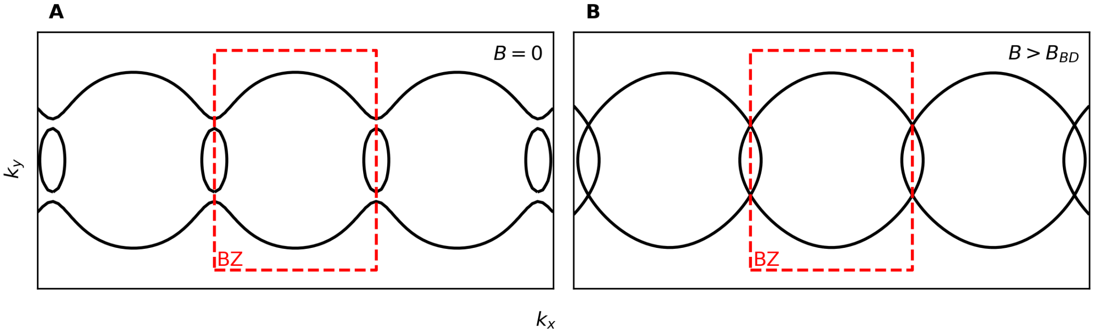

Figure 2.4: A schematic representation of a Fermi surface (black line) comprised of both a closed and open Fermi sheet separated by a gap. A repeated Brillouin zone is marked in red. At low fields (a) only a single orbit will be observed whilst at fields greater than the breakdown field associated with the gap (b), an additional high-frequency breakdown frequency may be observed.

and spin-down quasiparticles will be different and will pass through the Fermi energy either in or out of phase. An additional beating is introduced to the measured oscillatory signal. χ^* can be extracted through analysis of this additional beating [15].

2.4.6 Magnetic Breakdown

At sufficiently high magnetic fields, it is possible to observe oscillations with frequencies other than those associated with the closed extremal orbits of the Fermi surface. If the cyclotron energy of the quasiparticles is high enough and different Fermi sheets are separated by a sufficiently small gap in k-space, it is possible for them to tunnel between different Fermi sheets. In this instance, quasiparticles can complete closed orbits comprising of sections from different Fermi sheets and new breakdown frequencies will be generated. The probability of tunnelling is exponentially dependent upon magnetic field and is characterised by a breakdown field B_{BD}:

$$P \propto e^{-B_{BD}/B} \tag{2.50}$$

where B_{BD} is proportional to the square of the gap ($(\Delta k)^2$).

The first observation of magnetic breakdown was made by Priestley who observed high frequency oscillations in Mg that corresponded to orbits that were larger than the BZ [16]. Another scenario in which breakdown can occur is one in which there is tunnelling between open orbits that would otherwise not produce oscillations. This scenario is depicted schematically in Figure 2.4 in which tunnelling occurs between an open and closed Fermi sheet.

In summary, magnetic breakdown leads to the appearance of additional frequencies in the frequency spectrum of oscillatory quantities at frequencies that are equal to linear combinations of those associated with the fundamental orbits. Speaking qualitatively, at fields of the order of some characteristic breakdown field, B_{BD}, related to the size of a gap, the amplitude of the fundamental frequencies will be suppressed from their anticipated value as quasiparticle weight is transferred from the fundamental orbits to the breakdown orbits.

2.5 Quantum Critical Metals

The phase transition between an ordered and a disordered state is typically governed by thermodynamics and driven by thermal fluctuations. For second order phase transitions in which an order parameter goes to zero at the phase transition, temporally fluctuating patches of the ordered phase begin to appear in the disordered state with a characteristic length and time known as the *correlation length* ξ and *correlation time* ξ_t as the transition is approached. For a phase transition in T for example, the correlation length grows as temperature is reduced and diverges (extends over the entire sample) when $T = T_c$ where T_c is the critical temperature. One can imagine a similar transition where the tuning parameter is not temperature, but pressure, magnetic field or chemical composition for example. At high temperatures, thermal fluctuations still dominate and the phenomenology is much the same. At $T = 0$, it is still possible to tune a system through a phase transition by varying a non-thermal tuning parameter. In the case of pressure, the phase boundary is tuned to zero-temperature at $P = P_c$. As $T = 0$, it is clear than thermal fluctuations can not be the driving mechanism. The driving mechanism are quantum fluctuations deriving from Heisenberg's uncertainty principle. The $T = 0$ end point of the phase boundary is known as a quantum critical point (QCP).

In a quantum mechanical system, thermal fluctuations can be characterised by their own timescale given by [17]

$$L_T = \frac{\hbar}{k_B T} \tag{2.51}$$

There are now two relevant timescales that are both dependent upon temperature, ξ_t which characterises the quantum fluctuations of the ordered state and L_T which characterises the timescale of thermal fluctuations. If $\xi_t \ll L_T$, the system is principally governed by quantum fluctuations and thermal fluctuations do not play a major role. If the transition is from an ordered to disordered phase at $P = P_c$, the properties of the system are determined by the quantum ground state of the ordered phase for $P < P_c$ and disordered phase for $P > P_c$. If $\xi_t \gg L_T$, thermal fluctuations are

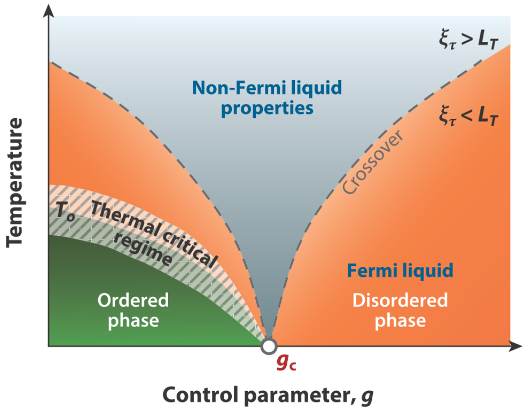

Figure 2.5: A schematic phase diagram showing the fan-like region of phase space within which the properties of a system are heavily influenced by a QCP at $T = 0$ (figure from [17]).

dominant and the properties of the system can deviate strongly from those of either ground state. As ξ_t diverges near P_c, the temperature at which L_t becomes relevant becomes increasingly small. A fan-like region of phase space can be delineated by the crossover where $\xi_t \sim L_T$. Within this fan, the properties of the system are strongly affected by fluctuations associated with the underlying QCP at $T = 0$. This is illustrated schematically in Figure 2.5.

Notable examples of systems in which it is postulated that an underlying QCP is responsible for the properties at finite temperature are the normal-state transport properties of cuprates [18] and $\mathrm{FeSe}_{1-x}\mathrm{S}_x$ [19]. In the former, it has been suggested that the doping at which the so-called *pseudogap* closes at $T = 0$ defines a QCP [20] that is responsible for the normal-state transport properties (e.g. a T-linear resistivity) at finite temperature [18]. Similarly, the temperature at which the nematic transition temperature is suppressed to $T = 0$ in $\mathrm{FeSe}_{1-x}\mathrm{S}_x$ has been shown to coincide with a similar evolution from Fermi-liquid-like T^2 resistivity to T-linear resistivity in the vicinity of the QCP [19].

2.5.1 Quadrature Magnetoresistance

Although not currently accepted to be a generic property of quantum critical metals, or a feature that is widely associated with quantum critical points, in light of the work presented here on $\mathrm{Tl_2Ba_2CuO_{6+\delta}}$, it is necessary to include an introductory foreword on the so called ‘quadrature’ magnetoresistance than has been associated with quantum critical points in a small number of systems, namely $\mathrm{La}_{2-x}\mathrm{Sr}_x\mathrm{CuO}_4$ (LSCO) [22], $\mathrm{BaFe_2(As_{1-x}P_x)_2}$ (P-Ba122) [21] and $\mathrm{FeSe}_{1-x}\mathrm{S}_x$ [23].

In the case of P-Ba122 with $x = 0.31$, both high-temperature T-linear and high-field H-linear

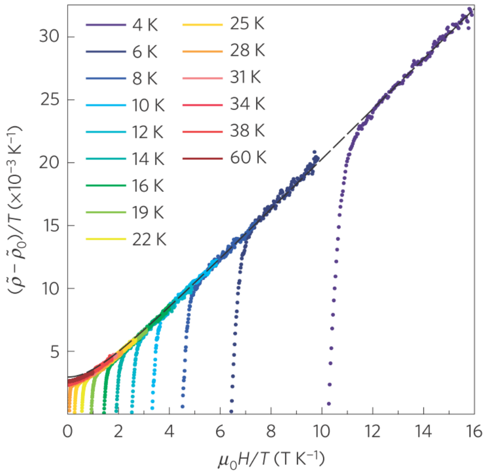

Figure 2.6: The characteristic quadrature collapse of field sweeps taken at different temperatures in P-Ba122 at $x = 0.31$ from [21].

behaviour are observed [21]. Furthermore, it has been empirically determined that the field- and temperature-dependence of the magnetoresistance is precisely described by:

$$\rho(H,T) - \rho(0,0) \propto \sqrt{(\alpha k_B T)^2 + (\gamma \mu_B \mu_0 H)^2} \tag{2.52}$$

where α and γ are coefficients that are determined by the high-T and high-B slopes respectively. That is, there is an equivalence between temperature and magnetic field and the magnetoresistance of P-Ba122 at $x = 0.31$ is described by the weighted quadrature sum of temperature and magnetic field energy scales. A natural consequence of such a relationship is that if $(\rho(H,T) - \rho(0,0))/T$ is plotted against H/T, all field-sweeps will collapse onto a single curve of the form $b\sqrt{1 + (\beta H/T)^2}$ regardless of the temperature at which they were taken. Indeed, this is what is experimentally found (Figure 2.6 from [21]).

A quantum critical point at $x = 0.31$ in P-Ba112 has been well established and corroborated by other experimental observations other than a strictly T-linear resistivity. $x = 0.31$ is also the doping at which there is a marked local enhancement of the specific heat jump at T_c, the dHvA mass [24] and penetration depth [25] (all of which can be interpreted as an enhancement of the quasiparticle effective mass). The quadrature form of the MR phenomenologically ties the origin of the T-linearity associated with the quantum critical point to an equivalent H-linearity.

A similar observation has been made in FeSe$_{1-x}$S$_x$ [23]. With $H \parallel c$, the low-field MR was found to be strictly H^2-dependent whilst the limiting high-field behaviour was found have an $H + H^2$-dependence. Although not strictly linear, after the subtraction of the low-field H^2 component, the remaining magnetoresistance was found to be quadratic at low field and linear at high field and could be perfectly fitted to a curve of the quadrature form $b\sqrt{1+(\beta H/T)^2}$. Furthermore, the fractional size of the quadrature component was found to be peaked at $x = 0.16$, the same doping at which T-linearity was found to extend down to lowest temperatures in the presence of a superconductivity-suppressing magnetic-field oriented $H \parallel ab$ [19].

Suggestively, the doping dependence of the relative size of the quadrature component is similar to that of the A coefficient of the T^2 resistivity. This is indicative of a scenario in which both the quadrature MR and mass enhancement associated with the nematic quantum critical point share a common origin. This was interpreted by the authors of [23] as evidence for the coexistence of an orbital H^2-component and an additional quadrature component of a quantum-critical nature that each contribute to the total magnetoresistance in $\mathrm{FeSe}_{1-x}\mathrm{S}_x$.

Lastly, in LSCO and for a range of dopings between $p = 0161$ and $p = 0.190$, the magnitude of the T-linear slope of the resistivity and the H-linear slope of the magnetoresistance (at low temperatures) were found to evolve with doping in unison suggesting, again, that they are of a common origin [22].

Chapter 3

Experimental Methods

The unifying feature of the studies presented in this thesis, and the derivation of its title, are the experimental techniques that have been deployed: transport measurements at low temperatures, high magnetic fields and under hydrostatic pressure. In this chapter, the methods used to achieve each of these three 'extreme' conditions are detailed. In addition, a small number of secondary methods are briefly discussed. Some finer details of the procedures are dependent upon the material being investigated. These material-specific procedures and methods are discussed later and in more detail in their relevant chapters.

3.1 Transport Measurements

Throughout this thesis, the standard four-point contact configuration was used to measure both resistivity and the Hall effect measurements. In this configuration, it is necessary to make at least four electrical contacts to each sample. Via two contacts, a current is passed from the source to the drain contact. In addition, a voltage is measured between two additional contacts such that contributions to the total loop resistance from both the measurement lines and contact resistances are excluded from the measurement. For all measurements presented in this thesis, an alternating excitation current with a frequency of the order of 20 Hz to 200 Hz and a magnitude of the order of 100 µA to 2 mA was supplied by a current source. The generated voltage was then measured using a lock-in amplifier. Higher currents were used if the signal-to-noise ratio was determined to be lower than desired and it could be verified that there was no self-heating occurring.

Whether it is the resistivity or Hall effect that is being measured is determined by the geometry of the contact locations. As is standard, in order to measure the resistivity, the four contacts were arranged such that they are all aligned along the same axis. The outer pair of contacts were then used as a source and drain for the excitation current whilst the inner pair were used to measure a voltage. Whilst it is necessary to maximise the distance between the two voltage contacts in order to maximise the measured signal, it is also important to maintain a suitable distance between the current and voltage contacts. This is to try to ensure that the current flow is homogeneous over the region of sample that the voltage measurement is sensitive to.

In order to measure the Hall effect, a transverse voltage is measured and, therefore, the voltage contacts should be positioned along an axis perpendicular to that through which the current contacts are positioned. Again, a suitable distance should be maintained between current and voltage contacts such that the current flow is homogeneous in the region of the sample that the measurement is sensitive to.

Care was taken to ensure that self-heating was not influencing the measured voltages. The resistance of the sample and the contacts to the sample are finite. Joule heating proportional to the resistance R and proportional to the square of the applied current I (I^2R) is expected. Heating was checked for by measuring the current dependence of the measured voltage. The measured voltage is expected to vary strictly linearly with the applied current as $V = IR$ (Ohm's law). If a sufficiently high current is applied that heating occurs and R changes, a non-linear evolution of V is observed with respect to I. Applied currents were always ensured to be well within the linear $I - V$ regime. This was checked at both high temperatures and low temperatures.

The materials studied in this thesis are quasi-two-dimensional. The behaviour within an *ab*-plane is markedly different from that along the *c*-axis. In this case, it is difficult to be sure that the current flow is strictly in the *ab*-plane such that a contribution from *c*-axis current flow is not included in the measurement of resistance. In the case where in-plane behaviour is desired and *c*-axis contributions are to be eliminated for example, care was taken to ensure that the *c*-axis is shorted. This was typically achieved by sputtering a highly conductive layer of gold onto the sample that shorts the *c*-axis of the material. Similarly, conductive silver paint is applied such that the *c*-axis is shorted. Details of specific procedures are described in the Experimental Details sections of the relevant chapters.

3.2 Magnetic Fields

The study of many correlated electron systems, and certainly high temperature superconductors, is greatly aided by the use of magnetic fields. In high temperature superconductors, the superconducting state can be suppressed by magnetic fields revealing the, often highly unconventional, normal state. More generally, the electronic response to the application of a field (as detailed in Chapter 2) can elucidate many finer details of an electronic system. In this work, measurements were performed up to 14 T at the University of Bristol and up to 38 T at the High Field Magnet Laboratory.

As was mentioned in the previous section, whether you choose to measure magnetoresistance or Hall effect dictates whether the voltage contacts should be placed in a longitudinal or transverse geometry. In practice, it is inevitable that there is a degree of contact misalignment and that any measurement of voltage will contain both a longitudinal and transverse (Hall) component in any contact geometry. To overcome this problem, measurements are taken in both positive and negative magnetic fields (the polarity of the field is reversed). The two datasets can then be symmetrized (or antisymmetrized) to isolate the longitudinal (or transverse) component of the total measured voltage.

3.2.1 Superconducting Magnets up to 14T

Superconducting magnets are coils of superconducting material (typically Nb_3Sn or NbTi) which are cooled to below their superconducting transition temperature. By their very nature, low-sweep rates at low energy consumption are possible and such magnets can be operated for long periods of time by entering into a ‘persistent mode’ in which a closed superconducting loop is created. Because they need to be kept cold, they are submerged in liquid helium which makes them particularly suitable for measurements at low temperatures.

Superconducting magnets are not without disadvantages. Flux trapping means that they often have strong remnant fields (finite field in the absence of current). Although this was not a hugely important consideration for most of the measurements presented in this thesis, it can affect the result of zero-field cool-downs and the any measurement that *is* strongly affected by small fields.

In this thesis, superconducting magnets capable of generating fields up to 14T were used. Although only some of the measurements presented in this thesis were performed in superconducting magnets, the superconducting magnets at the University of Bristol were used extensively in preparation for additional measurements at higher fields.

3.2.2 Bitter Magnets up to 38T

The majority of the measurements presented in this thesis were preformed at the High Field Magnet Laboratory, Nijmegen. There, there are five Bitter magnets, the largest of which is capable of achieving static fields of 38 T. Each magnet consists of multiple Bitter coils, stacked plates made from a Cu-Ag alloy, through which 40 kA can be passed. These magnets are resistive and, as a result, require a dedicated cooling system to maintain their temperature. The laboratory houses large stores of actively chilled water that are pumped through the magnet at a rate of $140\,\mathrm{l\,s^{-1}}$ whilst they are in operation.

Experimentally, measurements at such high fields come with a number of additional challenges. Firstly, measurement noise is a much larger concern than in a typical superconducting magnet. One reason for this is purely mechanical. The rapid and turbulent flow of high pressure water that is passed through the magnet in order to keep it cool introduces a lot of mechanical noise. Ensuring that the tail of the cyrostat and the magnet are not touching helps to minimise mechanical noise but is not a complete solution. Beyond this, it is difficult to mitigate this mechanical source of noise further without designing your experiment specifically to do so, as is necessary for scanning probe measurements, for example. The second large source of noise is electrical. Because 40 kA is required in order to generate the highest available magnetic fields, a dedicated electrical installation is needed to power the magnets and is housed in close proximity to the magnet and measurement equipment. Stray voltages are prevalent and a lot of care needs to be taken in order to minimise electrical noise. For example, by systematically changing how and which parts of your measurement circuit are grounded, it is easily possible to increase or decrease the amount of electrical noise by orders of magnitude.

The use of resistive Bitter magnets and the necessity to keep them cool imposes a second constraint. Although large buffers, stores of cooled water, are used to maintain the temperature of the magnets, measurements requiring long periods of time at highest fields will rapidly deplete this cooling capacity. If the water in the buffers becomes insufficiently cool to maintain the temperature of the magnets, the magnet needs to be turned off and the water re-cooled. This is a slow process and means that measurements should be planned to both minimise down-time whilst maximising the quantity of useful data that is acquired.

Secondly, miniaturisation of experimental apparatus is often necessary. The bore of each magnet is 32 mm in diameter and this space is further reduced after the insertion of a ^{4}He cryostat. The remaining space within which the experimental apparatus must fit is a cylinder with a diameter that is a little more than 15 mm. For this reason, smaller pressure cells were designed that are able to fit inside these magnets. The cylindrical effective sample space is reduced in length from ~ 1.5 cm to 5 mm and in from ~ 5 mm to < 2 mm in diameter. This severely constrains the maximum sample size when compared to that of a measurement at ambient pressure. This will be discussed further in the following section.

Lastly, because experiments are each allocated a finite number of magnet-hours (40 hours over one week for a typical experiment) and the laboratory operates a shift system, time is an additional major constraint.

3.3 High Hydrostatic Pressures

In many systems, and certainly in the case of cuprates for example, chemical-doping and temperature are the parameters most ordinarily varied to reveal the phase diagram. Hydrostatic pressure serves as an additional thermodynamic parameter that can be varied in a clean and controllable manner. In contrast to chemical-doping, the application of pressure allows for the systematic study of a single sample without the intrinsic introduction of disorder that comes with changes of chemical composition. Additionally, it is possible to mitigate a variety of random errors of a measurement associated with the measurement of multiple samples. In the simplest case, this might simply be the determination of the sample geometry. For example, the doping dependence of the Hall coefficient will likely contain random errors associated with the determination of a sample's thickness. In measurements performed on a single sample under pressure, this error is systematic and the evolution of R_H with respect to the control-parameter can be more easily determined.

A primary disadvantage of performing measurements under pressure is the limited sample space afforded by pressure cells. This severely constrains the maximum size of a sample and, therefore, the spacing of electrical contacts in the case of transport measurements. There is also an inherent risk to the sample. In the case of a failure that results in the instantaneous loss of pressure within the sample space, the samples and any apparatus (wires, thermocouples, heaters) inside of the cell will be crushed and or ejected from the the cell. Recovery of the sample is usually impossible.

3.3.1 Piston Cylinder Cells

Measurements presented in this thesis were performed using two different piston cylinder cell designs whose operating principles are nevertheless identical. The primary difference between them is a substantially reduced total diameter of the smaller variation to allow them to fit inside the 15 mm bore of a typical cryostat used in conjunction with the high-field magnets at the High Field Magnet Laboratory. Cells of the first, larger design were used for measurements in the superconducting magnets at the University of Bristol. The second, smaller set of cells were used for measurements at the High Field Magnet Laboratory.

Cell design and operating principle

In essence, a piston cylinder cell is simply a hollow cylinder of metal. The inner volume is filled with a pressure transmitting medium inside of which a sample is submerged. The two open ends of the cylinder are then sealed such that the fluid (and sample) is confined within a fixed volume. One seal is then pressed further inside the cylinder using a piston and hydraulic ram such that the confined volume is reduced and a hydrostatic pressure is applied to the submerged sample. A schematic illustration of the larger variety of piston cylinder cell used in this work is shown in Figure 3.1.

At one end of the bore of the cylinder, a feed-through is inserted. This not only serves as a means of sealing one end of the cell, it is also the component through which electrical access is made the sample space. This is discussed in more detail later. In particular, it is a copper ring around the inner neck of the feed-through that ultimately seals the sample space at this end of the cell. The feed-through is held in place by a backing-nut which is screwed into place behind it. The other end of the cell is plugged by a copper disk. It is this disk that is pressed by a piston. With the application of a large force and the generation of pressure within the cell, the copper disk and ring will flow and a total seal is made. The travel of the piston, and any generated pressure, is locked in place by tightening a lock-nut against the intermediate MP35N disk that holds the inner piston in place. The thread of the backing- and lock-nuts bear the load.

The pressure-bearing capacity, P_c of a piston-cylinder cell is given by

$$P_c = \sigma_y \ln \frac{b}{a} \tag{3.1}$$

where a and b are the inner and outer radii of the cylindrical cell body and σ_y is the yield-strength [26], the stress at which permanent deformation of the cell occurs. Naturally, a large ratio b/a is desired whilst retaining a sufficiently usable sample space volume and keeping the total size of the cell within the size of a cryostat. As shown in Figure 3.1, the cell body is comprised of two cylinders (an inner- and outer-cylinder). An interference fit between the two is created by heating the outer-cylinder to increase its inner diameter such that the inner cylinder (which would otherwise not fit) can be inserted. Upon cooling, the outer cylinder shrinks and applies an external pressure to the inner cylinder. This external pressure introduces internal stresses with and opposite sign to that generated by internal pressure and therefore increases the pressure-withstanding capacity of the cell. In practice, the maximum pressure achievable using typically sized piston cylinder cells is $\sim$ 2GPa if plastic deformation is to be almost entirely avoided. Pressures up to $\sim$ 2.5GPa are possible if a degree of cyclic deformation is deemed to be acceptable. Figure 3.3B shows the generated pressure within a pressure cell with increasing load from a hydraulic ram. The linear-regime up to $\sim$ 2 GPa corresponds to the pressure range within which there is little to no deformation of the cell. Beyond $\sim$ 2 GPa, the pressure-force curve is highly non-linear due to a widening of the cell body.

The outer surface of the cell body is threaded such that it can be suspended when pressure is applied. In this configuration, pressure is applied with the cell under longitudinal tension. If the cell were simply placed on top of a surface during the application of pressure, the cell body would be under longitudinal compression. Relaxation of the cell body would result in a loss of pressure in this configuration.

Feed-through preparation

The feed-through is the component through which electrical access is made from the laboratory to the confines of the pressurised sample space inside of the cell. It is consequently also the component that serves as an effective sample ‘stage’. A schematic and photograph of a two feed-throughs with samples mounted are shown in Figure 3.2. The feed-through is the most likely point of failure. In the best case, a small leak might be present and the cell will slowly depressurise. In the worst case, the component will totally fail and the cell will instantaneously depressurise resulting in the total loss of any samples mounted inside of the cell.

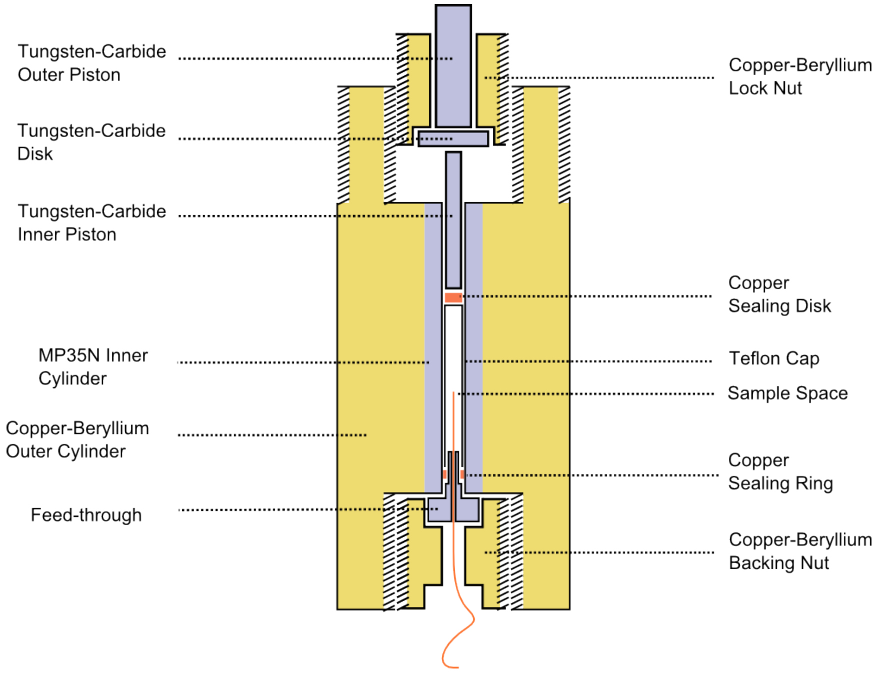

Figure 3.1: A schematic illustration of a piston cylinder cell with the various functional components labelled.

The feed-through is a hollow component through which copper wires are fed. The hole is then filled with Stycast (typically Stycast 2850, a two-part epoxy), a hard-setting epoxy. The cross-sectional profile of the hole through the feed-through is wide at each open end and narrow in the centre. This dramatically increases the pressure gradient the component can withstand. If the hole were simply cylindrical, for example, the Stycast plug would ’pop’ out at only moderate pressures. Although not required for the studies performed in this work, you could in principle run thermocouples or fibre optics into the cell in the same manner.

Any air bubbles or voids that are present in the Stycast will drastically compromise the pressure-withstanding capability of the feed-through. Stycast 2850FT is a two-part epoxy that requires thorough mixing. Introducing bubbles in therefore very easy. Equally, when filling the feed-through, it is easy to introduce voids if Stycast is loaded from both open ends. Once the two components of Stycast have been thoroughly mixed in their correct proportions, the mixture is held under vacuum for ~ 20 minutes to remove any air bubbles that have been introduced during mixing. Copper wires are first passed through the feed-through. Stycast can then be loaded into one side of the feed-through (typically the outside) whilst a syringe that is placed over the inside of the feed-through is used to draw (suck) the Stycast through. Once Stycast has visibly emerged from the other side of the feed-through, it is possible to load any additional Stycast without fear of creating a void.

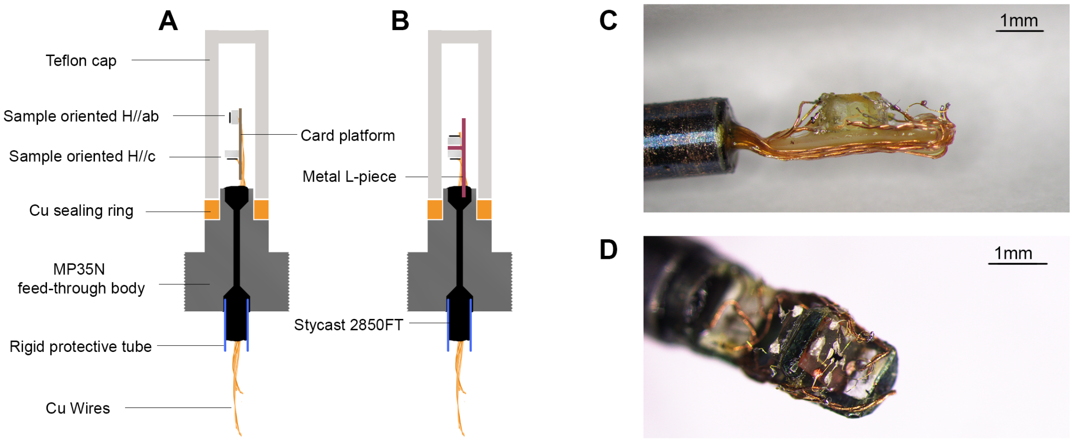

Figure 3.2: A: A schematic illustration of a feed-through prepared and assembled. The sample stage is simply comprised of a card surface onto which samples can be mounted. B: A feed-through, similar to that in A but with a machined structure onto which samples can be mounted has been pressed into Stycast on the inside of the feed-through. C: A photograph of a feed-through with samples mounted as per the schematic in A. D: A photograph of a feed-through with samples mounted as per the schematic B.

It essential that any residual Stycast is cleaned off of the feed-through and the copper wires in particular. Once the Stycast has cured, it is only possible to remove the Stycast abrasively which is likely to damage to the insulation thereby raising the prospect of electrical shorts. Cleaning of the copper wires was typically performed by carefully brushing them between two acetone-soaked cotton buds. Care was taken to ensure that the Stycast in the feed-through itself was not overly exposed to acetone in case its strength is compromised.

Once the epoxy has set, the wires on the inside of the feed-through are arranged to form a 'spine' onto which a thin sheet of card is attached. This piece of card serves as a platform onto which samples can be mounted. The ends of the copper wires are then arranged such that they can be soldered to the gold wires that make electrical contact to a sample. This configuration is illustrated in the schematic in Figure 3.2A and photographed in Figure 3.2C.

Alternatively, a sample stage can be machined and inserted into the inner-facing surface of Stycast such that there is a rigid platform onto which the sample can be mounted. This is particularly useful for orienting samples perpendicular to the long-axis of the pressure cell. This method was used for some measurements of the Hall-effect in $Tl_2Ba_2CuO_{6+\delta}$ in which both brass and MP35N L-shaped platforms were created onto which samples could be rigidly mounted. This did ensure that the sample orientation was secure. It was, however, found to compromise the stability of the Stycast and the reliability with which the highest pressures could be achieved. It was not universally adopted as a method for this reason. This configuration is illustrated schematically in Figure 3.2B and photographically in Figure 3.2D.

Pressure gauge

Determination of the pressure inside of the pressure cell was made using a suitable pressure gauge, an additional sample, that is mounted along side the samples of interest. In this work and as is typical, the four-point resistance of a coil of Manganin was used for this purpose. Pressure can be determined from the measured change in resistance, ΔR, from that measured at ambient pressure, R_0, using the following expression:

$$P = A(\Delta R/R_0) \tag{3.2}$$

where A is a coefficient to be determined [27]. In order to find the coefficient A, the resistance of a coil of Manganin and a Bi sample were measured as a continuous function of pressure at room temperature. Bi undergoes two structural phase transitions, one at 25.4 kbar and another at 27.0 kbar [27]. These two fixed points and a third at 0 GPa are sufficient to determine A. It was found that $A = 405$ kbar with an error of ±5 kbar estimated from the reproducibility of the result as opposed to the fit which would suggest that the error is substantially smaller. An additional quadratic term could have been considered in Equation 3.3.1 but was deemed not to be significant over the relevant pressure range of the cells being used given the error associated with A.

It is important that the length of Manganin wire is first coiled or otherwise shaped such that the total length is of the order of at least a few millimetres. The percentage change in resistance with pressure is small and it is possible that the effective point of contact to the Manganin will shift under applied pressure. The length needs to be sufficiently long that the change in resistance due to a shifting effective point of contact (which is constrained by the total contact size) is small relative to the intrinsic pressure dependence of the material.

After being coiled, it is important to then heat the coil in order to anneal out any internal stresses and defects that both the manufacturing process and subsequent coiling may have introduced. It is possible that stresses and defects will be annealed out with the application of pressure. In this case, an additional component to the pressure dependence will be introduced from which the intrinsic pressure dependence cannot be easily isolated. Following the work of [27], annealing at a temperature of 300 °C for at least 8 hours (typically overnight) was performed.

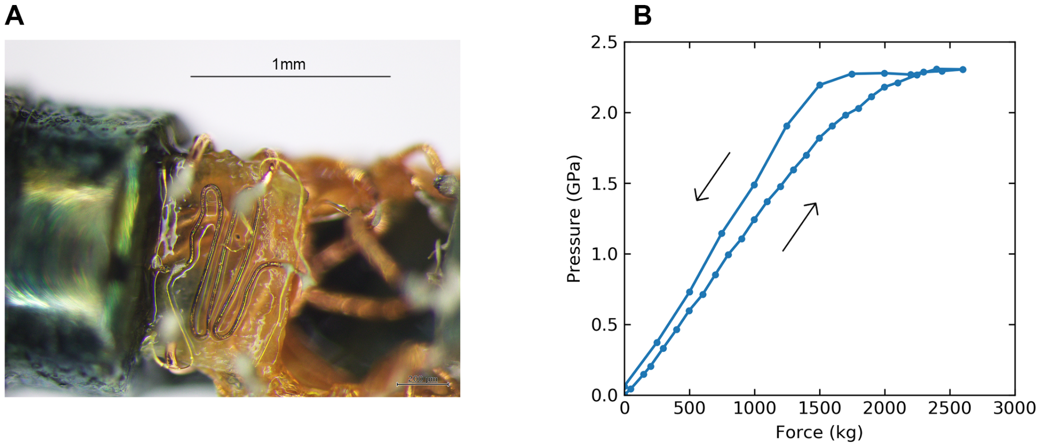

Figure 3.3: A: A length of annealed Manganin wire shaped such that it is ∼ 5 mm in length and mounted inside of a piston cylinder cell for high-field measurements at the HFML. B: The generated pressure as determined from the change in resistance of a length of Manganin with increasing applied force from a hydraulic ram.

3.3.2 Moissanite Anvil Cells

The highest pressure achieved for the study of condensed matter systems are reached using anvil cells (diamond anvil cells in particular) with the search for superconductivity at temperatures close to room-temperature in hydrides systems at hundreds of GPa motivating a lot of practical advancement [28, 29]. Restriction of the sample space to ∼ 10 µm limits their use for studies on the single crystal samples in this work. Here, moisannite anvil cells, an example of which is shown in Figure 3.4, are used for the simple reason that they are cheaper and larger.

Cell Design and Operation

The moissanite anvil cells used in this work are capable of reaching pressures up to 8 GPa. The basic operating principle is much the same as that of a piston cylinder cell. A force is applied to a piston that presses two anvils together which in turn compresses a sample space. The travel in the mobile anvil is then ‘locked in’ by tightening a lock nut such that the piston can be removed. The difference is that the sample space is made by confining the volume of a small hole drilled in a disk (or gasket) between the faces of two moissanite anvils. A schematic illustration and photograph are shown in Figure 3.4.

A typical gasket hole is drilled to a diameter of 150 µm to 400 µm (depending on the desired maximum pressure and sample size) and is typically ∼ 40 µm thick once prepared and ready to be used. The sample size is therefore far more severely constrained than when using piston cylinder cells. In addition, the pancake-like shape of the sample space constrains the orientation of the sample.

This is particularly relevant for quasi-two-dimensional materials which often grow as platelets in the *ab*-plane. A typical anvil-cell (and those used in this work) feature anvils with faces orientated perpendicular to the long axis of the cell. The orientation of a typical quasi-two-dimensional sample fixed to a face of the anvil is such that an applied magnetic field is parallel to the *c*-axis. Any other orientation requires that the cell is rotated (a option that is not possible with the cells used here in the magnets available at the High Field Magnet Laboratory), a different cell design is used, or the sample is cut and the pieces stacked such that the sample is effectively rotated by 90°.

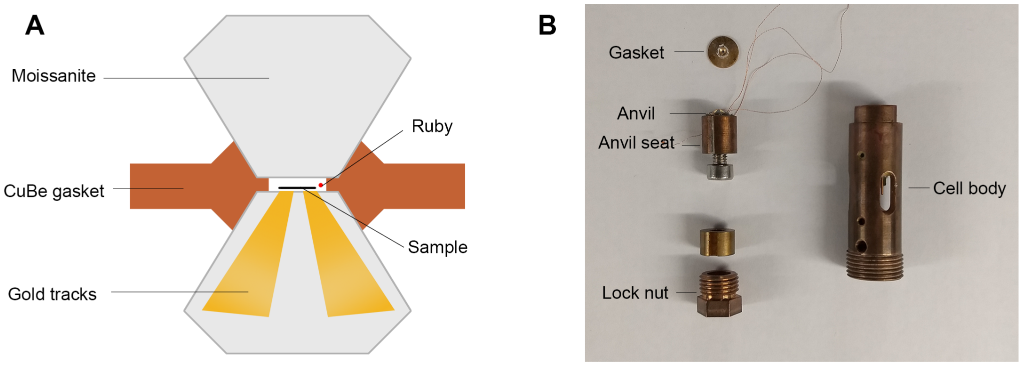

Figure 3.4: A: A schematic illustration depicting the enclosed sample-space volume between two anvils. B: A photograph of a moissanite anvil cell.

Masking the Anvils

The 'conventional' means of achieving electrical access from the laboratory to the pressurised sample space between the two anvils is to run copper wires through carefully cut grooves in the gasket. Here, this was not done. Instead, six gold tracks were evaporated onto the surface of one of the anvils using a fabricated mask. This is shown in both the schematic in Figure 3.4A and in the photograph in Figure 3.5. As well as being very reliable and robust, a further advantage to this method is that the same mask can be used to evaporate contacts onto a sample. The contacts on the sample and tracks on the anvil will then be perfectly aligned when the sample is placed on the anvil. Contact can then be made from the sample to the tracks using small droplets of silver paint. This simultaneously fixes the sample to the anvil and makes good electrical contact. Here, DuPont 4929N silver paint or H20E were typically used.

Figure 3.5: A back-lit photograph taken looking down through the anvils of a moissanite anvil cell. The silhouette of a sample and the patterned gold tracks are clearly visible.

Ruby Fluorescence

Unlike in the case of a piston cylinder cell, when using an anvil cell there is optical access to the sample space by virtue of the anvils being transparent. This makes anvil cells particularly suitable for optical measurements. Even if the principle measurement is not optical in nature, it is usual to use this capability for the determination of pressure. Ruby has a prominent doublet of peaks at 692.8 nm and 694.2 nm. The positions of these peaks has been found to be pressure-dependent, highly reproducible and has been calibrated against the equation of state of copper [30] and a wide variety of transition metals [31, 32].

A small piece of ruby is placed alongside the primary sample of interest. Pressure can be calculated using:

$$P = \frac{A}{B}\left((\frac{\lambda}{\lambda_0})^B - 1\right) \tag{3.3}$$

where λ_0 is the ambient pressure wavelength of the tracked peak and A, B are calibration constants. In this work, the constants used were $A = 1920\,\mathrm{GPa}$ and $B = 9.61$ from [32]. Figure 3.6 shows a representative set of fluorescence spectra from which pressure was determined and a schematic of the measurement apparatus.

3.3.3 Pressure Media

As has been mentioned, the application of a force from the ram is not to the sample directly, but to a piston which compresses an enclosed volume (the sample space) which is filled with a medium in which the sample is submerged. Thus, hydrostatic pressure is applied to the sample. In practice however, this will not strictly be the case as the hydrostaticisty of a medium is never perfect due

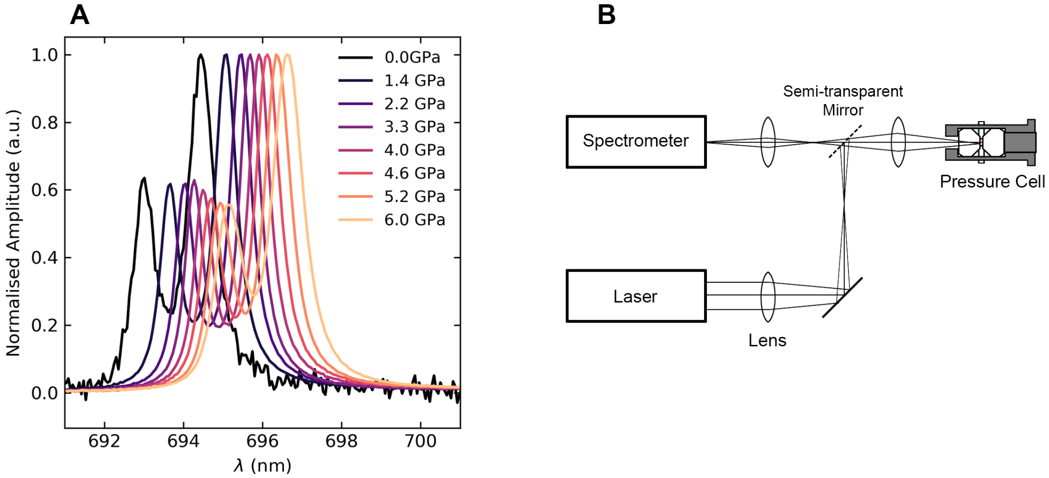

Figure 3.6: A: The measured fluorescence spectra of a piece of ruby placed inside of a moissanite anvil cell from which the applied pressure was determined. B: A schematic of the measurement apparatus.

to them having a non-zero shear strength. Additionally, solidification of the medium is inevitable at sufficiently high pressures. If the melting line of a medium increases such that it is a solid at room temperature (the temperature at which pressure is typically applied), the generation of uniaxial components becomes inevitable. The choice of pressure transmitting medium is therefore important. Even helium, which is widely regarded as being the best pressure medium available, solidifies at room temperature at 12.1 GPa [33].

There are three primary considerations when selecting a pressure medium. Firstly, the medium should be inert to both the sample and electrical contacts such that neither the sample itself nor the contacts (and their resistances) degrade. Secondly, the medium should remain hydrostatic over the range of pressures being studied. Vitally, the onset of non-hydostaticity should not occur in the vicinity of a feature in the measured data. Lastly, the ease with which a cell can be prepared should be considered. Although pressure media like argon or ethanol-methnol mixutures remain hydrostatic up to higher pressures than Daphne 7373, their volatility means that cell preparation needs to be fast and the chance of trapping small air bubbles in the medium is far greater.

In this work, Daphne 7373 was used for all piston cylinder cell experiments as it remains hydrostatic up to 2.2 GPa [34]. This is close to the maximum pressure that can be reached with a piston cylinder cell. For measurements performed with a moissanite anvil cell, glycerol was selected. It remains hydrostatic up to 5.5 GPa [35] and its low volatility relative to media with a similar hydrostatic range makes it relatively easy to work with.

3.3.4 Measurement of Temperature

In order to accurately measure the temperature of a sample inside of a pressure cell, it is necessary to locate the thermometer as close to the sample as possible. One approach might be to use a thermocouple that is passed into the pressurised sample space. This would both require additional calibration and adds another major point of failure. Instead, a thermometer was placed on the outside of the cell. Due to the thermal mass of the pressure cell, there is an inevitable decoupling of the sample and the thermometer.

Depending on the experimental apparatus being used, it may be necessary to wait for substantial periods of time at a fixed temperature before the temperature of the sample equilibrates with that of the thermometer. For resistive measurements, the stability of the resistance of the sample can be checked. Similarly, when measuring the temperature dependence continuously, the rate at which temperature is swept must be as low as practically possible. Large hysteric behaviour can be seen if the temperature is swept too quickly. This was explicitly checked for throughout this work.

3.4 Low Temperatures

Low temperatures reveal a wide range of novel phenomena. The example most relevant to this thesis is superconductivity. The work presented in this thesis was conducted at temperatures ranging between 0.3 K and 300 K.

3.4.1 Temperature Control

Temperature control was achieved using a Lake Shore Model 340/350 temperature controller. At zero field, a Cernox thermometer was used to measure temperature and a coil of resistive wire is used as a heater. The Lake Shore Model 340/350 temperature controller takes the resistance of a calibrated thermometer (Cernox) as an input and outputs a current to be supplied to the heater as determined by a PID (feedback) loop.

For measurements at low fields, if the temperature dependence of the quantity of interested allows, it is often the case that the magnetoresistance of a Cernox thermometer is sufficiently small to allow it to be used to regulate the temperature whilst sweeping the magnetic field. This is especially true at higher temperatures where the magnetoresistance of a Cernox is typically small. At high fields (and exacerbated at low temperatures) this is often not the case. In the absence of a thermometer that has been calibrated in field, one solution is to regulate the temperature at zero-field before fixing the heater power by entering ‘open loop’ mode on a Lakeshore temperature controller. As long as both the cooling power and heating power (magnetoresistance of the heater) is stable in both magnetic field and time, the temperature can be regulated in the presence of a magnetic field. A second solution that was adopted in this work was to utilise a capacitance thermometer which has no intrinsic field dependence. If this is done, it is necessary to first stabilise the temperature using a Cernox as capacitance thermometers are typically glassy materials whose calibration is unstable with thermal cycling. Afterwards, the temperature controller can be set to regulate using the newly determined capacitance of the capacitance thermometer whist the magnetic field is swept. The properties of the quantity being studied and practical constraints should dictate which method is selected.

3.4.2 Helium-4 Systems

At temperatures between 300 K and 4.2 K, ^{4}He is used as a coolant. For temperatures below the boiling point of ^{4}He (4.2 K), it is possible to achieve highly stable temperatures by regulating the vapour pressure of helium. The boiling point of helium is reduced upon reduction of the vapour pressure within the containing chamber in close agreement with that of an ideal gas. By controlling the pressure above a helium bath, it is therefore possible to regulate its temperature. This could be automated, but was typically done manually by adjusting the degree of pumping with a valve. Depending on the properties of the system, a typical base temperature of 1.3 K is achievable. Regulation of temperatures between 1.8 K and 2.1 K is made difficult by the superfluid transition of helium which often introduces a jump in temperature.

3.4.3 Helium-3 Systems

If temperatures lower than 1.3 K are required, a ^{3}He system can be used to reach temperatures as low as 300 mK. Its boiling point of 3.2K is lower than that of ^{4}He but this can be reduced to 300 mK, again by pumping to lower the pressure above the bath.

At the HFML, the ^{3}He system is double-walled to thermally isolate the sample space and inserted into a ^{4}He cryostat. Firstly, the ^{4}He is pumped to base temperature (importantly below the boiling point of ^{3}He). The ^{3}He can then be released into the sample chamber where it will condense into a liquid. The cavity between the ^{4}He and ^{3}He is then thoroughly pumped so that the sample chamber is thermally decoupled from the ^{4}He. The ^{3}He bath inside of the sample chamber can then be pumped to reach the lowest temperatures. Temperature regulation can be achieving by either controlling the pumping or applying small amount of heat from a heater on the sample stage. Because only a finite amount of ^{3}He is used, the system can only be kept cold for a finite amount of time. At the HFML, this period is typically many hours but care should be taken if lowest temperatures are required for prolonged periods of time.

The primary complication that using ^{3}He introduces is containment. ^{3}He is very rare and, therefore, very expensive. Although ^{4}He is typically recovered for reuse, small losses are accepted. ^{3}He losses, however, need to be kept as close to zero as is possible. Any part of the system that is expected to contain ^{3}He is first carefully leak-tested and pumped to a very good vacuum to avoid both the loss of ^{3}He and contamination with ^{4}He or air.

3.5 Other Methods

Although they were not the principle focus of the work presented in this thesis, other techniques were deployed. The following passages are brief outlines of these methods and where they were used.

3.5.1 AC Susceptibility

In order to determine the superconducting transition temperature, T_c, of a sample without making electrical contact, its AC susceptibility was measured. This was primarily done to investigate the annealing conditions required to produce samples of $Tl_2Ba_2CuO_{6+\delta}$. Aside from not requiring electrical contact to be made to the sample, AC susceptibility is favourable because it is a probe of the entire sample volume (resistivity is not). The homogeneity of the sample can thus be better evaluated.

In this method (detailed in [36]), two oppositely wound secondary coils are placed inside of a larger primary coil. A sample is placed inside one of the secondary coils. In the primary coil, a small sinusoidal magnetic field of the form $H = H_0 \cos \omega t$ is generated and a voltage that is proportional to $\frac{dM}{dt}$ is induced and measured across the secondary coil where M is the magnetisation of the sample. This voltage can be measured using a standard AC lock-in technique.

The total magnetic field is

$$B = \mu_0 (H + M) \tag{3.4}$$

or expressed in terms of the susceptibility χ:

$$B = \mu_0 (1 + \chi) H \tag{3.5}$$

The magnetisation of the sample is expected to be sinusoidal with a possible phase shift:

$$M = H_0(\chi\prime \cos \omega t + \chi\prime\prime \sin \omega t) \tag{3.6}$$

where $\chi\prime$ and $\chi\prime\prime$ are the real and complex components of the susceptibility. In the normal state, in the absence of losses it is expected that the response of the sample will be in-phase with the excitation field and therefore that $\chi\prime > 0$, $\chi\prime\prime = 0$. In the superconducting state, the complete Meissner condition requires that $B = 0$ within the sample. From equations 3.5 and 3.6, it is clear that $\chi = -1$ and $\chi\prime\prime = 0$ in this case. The only time $\chi\prime\prime$ is expected to be non-zero is in the mixed state during which losses associated with vortex motion might be anticipated.

Therefore, upon passing through T_c with decreasing temperature, a characteristic step in $\chi\prime$ with the onset of diamagnetism is expected. In addition, a characteristic peak in $\chi\prime\prime$ is observed.

3.5.2 EDX

Energy-dispersive X-ray spectroscopy (EDX) is a technique that is widely used to determine the composition of a sample through elemental analysis. A beam of x-rays is focused on the sample and the emission spectrum is analysed. Each elemental component of the sample has a different atomic structure and will contribute a different set of peaks to the total emission spectrum. Through comparison with test samples of known composition, the elemental composition of the sample-of-interest can be determined.

Later in this thesis, the resistivity of $\mathrm{FeSe}_{1-x}\mathrm{S}_x$ is presented as a function of S-doping and hydrostatic pressure. Although EDX was not performed on the samples measured in this work, EDX was performed on samples from the same growth batch by the crystal growers from Kyoto University and the University of Tokyo. In this work, nominal value of x derived from the constituent components of the growth procedure are used to denote the sulphur concentration. Nominal values of x are known to be approximately 80 % of those determined by EDX. This is discussed in more detail in the relevant chapter.

3.5.3 X-Ray Diffraction

X-Ray Diffraction (XRD) was used to determine the lattice parameters of ZrSiS at both room-temperature and 90 K. This was done in order to verify the structural similarity of our sample to those of both our collaborators and others more broadly.

In short, when exposed to monochromatic light, a periodic array of scatterers (atoms) will produce a periodic array of spherical emitters. Along most directions, the emitted spherical waves will destructively interfere. However, along directions that fulfil the Bragg condition, constructive interference will occur and a spot will be produced in the resultant diffraction pattern. When the spacing between scatters and the wavelength of the incident light are comparable, this effect is most noticeable. Hence, X-Rays are typically used. Through analysis of the diffraction pattern, the unit cell vectors and atomic sites can be determined.

3.5.4 Density Functional Theory

Throughout this thesis, density functional theory (DFT) studies are made reference to. DFT is particularly relevant to the quantum oscillation study of ZrSiS. The measured quantum oscillation frequencies are compared to those obtained by DFT calculations. Calculations were performed by Professor A. Carrington at the University of Bristol using WIEN2k, a package capable of performing all-electron ab-initio calculations by implementing the full-potential linearised augmented plane wave (LAPW) method [37].

Summarised very briefly, the LAPW is method for solving the Kohn-Sham equations. What is particular to this method is the choice of basis set. Within spheres centred at atomic sites, spherical harmonics multiplied by a radial function are used, while between atomic sites, plane waves are used. This naturally captures the localised, quickly-varying nature of solutions close to atomic sites and the delocalised, slowly-varying nature of solutions in interstitial regions. It is, for this reason, found to very accurate and computationally manageable with a typical desktop computer.

Chapter 4

$Tl_2Ba_2CuO_{6+\delta}$

The work in this chapter was motivated by this gap in our collective knowledge of the evolution of superconductivity and normal state transport in $Tl_2Ba_2CuO_{6+\delta}$ under hydrostatic pressure. Firstly, the tuning of the superconducting transition temperature with hydrostatic pressure and annealing conditions was revisited. Low-field resistivity and Hall effect measurements were then performed in magnetic fields up to 14 T in a number of samples to reveal both the similarities and differences in the dependence of the electronic properties on the superconducting transition temperature as it is tuned by both chemical doping and hydrostatic pressure.

Measurements at high magnetic fields have revealed highly unexpected features of the in-plane magnetoresistance that are more typically associated with quantum criticality. Although the microscopic origin of the phenomena remains unclear, it is highly unlikely to be a consequence of the putative quantum critical point at $p = 0.19$ that other measurements have been associated with. The magnetoresistance of $Tl_2Ba_2CuO_{6+\delta}$ appears to be dominated by an incoherent charge sector that can not be understood within conventional transport theory and is compatible with scattering defined by Planckian dissipation. Furthermore, this charge sector appears to be a generic property of the strange metal phase of overdoped cuprates and is pervasive across the entire overdoped region of the $p - T$ phase diagram.

The preparation of as-grown crystals and pressure cells for transport measurements was performed by the author. All of the presented measurements and subsequent analysis was also performed by the author.

4.1 Background

4.1.1 Crystallographic and Electronic Structure

$Tl_2Ba_2CuO_{6+\delta}$ (Tl2201) is a member of the Tl-Ba-Ca-Cu-O family of cuprates that were discovered in 1988 by Sheng and Hermann [38]. The crystallographic structure of Tl2201 is shown in figure 4.1. Common to all cuprates are Cu-O sheets stacked in planes oriented perpendicular to the c-axis, of which Tl2201 features two per (body-centred-tetragonal) unit cell. Intermediate Tl-O and Ba-O layers act as charge reservoirs from which holes are doped in and out of the Cu-O planes. As with all cuprates, the expectation is that the Cu-O derived states are those that are relevant to the electronic properties of the material.

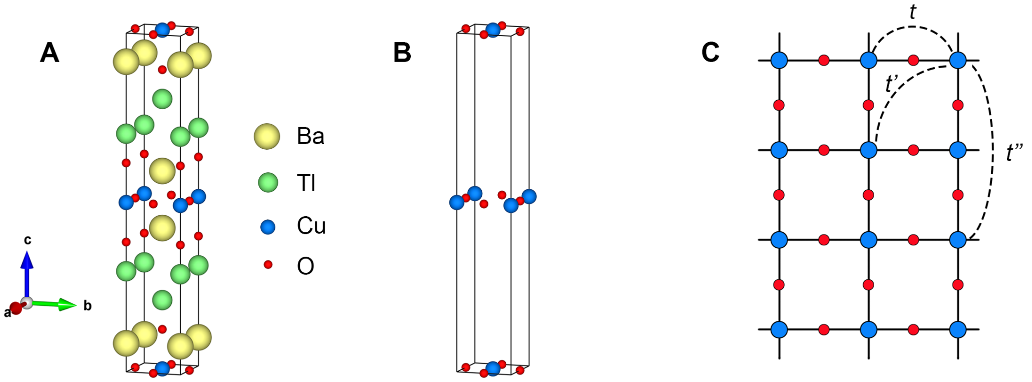

Figure 4.1: A: A single unit cell of the crystallographic structure of $Tl_2Ba_2CuO_{6+\delta}$ drawn using [39]. B: The same single unit cell as in A showing only the two-dimensional CuO_2 planes. C: A schematic representation of the CuO_2 planes showing the three primary hopping parameters from which the electronic structure can be derived. Details of this are in the main text.

The thallium-stochiometric material is found to be orthorhombic but Tl loss and the resultant Cu substitution onto the Tl site results in a transition to a tetragonal structure [40]. As a result, flux-grown samples, including the samples studied in this thesis, are always tetragonal. By changing of the amount of excess oxygen δ, the entirety of the overdoped side of the phase diagram can be accessed with an approximately linear relationship between δ and T_c [41]. The amount of excess oxygen is tuned by annealing procedures detailed later in this chapter. Optimally doped samples with no excess oxygen show superconducting transition temperatures as high as 90 K whilst fully oxygenated samples ($\delta = 0.1$) are found to be non-superconducting. The excess oxygen is interstitial and resides between the two TlO layers [42]. Also correlating with δ are the c-axis length which shrinks with increasing δ, and hole concentration n which increases with increasing δ [42].

Owing to the Fermi-liquid-like nature of the heavily overdoped system, non-interacting bandstructure calculations serve as a reasonable starting point from which the Fermi surface can be understood. Although calculations on the undoped stoichiometric compound [43] predict the existence of two sheets, a large hole-like sheet centred at (π, π) and a small spherical electron-like sheet at γ, repositioning of the chemical potential with doping brings calculation and experimental observation into agreement and only the large hole-like surface remains (see Figure 4.3). Alternatively, a simple tight-binding approach also yields a Fermi surface close to that which is experimentally observed, with a two-dimensional energy dispersion characterised by three hopping parameters:

$$\epsilon(k) = \epsilon_0 - 2t(\cos k_x + \cos k_y) + 4t'(\cos k_x \cos k_y) - 2t''(\cos 2k_x + \cos 2k_y) \tag{4.1}$$

Experimental determination of the fine details of the Fermi surface of Tl2201 has been made through measurement of quantum oscillations [44, 45], angle-dependent magnetoresistance (ADMR) [46, 47] and angle-resolved photoemission spectroscopy (ARPES) [43, 48] (Figure 4.3). Only a single high-frequency oscillation at 18 kT has been observed in quantum oscillations [44]. ADMR measurements [47] were able to reveal the particulars of the three-dimensional corrugations on what is otherwise a strongly two-dimensional Fermi surface. The overall shape of the Fermi surface can be parameterised by the following expression:

$$k_F(\phi, k_z) = k_{00} + k_{40}\cos(4\phi) + k_{21}\cos(k_z c/2)\sin(2\phi) + k_{61}\cos(k_z c/2)\sin(6\phi) + k_{101}\cos(k_z c/2)\sin(10\phi) \tag{4.2}$$

Cross-sectional slices and a three-dimensional view of the Fermi surface parameterised by the above equation with coefficients taken from [49] are shown in Figure 4.2.

Although hole doping p is typically not explicitly measured, it can be inferred from T_c. This is usually done using the relationship:

$$1 - T_c/T_{c,max} = 82.6(p - 0.16)^2. \tag{4.3}$$

This yields a parabolic dependence of T_c upon doping with a maximum in T_c at $p = 0.16$. This is found to be in very close agreement with the experimentally determined T_c of $La_{2-x}Sr_xCuO_4$ where the degree of atomic substitution x is thought to determine p directly and is widely used to infer the doping in other families of cuprates in which T_c is not tuned via simple atomic substitution. In overdoped Tl2201 where the Fermi surface geometry is precisely known, the Fermi surface volume can be used to infer p more directly. The hole doping of samples with $T_c = 10\,\mathrm{K}$ as determined

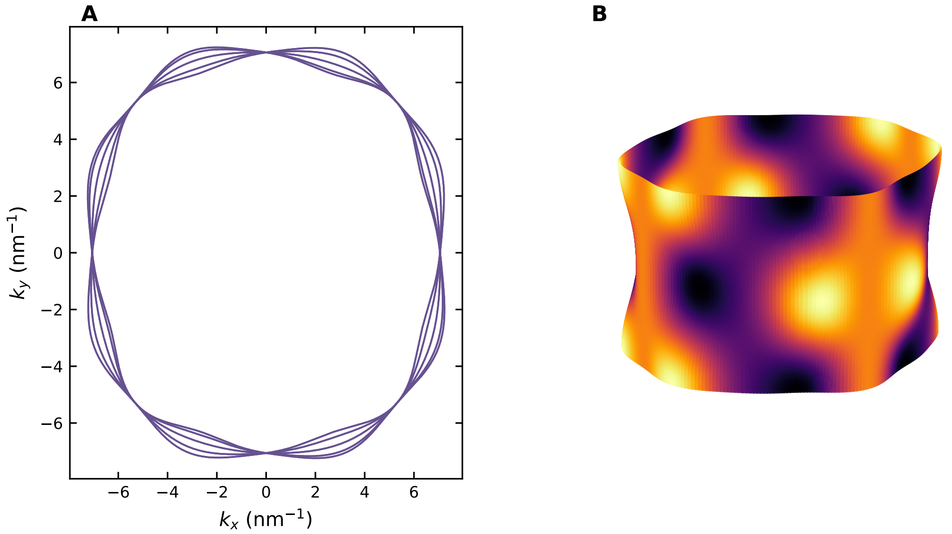

Figure 4.2: A: Cross-sectional slices at fixed k_z of the Fermi surface of Tl2201 parameterised by Equation 4.2 with coefficients taken from [49]. B: A three-dimensional view of the Fermi surface with the same parameterisation as in A. The colour-axis shows the magnitude of the in-plane k_F and has been applied to better illustrate the warping on what is otherwise a strongly two-dimensional Fermi surface.

by de-Haas van Alphen measurements was found to be $p = 0.30$ [45]. This is substantially larger than would be inferred from the aforementioned parabolic relationship (which would suggest that samples are non-superconducting at dopings greater than 0.27) presumably due to the lower levels of disorder found in Tl2201 relative to other overdoped cuprates. For this reason, in this work, the following parabolic is used to infer p from T_c:

$$1 - T_c/T_{c,max} = 46.5(p - 0.16)^2 \tag{4.4}$$

4.1.2 Transport Properties of Overdoped Cuprates

The phenomenological features of the in-plane resistivity across the temperature-doping phase diagram of the cuprates is summarised in Figure 4.4A. On the overdoped side of the phase diagram, the in-plane resistivity evolves from linear-in-temperature at optimal doping to quadratic-in-temperature once superconductivity is totally suppressed. In other words, the temperature dependence is Fermi-liquid like at and after the edge of the superconducting dome on the overdoped side and is distinctly non-Fermi-liquid-like at optimal doping. This unconventional regime around optimal doping is often termed the ‘strange metal’ regime. The smooth evolution between quadratic and linear behaviour can be modelled as the evolution of a single smoothly varying power law T^n where n evolves from

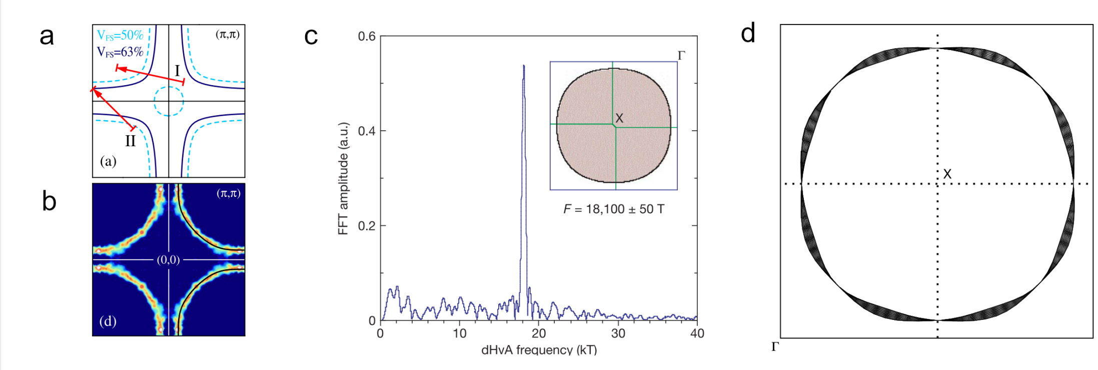

Figure 4.3: **Theoretical and experimental determination of the Fermi surface of $\mathbf{Tl_2Ba_2CuO_{6+\delta}}$.** (a) The Fermi surface of stoichiometric Tl2201 determined from non-interacting bandstructure calculations at half filling (pale-blue dashed) and 0.63 (dark blue) from [48]. (b) Determination of the Fermi surface using ARPES from [48]. (c) The de-Haas van Alphen frequency spectrum revealing a single frequency at 18 kT and the inferred Fermi surface volume from [44]. (d) A projection of the three-dimensional Fermi surface onto the ab-plane as determined from ADMR measurements [47].

two to one as optimal doping is approached from the Fermi-liquid-like overdoped regime. Alternatively, the smooth evolution can be interpreted as the sum of quadratic and linear components whose relative contributions have different doping dependencies. The doping dependence of the in-plane and out-of-plane resistivity is presented in Figure 4.4B. Phenomenologically, the same behaviour is exhibited in the c-axis resistivity. There is, however, a factor of ~ 1000 anisotropy in the magnitudes of the $ab-$ and $c-$axis resistivities as illustrated in 4.4C.

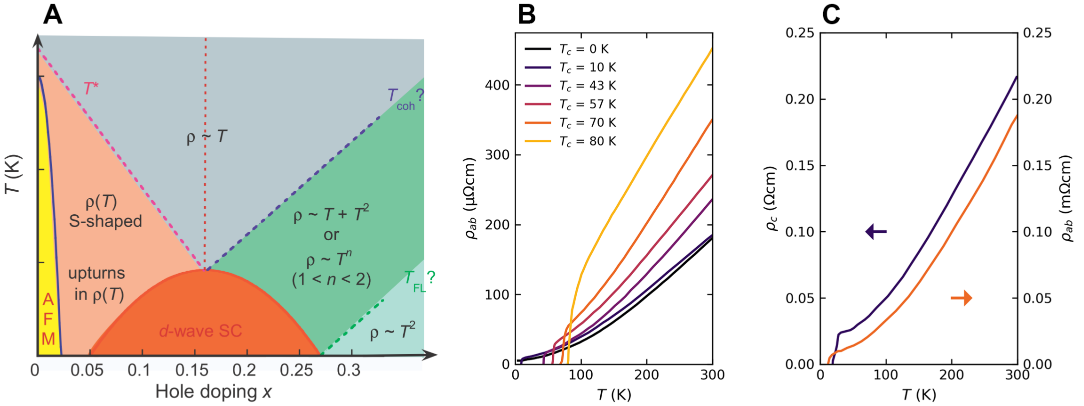

Figure 4.4: A: The schematic phase diagram of cuprates illustrating the evolution of the in-plane resistivity with doping and temperature (from [18]). B: The in-plane resistivity of Tl2201 for samples with different T_c (data from [50]) C: ρ_c and ρ_{ab} for samples of Tl2201 with similar T_c illustrating the factor ~ 1000 anisotropy of the resistivity (data from [51]).

Contrary to what might be expected from a system with a Fermi surface comprised of a single band, the Hall coefficient has a strong temperature and doping dependence as illustrated in Figure

4.5.

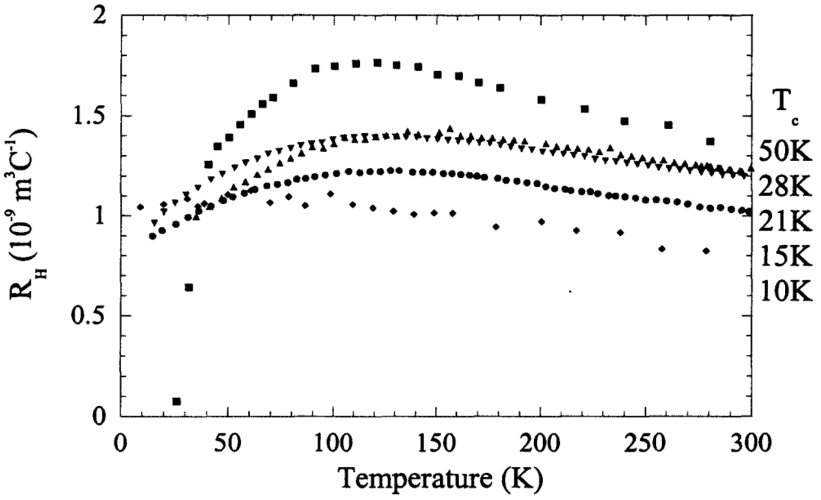

Figure 4.5: The temperature dependence of the Hall coefficient for samples of Tl2201 with different T_c (from [50]).

A comparison between resistivity and Hall effect reveals a disconnect that is difficult to fully reconcile. In the strange metal regime, the cotangent of the Hall angle $\cot\theta_H(T)$ has a quadratic temperature dependence whilst the resistivity has a linear temperature dependence. This apparent discrepancy is a characteristic feature of the strange metal phase and suggests that the two probes are sensitive to different scattering mechanisms.

Measurement of the *c*-axis magnetoresistance as a magnetic field is rotated in the *ab*-plane revealed a temperature-dependent anisotropy of the in-plane mean free path [51]. This finding was corroborated by subsequent ADMR measurements [47, 52]. In addition to revealing much about the structural form of the Fermi surface of Tl2201, ADMR measurements indicated that the total scattering rate could be decomposed into two components each with their own dependence upon *k*-space location, temperature and doping (T_c). A summary of these findings is presented in figure 4.6. One component to the total scattering rate is found to be isotropic around the Fermi surface, quadratically dependent upon temperature and independent of doping at least up to $T_c =$ 40 K. The second component is found to be highly anisotropic around the Fermi surface with a four-fold symmetry, linearly dependent upon temperature and linearly dependent upon T_c (up to $T_c = 40\,\mathrm{K}$). That is, the anisotropy increases as optimal doping is approached from the nominally Fermi-liquid-like regime.

The decomposition of the total scattering rate into two discrete components with their own temperature dependencies indicates the presence of two distinct scattering mechanisms or charge

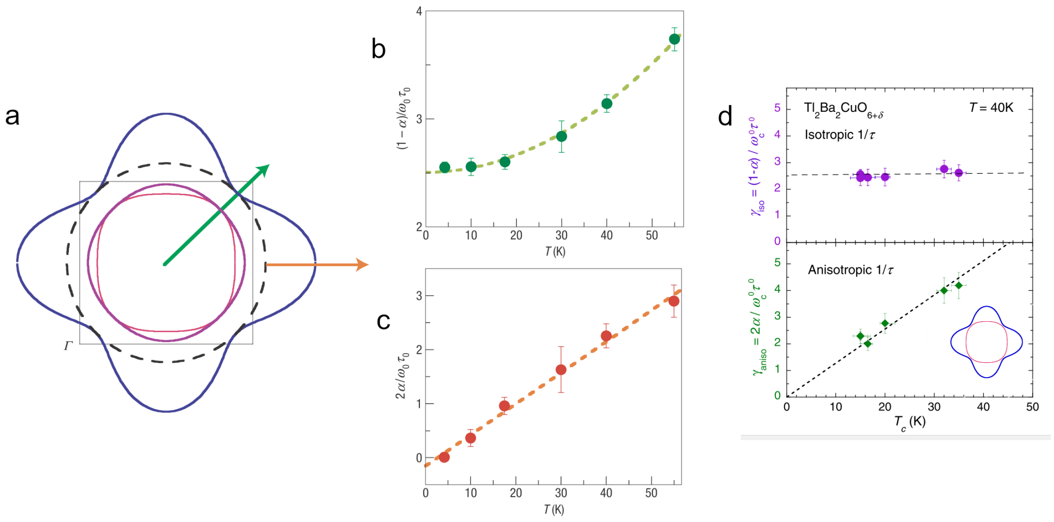

Figure 4.6: **Properties of the scattering rate of $Tl_2Ba_2CuO_{6+\delta}$.** (a) The k-dependence of the total scattering rate (blue) of Tl2201 around the Fermi surface (red). The total scattering rate can be separated into two components, one isotropic (black dashed) and one anisotropic (purple). The temperature dependence of the isotropic component (b) and the anisotropic component (c). (d) The evolution of both the isotropic and anisotropic scattering rates with T_c.

sectors. The presence of two distinct charge sectors may be the root cause of the apparent disconnect between the resistivity and Hall effect in the strange metal regime of overdoped cuprates.

4.1.3 Pressure-Induced Oxygen Ordering

As is common amongst cuprates, the T_c of Tl2201 is strongly dependent upon hydrostatic pressure. Tl2201 is, however, unusual amongst cuprates in that hydrostatic pressure is found to suppress superconductivity for nearly all dopings greater than optimal doping, for which only a relatively minor enhancement is observed (see Figure 4.8). Studies of the pressure dependence of T_c have lead to insights into the microscopic mechanisms responsible for this reduction of T_c with pressure. The principle finding is the failure of T_c to return to its ambient pressure value after the release of pressure at low temperatures [53, 54]. This has been attributed to the role of pressure induced oxygen migration, an effect which is quenched at low temperatures where the interstitial oxygen is rendered immobile. In fact, it has been found that in the absence of oxygen migration (the application of pressure at low temperatures), the strong pressure dependence of T_c is reduced to almost zero for all accessible dopings [55].

Systematic study of the relaxation of T_c back from its suppressed value to its original ambient pressure value with both time and annealing temperature has been cited as evidence of pressure-induced ordering of oxygen in which two distinct ordering phenomena (one at low-temperature and one at high-temperature) have been identified [55]. The low temperature ordering is suggested to be between two degenerate sites within a single unit cell whilst the high temperature ordering process involves oxygen migration between adjacent unit cells. These findings have been corroborated by subsequent hard-sphere modelling of oxygen diffusion [56].

In summary, the implication of the aforementioned work is that T_c is not only sensitive to the quantity of interstitial oxygen present in the system, but to the location and/or ordering of the oxygen as well. Additionally, neutron powder diffraction studies on a sample with $T_c = 46\,\mathrm{K}$, a doping near to where dT_c/dP is maximal, have shown that the linear compressibilities at 60 K of the $a-$ and $c-$axes are within 10 % and 3 % (both reduced) of their room-temperature values respectively [57]. It is therefore unlikely that the minor reduction of crystallographic compressibility can account for the near-total suppression of the pressure dependence of T_c at low temperatures and that the mobility and ordering of interstitial oxygen is the likely cause. The precise nature of the migration is as of yet unknown, though one could speculate that long-range ordering, short-range phase separation or clustering could occur and all of which could be pressure dependent.

4.1.4 Motivation

Tl2201 is a sufficiently clean system for quantum oscillations to be observed [44, 45]. Analysis of the field dependence of quantum oscillations indicate that the mean-free-path ℓ is of the order of 300 Å [44]. Typical residual resistivities are an order of magnitude lower than in Bi- and La-based cuprates at comparable dopings [58]. The entire overdoped side of the doping-temperature phase diagram is accessible. This is a region of phase space free of additional electronic phases like charge-order, spin-order and the pseudogap. The details of the Fermi surface in the most overdoped samples are also very well characterised. Consisting of a single strongly two-dimensional Fermi sheet, it has a simple structure. It is, therefore, a relatively simple system from which the emergence of superconductivity can hopefully be understood.

Additionally, it is a relatively simple system in which the effect of pressure on the normal-state transport properties of the cuprates can be studied. Both pressure and the addition of holes through chemical doping suppress T_c. A direct comparison can therefore be made of the effect each mechanism has on the normal-state transport properties.

4.2 Experimental Details

4.2.1 Sample Preparation

All the crystals studied in this chapter were synthesised at a special facility at the University of Cambridge by Carsten Putzke (from the University of Bristol) and Professor John Cooper (from the University of Cambridge) using a self-flux technique similar to that which is detailed in Ref [50]. In summary, high purity oxides of the necessary elements are ground into a fine powder and made into pellets which are heated in a sealed crucible. Although precautions are taken to minimise thallium loss, the resultant samples have a small thallium deficiency and copper excess. They are therefore tetragonal in structure. The samples are thin platelets with black, mirror-like surfaces. Thin samples that were free of visible defects and flux were selected. A typical as-grown crystal is shown in Figure 4.7A.

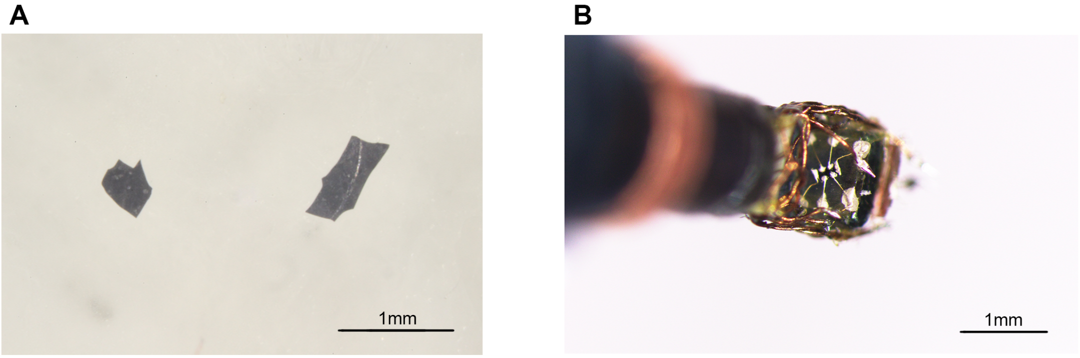

Figure 4.7: A: A photograph of a typical as-grown single-crystal of $Tl_2Ba_2CuO_{6+\delta}$. B: A sample that has been prepared following the procedures detailed in the main text and mounted for measurements in a piston cylinder cell.

Samples were first cut using a wire-saw into a rectangular shape with a total aspect ratio of $\sim$ 3:1. A larger aspect ratio would be preferable for a more accurate determination of resistivity from resistance, but the dimensions of a typical as-grown crystal prevent samples from being made longer. Cutting them such that their width is smaller is possible, but the samples become increasingly fragile. Additionally, for measurements of Hall resistivity, the contact size becomes relatively large as the sample width becomes small.

In order for good electrical contact to be made reliably to the samples, it was found that it was necessary to first sputter on a thin layer of copper ($\sim 20\,\mathrm{nm}$) followed by a thicker layer of gold ($\sim 200\,\mathrm{nm}$). The choice was made to preferentially use a sputterer over an evaporator. Little (if any) material was found to be deposited onto the sides of the samples due to the line-of-sight nature of deposition when an evaporator is used. The use of a sputterer ensured that material was also deposited on the exposed sides of the sample as well as the top surface. The hope was that this would help to short the *c*-axis and help to mitigate the introduction of an out-of-plane component to the measured resistance. This is of particular importance because of the particularly large out-of-plane anisotropy in Tl2201 (shown in Figure 4.4C).

Gold wires of an appropriate diameter could then be fixed to the gold contact pads using DuPont 4929N silver paint. The contact with its silver-paint contacts was then baked in a tube furnace in an atmosphere of flowing oxygen at 425° for 15 minutes. By following this procedure, contacts with a resistance of less than $5\,\Omega$ were consistently produced with the best being less than $1\,\Omega$. In the few cases where contacts were substantially worse, the reapplication of DuPont 4929N silver paint and a subsequent re-baking of the contacts in flowing oxygen at 425° for a further 15 minutes was found to improve the contact resistances in some cases. A prepared sample that has been mounted for measurement in a piston cylinder cell is shown in Figure 4.7B.

4.2.2 Tuning T_c

After following the aforementioned procedure to make electrical contact to the samples, the samples were reannealed in a tube furnace at an appropriate temperature and atmosphere to tune the superconducting transition temperature to a desired value.

The quartz tube of the furnace was ensured to be clean by first rinsing it with propanol before heating it to a temperature much higher than that at which samples are to be annealed at. Before inserting a sample, a new temperature is set dependent upon the desired transition temperature and a flow of the desired gas is then passed through the tube. Samples were fixed to a small quartz substrate by their gold wires such that they could be picked up without needing to touch them directly. They were then placed in an alumina boat that was inserted into the pre-heated tube furnace. In the case where samples were annealed prior to electrical contact being made (or annealed prior to a non-contact measurement), a small box was created by folding a piece of gold foil. Samples were then placed inside the box and into an alumina boat. The samples could then be picked up and moved without risk of damaging or losing them.

Generally, higher transition temperatures are reached by annealing at higher temperatures and in lower partial pressures of oxygen. The obtained transition temperatures were found to be in accordance with previous studies [49, 50]. Also in accordance with previous findings was the necessity to anneal samples for short periods of time in comparison to other cuprates. Anneal times were typically around one hour. Longer annealing times did not reliably produce superconducting transitions that were any sharper, but there was an increased risk of sample or contact degradation. Samples with superconducting transitions that were not adequately sharp were repeatedly reannealed for a similarly short period of time. It was also found that annealing at temperatures greater than 550 °C greatly increased the probability of the sample decomposing or the electrical contacts substantially degrading. For this reason, to achieve transition temperatures greater than 30 K, samples were annealed in an atmosphere of 2 % O_2 in N_2 as this allowed comparable transition temperatures to be reached at lower annealing temperatures.

Because the anneal times are very short [50], the majority of a sample is annealed in a matter of minutes. It is therefore likely that oxygen will enter in the short period of time after the sample is removed from the furnace and left to cool to room temperature in air. Quenching the sample quickly (with the use of liquid nitrogen for example) was not possible due to the detrimental effect this has on the electrical contacts. Samples were cooled as quickly as possible by placing them on a copper block immediately upon their removal from the furnace. Evidence for this is the presence of a ‘tail’ in the resistive transition that could be due to the surface becoming oxygenated as the sample cools. Although not systematically studied, it is anecdotally found that the sharpness of the superconducting transition is affected more strongly by how quickly the sample can be cooled than by annealing for substantially longer periods of time. It is thus expected that the ‘tail’ to the superconducting transition is a consequence of oxygenation of the sample surface rather than bulk inhomogeneities. The presence of this ”tail” introduces a discrepancy between T_c defined as the temperature at which $R = 0\,\Omega$ and T_c defined as the temperature at which R is 50 % of its normal state value for example. Throughout this thesis, T_c is typically defined as the temperature at which $R = 0\,\Omega$. However, in the case of Tl2201, the chosen definition of T_c will be specified and might be chosen to be the midpoint of the superconducting transition if it is believed that this is a closer reflection of the bulk property of the sample.

4.3 In-plane Transport Under Pressure

This section presents a comparison of the evolution of both T_c and the in-plane Hall effect with the application of hydrostatic pressure and with p (tuned via oxygen annealing). For the measurement of the Hall effect, three samples were prepared. Additional $T_c(P)$ data is also included from samples that were prepared for in-plane resistivity measurements at high fields (detailed later). The details of each sample for which data is presented in this section are shown in Table 4.1.

Table 4.1: A summary of the samples for which data is presented in this section.

Sample	T_c(P = 0 GPa)	p	Measurement
311014.A9	40 K	0.269	Resistivity
C24	39 K	0.27	Hall Effect
311014.J3	35 K	0.275	Resistivity
3077.5	31 K	0.28	Hall Effect
311014.A16	21 K	0.29	Hall Effect, Resistivity

Each sample was mounted on a feed-through for measurement in a piston cylinder cell and were oriented such that the applied magnetic field was parallel to the *c*-axis. Those samples for which the Hall effect was studied were measured in magnetic fields up to 12 T in a superconducting magnet at the University of Bristol. The magnetic field was applied in both the positive and negative directions such that the anti-symmetric (Hall) component could be isolated from the longitudinal magnetoresistance.

4.3.1 The Evolution of T_c

With the application of pressure, the T_c (most typically defined by the temperature at which $R = 0$) of each sample was suppressed in good accordance with existing literature results. The pressure dependence of T_c and the T_c dependence of dT_c/dP is presented in figure 4.8. dT_c/dP is determined from the value of T_c at ambient pressure and the lowest measured pressure. In each case, T_c was suppressed monotonically with increasing pressure and the maximal value of dT_c/dP was found to be in the sample with an ambient pressure $T_c = 40\,\mathrm{K}$. To determine T_c, the temperature was swept up and down through the superconducting transition at 0.1 K/min. Even at this slow sweep rate, the thermal lag between the thermometer and the sample caused a 1 K discrepancy between the positive and negative temperature sweeps. By stabilising the temperature at discrete points in the vicinity of T_c, it was determined that simply taking the midpoint between the positive and negative sweep was sufficient to determine the true transition temperature.

4.3.2 Low-Field Hall Effect

Representative data illustrating the magnetic field dependence of R_{xy} are shown in figure 4.9 (left panel). At low temperatures and low fields, superconductivity evidently suppresses the measured signal. At sufficiently high fields and temperatures, R_{xy} is found to increase linearly and the Hall coefficient is therefore found to saturate. At low temperatures, a maximum of 12 T was applied. At higher temperatures where superconducting fluctuations were totally absent and R_H was found to

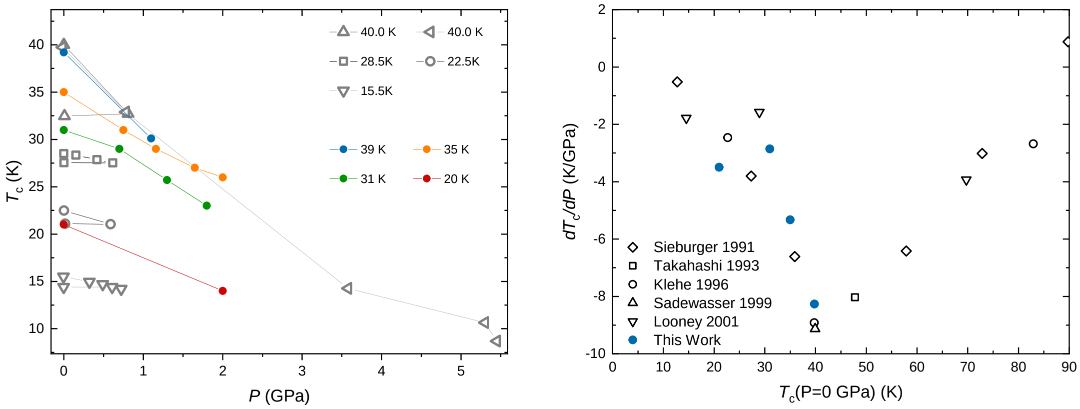

Figure 4.8: Left: The pressure dependence of T_c for samples of Tl2201 at number of dopings measured in this work (coloured points) and from previous measurements (open points) [53]. Right: dT_c/dP for the samples measured in this work (blue) and previous measurements (open points) (data from [55] and the references therein)

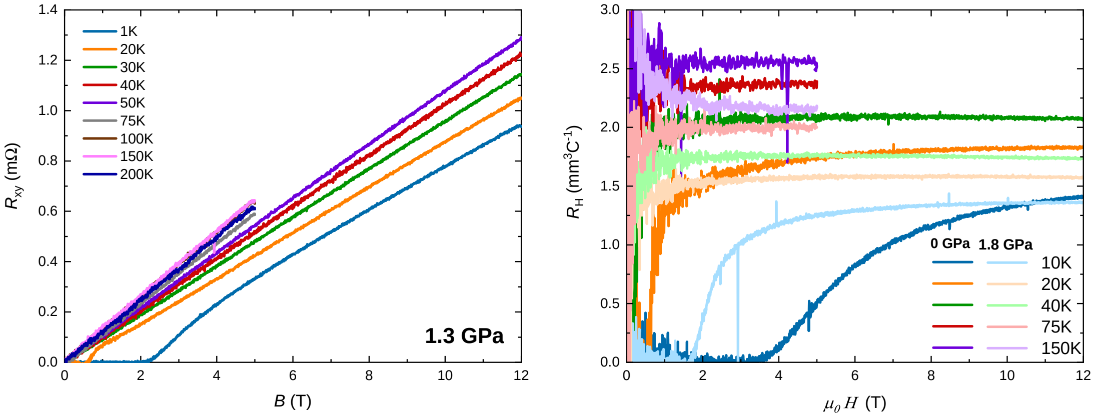

Figure 4.9: Left: A representative set of $R_{xy}(H)$ curves measured at 1.3 GPa for a $T_c = 30$K samples of Tl2201. Linearity at the highest measured fields indicates that R_H has reached a saturated value. Right: The field dependence of $R_H(= R_{xy}/B)$ at ambient pressure and at 1.8 GPa at select temperatures for direct comparison. A clear suppression of the saturating value is observed.

be independent of magnetic field, a lower maximum field of 5 T was applied.

In the right panel of Figure 4.9, the Hall coefficient is shown at both 0 GPa and 1.8 GPa at a select few temperatures. The large increase in the noise and divergence of R_H as zero field is approached is due to the numerical error associated with the division of an increasingly small number (as $\mu_0 H \to 0$). At ambient pressure and at 10 K, it is clear that insufficient field has been applied for the true normal state value of R_H to be reached. With the suppression of T_c with pressure, 12 T is found to be sufficient at the same temperature. With increasing pressure, there is a clear suppression of R_H at all temperatures.

In figure 4.10, the evolution of the temperature dependence of R_H with applied pressure (coloured points) in the $T_c(0\,\text{GPa}) = 31$ K sample and with chemical doping (open points from [50]) is shown.

A scale factor has been applied to the data measured in this work such that the ambient pressure values falls on top of the literature data for a sample with a highly comparable T_c. This scale factor is within the error associated with the determination of the sample geometry. This error is primarily as a result of uncertainty in the thickness of the sample, but is also due to the contact size relative to the total sample size, and is estimated to be as large as 30 %. Qualitatively, the form of R_H retains the same features, namely, a maximum at around 150 K. This maximum is clearly suppressed with both increasing hydrostatic pressure and increasing hole doping and can be understood to be a consequence of a suppression of anisotropic scattering with increasing hole doping (and reducing T_c) (see figure 4.6).

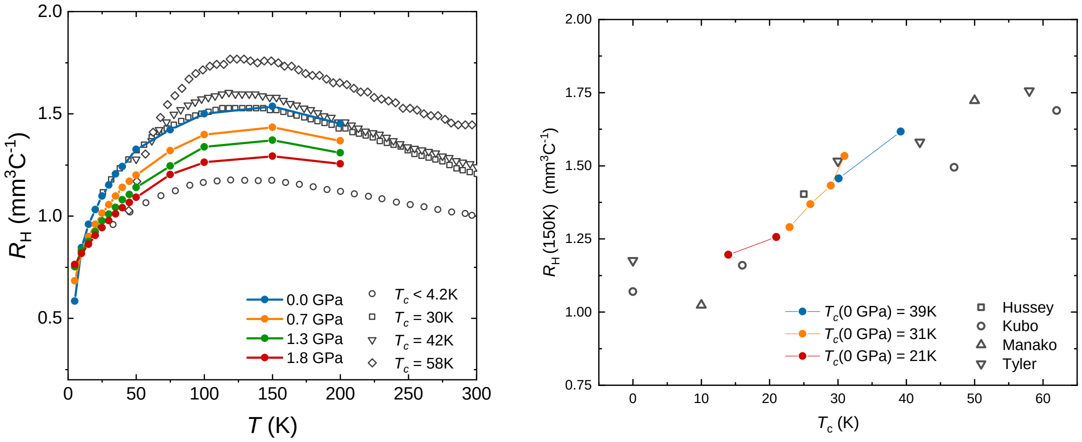

Figure 4.10: Left: The temperature-dependence of the Hall coefficient for a $T_c = 30\,\mathrm{K}$ crystal at pressures up to 1.8 GPa (coloured points). Also plotted are the temperature dependence of the Hall coefficient for different dopings at ambient pressure with data from [50]. Right: The magnitude of R_H at 150 K plotted against T_c as T_c is suppressed with the application of pressure for three samples (coloured points). R_H at 150 K at ambient pressure for different dopings (open points) with data taken from [50, 51, 59, 60]

.

To quantify the magnitude of this effect, in figure 4.10B the value of R_H at 150 K (the closest temperature to where R_H is maximal) has been plotted against T_c as it evolves with pressure (coloured points) for all three samples and with chemical doping (open points). In the case of the $T_c = 21\,\mathrm{K}$, 39 K samples, no scaling of the data has been performed. The evolution of R_H with T_c at ambient pressure is approximately linear up to $T_c = 50\,\mathrm{K}$. Random scatter is likely due to the geometric errors associated with determining sample dimensions (thickness in this instance). As a function of hydrostatic pressure, quantitatively the same evolution is found. For all three samples, $R_H(150\,\mathrm{K})$ was suppressed at a rate that is in very close agreement with what would be expected if T_c was suppressed via changes in chemical composition.

4.3.3 Discussion and Outlook

The work presented here does little to elucidate the fundamental origins of superconductivity, or the microscopic details of the role of pressure in overdoped Tl2201. However, it is interesting to note that despite the two mechanisms for tuning T_c being distinct in their nature, the effect of both mechanisms on the in-plane transport properties is remarkably similar. That is, the evolution of $R_H(T)$ and $R(T)$ with pressure and doping is highly comparable. Microscopically, it is easy to imagine how the addition of interstitial oxygen might change the carrier density and thus have an effect on the in-plane transport properties. This might also have been said in the case of the application of hydrostatic pressure. With the compression of the crystallographic lattice parameters, it is foreseeable that there will be a change in orbital overlap, for example, that will result in an effective charge transfer to the CuO planes. However, the reduction of dT_c/dP to values close to zero for all accessible dopings [53, 54] suggests that the effect of changing lattice parameters has a minimal effect on T_c, and by inference, on the in-plane transport properties. Of course, the effect on the in-plane transport properties in the case where pressure is only applied at low temperatures has not been explicitly checked here or elsewhere.

The work presented in this section shows that there are strong similarities between the evolution of the in-plane transport properties of Tl2201 as T_c is tuned by pressure and chemical doping. This is somewhat surprising because the two mechanisms are distinct. The suppression of T_c via the introduction of additional oxygen is expected to increase disorder whilst applying pressure (also suppressing T_c) has been shown to induce oxygen ordering and therefore decrease disorder. This suggests that the in-plane transport properties and superconductivity in overdoped Tl2201 are tied such that a suppression of T_c, regardless of the mechanism, is likely to change the normal-properties in broadly similar ways. The introduction of disorder via electron-irradiation or the application of uniaxial strain could serve as other means of changing T_c to test this hypothesis.

Lastly, the evolution of the $R_H(T)$ with pressure is suggestive of a reduction in scattering comparable to that with the addition of oxygen. As has been mentioned previously, the peaked form of $R_H(T)$ has been attributed to anisotropy in the in-plane scattering rate. Furthermore, the evolution of $R_H(T)$ with doping has been qualitatively modelled with success by incorporating this in-plane anisotropy and it's doping dependence [52]. Although $R_H(T = 0\text{ K})$ is somewhat obscured by superconductivity, simple extrapolation back to $T = 0$ suggests that $R_H(T = 0\text{ K})$ is substantially less sensitive to pressure compared with $R_H(T = 150\text{ K})$. In Tl2201, $R_H(T = 0\text{ K})$ has been determined to be in close agreement with the limit in which scattering is isotropic [61]. The implication is that anisotropic component of the total scattering rate is more sensitive to pressure than the isotropic component. This is again consistent with the doping dependence in which the linear-in-T anisotropic component is suppressed by $\sim 50\,\%$ between $T_c = 30$ K and $T_c = 20$ K whilst the isotropic component is found to be independent of T_c [52].

It is an open question whether quantum oscillations have only been observed in highly overdoped Tl2201 simply due to an increase in scattering as optimal doping is approached, or whether there is a fundamental restriction imposed by the nature of the strange metal phase. The application of pressure to Tl2201 may serve as a means of suppressing disorder such that quantum oscillations can be observed closer to optimal doping that has currently been possible. Such observations may reveal more about the nature of the strange metal phase. This, in fact, was the original motivation for the next section of this thesis.

4.4 Incoherent In-Plane Transport at High Fields

In this section, the in-plane magnetoresistance of overdoped Tl2201 is studied in fields up to 35 T. 8 samples were measured with a range of dopings (Fig 4.11A) all of which are far from p^*, the critical doping at which an H-linear MR has been observed in LSCO, and all of which exhibit the same H-linear MR and quadrature scaling.

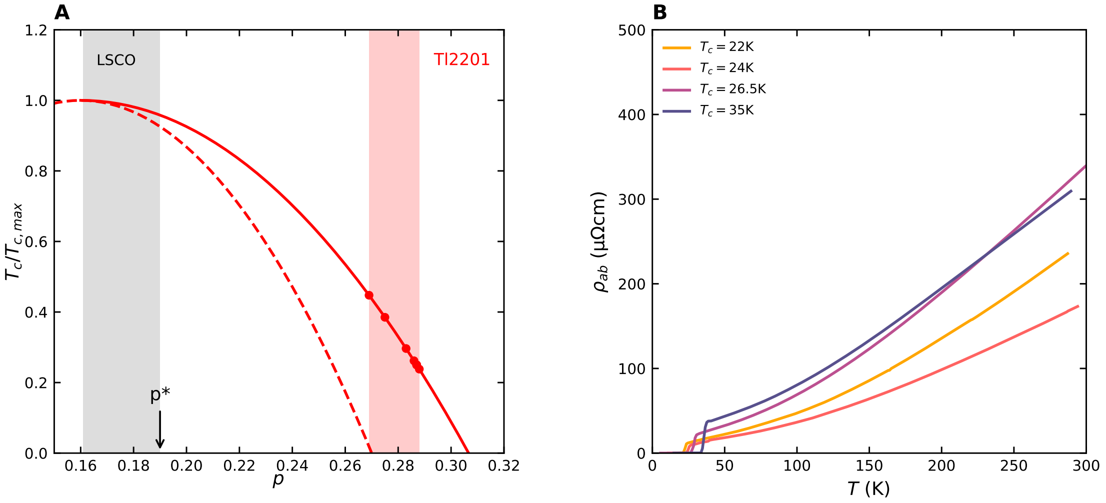

Figure 4.11: **A:** The superconducting dome (red-solid) of Tl2201 and other overdoped cuprates (red-dashed) defined by Equations 4.4 and 4.3 respectively. Red dots mark the doping of samples measured in this section. The grey and red regions illustrate the doping ranges over which H-linear MR has been observed in LSCO (grey) and Tl2201 (red). **B:** A representative collection of zero-field resistivity curves for the Tl2201 measured in this section.

All eight samples were measured with a magnetic field applied $H \parallel c$ whilst some were also measured with $H \parallel ab$. Three samples were measured with the application of hydrostatic pressures up to 2 GPa in order to study the evolution of the high-field MR with T_c (or carrier density) without the intrinsic introduction of disorder associated with doping. (In fact, pressure is expected to decrease disorder though oxygen ordering as discussed in more detail in 4.1.3.) A summary of the samples and conditions under which they were measured is presented in Table 4.2. Also presented are a representative selection of zero-field, ambient pressure $R(T)$ curves.

It is noted that there is a sizeable variation in the absolute value of the room-temperature value of ρ. This could be indicative of c-axis mixing. It is however, believed to be a result of the relatively large size of the contacts when compared with the total size of the sample. All of the samples measured were prepared for measurement inside a pressure cell. As such, the contact sizes are made larger to increase their mechanical strength and the samples are necessarily small in order to fit inside the pressure cell. Consequently, the error in the determination of geometrical parameters is larger than would be the case for an ambient pressure measurement leading to a larger spread in the absolute values of resistivity. The issue of c-axis contamination and the implications this has on our analysis and conclusions is nevertheless discussed in more detail later.

Sample	T_c(0 GPa)	Inferred Doping	Field Orientations	Pressures
Tl2201 - J1	22 K	0.287	$\mathbf{H} \parallel c$	0 GPa
Tl2201 - J3	35 K	0.275	$\mathbf{H} \parallel ab$ (0 GPa), $\mathbf{H} \parallel c$	0-2 GPa
Tl2201 - J5	26.5 K	0.283	$\mathbf{H} \parallel ab, \mathbf{H} \parallel c$	0 GPa
Tl2201 - J8	23 K	0.287	$\mathbf{H} \parallel c$	0 GPa
Tl2201 - J9	24 K	0.286	$\mathbf{H} \parallel ab$, $\mathbf{H} \parallel c$	0 GPa
Tl2201 - J10	22 K	0.287	$\mathbf{H} \parallel ab$, $\mathbf{H} \parallel c$	0 GPa
Tl2201 - A9	40 K 26 K (2 GPa)	0.269	$\mathbf{H} \parallel c$	0-2 GPa
Tl2201 - A16	20 K 14 K (2 GPa)	0.289	$\mathbf{H} \parallel c$	0-2 GPa

Table 4.2: A summary of the samples and measurement conditions for which data is presented in this section.

4.4.1 High-Field Linearity and Quadrature Scaling

In Figure 4.12A, D and G, $\rho(H,T)$ with $H \parallel c$ is presented for three representative samples with $T_c = 23\,\mathrm{K}$, 26.5 K, 35 K respectively. In accordance with expectation, at temperatures greater than T_c such that the zero-field normal state behaviour is visible, the low-field behaviour is quadratic-in-field. This can be explicitly seen in the derivatives shown in panels B, E and H of the same figure. The low-field derivative passes through zero with a finite linear slope. Contrary to expectations, the high-field behaviour crosses over from H^2 to strictly H-linear. Again, this is clearly shown by the flat derivatives at high field. Notably, the high field slope of $\rho_{ab}(H)$ appears to be independent of temperature. Indeed, the high-field derivatives appear to saturate at a temperature-independent value.

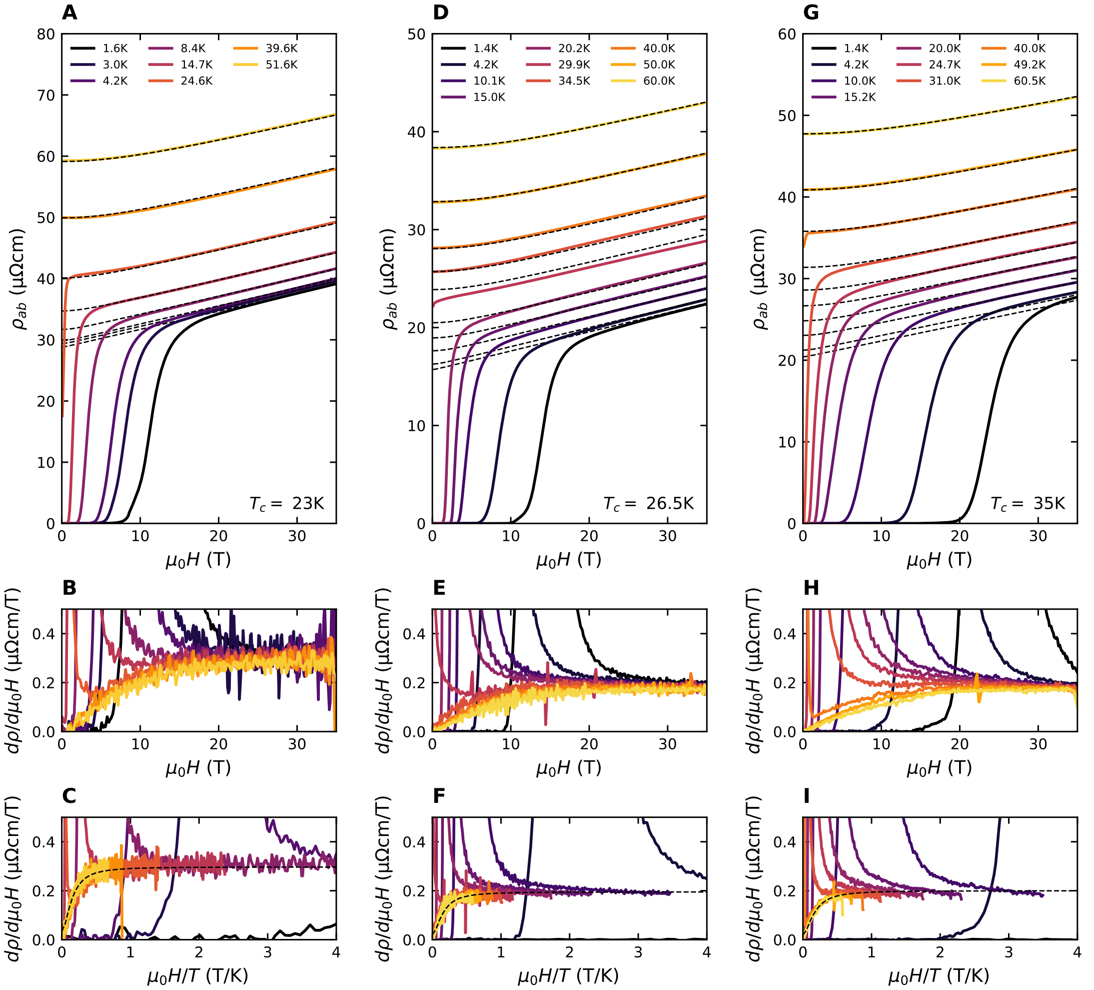

Figure 4.12: A: $\rho_{ab}(H)$ sweeps measured at different fixed temperatures with $H \parallel c$ for a sample with $T_c = 23\,\mathrm{K}$. The normal state portions have been simultaneously fitted to the sum of a quadrature and orbital resistive components to the total resistivity as described by Equation 4.7 (dashed lines). B: The derivatives of $\rho_{ab}(H)$ from panel A. In the absence of superconductivity, low-field quadraticity crosses over to high-field linearity. C: The same derivatives as those presented in panel B plotted against $\mu_0 H/T$. All of the curves collapse onto a single derivative of the characteristic quadrature form (dashed line). Equivalent plots are shown in panels D, E, F and G, H, I for samples with $T_c = 26.5\,\mathrm{K}$ and $35\,\mathrm{K}$ respectively.

These features are highly reminiscent of the quadrature form of the MR discussed in Section 2.5.1 in the context of P-Ba122, $FeSe_{1-x}S_x$ and LSCO. Recall that for P-Ba122 [21], for example, the form of the MR was shown to be described by

$$\rho(H,T) = \rho_0 + \sqrt{(\alpha k_B T)^2 + (\gamma \mu_B \mu_0 H)^2} \tag{4.5}$$

There, $\rho_0 = \rho(0,0)$ was found by extrapolating back both the T-linear $\rho(T,0)$ and H-linear to $\rho(0,H)$. This is not so easy to do in the case of Tl2201 as overdoped cuprates are characterised by $\rho_{ab}(0,T)$ that is comprised of both a linear and a quadratic term, thus, the linear extrapolation to zero temperature is not possible. It may be possible to make an estimate of $\rho(0,0)$, but such an estimate would have to assume a form of the MR in the superconducting state.

However, it is possible to proceed via a different route. The derivative of the quadrature form of the MR (Equation 4.5) with respect to magnetic field is

$$\frac{d\rho(H,T)}{d\mu_0 H} = \frac{(\gamma\mu_B)^2\mu_0 H}{\sqrt{(\alpha k_B T)^2 + (\gamma\mu_B\mu_0 H)^2}} = \frac{\mu_0 H}{T}\frac{(\gamma\mu_B)^2}{\alpha\sqrt{(1+(\frac{\gamma\mu_B}{\alpha k_b})^2(\frac{\mu_0 H}{T})^2}} \tag{4.6}$$

This is also true if a temperature dependence to the residual resistivity that is subtracted from the total MR is considered (if $\rho_0 \to \rho_0(0,T)$ in Equation 4.5). It follows that the derivatives should therefore collapse in a similar manner to $(\rho - \rho_0)/T$ if plotted against $\mu_0 H/T$. Indeed this is found to be the case as shown for all three samples presented in Figure 4.12 (panels C, F and I) where dashed lines are fits to the form described by Equation 4.6. Of course, by taking the derivative, any temperature dependence of the subtracted term (ρ_0 in Equation 4.5) will have been removed. It can be concluded that the field-dependent contribution to $\rho_{ab}(H,T)$, that remains after the subtraction of a (possibly) temperature-dependent but field-independent residual resistivity from each field-sweep, is of the quadrature form.

We now turn to the issue of the residual resistivity. In the simplest case, and as was the case in P-Ba122, is one in which $\rho_0 = \rho(0,0)$. For each sample, an estimate of $\rho_{ab}(0,0)$ was made by linearly extrapolating $\rho(H)$ at the lowest measured temperature (typically 1.4 K). $(\rho(H,T) - \rho(0,0))/T$ has been plotted against H/T in Figure 4.13A, C and E for the same three samples. Dashed lines are to the quadrature form. For high H/T (low T) shown in the upper half of each panel, the data is found to approximately collapse, although superconductivity obscures much of the data. At low H/T (high T) shown in the lower half of each panel, large deviations from quadrature scaling are observed. The linear extrapolation back to zero field using the lowest temperature data is only one method for estimating $\rho(0,0)$. However, even if $\rho(0,0)$ is included as a free parameter and the normal state regions of the data are simultaneously fitted to $\rho(H,T)$ described in Equation 4.5, it

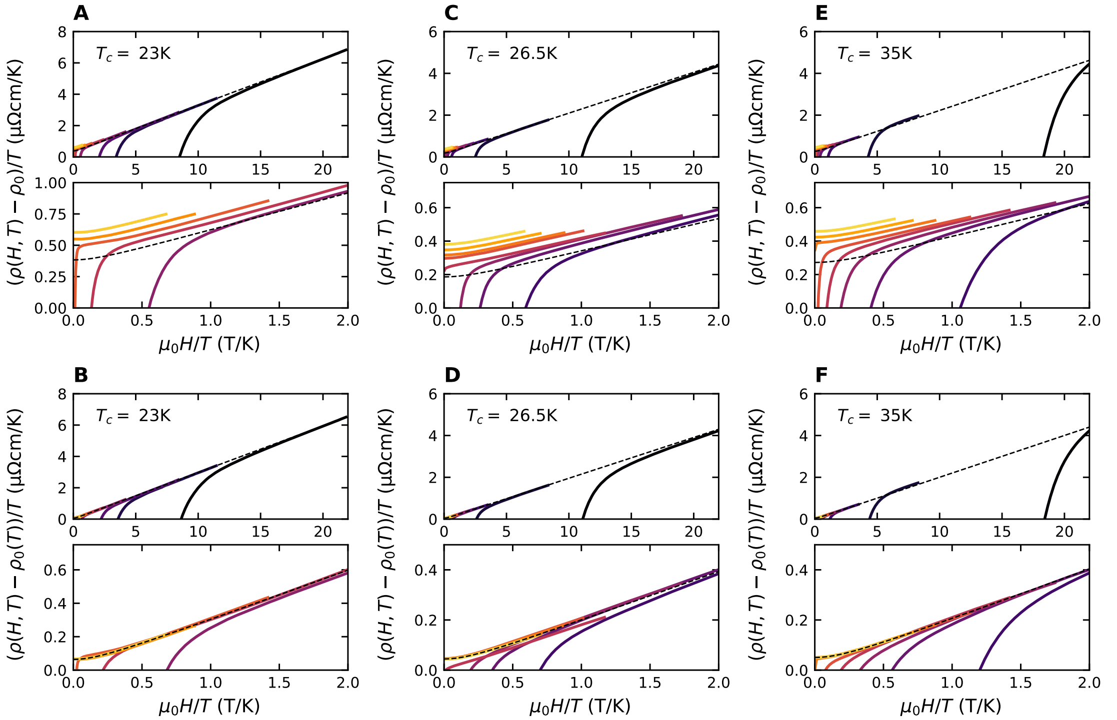

Figure 4.13: A: Plots of $(\rho - \rho_0)/T$ against H/T for a $T_c = 23\,\mathrm{K}$ samples of Tl2201 at high H/T (top) and low H/T (bottom) in which collapse of the data is expected if $\rho(H,T)$ is accurately described by Equation 4.5 where the subtracted residual resistivity is both field- and temperature-independent. B: Plots of $(\rho - \rho_0)/T$ against H/T for the same sample as in A in which collapse of the data onto a curve of the quadrature form is observed. A temperature dependence to the subtracted resistivity was considered in this case. Equivalent plots for samples with $T_c = 26.5\,\mathrm{K}$ and $35\,\mathrm{K}$ are presented in panels C, D and E, F respectively.

was not found possible to find a temperature- and field-independent residual resistivity that would either fit the measured $\rho_{ab}(H,T)$ shown in Figure 4.12 or result in a collapse of the data.

The zero-field resistivity of overdoped Tl2201 is known to be well described by the sum of T-linear and T-quadratic terms [62]. It therefore seems sensible to consider the case where

$$\rho(H,T) = \rho_0 + AT + BT^2 + \sqrt{(\alpha k_B T)^2 + (\gamma \mu_B \mu_0 H)^2} \tag{4.7}$$

That is, $\rho_0 \rightarrow \rho_0 + AT + BT^2$. The regions of ρ_{ab} that are at sufficiently high (H,T) to be unambiguously normal state were simultaneously fitted to Equation 4.7. These fits are shown as dashed lines in panels A, D and G of Figure 4.12. Overall, the fits are remarkably good. In panel D, there is a single field-sweep (labelled to be at $T = 20.2K$) for which the data was found to not fit. Comparison of $\rho(0, T = 20.2K)$ with $\rho(T)$ measured separately indicates that the determination of temperature for this sweep was inaccurate. Performing the same procedure in which $\rho(H,T) -$

$(\rho_0 + AT + BT^2)$ is plotted against H/T, a collapse of the data is observed and is shown in panels B, D, and F of Figure 4.13.

In summary, the field- and temperature-dependence of the in-plane resistivity can be very closely described by by Equation 4.7. That is, it is described by a field-dependent quadrature component in series with a polynomial temperature-dependent component that is typically used to describe the in-plane resistivity. That quadrature component can be isolated by taking the derivative of ρ with respect to magnetic field. When this is done, the resistivity curves measured at different temperatures collapse onto a universal curve when plotted against H/T as is expected from an MR of a quadrature form. As is discussed in Section , the magnitude and form of the MR is not easily be derived from Boltzmann transport theory.

4.4.2 Angular Dependence

The MR of three samples was also measured with the magnetic field applied in-plane ($H \parallel I \parallel ab$). In this configuration, there should be no Lorentz component. $\rho_{ab}(H,T)$ is presented in Figure 4.14 for both magnetic field configurations for direct comparison. The two samples for which data is presented have $T_c = 26.5\,\mathrm{K}$ (panels A, C) and $35\,\mathrm{K}$ (panels B, D).

Qualitatively, the behaviour is the same in both field orientations. In both orientations, the MR has the same quadrature form in which low-field H^2 behaviour crosses over to linearity at high-field. Due to the huge anisotropy of H_{c2}, it was not possible to suppress superconductivity at temperatures substantially below T_c in when $H \parallel ab$. It was therefore not possible to measure $\rho_{ab}(H,T)$ in a regime within which strictly H-linear behaviour extends over a large field-range. However, the derivatives shown in panels C and D (right) of Figure 4.14 strongly suggest that in the presence of a sufficiently large field, H-linearity would be strictly adhered to and that the saturating value of the high-field slope would be 1.5-2 times larger when $H \parallel ab$ compared with when $H \parallel c$.

The absolute value of $\rho_{ab}(H,T)$ at high fields is insensitive to magnetic field orientation. This is markedly different to the strongly anisotropic ρ_c in which ADMR oscillations could be observed. A 300% increase in the magnitude of ρ_c [63] is observed as the field is rotated from $\parallel ab$ to $\parallel c$ at $45\,\mathrm{T}$. Here, $\rho_{ab}(H = 35\mathrm{T})$ only exhibits a $7\,\%$ and $3\,\%$ increase in the two samples presented in Figure 4.14.

An insensitivity of form of the $\rho(H,T)$ with respect to changes in applied magnetic field orientation is highly unexpected of an MR that is derived for orbital mechanisms. One explanation is that the charge carriers responsible for the observed quadrature MR are not coherent quasiparticles

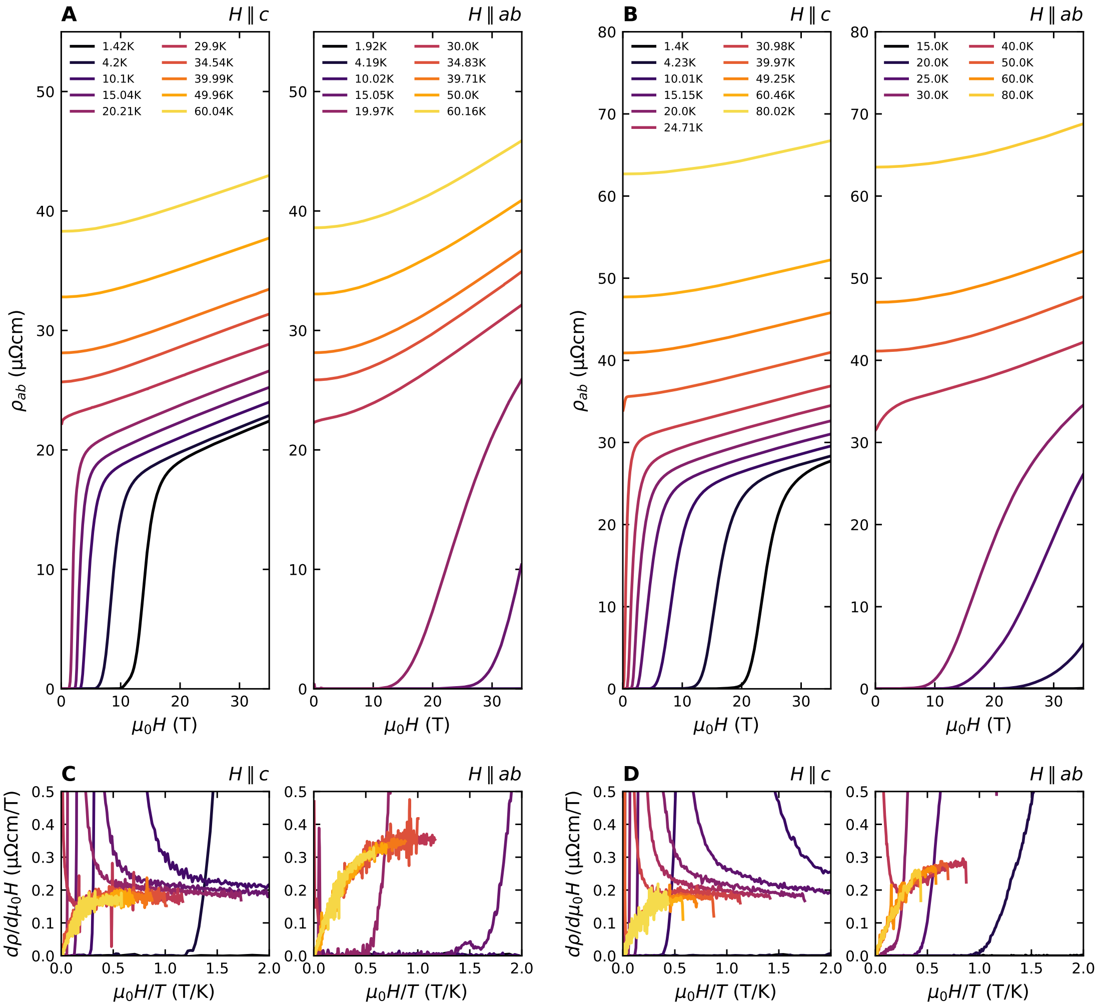

Figure 4.14: A: (left) $\rho_{ab}(H,T)$ with $H \parallel c$ (also presented in Figure 4.12D) for Tl2201 with $T_c = 26.5\,\mathrm{K}$. (right) $\rho_{ab}(H,T)$ with $H \parallel ab$ for the same sample. C: The derivatives of the field-sweeps shown in A. Plots equivalent to A and C are presented in panels B and D for a sample with $T_c = 35\,\mathrm{K}$ (for which $H \parallel c$ data is also shown in Figure 4.12G).

and therefore do not adhere to standard transport theories (Boltzmann transport theory) that have been successfully used to model the ADMR [47, 49, 52] in Tl2201.

4.4.3 A Comparison with the Shockley-Chambers Tube Integral Formula

The Shockley-Chambers tube integral formula (SCTIF), a derivative of the Boltzmann transport equation modified for quasi-two-dimensional systems, has been utilized extensively to numerically calculate the transport properties of cuprates. It allows for the computation of the conductivity tensor in both high- and low-field limits. A notable success of the SCTIF that is relevant to this work in particular is the simulation and fitting of the ADMR ($I \parallel c$) in highly overdoped Tl2201 [63] from which a Fermi surface that was later corroborated by quantum oscillation studies [64] was derived. As detailed in Section 4.1.2, the application of the SCTIF to temperature dependent ADMR studies at different dopings revealed an anisotropy to the in-plane scattering rate with a doping dependence that was able to account for both the temperature- and doping-dependence of R_H. More recently, the SCTIF has been applied to successfully reproduce the in-plane $\rho_{xy}(B)$ of Tl2201 over the entirety of the overdoped side of the phase diagram [65]. In general, for a two-dimensional Fermi surface, the elements of the conductivity tensor are:

$$\sigma_{ij} = \frac{e^3 B}{2\pi^2 \hbar^2 c} \int_0^{2\pi} d\phi \int_0^{\infty} d\phi\prime \frac{v_i(\phi) v_j(\phi - \phi\prime)}{\omega_c(\phi)\omega_c(\phi - \phi\prime)} e^{\int_\phi^{\phi'} \phi\prime\prime/\omega_c(\phi\prime\prime)\tau(\phi\prime\prime) d\phi\prime\prime} \tag{4.8}$$

where ϕ is the in-plane (azimuthal) angle, $i, j \in (x, y, z)$.

First, a direct comparison is made between the measured in-plane magnetoresistance with $H \parallel c$ of our samples at high fields, and that predicted by numerical computation of the Shockley-Chambers tube integral formula in the same current and field orientations. Secondly, the out-of-plane response ($I \parallel c$), again for $H \parallel c$, is numerically computed and compared to the presented experimental data in order to ascertain whether c-axis mixing is likely to be present in our results and to determine whether it should influence our analysis and conclusions.

The In-Plane Response ($I \parallel ab$, $H \parallel c$)

In order to calculate the in-plane response, only an in-plane anisotropy to both k_F and $\omega_c \tau$ was considered. Specifically:

$$k_F(\phi) = k_{00} + k_{40}\cos(4\phi)$$

and:

$$\omega_c\tau(\phi) = (\omega_c\tau)_0/(1 + \gamma(T)\cos(4\phi))$$

where k_{00}, k_{40} and the temperature-dependent anisotropy factor $\gamma(T)$ and $(\omega_c\tau)_0(T)$ are experimentally determined from fits to ADMR measurements and can be found through their relationship to the temperature dependencies of the isotropic and anisotropic scattering rates: $(1-\gamma)/(\omega_c\tau)_0 = A_{iso} + B_{iso}T^2$, $2\gamma/(\omega_c\tau)_0 = A_{aniso} + B_{aniso}T$ [49, 52]. If the angle dependence of $(\omega_c\tau)_0$ is attributed solely to τ while ω_c is assumed to have a linear dependence upon magnetic field, Equation 4.8 can be rewritten as:

$$\sigma_{ij} = \frac{e^3B}{4\pi^2\hbar^2c\omega_c^2}\int_0^{2\pi} d\phi \int_0^{\infty} d\phi' v_i(\phi)v_j(\phi-\phi')e^{\int_\phi^{\phi'} \phi''/\omega_c(\phi'')\tau(\phi'')} \tag{4.9}$$

The parameters used to define the Fermi surface and the temperature dependence of $\omega_c\tau$ are taken from [49] for a sample with $T_c = 20\,\mathrm{K}$ and are the same as those used recently to model the in-plane Hall response of Tl2201 [65]. They are listed in Table 4.3. Note that not all of them are relevant to this calculation.

Parameter	Value
k_{00}	$0.0728\,\mathrm{nm}^{-1}$
k_{40}/k_{00}	-0.033
k_{21}	$0.0031\,\mathrm{nm}^{-1}$
k_{61}/k_{21}	0.7
k_{101}/k_{21}	-0.3
A_{iso}	2.43
B_{iso}	$3.13 \times 10^{-4}\ \mathrm{K}^{-2}$
A_{ani}	$0.135\ \mathrm{K}^{-1}$
B_{ani}	$6.11 \times 10^{-2}\ \mathrm{K}^{-1}$

Table 4.3: Parameters derived from ADMR fits for a sample with $T_c = 20\,\mathrm{K}$ from [49].

Both in-plane ρ_{xx} and ρ_{xy} have been simulated between 0 K and 100 K and in magnetic fields up to 50 T and are presented in Figure 4.15A/B. The zero-field resistivity is found by extrapolating $\rho_{ab}(\mu_0H)$ to zero field. The absolute value of $\rho_{xx}(T)$ (more clearly shown in Figure 4.15C) is highly comparable to those shown in Figure 4.11. The largest discrepancy is a factor of ~ 2. The fact that the same quadrature behaviour is seen in all of our samples regardless of the absolute value of ρ_{xx} suggests that the quadrature MR does not originate from *c*-axis mixing and is not tied to disorder.

The second notable feature of the simulated data is that the magnitude of $\Delta\rho$ (shown explicitly in Figure 4.15D) is markedly smaller than is observed in experiment. At 35 T, the highest fields experimentally applied, $\Delta\rho$ has a maximal value at ~60 K of 0.4 μΩcm. This is an order of magnitude

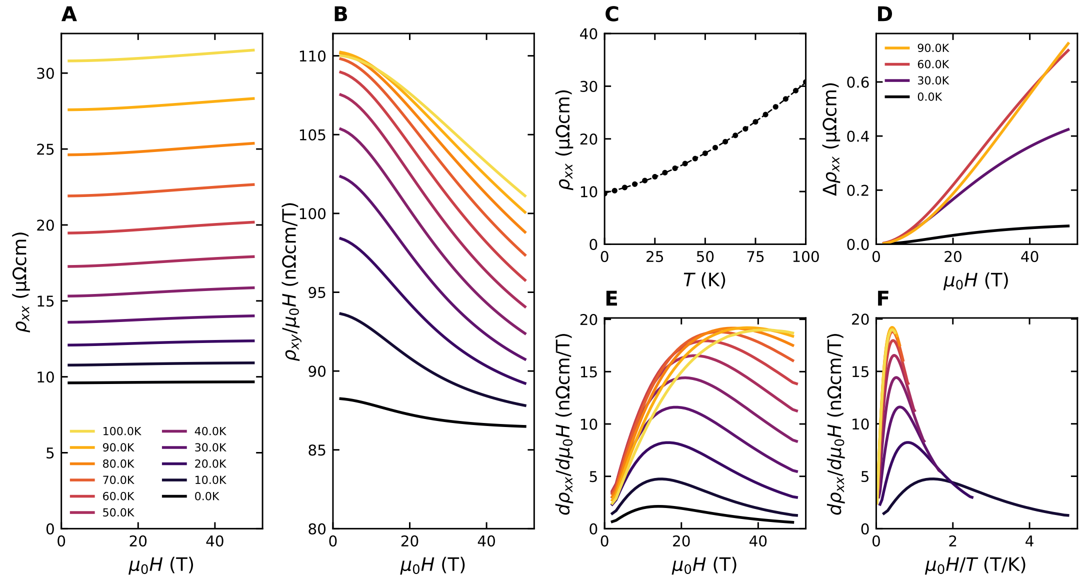

Figure 4.15: The field dependence of ρ_{xx} (A) and $\rho_{xy}/\mu_0 H$ (B) at different temperatures. C: The zero-field $\rho_{xx}(T)$. The dashed line is a fit to $\rho_c = AT + BT^2$. D: $\Delta\rho_{xx}$ for select temperatures. E: The derivative of ρ_{xx} with respect to magnetic field. F: A demonstration of the failure of the SCTIF to produce a magnetoresistance that collapses as is anticipated if it were of a quadrature form.

smaller than is experimentally observed. Even once the experimental data is scaled to account for a discrepancy in the absolute magnitude of $\rho_{xx}(T)$, a factor of $\sim 6-7$ remains. Additionally, the calculation uses parameters derived from fits of ADMR to a sample with T_c =20 K. The largest discrepancies are seen in samples with higher T_c which is in accordance with expectation as $\rho(T = 300\text{K})$ increases as optimal doping is approached.

The fact that $\Delta\rho$ is temperature dependent at all is contrary to the experimental result. At low temperatures, the SCTIF predicts that $\Delta\rho$ vanishes. This is a consequence of the vanishing anisotropy of $1/\tau$ at low temperatures. It is clear from $d\rho_{xx}/d\mu_0 H$ (Figure 4.15E) that the high-field slope is strongly temperature dependent. Additionally, H-linearity is not found to occur at any temperature. The high-field behaviour is sub-linear. This temperature dependence to the MR and distinct lack of linearity at high fields prevent the characteristic quadrature collapse of $d\rho_x x/d\mu_0 H$ when plotted against H/T from occurring (Figure 4.15F).

The Out-of-Plane Response ($I \parallel c$, $H \parallel c$)

The out-of-plane response was also simulated using the SCTIF. In this case, additional c-axis corrugations of the Fermi surface were included in the parameterisation of k_F so that:

$$k_F(\phi,\kappa) = k_{00}(1+\frac{k_{00}}{k_{40}}\cos(4\phi)) + k_{21}\cos(\kappa)(\sin(2\phi)+\frac{k_{61}}{k_{21}}\sin(6\phi)+\frac{k_{101}}{k_{21}}\sin(10\phi))$$

An additional integral over κ (along the k_z direction) is now necessary. Since $I \parallel H \parallel c$, only σ_{zz} needs to be calculated in order to determine $\rho_c = 1/\sigma_{zz}$ and is given by:

$$\sigma_{zz} = \frac{e^2}{4\pi^3\hbar^2\omega_c^2 c}\int_{-\pi/2}^{\pi/2} B d\kappa \int_0^{2\pi} d\phi \int_0^{\infty} d\phi' v_z(\phi,\kappa) v_z(\phi-\phi',\kappa) e^{\int_{\phi}^{\phi'} \phi''/\omega_c(\phi'')\tau(\phi'')} \tag{4.10}$$

The same parameters that are listed in Table 4.3 were used here as well.

The field-dependence of ρ_c has been calculated for temperatures up to 150 K and in magnetic fields up to 50 T and is presented in Figure 4.16A. Again, the zero-field resistivity is found by extrapolating $\rho_c(\mu_0 H)$ to zero field and is presented in Figure 4.16B. The issue at hand is that there is little discernible difference between $\rho_c(T)$ and $\rho_{ab}(T)$ other than a large multiplicative prefactor. Thus, in a measurement of $\rho_{ab}(T)$, it is difficult to differentiate between c-axis mixing and error arising from uncertainty in sample geometry for example. This of particular concern due to the degree of anisotropy in Tl2201.

However, within the SCTIF formalism, there are again distinct discrepancies between the experimental observation and simulated ρ_c. In particular, there is a strong temperature dependence to the high-field slope and failure to reach a limiting H-linear behaviour, especially at low temperatures. This is most clearly seen in Figure 4.16C. A finite quadratic component persists to highest fields. It is noted that at higher temperatures, temperature-independent high-field quasi-linearity and a T-independent high-field slope is somewhat recovered. However, the temperatures at which these properties are recovered are substantially higher than those below which a quadrature MR are experimentally observed. As a result, and as is demonstrated in 4.16D, the derivatives of the field sweeps do not collapse for all temperatures and are not of the characteristic quadrature form.

Finally, Kohler scaling is examined within the SCTIF and as observed in measured Tl2201. In simulations (Figure 4.16E), Kohler scaling is observed at high temperatures whilst at low temperatures, there is a distinct deviation with curves falling progressively higher as temperature is decreased. In experiment, there is a similar recovery of Kohler scaling in equivalent plots. The deviation at lower temperatures is distinct in that curves fall sequentially lower with decreasing

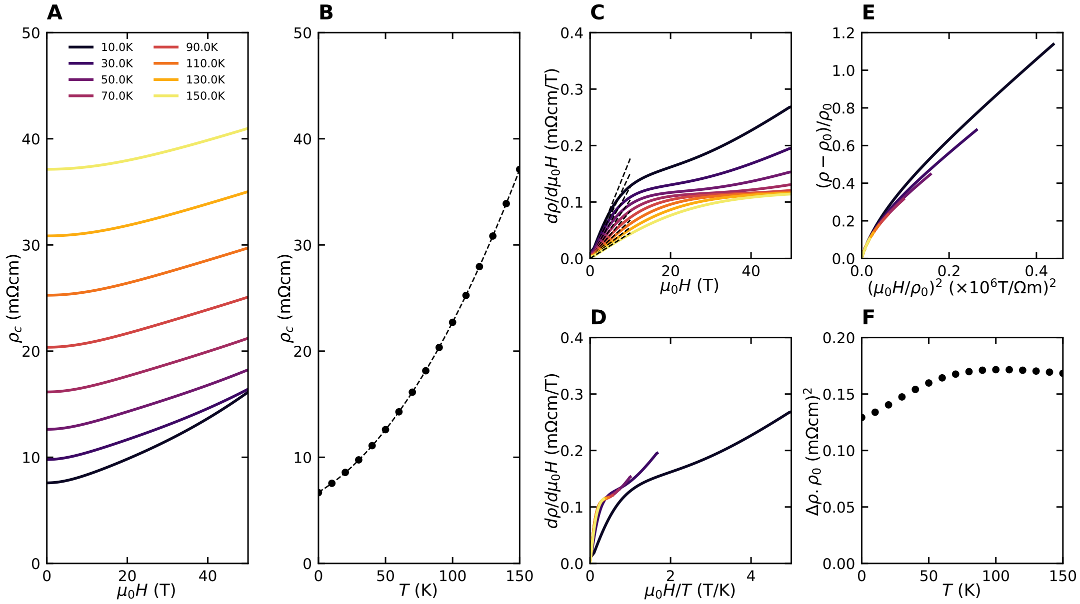

Figure 4.16: A: The field dependence of ρ_c as simulated using the SCTIF. B: The zero-field temperature dependence $\rho_c(T)$ from extrapolations of $\rho_c(H)$ to zero field. The dashed line is a fit to $\rho_c = AT + BT^2$. C: The derivative of $\rho_c(H)$ D: A demonstration of the failure of the derivative to collapse as is expected of a quadrature MR. E: A Kohler plot illustrating a deviation from Kohler scaling at low-T and recovery at high T. F: The temperature dependence of $\Delta\rho_c.\rho_c(0)$ at 1 T.

temperature suggesting that the origin of the violation of Kohler's scaling in Tl2201 is distinct from that which is predicted by conventional transport theory. In addition, $\Delta\rho.\rho_0$ presented in Figure 4.16F only increases by approximately 30 % between 0 K and the temperature at which it is maximal if computed using the SCTIF. In the experiment, Tl2201 demonstrates an increase of 150 % between 25 and 150 K. If extrapolated to 0 K, this could be substantially higher. It appears that the degree of Kohler violation seen in Tl2201 cannot be described within the SCTIF even if a c-axis contribution is considered.

In summary, the comparison between the in-plane MR of Tl2201 as measured in experiment and the properties predicted within the SCTIF formalism in both $H \parallel ab$ and $H \parallel c$ suggest that the quadrature MR is intrinsic to ρ_{ab} in overdoped Tl2201 and cannot be described within conventional transport theory. The degree of c-axis contamination is expected to be random between samples, therefore, the universality and consistency of the measured data is highly unlikely to be attributable to a c-axis component. Moreover, the strictly H-linear behaviour that is experimentally observed at high-fields is highly unlikely to be reproduced through a random admixture of ρ_{ab} and ρ_c within a conventional transport formalism like the SCTIF, especially when neither ρ_{ab} nor ρ_c are expected to produce a strictly H-linear MR.

4.4.4 Series or Parallel Conduction Channels

Thus far, it has been assumed that the two components of the MR (conventional and quadrature) are such that that their resistivities sum such that $\rho_{ab} = \rho_{con} + \rho_{quad}$ (as in the case of resistors that are in series). This is consistent with the analysis of P-Ba122 [21] where ρ_{orb} was simply ρ_0. Here, it has been postulated that $\rho_{con} = \rho_0 + AT + BT^2$ and that the analysis is otherwise unchanged so that:

$$\begin{aligned}\frac{1}{\sigma} = \frac{1}{\sigma_{con}} + \frac{1}{\sigma_{quad}}, \qquad \rho_{ab} &= \rho_{con} + \rho_{quad} \\ &= \rho_0 + AT + BT^2 + \sqrt{(\alpha k_B T)^2 + (\gamma \mu_B \mu_0 H)^2}\end{aligned} \tag{4.11}$$

Physically, this might be expected in a scenario in which the two conduction channels are separated in real-space. Alternatively, it is conceivable that they are in fact separated in k-space. In which case, it might be more appropriate to consider parallel conduction channels in which conductivities are simply summed and resistivities are added in parallel as in the case of two parallel resistors. In this scenario:

$$\begin{aligned}\sigma = \sigma_{con} + \sigma_{quad}, \qquad \frac{1}{\rho_{ab}} &= \frac{1}{\rho_{con}} + \frac{1}{\rho_{quad}} \\ &= \frac{1}{\rho_0 + AT + BT^2} + \frac{1}{\rho_0' + \sqrt{(\alpha k_B T)^2 + (\gamma \mu_B \mu_0 H)^2}}\end{aligned} \tag{4.12}$$

In Figure 4.17, the same in-plane MR data from a single sample is presented with fits to ρ_{ab} of both forms given in Equations 4.11 and 4.12. The left-hand panels contain fits to a total MR in which resistivities are added in series (as per Equation 4.11) whilst the right-hand panels contain fits to a total MR in which conductivities are added in series (as per Equation 4.12). In both cases, only the data that was sufficiently far from the superconducting transition to be unambiguously considered normal state was fitted. The same subset of the data was fitted in both cases. Only field sweeps at fixed temperatures are fitted. The dashed-lines in other panels are derived from the optimised parameters from fits to $\rho(B)$.

At the highest temperatures presented (those in which there is no superconductivity at low field), there is little difference between the quality of the fits to $\rho_{ab}(\mu_0 H)$ in either scenario (Figure 4.17A/C). The principle discrepancy arises at low temperatures. In the case where resistivities are added in series (Figure 4.17A), the extent of the H-linearity simply extends to lower fields as temperature decreases. Conversely, when conductivities are added (Figure 4.17C), $1/\rho_{quad}$ becomes increasingly small and effectively shorts out the parallel conduction channel resulting in marked reduction of ρ_{ab} as both T and H approach zero. The conductivity of the incoherent channel diverges. In fact, in order to fit the data with this model at all, it was necessary to include a second residual resistivity, ρ_0', in the quadrature sector to prevent exactly this phenomena.

The physical origin or interpretation of such an residual resistivity in the quadrature component is unclear. Such a downturn in the resistivity of overdoped cuprates has not been reported. The usual approach for elucidating the normal state transport behaviour in the superconducting state (and access the normal state in the temperature range at which this anomalous downturn might be

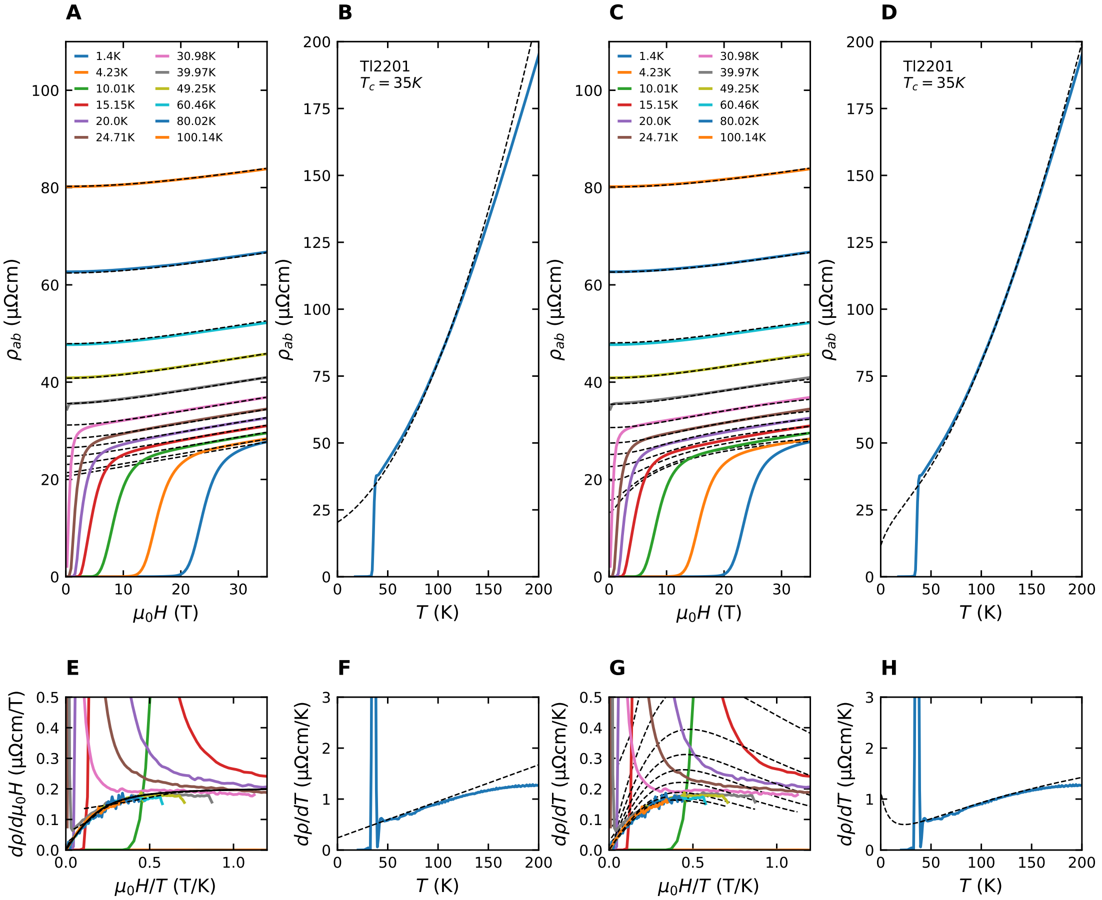

Figure 4.17: A(C): The measured MR of Tl2201 with $T_c = 35\,$K and with $H \parallel c$. Dashed lines are fits to the normal state portions of the data to models in which resistivities (conductivities) add in series as explicitly shown in Equation 4.11(4.12). B(D): The measured zero-field resistivity (solid blue) and the resistivity derived from the fits to the MR (dashed) in the case where resistivities (conductivities) are added in series. E(G): The derivatives of the measured (solid lines) and fits (dashed line) plotted against H/T for the case where resistivities (conductivities) are assumed to add in series. F(H): The derivatives of the measured $\rho(T)$ and corresponding fit shown in panel B(D).

expected) is to apply a magnetic field. However, in the presence of a magnetic field, the quadrature form of the MR prevent, or at least suppress, a divergence of the quadrature conductivity such that it may not be observed. Of course, the model in which resistivities add in series does not preclude the existence of a ρ_0', but it would be indistinguishable from ρ_0.

The divergence of the quadrature conductivity as H and T both approach zero manifests itself most clearly as in the derivative. Figures 4.17E(G) show the derivatives of the MR plotted against H/T for the case where resistivities (conductivities) are added in series. When resistivities are added in series, each of the derivatives collapses (as has been shown previously) onto a single curve. Multiple fits (dashed lines) are shown but fall on top of one another. When conductivities are added, the form of the derivative becomes highly temperature dependent. The high-field limiting behaviour is no longer H-linear (it is sublinear, especially at low temperatures) and collapse of the data does not occur.

A limitation of the model in which resistivities are added in series is that there is no mechanism by which $\rho(T)$ will crossover from quadratic at low-T to linear at high-T as is experimentally observed [50, 62]. One mechanism for resolving this is to introduce an additional term to the effective scattering rate such that

$$\frac{1}{\Gamma_{total}} = \frac{1}{\Gamma_{ideal}} + \frac{1}{\Gamma_{max}}$$

as was suggested in [18] where Γ_{max} can be set by the lattice spacing using the so-called Mott-Ioffe-Regel limit which assumes that the mean-free-path is set by the lattice spacing. With the introduction of Γ_{max}, the low-T quadraticity in $\rho(T)$ is lost at high temperatures where linearity is recovered in good agreement with experiment [18, 62]. Without it, the T-quadratic term will persist indefinitely as explicitly shown in Figure 4.17F. Naturally, inclusion of higher temperature data will result in increasingly bad fits to a model in which resistivities are added in series not because $\rho(\mu_0 H)$ becomes non-quadrature, but because the model fails to account for the behaviour of $\rho(T)$ at high temperatures.

On the contrary, this is a feature of the data that is well reproduced by the model in which conductivities are added in series. The addition of resistivities in parallel (conductivities in series) naturally provides an analogous mechanism by which $\rho(T)$ can saturate at high temperatures. As a result, $\rho(T)$ (shown in Figure 4.17D) that was determined from fits to $\rho(H, T)$ using the model in which conductivities add in series is in closer agreement with the experimental data at high temperatures. However, the same divergence of the quadrature conductivity at low-T and low-B

causes an anomalous decrease in $\rho(T)$ at low temperatures as well.

This observation is somewhat reflected in the sensitivity of the fit parameters to the temperature range of the field sweeps that are included in the fitting procedure. Table 4.4 shows the converged parameters for fits in both scenarios to the data presented in Figure 4.17 including only data up to $T = T_{max}$. Also included in the table is the derived parameter α/γ and some statistical metrics: the sum of the squared residuals ($\sum_i (y_i - f_i)^2$), R^2 ($= 1 - \sum_i (y_i - f_i)^2 / \sum_i (y_i - \overline{y})^2$) of the entire fitted data and $R^2_{T=50\mathrm{K}}$. The latter shows how inclusion of additional data to the total fit diminishes the quality of the fit to the data at 50 K.

Parameter	$T_{max} = 50$K	$T_{max} = 101$K	$T_{max} = 130$K	$T_{max} = 210$K
ρ_0 ($\mu\Omega$cm)	20.3	20.3	20.3	15.8
A ($\mu\Omega$cm/K)	0.195	0.189	0.189	0.164
B ($\mu\Omega$cm/K^2)	0.0036	0.0036	0.0036	0.0026
α ($\mu\Omega$cm/meV)	0.499	0.570	0.588	2.619
γ ($\mu\Omega$cm/meV)	3.466	3.499	3.520	6.062
α/γ	0.144	0.162	0.167	0.432
$\sum_i (y_i - f_i)^2$	2.53E-16	6.75E-15	6.81e-15	2.08e-13
R^2	0.9993	0.9999	0.9999	0.9998
$R^2_{T=50\mathrm{K}}$	0.9971	0.9986	0.9987	0.9404
ρ_0 ($\mu\Omega$cm)	32.7	31.6	30.7	34.4
A ($\mu\Omega$cm/K)	0.280	0.189	0.171	0.189
B ($\mu\Omega$cm/K^2)	0.0056	0.0058	0.0054	0.0064
ρ_0' ($\mu\Omega$cm)	27.1	18.4	0.0	17.5
α ($\mu\Omega$cm/meV)	24.0	33.0	44.25	27.6
γ ($\mu\Omega$cm/meV)	65.0	99.8	142.4	67.6
α/γ	0.369	0.330	0.310	0.408
$\sum_i (y_i - f_i)^2$	2.17E-16	8.97E-15	1.44e-14	9.24e-14
R^2	0.9994	0.9998	0.9999	0.9999
$R^2_{T=50\mathrm{K}}$	0.9998	0.9960	0.9820	0.9908

Table 4.4: The converged parameters of fits of $\rho(H,T)$ of a $T_c = 35$ K crystal of Tl2201 with $H \parallel c$ for which data is presented in Figure 4.17 to an MR of the form described in Equation 4.11 (top) and Equation 4.12 (bottom).

In the $\rho_{total} = \rho_{con} + \rho_{quad}$ scenario, the general stability of the fits is very good. The converged parameters do not substantially change with increasing T_{max} until $T \sim 50$K where the inability to account for T-linearity necessarily results in huge deviations. As is expected, A and α, the two temperature coefficients are the parameters that vary most as T_{max} is increased. The same cannot be said for the fits to $\sigma_{total} = \sigma_{con} + \sigma_{quad}$. Although the total R^2 remains high and the fit is good, all of the free (except perhaps B) parameters are substantially more sensitive to T_{max} and do not evolve in a systematic manner. ρ_0' in particular, varies from $\sim 30\mu\Omega$cm to $0\mu\Omega$cm, drastically changing the low-T, low-H behaviour. Similarly, this is also reflected in $R^2_{T=50K}$ which is found to be more adversely affected by inclusion of higher temperature data in fits to this model as well.

Finally, it should be noted that the sum of the squared residuals quickly becomes worse for the model in which conductivities are added in series.

In summary, it is difficult to totally preclude one scenario entirely, though the addition of resistivities is favoured over the addition of conductivities. Different features of the data are better described by either. However, the low-T and low-H divergence of σ_{quad} gives rise to marked features in the field- and temperature- dependencies of ρ_{ab} that are not seen experimentally. Similarly, a high-field deviation from H-linearity to sublinearity in ρ_{ab} is not observed in any of the 8 samples measured. These unobserved features also suggest that the derivatives of the MR should not collapse in the manner in which they are observed to.

Furthermore, a simple analysis of the stability of the fits to the inclusion of higher temperature data highlights the instability of fits to the model in which conductivities are added in series. The model in which resistivities are added both better fits the experimental data and is less sensitive to T_{max}. Furthermore, in the case where resistivities are added, the progressive evolution of the converged parameters at high-T that is reflective of the model's inability to fit the highest temperature data can be physically understood. The non-systematic evolution of the parameters in the alternative model are likely a symptom of an inherent discrepancy between the model and experimental data.

4.4.5 The Doping and Pressure Dependence of the Quadrature MR

The evolution of the quadrature MR with doping has also been evaluated. Because the MR is found to collapse sufficiently well, it is possible to fit a field sweep performed at a single temperature to extract the quadrature parameters α and γ. This way, the fitting procedure is not influenced by the temperature dependence of $\rho(H,T)$ and only requires fitting to a quadrature MR plus a residual resistivity: $\rho(H,T=50K) = \rho_0 + \sqrt{(\alpha k_B T)^2 + (\gamma \mu_B \mu_0 H)^2}$. The influence of the temperature dependence varies between samples depending on how many and the temperatures at which field sweeps were performed. The temperature chosen was 50 K because it is sufficiently above the superconducting transition temperature of all samples whilst being low enough to exhibit both the low-field quadratic and high-field linear behaviour in field. It is also a temperature (within 1.5 K) at which a field sweep was measured for all samples.

Figure 4.18A shows $\rho_{ab}(H,T=50\text{K})$ for a representative sample with a magnetic field applied both $H \parallel ab$ and $H \parallel c$. Dashed lines are fits to a quadrature MR plus a residual ρ_0. As is more clearly seen in the derivative (Figure 4.18B) the crossover from quadraticity to linearity occurs at

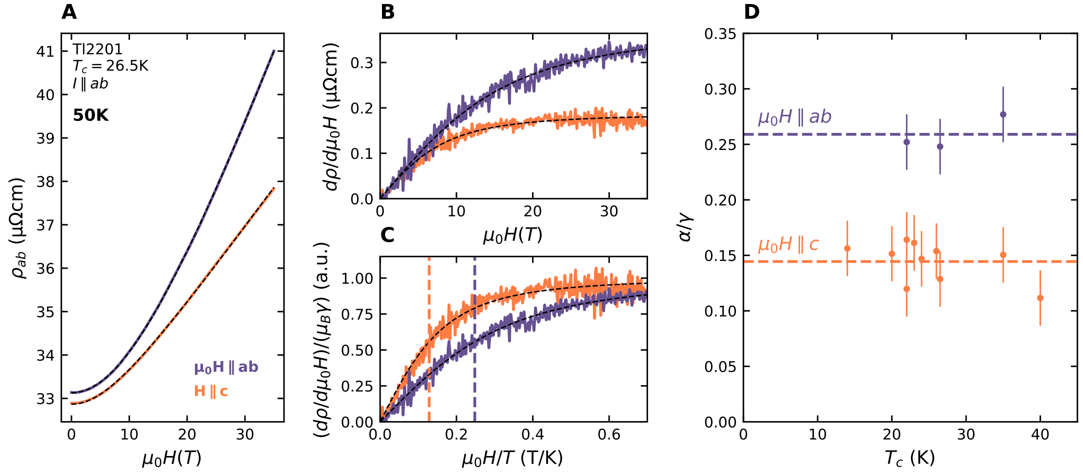

Figure 4.18: A: The MR of a representative sample at 50 K with a magnetic field applied in- and out-of-plane. Dash lines are fits of a quadrature form. B: The derivative of the measured MR and fits (dashed) in (A). C: The derivatives and fits (dashed) in (B) scaled by $\mu_B\gamma$. Coloured dashed lines indicate the ratio α/γ. D: The T_c-dependence of α/γ for all measured samples.

a higher field when $H \parallel ab$. The high-field slope is also greater. The crossover from quadratic-in-field to linear-in-field is determined by the ratio α/γ. In Figure 4.18C, the derivative is divided by $\mu_B\gamma$ and plotted against $\mu_0 H/T$. The coloured dashed lines indicate the ratio α/γ. Conveniently, α/γ is a quantity that is unaffected by multiplicative prefactors applied to the measured MR. It is therefore possible to directly compare α/γ between different samples without needing to consider errors arising from the determination of samples geometry for example. In Figure 4.18D, α/γ is plotted against T_c for all samples regardless of pressure and for both field orientations. The error bars are reflective of the scatter in the absolute value of α/γ between samples with a similar T_c.

Although α/γ can be directly compared between samples, the absolute magnitude of either is affected by errors associated with the determination of sample geometry for example. However, the application of pressure allows for the T_c-dependence of α/γ and the magnitudes of α and γ (and other fit parameters) to be explored in a single sample. Inter-sample variation is avoided.

To this end, the pressure dependence of $\rho(H,T)$ between ambient pressure and 2.0 GPa with (nominally) $H \parallel c$ is presented in Figure 4.19 for the same $T_c = 35$ K sample for which data is shown in Figure 4.17. An attempt was made to measure comparable temperatures at each pressure such that the data at each pressure can be easily compared. Global fits (dashed lines) to $\rho(H,T)$ have been made at each pressure to an MR of the form described in Equation 4.11 in which the coherent and incoherent sectors each contribute to the total resistivity in an additive manner. At each pressure, $\rho(H,T)$ is shown in row A of 4.19, the derivatives are shown in row B, the derivatives plotted against H/T are shown in row C and the characteristic collapse of $(\rho - \rho_0)/T$ is illustrated in row D.

It was noted that values of H_{irr} (the field below H_{c2} at which vortex motion results in a finite resistance) and the magnitude of the MR were marginally larger than were measured outside of the pressure cell when the sample could be oriented with respect to the applied magnetic field using a rotating sample stage. This is illustrated in Figure 4.20 where field sweeps performed at similar temperatures with $H \parallel c$ (dashed lines), $H \parallel ab$ (dotted lines) aligned using a rotating samples stage and in the pressure cell (solid line). H_{c2} and H_{irr} are both at intermediate values between the two aligned cases. Sample misalignment is suspected to be the cause. A primitive estimate of the misalignment can be made using the following expression for the anisotropy of H_{c2} [66]:

$$H_{c2}^{GL}(\theta) = H_{c2}^{H\parallel c}/\sqrt{\cos^2(\theta) + \Gamma^{-2}\sin^2(\theta)} \tag{4.13}$$

and apply it to the vortex melting field at 25 K. The anisotropy ratio $\Gamma = 30$ was found to both closely describe the data (see Figure 4.20B) and be in accordance with the anisotropy of the normal-state resistivity ($\sqrt(\rho_c/\rho_{ab}$, see Figure 4.4C). The value of H_{irr} is consistent with misalignment as large as 45°. It should be noted that $dH_{irr}/d\theta$ is shallowest at low angles. The uncertainty in the estimate is necessarily large and more likely to overestimate than underestimate. This substantial misalignment should be noted, but does not hugely alter the following analysis nor the conclusions drawn.

Although it is clear from Figure 4.19A that the normal state is not reached at lowest temperatures and at low pressures, it is still possible to predict the normal state behaviour from fits to what normal state is available at higher temperatures (dashed lines). With the sequential suppression of T_c with pressure, more normal state becomes accessible. Indeed, the fits at low temperatures become increasingly close to the measured resistivity as one would hope.

In Figure 4.21A, the pressure-dependence of the absolute magnitudes of α and γ are presented. The ratio α/γ is shown in Figure 4.21B and is found to be at a value between those found for the same sample with $H \parallel ab$ and $H \parallel c$. This, again, is consistent with the sample being misaligned inside of the pressure cell such that H is oriented at an intermediate angle. Notably, α, γ and α/γ each exhibit a systematic pressure dependence. Both decrease with increasing pressure (and decreasing T_c) with γ being the more pressure dependent of the two in absolute terms. The systematic decrease of both α and γ suggests that the magnitude of the quadrature component diminishes with pressure (and decreasing T_c).

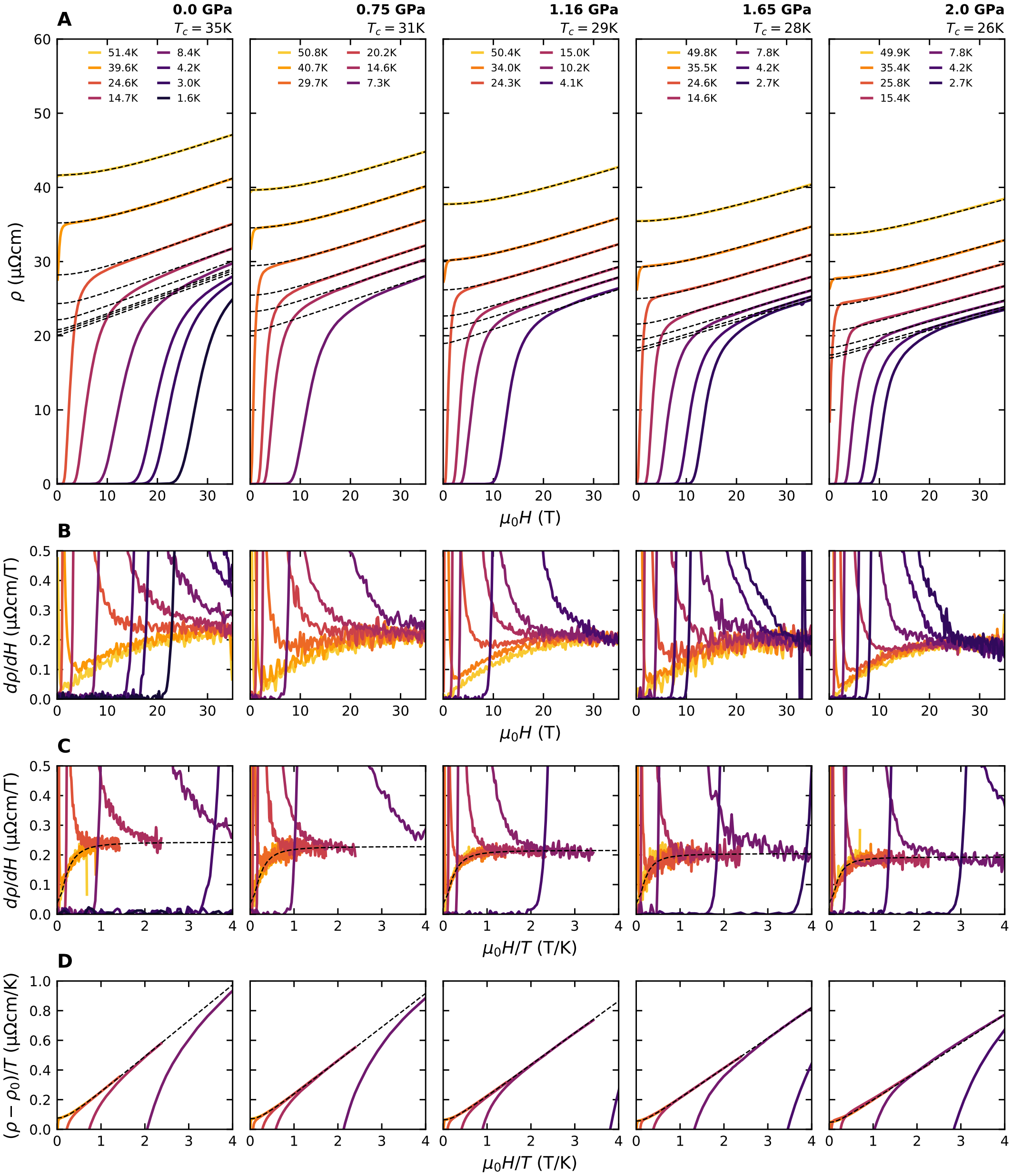

Figure 4.19: A: The evolution with pressure of $\rho_{ab}(H,T)$ of the $T_c = 35\,\mathrm{K}$ sample. Dash lines are simultaneous fits to MR in Equation 4.11. B: Derivatives of the MR presented in A. The derivatives presented in B plotted against H/T. Dashed line is derived from the fits to the MR in panel A and is of a quadrature form. D: Plots of $(\rho - \rho_0)/T$ against H/T for which a characteristic collapse of the data is observed.

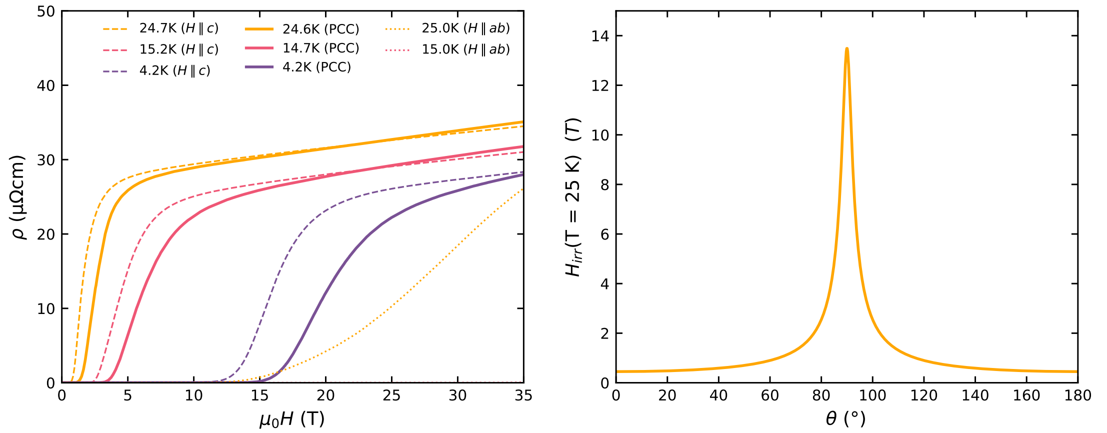

Figure 4.20: A: A comparison of $\rho(H)$ at select temperatures measure with the field oriented $H \parallel ab$ (dotted lines), $H \parallel c$ (dashed lines) and as measured in the pressure cell (solid lines). The anisotropy of H_{irr} at 25 K from which the misalignment of the sample in the pressure cell with respect to the magnetic field can be estimated.

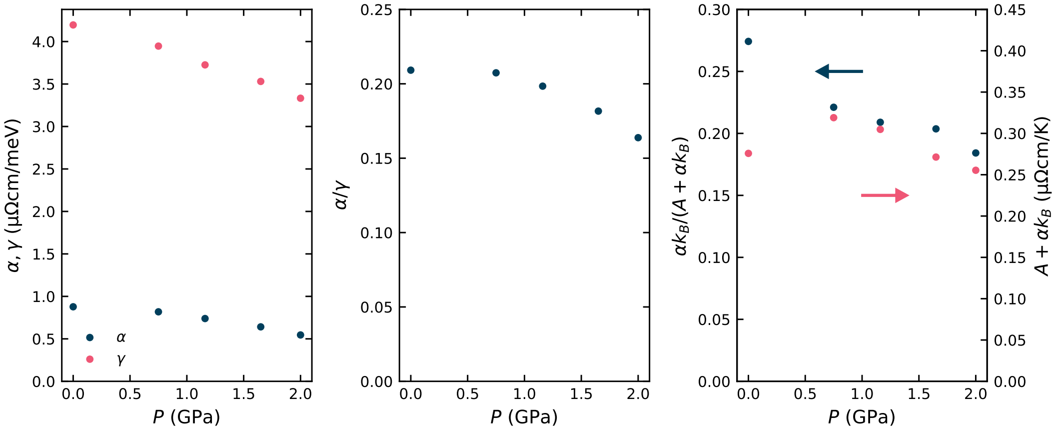

Figure 4.21: A: The pressure dependence of both α and γ up to 2 GPa in Tl2201 with $T_c(0GPa) = 35\,\mathrm{K}$. B: The pressure dependence of α/γ. The pressure dependence of both the ratio $\alpha k_B/(A+\alpha k_B)$ and the total zero-field T-linear term $A + \alpha k_B$

The evolution of α/γ is more difficult to interpret microscopically. Phenomenologically, it indicates that the energy scale associated with magnetic field becomes increasingly dominant compared with that associated with temperature such that the crossover to H-linear behaviour occurs at progressively lower fields as pressure is applied. If one were to attempt to extrapolate this behaviour to substantially higher pressures than those measured here, it might be concluded that α/γ would approach zero at a pressure in the vicinity of 6-8 GPa. If $\alpha/\gamma = 0$, being a proxy for the field at which there is a crossover from linear-in-H to quadratic-in-H behaviour, is the condition for H-linearity extending down to zero temperature. Intriguingly, 6-8 GPa is the pressure at which one might anticipate having totally suppressed T_c (if dT_c/dP were to remain roughly independent of pressure) at this doping (see Figure 4.8). Strictly H-linear behaviour down to lower temperatures at the overdoped edge of the superconducting dome would be highly expected.

In the absence of a magnetic field, the resistivity in Equation 4.11 reduces to $\rho(T) = \rho_0 + (A + \alpha k_B)T + BT^2$. One might hope that the entire linear-component of the zero-field resistivity comes from the quadrature component. This is, however, not the case. Figure 4.22 shows the measured $\rho(H,T)$ of two samples. Fits have been made to the form of $\rho(H,T)$ given in Equation 4.12 (black dashed lines) in which an AT term is included such that the total linear component of the zero-field resistivity is $(A + \alpha)T$. Fits have also been made to the same expression but with $A = 0$ such that all of the zero-field linearity is assumed to originate from the quadrature component and the total linear component of the zero-field resistivity is simply αT. It is clear that that the data can not accurately be modelled by the latter form of $\rho(H,T)$ and that both A and α need to be considered.

The evolution of the total zero-field T-linear coefficient $A + \alpha k_B$ and $\alpha k_B/(A + \alpha k_B)$, the ratio of the T-linear quadrature term to the total T-linear coefficient, with pressure is shown in Figure 4.21C. At ambient pressure, 30 % of the total T-linear component of the zero-field resistivity is attributable to the incoherent sector. This fraction reduces with increasing pressure (decreasing T_c).

It is clear that the quadrature component of $\rho(H,T)$ can not account for the total T-linear coefficient measured in zero magnetic field. It is intriguing to note that the evolution of both is somewhat similar.

4.4.6 Discussion and Outlook

A parallel study was performed by Maarten Berben at the High Field Magnet Laboratory on Bi2201 over a similar range of dopings. Bi2201 is known to be substantially more disordered than Tl2201 as evidenced residual resistivities that are $\sim$ 10 times larger than in Tl2201 [58]. Although not

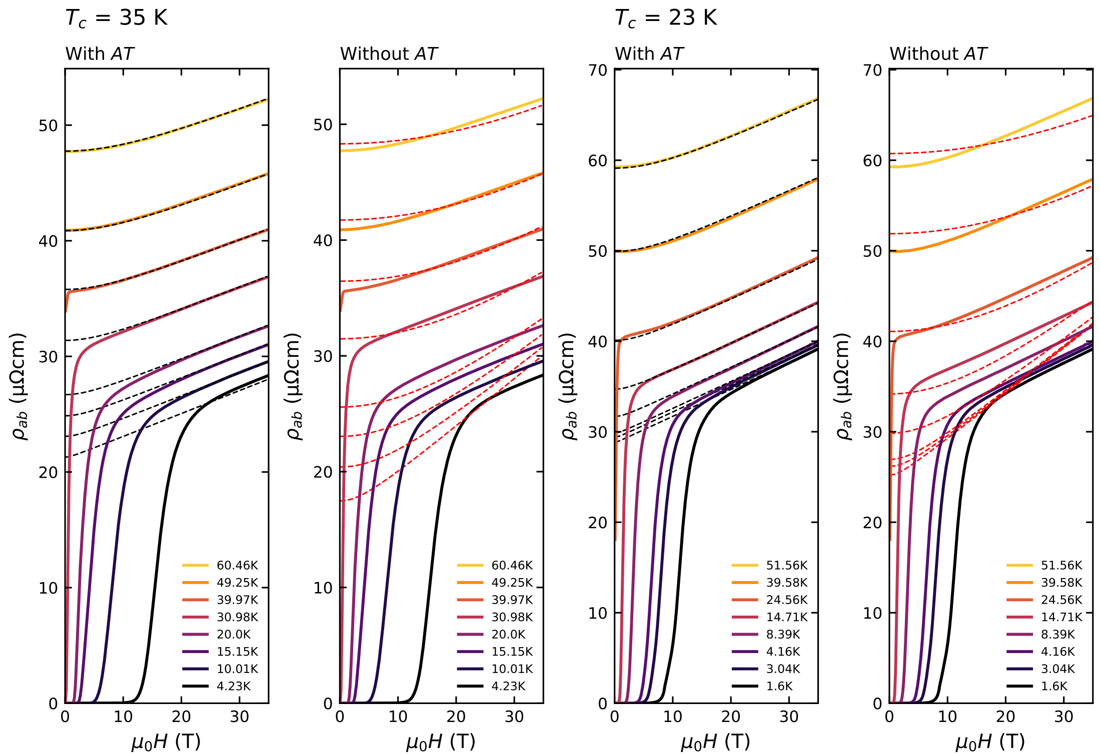

Figure 4.22: Fits of the measured $\rho(H,T)$ for two samples. Fits have been made to Equation 4.12 that includes an AT term (black dashed lines) and the same expression in which AT is set to zero (red dashed lines).

presented here, the data from this thesis and that of the parallel study of Bi2201 can be found elsewhere [67]. Remarkably, the same form of the in-plane MR was also observed with a high-field linearity of a highly comparable magnitude and the same insensitivity to field-angle. The fact that the MR is found to be the same in two materials in which ρ_0 varies by more than an order of magnitude evidences that the quadrature MR is insensitive to impurity scattering as is expected in normal metals where the MR scales with $(\omega_c\tau)^2$. The quadrature expression itself implies that ρ_0 has no effect upon the MR.

A notable difference between the Bi2201 and Tl2201 systems is that the ratio α/γ is nearly 10 times larger in Bi2201. The high field linear slope in $\rho(H)$ is very similar in the two materials. We infer that γ is also comparable. We therefore conclude that it is α that is substantially bigger in Bi2201 than in Tl2201. Although a direct link between the total conventional T-linear resistivity and the quadrature T-linear resistivity in the absence of a magnetic field has not been found, it is intriguing that both A and α are larger in Bi2201. One could hypothesise that it related to the factor of ~ 10 larger residual resistivity in Bi2201, but it is hard to imagine how the field dependence of ρ remains unaffected whilst the temperature dependence *is* affected.

In the aforementioned cases of P-Ba122, $FeSe_{1-x}S_x$ and LSCO, the dopings at which the quadrature MR was observed were all in close proximity to a well established quantum critical point. What is highly curious here, is that the dopings are all far from p^*, the doping at which there are claims of a QCP associated with the closing of the pseudogap [20, 68] (illustrated in Figure 4.11). If the quadrature MR were to be attributed to a QCP, it would perhaps be tempting to choose that at which T_c is suppressed to 0 K. However, over the range of dopings measured, there is no evidence that the effect grows with decreasing T_c and moderate evidence that, on the contrary, the quadrature MR diminishes with increasing p (decreasing T_c). It appears to be a more general property of the overdoped strange metal regime. of Tl2201.

The microscopic origin of the quadrature MR still remains unclear. The fact that it is highly insensitive to field angle and is characterised by a high-field H-linearity that is independent of temperature (and therefore independent of τ) suggests that its origin is not orbital in nature. As shown in Section 4.4.3, the phenomena could not be replicated even qualitatively using the same conventional transport formalism (SCTIF) that successfully models both the in-plane Hall response and the field-angle-dependence of c-axis transport in Tl2201. The insensitivity to τ shown here is mirrored by measurements of $FeSe_{1-x}S_x$ in which highly comparable quadrature MR was found in samples with residual resistivity that differed by a factor of ~ 5 [23]. This core discrepancy suggests that the origin of the in-plane MR presented here is fundamentally distinct from that of c-axis transport and in-plane Hall response and that there are two discrete charge sectors in OD Tl2201. The first is comprised of coherent quasiparticles that adhere to ‘conventional’ transport theory that, with an anisotropic $\tau(k)$, govern the Hall and c-axis response. The second is incoherent, non-quasiparticle-like and governs the in-plane MR.

The linear-in-temperature resistivity in a wide range of cuprate families has been associated with so-called *Planckian dissipation* [69–71], a regime in which scattering is defined by a minimal scattering time (or maximal scattering rate) $\tau_\hbar = \hbar/k_BT$ [72]. If the quadrature component of the MR is rewritten as $\sqrt{1+(\frac{\gamma\mu_B\mu_0H}{\alpha k_BT})^2}$, it can be equated to $\sqrt{1+(\omega_c\tau^*)^2}$ where τ^* is an effective scattering rate associated with the incoherent component. Using $\mu_B = e\hbar/2m_e$ and $\omega_c = e\mu_0H/m_e$, it can be shown that:

$$\begin{aligned}\tau^* &= \frac{\gamma}{\alpha}\frac{\mu_B}{\omega_c}\frac{\mu_0 H}{k_b T}\\ &= \frac{\gamma}{\alpha}\frac{e\hbar}{2m_e}\frac{m_e}{e\mu_0 H}\frac{\mu_0 H}{k_B T}\\ &= \frac{\gamma}{2\alpha}\frac{\hbar}{k_B T}\end{aligned} \tag{4.14}$$

With reference to Figure 4.18, the value of α/γ was found to be 0.15 when $H \parallel ab$ and 0.25 when $H \parallel c$. This would infer that $\tau^* = 3.3\hbar/k_B T$ or $2\hbar/k_B T$, both of which are $\sim \pi\hbar/k_B T$. Thus, the quadrature magnetoresistance of OD Tl2201 presented here is found to be consistent with a system in which Planckian dissipation sets the scattering rate. Curiously, it was m_e and not m^* that was used in the definition of ω_c. If the magnitude of the MR is indeed set by the Planckian limit, it therefore appears that the relevant mass of the charge carriers is m_e and not m^*. If so, this indicates that the incoherent sector is somehow immune to the Fermi-liquid renormalisation of m (and presumably other quantities), though it is noted that increasing τ^* by a factor of $m^* \sim 5$ [73] would still not be completely inconsistent with the Planckian limit. The only material-specific parameter used in this analysis is the ratio α/γ, the origin of which remains unclear. A more definitive understanding of the origins of Planckian dissipation are required in order to determine whether the incoherent charge carriers observed in this work or the carriers in other materials that have been claimed to be defined by Planckian dissipation are in fact immune to Fermi-liquid renormalisation of their properties (including their mass) or not.

The incoherent component of $\rho(H, T)$ contributes a T-linear component α to the zero-field resistivity. If the MR is associated with Planckian dissipation, it therefore follows that the zero-field resistivity is also associated (at least in part) with Planckian dissipation as well. This idea is supported by measurements of a variety of other cuprates closer to optimal doping [69] in which a scattering rate consistent with Planckian dissipation could be found from the linear slope of the zero-field resistivity. The fact that $\alpha/(A + \alpha)$ is found to be suppressed with doping (decreasing T_c) suggests that as optimal doping is approached, a growth of the proportion of the total T-linear coefficient that is attributable to the incoherent sector is expected to grow and may be the same linear-in-temperature phenomenon that has been associated with Planckian dissipation in other cuprate families including Bi2212, LSCO and Nd-LSCO [69].

A notable difference between the nature of the incoherent MR in Tl2201 compared with that in other families of unconventional superconductors (P-Ba122 and $FeSe_{1-x}S_x$) is the isotropy demonstrated in Section 4.4.2. In $FeSe_{1-x}S_x$ and P-Ba122, the quadrature MR is strongly enhanced when H is oriented $\parallel c$. Given the quasi-two-dimensional Fermi surfaces of both systems, such an anisotropy may not be totally surprising and may indicate that the phenomenon is governed by orbital transport theory. The same argument could be made for Tl2201, but the anisotropy is not observed. One possible explanation is that the application of a magnetic field adds an additional energy scale that leads to an equivalent H-linearity to that of the T-linearity that is well established to be associated with the strange metal regime in overdoped cuprates.

Both $FeSe_{1-x}S_x$ and P-Ba122 are multi-band systems whilst overdoped cuprates are single-band materials. The possibility of segregating the coherent and incoherent sectors by Fermi surface sheet, for example, is therefore not possible. It is plausible that the gapping out of the anti-nodal regions of Fermi-surface that is often attributed to the pseudogap in overdoped cuprates is associated with the generation of this incoherent sector. This so-called nodal-antinodal-dichotomy is revealed by ARPES measurements in which it is found that the Fermi surface is broken into disconnected Fermi arcs in the nodal directions [74]. It is possible that the coherent sector governed by orbital transport resides at the nodal regions where the Fermi surface is known to persist as optimal doping is approached whilst the incoherent sector is generated at the anti-nodal regions whether the Fermi-surface is lost at lower dopings. The high-field, low-temperature Hall number n_H (related to the number of carriers) is found to drop gradually from $1+p$ to p at dopings as high as $p = 0.27$ [65] in Tl2201 and Bi2201. This gradual loss of carriers is somewhat consistent with a picture in which there is a progressive loss of coherent quasiparticles and a growth of an incoherent sector as optimal doping is approached. At the dopings measured in this work, ARPES does detect sharp quasiparticle excitations around the entirety of the Fermi surface [75]. This finding suggests that ARPES is insensitive to the incoherent sector or there is a disjunction between the single particle and collective response in overdoped cuprates.

A linear magnetoresistance is not unique to cuprates or ‘strange metals’. Aluminium is a simple metal in which a linear magnetoresistance has been attributed to variations in sample thickness [76]. It is known that disorder, which can be modelled using random resistor networks [77], can generate large magnetoresistances. And indeed, disorder has been invoked as a possible means of generating a magnetoresistance with the precise field-temperature-scaling reported in this chapter [78]. The essential ingredient in the modelling in [78] is a periodic (and binary) variation of the charge carrier density along the current axis of the sample that are the result of disorder. Whether this behaviour extends to models in which the carrier density varies less predictably remains unclear. Whilst this is certainly intriguing and may eventually be shown to be the origin of the quadrature MR reported here, it is difficult to imagine how the same quadrature behaviour is seen in both Tl2201 and Bi2201, systems with levels of disorder that result in residual resistivity that differ by more than an order of magnitude. Along a similar line-of-thought, a linear-in-field and linear-in-temperature regions of $\rho(H,T)$ have been reproduced in models that invoke a similar binary distribution of mesoscopic disorder [79]. Strict $H-T$-scaling was not found for more complex distributions. Whilst the authors note that two-component distribution is possibly relevant to iron pnictides in which multiple Fermi sheets might justify binary (or at least low-order) distributions of disorder, it is anticipated that cuprates should be described by continuous distributions of disorder that do not result in quadrature scaling.

4.5 Concluding Remarks

In summary, a low-field study of the in-plane transport of overdoped Tl2201 has been presented as T_c is tuned using two distinct mechanisms, chemical doping and the application of hydrostatic pressure. It is curious to see that despite fundamental differences between the two mechanisms and the origin of the suppression of T_c being different in both cases, the in-plane transport properties appear to evolve very similarly. This suggests that the normal state electronic properties and superconductivity are linked such that they are likely to evolve in unison with respect to each other regardless of the chosen tuning parameter. A more detailed microscopic understanding of the role of pressure and the nature of oxygen migration should elucidate this issue.

Secondly, the in-plane MR of highly overdoped Tl2201 has been studied as a function of both doping and pressure. The coexistence of two distinct current-carrying sectors has been established where one is governed by the same 'conventional' transport theory that successfully models both the in-plane Hall resistivity and *c*-axis ADMR, and the other incoherent sector is entirely unconventional as evidenced by its insensitivity to impurity scattering, quadrature scaling and angular isotropy. Further, it is consistent with a sector in which scattering is at the Planckian limit. In contrast with other systems in which a similar quadrature MR is observed (namely P-Ba122, $FeSe_{1-x}S_x$ and LSCO), the origin can not be easily attributed to proximity to an established quantum critical point. In contrast, it appears that quantum criticality is a generic property that is pervasive across the strange metal phase in Tl2201. In a parallel study of Bi2201 [67], the same quadrature MR and quadrature collapse has been observed. It is therefore believed that the same dissection of charge carriers into orbital and incoherent sectors also applies to Bi2201 and, by extension, to the strange metal regime in overdoped cuprates more generally.

To both further our understanding of the affect of pressure on the normal state transport properties that appear to be governed by 'conventional' transport theory (such as R_H and ρ_c) and those that are not (in-plane MR), higher pressures should be sought. In the former case, higher pressures applied to a wider range of dopings will clarify the equivalence (or lack therefore of) between pressure and doping as a means of tuning both T_c and the normal state transport properties of overdoped cuprates. In the latter case of the in-plane MR, it would instructive to use pressure to entirely suppress superconductivity and see whether or not signatures of incoherent transport persist beyond the superconducting dome. This could also be achieved through suppression of T_c with doping, but would require annealing in high pressure oxygen which has not as of yet been performed successfully in Tl2201 [49].

Chapter 5

$YBa_2Cu_3O_{7-x}$

This primary objective of the work in this chapter was to further elucidate the interplay between superconductivity and charge order in the cuprates. To this end, samples of $YBa_2Cu_3O_{7-x}$ were prepared for measurement of the Hall effect at high fields. Measurement of the zero-crossing temperature of the Hall coefficient was used as a resistive measure of the strength of charge order whilst the superconducting transition temperature served as a measure of the strength of superconductivity. By tracking the progression of both with increasing hydrostatic pressure in samples annealed to different dopings, further light has been shed upon the interplay between the two phases.

Preparation of the $p = 0.11$ samples and pressure cells used for their measurement was performed by Dr C. Putzke with assistance from the author. Preparation of $p = 0.12$ sample pressure cell used for its measurement was performed by Dr. S. Badoux. The author assisted with the collection of all of the presented data and performed all of the following analysis that is presented in this chapter.

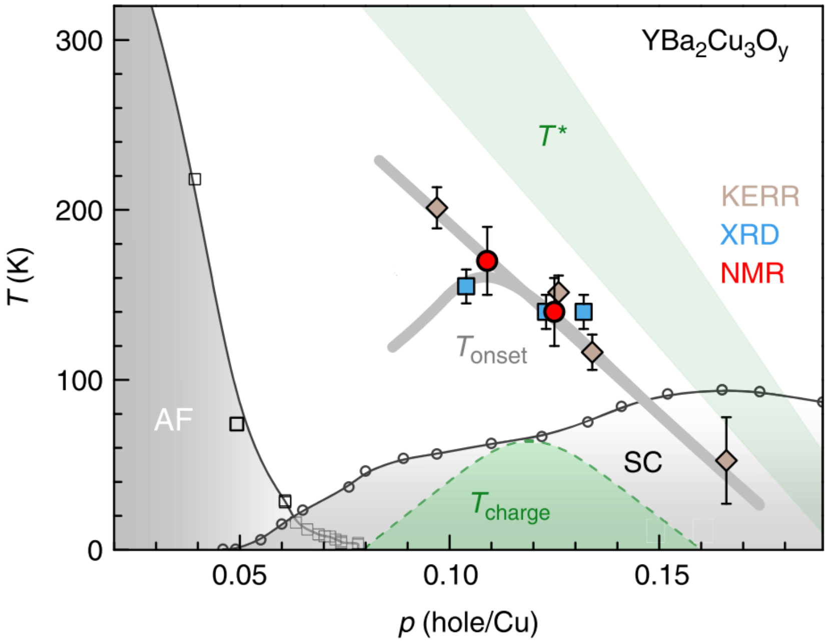

Figure 5.1: The temperature-doping phase diagram of $YBa_2Cu_3O_{7-x}$ from [80]. The parent antiferromagnetic insulating state is rapidly suppressed with increasing hole concentration p. In the vicinity of $p = 1/8$, charge order is onset below T_{onset}. With the application of a magnetic field, long range charge order stabilises below T_{charge}.

5.1 Background

A complete understanding of the electronic properties of the cuprate family of high-temperature superconductors, including the microscopic origin of superconductivity, has so far eluded us despite more than thirty years passing since their discovery [5]. This is undoubtedly in part due to the numerous novel electronic phases that either appear in the vicinity of or coexist with superconductivity. $Tl_2Ba_2CuO_{6+\delta}$, the subject of the previous chapter, is an overdoped cuprate and although strongly correlated and certainly a 'strange' metal, does not feature the wide range of novel electronic states that are exhibited by underdoped cuprates.

$YBa_2Cu_3O_{7-x}$ is one such underdoped cuprate. A schematic of the T-p phase diagram illustrating the principal electronic phases is shown in Figure 5.1. The parent compound is an antiferromagnetic Mott insulator. The disappearance of the antiferromagnetic state is accompanied by the emergence of superconductivity near to $p = 0.05$. Also present on the underdoped side of the phase diagram and of particular note are a region of charge order centred at $p = 1/8$, a translational symmetry-breaking phase with a periodicity that is not that of the crystal lattice, and the pseudogap phase (the onset of which is denoted by T^*) within which a partial loss of quasiparticle states at the Fermi energy is observed.

Whether there is a direct physical connection between these phases remains unresolved. One open question that is particularly relevant to this chapter is whether or not there is a degree of interplay, for instance a mutual enhancement or direct competition, between the superconducting and charge ordered phases. In this section, an introduction to charge order in the cuprates and $YBa_2Cu_3O_{7-x}$ in particular is presented. Following this, a brief summary of the experimental evidence regarding the influence of charge order and superconductivity upon each other is given.

5.1.1 Charge Order in the Cuprates

The first tentative signs of a charge-density wave (CDW), or charge order (CO), in cuprates emerged from neutron scattering experiments in $La_{2-x}Sr_xCuO_4$ with $x = 0.08$ [9] and $x = 0.11$ [10] in which the line shape of two-dimensional antiferromagnetic order evolved from a Lorentzian at room temperature to a line shape consisting of two incommensurate peaks at low temperatures. This spin order was soon found to have a momentum structure characterised by four Q-vectors ($\mathbf{Q}_{SO} = (1/2 \pm \delta_{IC}, 1/2, L)$ and $\mathbf{Q}_{SO} = (1/2, 1/2 \pm \delta_{IC}, L)$)) where δ_{IC} is a doping dependent degree of incommensurability [81]. A leading candidate phenomena responsible for the aforementioned magnetic structure was stripe-order, a phase in which both spin- and charge-order are present each with their own associated Q-vectors that are geometrically related. A requirement of such a scenario, however, is an orthorhombic distortion that breaks the four-fold symmetry of the Cu-O planes. The simultaneous measurement of peaks associated with both charge- and spin-order with the anticipated relationship $\delta_{CO} = 2\delta_{SO}$ in Nd-doped LSCO confirmed this scenario [6]. The substitution of La for Nd provides the necessary symmetry-breaking distortion. This finding was corroborated by real-space observation of charge order using scanning tunnelling microscopy, a spectroscopic probe that is sensitive to charge density directly. Modulations in the differential (between 5 T and 0 T) tunnelling conductance with a four-fold symmetry were also observed in the normal-state vortex cores.

Since these original observations, charge order has been detected in many families of cuprates in the vicinity of $p = 1/8$ and is generally accepted to be universal feature of the cuprate phase diagram. Owing to the ability to cleave atomically flat surfaces in relatively large samples, members of the Bi-based compounds lend themselves to surface and scattering measurements. In this family of cuprates, it is possible to perform scanning tunnelling microscopy and scattering measurements on the same crystal [7, 8]. Thus, verification that real-space modulations and periodicity manifesting

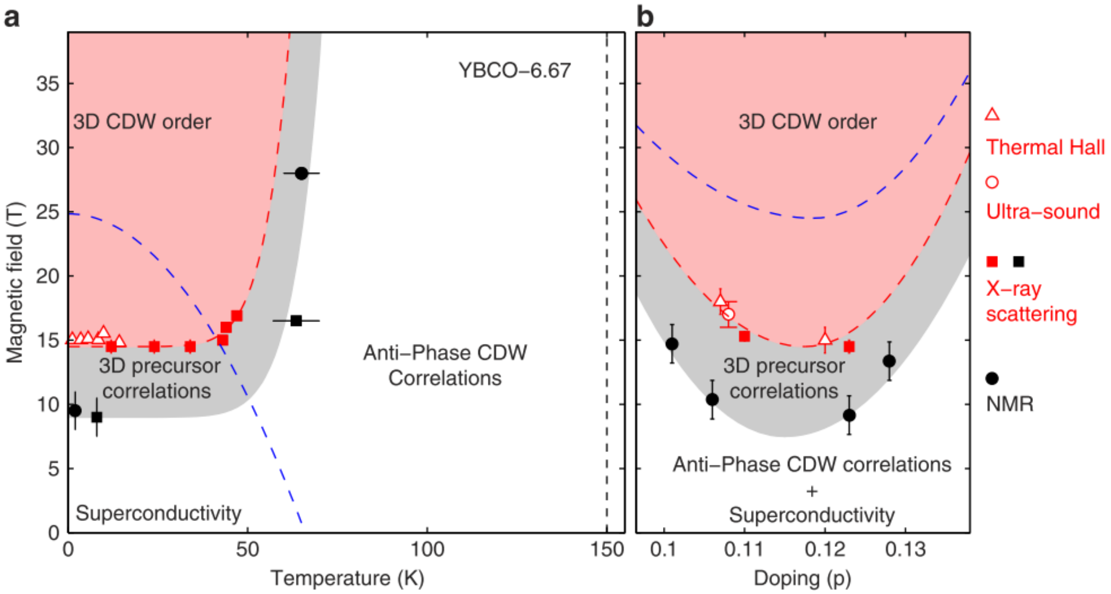

Figure 5.2: Both the (a) H-T and (b) H-p phase diagrams of $YBa_2Cu_3O_{7-x}$ from [85]. In addition to two-dimensional charge order, a precursor regime from which a three-dimensional CDW stabilises is present at low temperatures and high magnetic fields.

as peaks in reciprocal-space arise from a common phenomena was obtained.

5.1.2 Charge Order in YBCO

Though appearing much later than in other families of cuprates, both NMR [80, 82] and x-ray scattering studies [83, 84] provide direct evidence of a charge density wave in YBCO. The nature of charge order in $YBa_2Cu_3O_{7-x}$ can be summarised with reference to the H-T and H-p phase diagrams of $YBa_2Cu_3O_{7-x}$ presented in Figure 5.2 and taken from [85] in which the results of multiple experimental probes are combined.

Resonant x-ray scattering measurements [83] observed a peak at the same incommensurate in-plane wave vector $\mathbf{Q} = (0.31, 0)$ with an onset temperature at 150 K provided the first direct evidence of charge order in $YBa_2Cu_3O_{7-x}$. This onset temperature is found to be independent of magnetic field. Further x-ray studies [86, 87] revealed that the onset temperature is doping dependent and takes on a maximum value of 150 K at a doping $p = 1/8$. With the application of a magnetic field, another component to charge order emerges in addition to the aforementioned two-dimensional charge order that is observed in the absence of a magnetic field [85]. NMR measurements observed a splitting of the ^{63}Cu(2) lines at 50 K and at 28.5 T [82] . This result was determined to be consistent with the emergence of a unidirectional charge density wave. Secondly, a clear distinction between both the high-field and zero-field charge ordered regimes was drawn [80].

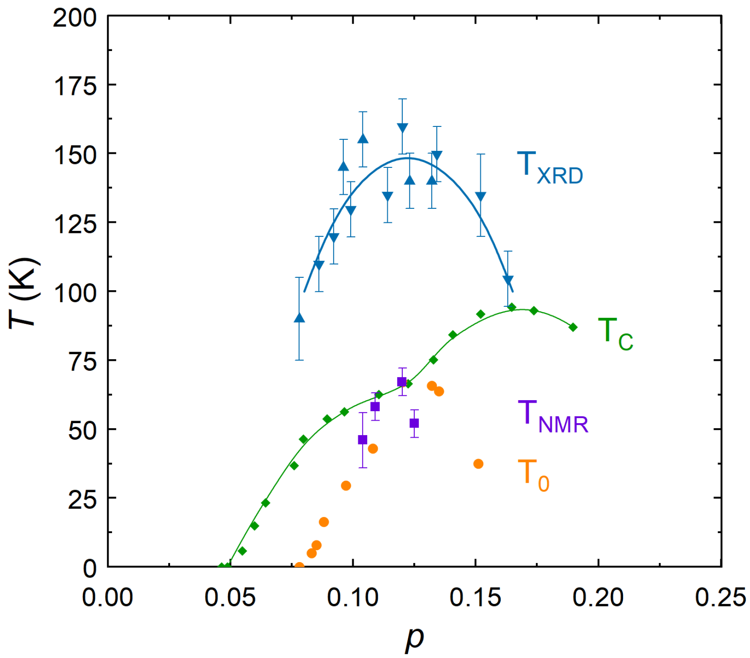

Figure 5.3: The temperature-doping phase diagram of $YBa_2Cu_3O_{7-x}$. The doping dependence of the superconducting phase transition (green diamonds from [88]) features an anomalous plateau at $p = 1/8$. This plateau coincides with the maximal onset temperature of charge order as determined by both x-ray diffraction studies (blue triangles up/down from [86]/[87]) and NMR studies (purple squares from [82]). The onset of charge order as inferred by the characteristic temperature T_0 (orange circles from [89]).

5.1.3 Charge Order in Transport

Although not as direct a measurement as NMR or XRD, there are signatures of charge order in the transport properties of YBCO at and around $p = 1/8$. The observation of low frequency quantum oscillations in R_{xy} of ortho-II ordered Y123 ($T_c = 57\,\mathrm{K}$, $p = 0.11$) [90] and in both R_{xx} and R_{xy} of Y124 [64] with frequencies of 530 T and 660 T respectively revealed the presence of small Fermi pockets. This is in contrast with the high frequency oscillations seen in strongly overdoped $Tl_2Ba_2CuO_{6+\delta}$ at $p = 0.30$ (18 kT) [44]. Later measurement of de-Haas van Alphen oscillations in Y123 showed that the angle dependence is consistent with those of a quasi two-dimensional Fermi sheet [91]. Quantum oscillations themselves are unable to reveal the charge sign of the carriers, but a change in the sign of R_{xy} (and R_H) from positive (as also seen in overdoped cuprates) at high temperatures to a much larger negative value at low temperatures implies that the dominant carrier-type is electron-like at low temperatures [89]. In combination, these two experimental results are highly indicative of a Fermi surface reconstruction from a hole-like Fermi surface, as observed in overdoped cuprates at high temperatures, to a predominantly electron-like Fermi surface at low

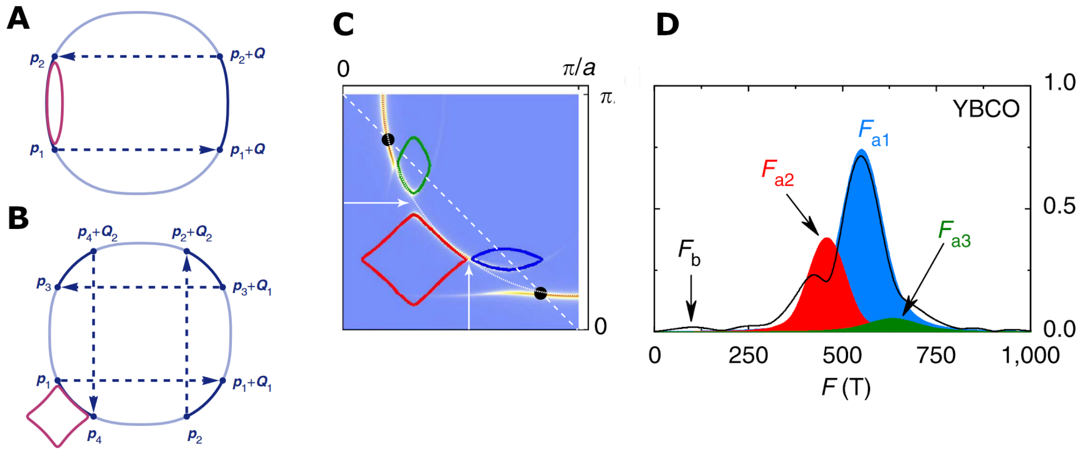

Figure 5.4: A-B: A schematic illustrating the Fermi surface reconstruction due to charge order with one (A) and two (B) wavevectors from [92]. C: A proposed form of the Fermi surface in the presence of charge order at high fields that is qualitatively consistent with a quantum oscillation study (D). Both C and B are from [93]

.

temperatures.

Furthermore, the range of dopings over which a change of sign in R_H is observed would suggest that the Fermi surface reconstruction is a consequence of the onset of charge order. T_0, defined as the temperature at which the Hall coefficient crosses 0 K, serves as a useful measure of the temperature at which this Fermi surface reconstruction occurs. As a function of doping, T_0 is found to form a dome centred at $p = 0.125$ [89]. This dome in the temperature-doping phase diagram coincides closely with the domes obtained by the aforementioned x-ray [86, 87] and NMR [82] studies that are able to probe the onset of charge order more directly. This result is illustrated in Figure 5.3. One may therefore conclude that T_0 serves as a convenient resistive measure of the temperature at which charge order stabilises. This premise forms the basis of the work presented later in this chapter.

It should be noted that despite the measurement of R_H, quantum oscillations and ARPES, all of which are able to reveal something about the properties of the Fermi surface, as well as detailed knowledge of the $Q-$vectors associated with both magnetic and charge order (two-dimensional and three-dimensional phases) from scattering experiments, the structural form of the Fermi surface of underdoped cuprates in the presence of charge order remains ambiguous. A form of the Fermi surface that is consistent with evidence ascertained from each experimental probe has yet to be determined.

Figures 5.4A and 5.4B (from [92]) show two possible reconstructed Fermi surfaces in which back-folding of the BZ has been performed with both one and two wavevectors. In both cases, small Fermi pockets are formed. Figure 5.4C shows a candidate form of the reconstructed Fermi surface that is qualitatively consistent with quantum oscillations (Figure 5.4D) observed in samples with $p = 0.11$ and $p = 0.12$. Quantum oscillations are necessarily observed at high magnetic fields and thus a reconstruction of the Fermi surface with two wavevectors is likely required to reconcile with the experimental data.

5.1.4 Competition Between Superconductivity and Charge Order

Whether or not there is mutual competition between charge order and superconductivity, that is that the strengthening of one phase intrinsically weakens the other, in the cuprates is widely discussed. A notable feature of the cuprate phase diagram in the vicinity of charge order is a plateau in T_c [88] which could be interpreted as a local suppression of superconductivity as a consequence of the presence of charge order. Accompanying this suppression in T_c is a local suppression of H_{c2} strong enough to produce a local minimum at $p = 1/8$ that is highly suggestive of a charge-order induced suppression of superconductivity [94]. After the onset of charge order below 150 K, the intensity of the x-ray peak associated with charge order is attenuated at temperatures below T_c. This attenuation is reduced with the application of a magnetic field that suppresses superconductivity [84]. This is highly suggestive of a suppression of charge order by the presence of superconductivity. More precisely, this is evidence to suggest that the pairing of electrons in the superconducting state is detrimental to charge order. It is less clear, however, whether the presence of charge order is inherently detrimental to superconductivity. The local suppression of T_c and H_{c2} that is widely ascribed to charge order could, for example, have another origin that serves to both suppress superconductivity and stabilise charge order in a manner that does not necessitate mutual competition between charge order and superconductivity in all instances.

Pressure is an additional tuning parameter that allows for the systematic study of both the charge ordered and superconducting states. Motivated by the aforementioned debate regarding the interplay between the two states, the intent of work presented in this chapter is to measure the strength of superconductivity (T_c) and track any change in T_0 (a proxy for the strength of charge order) with the application of hydrostatic pressure in single crystal samples of Y123 at dopings in the vicinity of $p = 1/8$. Over the pressure range accessible here, it is known that hydrostatic pressure enhances T_c linearly in Y123 at $x \sim 1/8$ [56]. One would therefore anticipate that a corresponding linear suppression of charge order. To this end, single crystals of Y123 were prepared with $x \sim 1/8$ and measured in high fields and under hydrostatic pressure. Details follow in the proceeding sections.

Sample	$T_c(P = 0\text{GPa})$	Doping	Pressure Cell	P_{max}
T96	61 K	0.11	PCC	2.6 GPa
C161	60 K	0.11	MAC	6.0 GPa
CuJ2	67 K	0.12	MAC	3.1 GPa

Table 5.1: A summary of each of the samples for which data is presented in this work.

5.2 Experimental Details

Single crystals of Y123 were grown via the usual flux method detailed in [95]. Two were annealed to a doping $p = 0.11$. This was achieved by annealing them for 8 days at 580° in an atmosphere of 2 % oxygen in nitrogen. They were quenched to room temperature with the use of liquid nitrogen. The first was loaded into a PCC whilst the second was mounted inside a MAC. A third sample was annealed for 8 days at 650° in pure oxygen resulting in a doping $p = 0.12$. In all cases, doping was estimated from T_c [88]. This too was prepared for measurements in a MAC. A summary of the samples is presented in Table 5.1. For measurements performed in a PCC, Daphne 7373 was used a pressure transmitting medium whilst glycerol was used for measurements performed with a MAC.

Electrical contact was made to each sample by first sputtering gold contacts onto their surfaces in a configuration suitable for measurement of the in-plane Hall resistance ($I \parallel ab$). Measurements were performed at the High Field Magnet Laboratory in magnetic fields up to 35 T. The field was oriented $H \parallel c$. Field sweeps were performed at fixed temperatures with the magnetic field applied in both the positive and negtive field directions. The Hall component was isolated from the total signal by anti-symmetrising the data. The Hall coefficient was then determined using

$$R_H = \frac{R_{xy}t}{B} \tag{5.1}$$

where t is the thickness of the sample.

5.3 Results

5.3.1 The Evolution of T_c with pressure

As with many cuprates, it is known that the superconducting transition temperature of $YBa_2Cu_3O_{7-x}$ in the range of dopings measured in this work is initially enhanced with the application of pressure. At sufficiently high pressures, the enhancement diminishes and T_c is eventually suppressed. The pressure at which this occurs is dependent upon the doping of the sample.

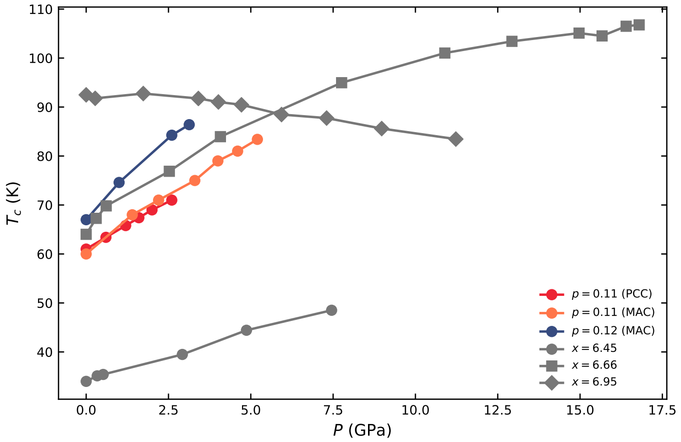

Figure 5.5: The pressure dependence of the superconducting transition temperature of Y123. The samples measured in this work are represented by coloured points. The error is comparable to the point size. The grey points are from [56].

The pressure dependence of the T_c the samples measured in this work and those of various dopings measured by Sadewasser and coworkers [56] is presented in Figure 5.5 for a number of dopings. Here, the T_c was taken as the temperature at which the resistance fell to within the noise floor. In good agreement with the previous study, T_c was found to increase monotonically and smoothing for samples with dopings of $p = 0.11$ and $p = 0.12$.

If a simple linear fit is made to the data presented in Figure 5.5, dT_c/dP is found to be 3.9(1) K/GPa for Sample T96 ($p = 0.11$, PCC), 4.4(1) K/GPa for Sample C161 ($p = 0.11$, MAC) and 6.2(1) K/GPa for Sample CuJ2 ($p = 0.12$, MAC). It would appear that superconductivity is more rapidly enhanced for $p = 0.12$ compared with $p = 0.11$. Given that dT_c/dP is negative for $x = 6.95$ ($p = 0.17$ [88]), one would expect that the doping for which dT_c/dP is maximal is between $p = 0.12$ and $p = 0.17$ but closer to $p = 0.12$.

5.3.2 High-Field Hall Effect

The magnetic field dependence of the Hall resistance and Hall coefficient of Sample T96 ($p = 0.11$) measured in hydrostatic pressures up to 2.6 GPa are presented in Figure 5.6. Data for the other two samples can be found in the appendices at the end of this chapter. For all pressures, R_{xy} is found to be positive and highly linear down to lowest fields for temperatures greater than T_c where the normal state is accessible even in the absence of a magnetic field. This indicates the presence of a predominately hole-like Fermi surface. Accordingly, R_H is found to be positive for all fields and approximately independent of magnetic field. The computed values of R_H at low

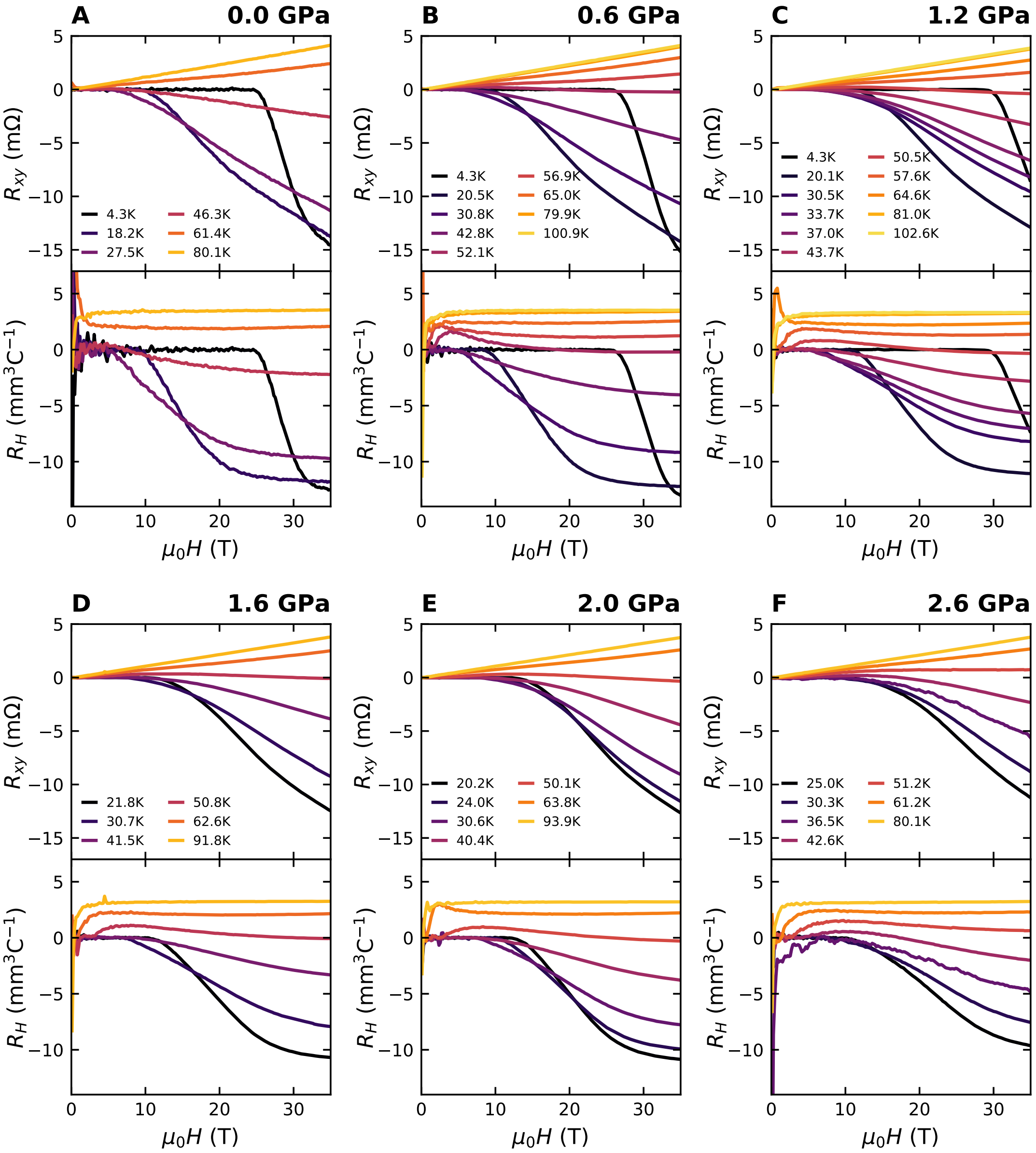

Figure 5.6: The magnetic field dependence of the Hall resistance (top of each panel) and Hall coefficient (bottom of each panel) at fixed temperatures for $p = 0.11$ (Sample T96). The data in each panel is measured at a different (indicated) hydrostatic pressure.

fields are highly inconsistent, deviate from field-independence and are sometimes divergent. This is due to numerical errors associated with dividing by an increasingly small number (H). At lowest temperatures, $R_{xy} = 0$ until there is a sufficient magnetic field to suppress superconductivity. At highest fields and at low temperatures, R_{xy} is found to be negative with a larger magnitude than at high temperatures. R_H is found to approximately saturate at the highest measured fields.

It is clear that with increasing pressure (and increasing T_c), that there is insufficient field to fully suppress superconductivity at low temperatures. At 1.2 GPa (Figure 5.6C), for example, there is clearly insufficient field to fully suppress superconductivity at 4.2 K. It is still possible to ascertain the sign of R_H despite this.

At elevated pressures and at some intermediate temperatures, the sign of R_H changes as a function of field. Clear example of this can be seen in $R_H(\mathrm{P = 1.2GPa, T = 50.5K})$ (Figure 5.6C) and $R_H(\mathrm{P = 2.6GPa, T = 40.2K})$ (Figure 5.6F). In both cases, R_H is positive at field immediately above H_{irr} but passes through zero and becomes negative at the highest measured fields. This finding and its implications will be discussed in more detail later.

The evolution of the high-field Hall coefficient with temperature was studied in order for T_0, the temperature at which $R_H = 0$, to be found. Figure 5.7A-C shows the evolution with pressure of the temperature dependence of $R_H(\mu_0 H = 35\mathrm{T})$ for each of the three samples. The lower panels (Figure 5.7D-F) shows the same data in the vicinity of $R_H = 0$. At each pressure, the three data points closest to $R_H = 0$ have been fitted to a quadratic (lines). T_0, the temperature at which $R_H = 0$, was found by finding the root of the obtained curve. T_0 has been indicated by a cross at each pressure. In order to minimise the error in the determination of T_0, an attempt was made to perform field sweeps at temperatures close to where $R_H = 0$.

For $p = 0.11$ and at the highest measured pressures (5.2 and 6.0 GPa), there is insufficient magnetic field to suppress superconductivity at sufficiently high temperatures to determined T_0. Although superconductivity could not be fully suppressed there was sufficient field to ascertain that R_H is negative at 20.1K ($R_H(\mu_0 H)$ can be found in Figure 5.14). This is sufficient to determine T_0 with the understanding that it is greater than 20.1K and less than 25.1K. At 6.0 GPa, however, no change of sign could be observed before H_{irr} exceeded the highest available field strength and T_0 could not be ascertained. If one were to naively determine T_0 ignoring the influence of superconductivity, an increase of T_0 would be inferred between 5.2 and 6.0 GPa.

In the case of Sample C161 ($p = 0.11$, MAC), 1.4 GPa of pressure was applied prior to commencing measurements at high field. This decision was made to minimise the possibility of a pressure cell failure with the application of pressure disrupting further measurements at an inopportune moment.

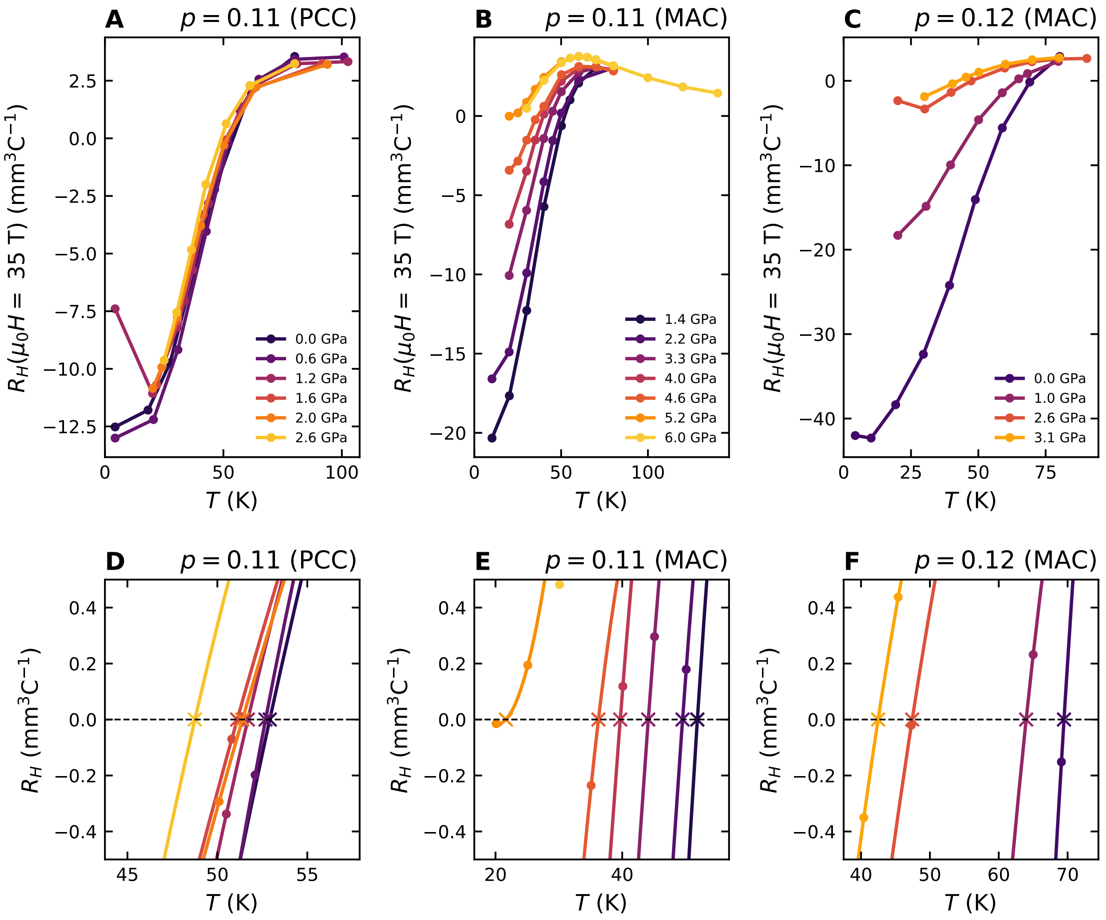

Figure 5.7: A-C: The evolution of the high-field Hall coefficient with pressure for each of the three samples. D-F: An expanded view of $R_H(\mu_0 H = 35\mathrm{T}, T)$. Lines are polynomial fits to the data in the vicinity of $R_H = 0$ from which T_0 (indicated by crosses) has been determined.

For this reason, T_0 was not determined at ambient pressure for this sample. T_0 was determined in Sample T96, a sample with the same (or similar) doping.

5.3.3 The evolution of T_0 with pressure

The pressure dependence of T_0 is presented in figure 5.8 for all three samples. A good degree of overlap in the measured pressure range and agreement in the values of $T_0(P)$ for the two samples at $p = 0.11$ is a strong indication that sample dependence is not a concern and that the two curves together represent the true pressure dependence over the full range of pressures that have been measured. It is clear that at both $p = 0.11$ and $p = 0.12$, there is an overall suppression of T_0 with increasing pressure. If T_0 is interpreted as being a proxy for the temperature at which change order onsets, this is evidence to suggest that charge order at 35 T is suppressed by hydrostatic pressure.

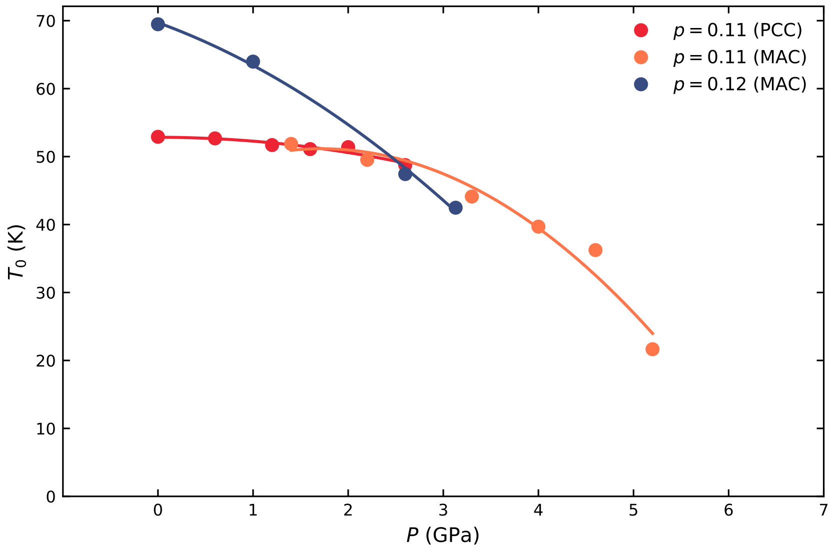

Figure 5.8: The pressure dependence of T_0 measured in three samples of Y123 (two dopings). The uncertainty in the determination of T_0 is comparable to the point size. The lines are guides to the eye only.

Interestingly, at $p = 0.11$ and at low pressures, T_0 remains relatively temperature independent. There is a finite but small negative slope up to 2 GPa. This is in stark contrast with the data $p = 0.12$. It is difficult to ascertain the low pressure slope of $T_0(P)$ without further data points at this doping, but it is clear that either the magnitude of the slope at lowest pressures ($dT_0/dP(0\,\mathrm{GPa})$) is greater or the range of pressures at which it remains small is markedly reduced. A much larger suppression of T_0 is certainly observed at 1 GPa at the higher doping. Importantly, this is despite the fact that the ambient pressure value of T_0 at $p = 0.11$ is 25% lower than at $p = 0.12$. The suggestion is therefore that despite the onset of charge order being at a lower temperature at the lower doping (and is therefore presumably less robust against temperature), charge order is somehow more robust against pressure at $p = 0.11$ than it is at $p = 0.12$. Indeed, this conclusion is also supported by the data at higher pressures. The two pressure dependences cross at around 2.2 GPa indicating that charge order is stronger at high pressures at $p = 0.11$ than it is at $p = 0.12$. Although there is insufficient data to estimate the value with a good degree of confidence, it is likely that T_0 will be suppressed to zero temperature with a pressure close to 5 GPa for $p = 0.12$, a pressure at which T_0 is found to remain finite at $p = 0.11$.

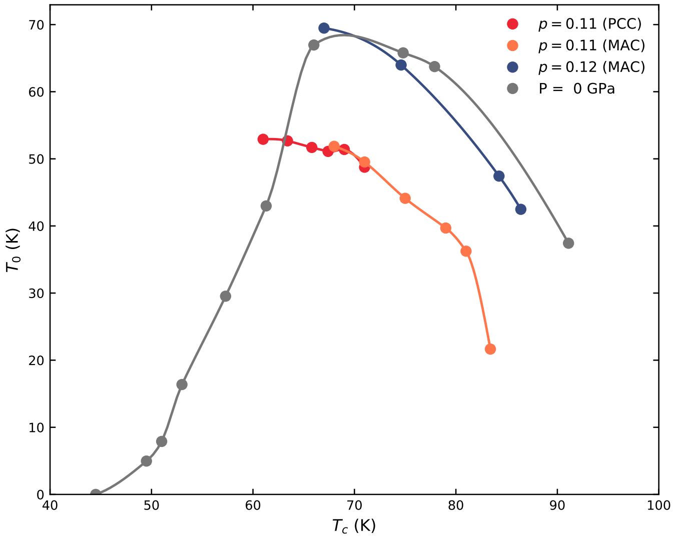

Figure 5.9: The evolution of T_0 with respect to T_c in Y123. The coloured data points are for the three samples measured in this work and the error is comparable to the size of the points. The grey points are data measured as a function of doping at ambient pressure from [89]. The lines are guides to the eye only.

5.3.4 The evolution of T_0 with T_c

Previously, the evolution of T_0 (a measure of the strength of charge order) and T_c (a measure of the strength of superconductivity) have each been discussed with respect to a mutual tuning parameter (hydrostatic pressure). In order to more directly evaluate how these two phases influence each other, it is informative to see how their strengths evolve with respect to each other. With this in mind, T_0 has been plotted against T_c for all three samples and is presented in figure 5.9. Also plotted on the same axes is the doping dependence of T_0 at ambient pressure with data taken from [89]. At $p = 0.12$, there is close agreement between the ambient pressure value of T_0 found here and the value found in the previous study. The discrepancy is larger at $p = 0.11$ ($\sim 10\,\mathrm{K}$). As mentioned previously, the fact that there is a strong degree of consistency between the values of both T_c and T_0 in the two samples measured in this work would suggest that the value of $T_0(T_c = 61\,\mathrm{K}) = 53\,\mathrm{K}$ is robust. As the authors of [89] also demonstrate, their value of T_0 is markedly lower than previous measurements would suggest. Although sufficiently low temperatures were not reached to observe T_0, the temperature dependence of R_H for a sample with $T_c = 60\,\mathrm{K}$ (labelled $y = 6.70$) measured by Segawa and Ando is higher still [96]. A primitive extrapolation of their data would suggest that T_0 is close to 60 K albeit at a lower field of 14 T.

A number of striking features are apparent in $T_0(T_c)$ that were less clear in the individual pressure dependencies of either. Firstly, the evolution of T_0 at the two dopings do not cross. For all measured values of T_c, the value of T_0 is higher for $p = 0.12$ than it is for $p = 0.11$. Furthermore, there is no evidence to suggest that this observation is likely to reverse as pressure is increased and T_c is further enhanced. On the assumption that both trends continue to evolve smoothly with no marked change in behaviour occurring in either, it is likely that T_0 will be suppressed to zero temperature at $p = 0.11$ at a T_c lower than that at which T_0 will be suppressed to zero temperature at $p = 0.12$. This result is contrary to what might have been assumed from examining the pressure dependence of T_0 alone and is a consequence of the higher dT_c/dP at $p = 0.12$.

Secondly, at $p = 0.12$, there is a close agreement between the evolution of T_0 with respect to T_c under both increasing pressure and hole doping. The suppression is perhaps slightly faster under hydrostatic pressure. It could therefore be inferred that there is a degree of equivalence between these two tuning parameters. That is to say that the application of pressure has the effect of adding holes (perhaps via an effective charge transfer mechanism) that is in some sense equivalent to adjusting the chemical composition. This hypothesis is clearly not so simply applicable to $p = 0.11$. Whether there is an equivalence between doping and pressure is discussed in more detail later.

5.3.5 Field Dependence of T_0

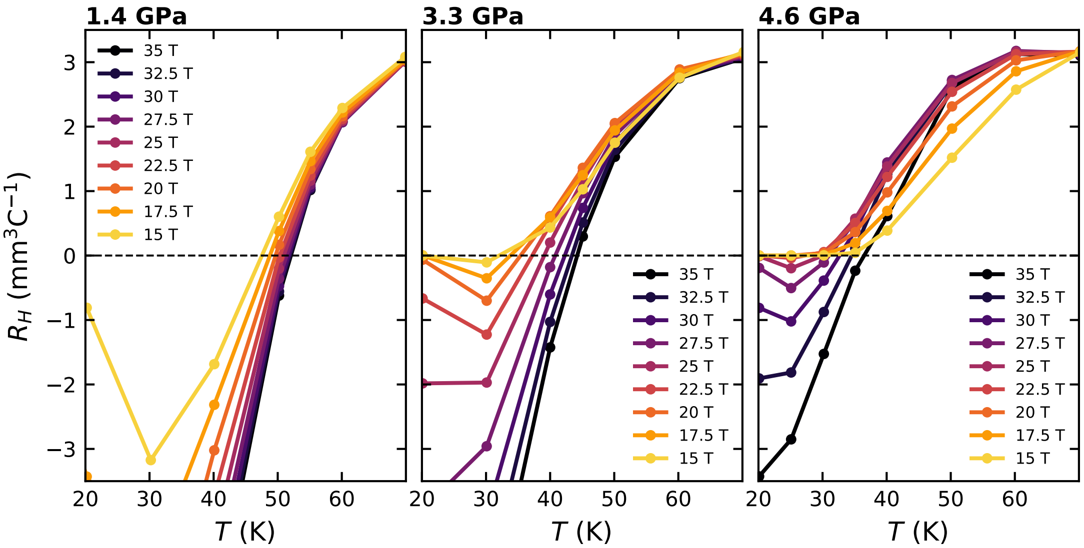

Figure 5.10: The temperature dependence of R_H for Sample C161 ($p = 0.11$, MAC) for three representative pressures. At each pressure, R_H has been been evaluated by taking cuts through $R_H(H)$ at different values of H.

The dependence of T_0 on magnetic field is a further point to consider. As previously mentioned, at various points in pressure-temperature space, R_H does not reach a saturated value at highest fields. In the simplest case, this is attributable to the application of insufficient field to suppress superconductivity completely. At magnetic fields less than H_{c2} but greater than H_{vs} (the field above which vortex motion generates a finite resistivity in the superconducting state), the influence of superconductivity needs to be considered carefully. In Figure 5.10, the field dependence of R_H has been evaluated at different magnetic field strengths at three representative pressures in Sample C161 ($p = 0.11$, MAC). It is clear that $R_H \to 0$ at low fields and low temperatures as is expected as superconductivity is enhanced. At 6.0 GPa (5.14G), it is clear that insufficient field was applied to suppress superconductivity. Importantly, precluding the possibility that the onset of superconductivity causes an anomalous change in the current path in the vicinity of the superconducting transition, one would only expect the magnitude of R_H to be suppressed with decreasing field.

However, it is equally possible that there is a genuine normal-state field-dependence to R_H and, in fact, this is apparent at particular temperatures and pressures at which R_H is found to be zero in the superconducting state, positive at fields immediately above H_{irr} and negative at 35 T. This is clearly illustrated in Figure 5.10 at temperatures for which R_H changes sign. A clear example of this can be seen in $R_H(\mathrm{H, P = 1.4GPa, T = 50K})$. Similarly, $R_H(\mathrm{H, P = 1.4GPa, T = 50K})$ both increases and passes through zero as H is reduced to 25 T. It is subsequently suppressed to $R_H = 0$ with a further decrease in field. The change in sign of $R_H(B)$ cannot be attributed to superconducting fluctuations.

The underlying reason for a sign-change in $R_H(B)$ is difficult to establish from these transport measurements alone. One possibility is that there is a Fermi surface reconstruction in field. This could be the stabilisation of three-dimensional charge order for instance. A second possibility is that the reconstructed Fermi surface in the presence of charge order contains multiple Fermi sheets (multiple pockets) where one is electron- and another is hole-like for instance. In this case, multi-band effects could result in a field-dependence to R_H that involves a change of its sign.

5.3.6 Estimation of H_{c2}

There is no distinctive feature in either $R_{xx}(H)$ or $R_{xy}(H)$ to denote the complete suppression of superconductivity and resultant restoration of the normal state with either temperature or magnetic field. In particular, the transition from the superconducting state to the normal state with magnetic field is broad. It is therefore difficult to determine H_{c2} from resistive measurements. At fields greater than H_{vs}, vortices become depinned and their dissipative motion results in a finite resistance. H_{vs}

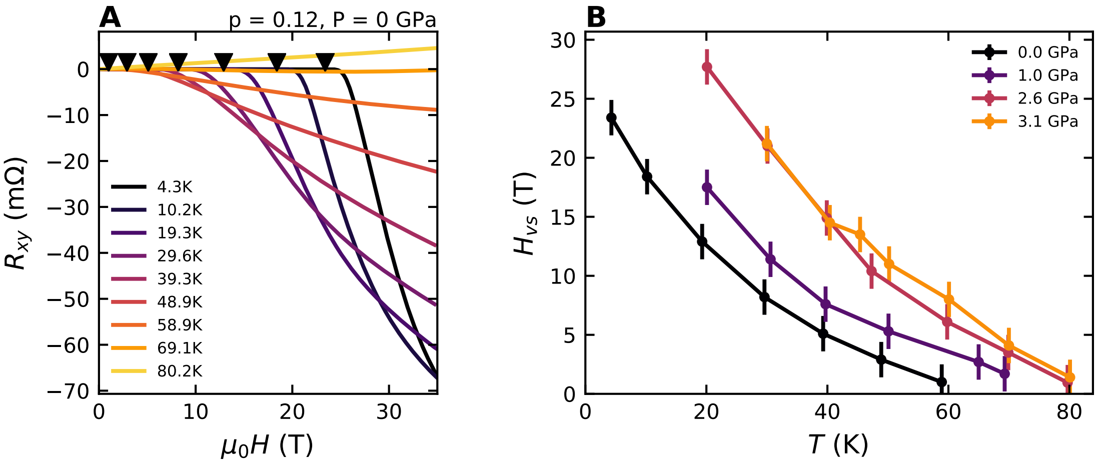

Figure 5.11: A: $R_{xy}(H)$ at ambient pressure and at different temperatures for $p = 0.12$ (Sample CuJ2). Arrows denote H_{vs}, the field strength at which R_{xy} fell to within the noise floor.

is somewhat less ambiguous to determine. In the simplest case (one in which there is no quantum vortex liquid state), the H_{c2} and H_{vs} should converge at $T = 0$. It is therefore possible to estimate H_{c2} from the temperature dependence of H_{vs}.

$R_{xy}(H, T)$ is presented in Figure 5.11A for $p = 0.12$ at ambient pressure. Black arrowheads denote the determined values of H_{vs}, the magnetic field at which R_{xy} fell to within the noise floor. In Figure 5.11B, the $H_{vs}(T)$ is presented for the same sample ($p = 0.12$) at different pressures. Both the enhancement of H_{c2} and T_c with increasing pressure can be seen.

The temperature dependence of H_{vs} is indicative of the degree of disorder in the sample. In clean sample, the density of pinning sites is small and only a small field is required to induce vortex motion. Conversely, vortices are strongly pinned in more disordered samples and H_{vs} is larger as a consequence. The degree of pinning is not anticipated to be pressure dependent. With this assumption, it is expected that $H_{vs}(T)$ measured at different pressures should collapse if scaled by both T/T_c and H/H_{c2}. Figure 5.12 shows H_{vs}/H_{c2} vs T_c where H_{c2} has been selected such that each curve collapses onto that which is taken at lowest pressure. H_{c2} as directly determined from thermal conductivity [94] is found to be the same (24(2) T) for both $p = 0.11$ and $p = 0.12$. To satisfy that H_{vs}/H_{c2} extrapolates to 1 at $T = 0$, H_{c2} is required to be slightly higher in this study (28 T and 26 T respectively for $p = 0.11$ and $p = 0.12$). This is within the experimental uncertainty. The value of H_{c2} for Sample C161 ($p = 0.11$, MAC), for which measurements were not performed at ambient pressure, was chosen to match Sample T96 ($p = 0.11, \mathrm{PCC}$). This assumption appears to be valid within the uncertainty. H_{vs}/H_{c2} does extrapolate to ∼1 as $T = 0$

It is noted that for Sample T96 ($p = 0.11$, PCC), there are points which fall markedly above the collapsed curves. These points are a true reflection of where R_{xy} was found to drop to within the noise floor. However, these are regions of $H-T-P$ phase space in which R_H was found to change sign in field. It is expected that there are regions of $H-T-P$ phase space in which the normal state value $R_{xy}(H)$ is in fact zero or very small for an extended (a few tesla) field range. If this is the case, the value of H_{vs} determined by the criterion applied here will be higher than the true value of H_{vs}.

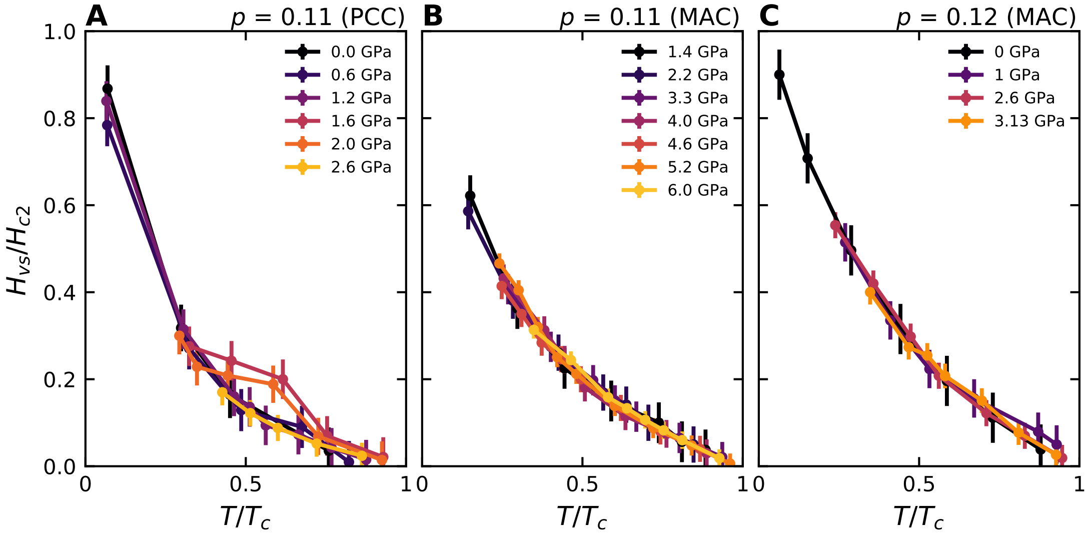

Figure 5.12: H_{vs}/H_{c2} vs T_{T_c} for each of the three samples. H_{c2} is selected such that the curves collapse onto the ambient pressure curve for which H_{c2} can be corroborated with determination from other studies [94].

Finally, H_{vs}/H_{c2} vs T/T_c is presented for each of the three samples (Figure 5.12). Although the uncertainty is large, H_{c2} is found to monotonically increase for both dopings. The rate of increase is found to be larger for $p = 0.12$, a finding consistent with the larger value of dT_c/dP. The estimation of H_{c2} via this method comes with a large degree of uncertainty. Despite this, it could be concluded that the slope dH_{c2}/dP increases at 4.5 GPa for $p = 0.11$ or the evolution up to 6 GPa is non-linear. This is somewhat surprising given that T_c is found to increase with a strong degree of linearity. However, the relationship between T_c and H_{c2} is not completely clear in the range of dopings considered here as evidenced by a local minimum in H_{c2} [94] and only a local plateau in T_c occurring at $p = 1/8$ [88]. If a mutual competition between charge order and superconductivity is supposed, the implication is that H_{c2} is more strongly suppressed than T_c. In this scenario, a linear increase in T_c accompanied by a super-linear increase in H_{c2} is perhaps not so surprising.

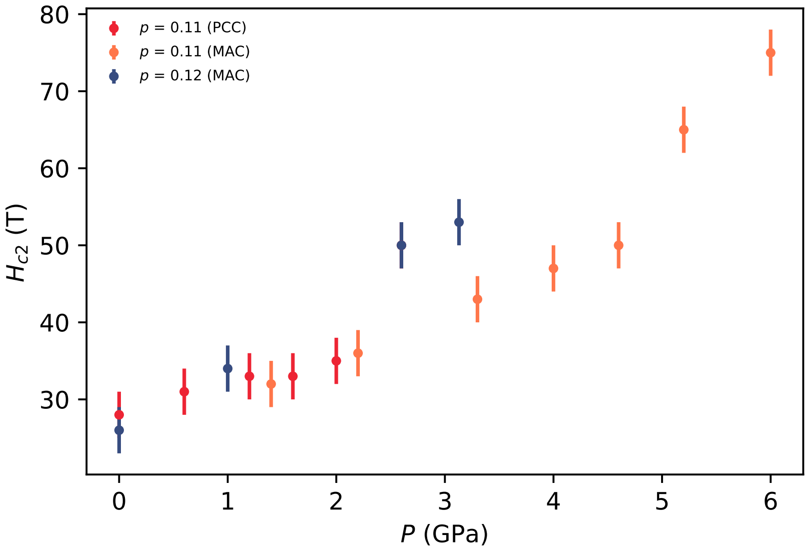

Figure 5.13: The pressure dependence of H_{c2} for all three samples where H_{c2} was estimated by extrapolating the measured temperature dependence of H_{vs} to $T = 0$.

5.4 Discussion and Outlook

Whether there is a mutual competition between charge order and superconductivity is difficult to unambiguously ascertain. For $p = 0.11$, up to 2.6 GPa there is only a minor suppression of T_0 (which can be interpreted as a minor suppression of charge order) despite a 10 K increase in T_c. This observation appears to be at odds with the core premise that superconductivity and charge order are in mutual competition. More specifically, it could be concluded that the pressure-induced enhancement of T_c failed to suppress charge order. Alternatively put, the lack of suppression of T_0 presented here suggests that the enhancement in T_c is not the result of a pressure-induced suppression of charge order.

Although the measurements presented here cannot ascertain the influence of pressure on the stability of charge order in Y123 directly, with reference to other systems, one might predict that pressure suppresses charge order. This is usually found to be the case because, generally speaking, the application of hydrostatic pressure increases phonon frequencies by increasing the stiffness of the lattice. Additionally, increased orbital overlap typically leads to an increasingly three dimensional Fermi surface in which nesting, a driver of charge order, is reduced. This makes the apparent stability of charge order at $p = 0.11$ for pressures up to 2.6 GPa more surprising still. There has been a reports of x-ray studies which claim that hydrostatic pressure fully suppresses charge order at pressures as low as 1 GPa [97, 98]. There, a phonon-softening at $\mathbf{Q}_{CDW}$ was found to be highly fragile to the application of pressure. These studies, however, were performed in the absence of a magnetic field and are therefore presumably only sensitive to the onset of two-dimensional charge order. Out of necessity, the measurements performed here are performed at high field where three-dimensional charge order is stabilised. One might therefore conclude that three-dimensional charge order is more robust against pressure than two-dimensional charge order in Y123. Alternatively, it is possible that the application of a magnetic field has suppressed superconductivity such the aforementioned phonon anomaly may return at pressures greater than 1 GPa.

At higher pressure and for the same doping, there is a gradual non-linear suppression of charge order accompanied by a linearly increasing T_c. One would expect from the evolution of T_0 with pressure that the CDW could be fully suppressed with pressure. If such a critical pressure exists in Y123 at the dopings measured in this work, one would anticipate from Figure 5.9 that it is in the vicinity of 5.6 GPa - 6 GPa in both cases with the value being higher for the lower of the two dopings. There is no indication that it has been reached up to 6 GPa at $p = 0.11$ in this work nor in the work of Sadewasser et al [56] at the same doping. The lack of a features in the evolution of T_c with pressure is a further indication that the two phases are not in mutual competition. To the contrary, the slope of the pressure dependence of T_c appears to smoothly decrease up to 17 GPa [56].

What is difficult to rule out is the possibility that pressure intrinsically enhances both superconductivity and charge order in this pressure range and at this doping ($p = 0.11$) and that the mutual competition between the two phases negates the enhancement of T_0 such that the T_0 remains stable up to 2.6 GPa. The expectation in this instance would be that in the absence of charge order, dT_c/dP would be greater than the observed value and that in the absence of superconductivity, dT_0/dP would be positive. In order to account for the increasingly negative dT_0/dT_c at pressures greater than 2.6 GPa, the argument would presumably be that the increasingly strong superconducting state begins to outweigh the enhancement of charge order with pressure. In order to explain the absence of a region of stability of T_0 with respect to increasing pressure and T_c at $p = 0.12$, this argument would require that the competition between superconductivity and charge order is stronger at this doping.

The evolution of T_0 with respect to T_c at both $p = 0.11$ and $p = 0.12$ can perhaps be explained by the combination of two competing effects. The first is a degree of equivalence between the application of hydrostatic pressure and hole doping via adjustment of the chemical composition. It can be reasonably hypothesised that the application of pressure will result in a degree of pressure-induced effective doping by means of charge transfer to the CuO_2 planes. That is, there is an inherent tendency for the pressure dependence to follow the doping dependence. At $p = 0.11$, the pressure-induced doping dependence (if it follows the measured doping dependence) of T_0 is strongly positive but diminishes at higher pressures. Again, if it follows the measured doping dependence, this effect would become negative at sufficiently high pressures. At $p = 0.12$, however, there is minimal doping dependence to T_0 at low pressures. At higher pressures, again, the dT_0/dp becomes increasingly negative. If hydrostatic pressure and oxygen content were strictly equivalent, a strong increase in T_0 would be anticipated at low pressures followed by a saturation and subsequent decrease at highest pressures. This is clearly not the case. The second effect is an intrinsic suppression of charge order with pressure. If both effects are considered, one might expect that $dT_0/dP \sim dT_0/dP_p + dT_0/dP_{in}$ where $dT_0/dP_p = (dT_0/dp)(dp/dP)$ and dT_0/dP_{in} is an intrinsic pressure dependence.

At $p = 0.11$ and at low pressures, these two effects are in competition and the net result is that there is no change in T_0 because the two effects negate each other. As the doping dependence becomes increasingly weak and eventually becomes negative, the total pressure dependence becomes increasingly negative as well. At $p = 0.12$, the suppression of charge order with pressure is accompanied by minimal doping dependence. The net result is a suppression of T_0 with respect to pressure. With increasing pressure, the doping dependence of T_0 starts small ($dT_0/dP_p \sim 0$) and becomes increasingly negative. The evolution of T_0 becomes increasingly negative as well. In this picture it is still difficult to unambiguously determine whether or not the suggested suppression of charge order with hydrostatic pressure is intrinsic to the application of pressure itself, or arises indirectly as a consequence of the enhancement of the superconducting phase.

5.4.1 High-Field and Low-Field Charge Order

A core assumption made throughout the discussion thus far is that the T_0, a quantity measured at 35 T in the absence of superconductivity, is reflective of the strength of charge order at 0 T, the field at which the strength of superconductivity is evaluated via measurement of T_c. Furthermore, it is unclear whether measuring the strength of charge order in the absence of superconductivity allows a fair comparison to be made and the influence of one phase upon the other to be evaluated at all. These concerns are inherent to transport measurements in which superconductivity needs to be suppressed in order for a signal to be measured. For this reason, if one was to be highly cynical, it could be argued that transport is an inherently inadequate tool for the task at hand.

To address the first issue, the nature of high- and low-field charge order in Y123 needs to be considered. At high temperatures and/or low magnetic fields, the *c*-axis coherence length of charge order has been found by x-ray studies to be small making the charge structure two dimensional in the *ab*-plane. At temperatures below the superconducting transition, two dimensional charge order is suppressed but is enhanced with the application of a magnetic field. At temperatures above T_c, the 2D charge order is independent of field [84]. At higher magnetic fields an additional three-dimensional charge ordered structure is formed [85, 99]. Before its total formation, a precursor regime exists in which the $b-$ and $c-$axis coherence lengths grow. At lowest temperatures, the precursor regime begins at around 10 T and stable three-dimensional charge order is seen at 15 T at $p = 0.12$. The deviation of R_H from its $1/T$ high-temperature behaviour occurs at temperatures higher than both the temperatures at which three-dimensional charge order is stable and even above the precursor regime. This is the case in both the presence and absence of a magnetic field. This would indicate that the subsequent fall of R_H is a consequence of the two-dimensional charge order as opposed to the three-dimensional charge order. So although the presence of high-magnetic fields is necessary to access the normal state such that R_H can be measured, it is likely that T_0 is a characteristic temperature associated with the same two-dimensional charge order that has been widely associated with the plateau in T_c at $p = 1/8$ in the absence of a magnetic field.

The issue becomes further complicated when the application of hydrostatic pressure is considered. Inelastic x-ray scattering experiments performed under hydrostatic pressure on $YBa_2Cu_3O_{6.6}$ ($p = 0.12$) have found that with the application of as little as 1 GPa, phonon anomalies associated with charge order completely disappear [97]. The implication is that there is a pressure-induced suppression of charge order with relatively low hydrostatic pressures. The same phonon anomalies were found to be present in $p = 0.134$, a doping at a T_c close to that at $p = 0.12$ with the application of 1 GPa. This eliminates the possibility that pressure-induced doping was the underlying cause of the suppression of charge order with pressure. Regarding the presence (or lack of) competition between superconductivity and charge order, it is again difficult to discriminate between an intrinsic pressure-induced suppression or an indirect suppression due the enhancement of superconductivity. The rate of suppression appears to be incompatible with the smooth and featureless enhancement of T_c. Importantly, however, it further raises the question of whether or not the evolution of the high-field Hall coefficient is a reasonable indicator that reflects the behaviour of two-dimensional charge order. It is difficult to reconcile the swift extinction of charge order at 1 GPa with the observed evolution of R_H here.

Contrary to the aforementioned x-ray experiments, evidence for the persistence of charge order to higher pressures can be found in reports of NMR experiments [100, 101]. Pressures of 1.9 GPa were found to only have a minimal effect on the stability of charge order (of either variety) at $p = 0.109$ [100], a view that is far more consistent with what is found here. The observation of quantum oscillations with slow frequencies at pressures up to 0.84 GPa are a further indication that the Fermi surface remains fully reconstructed at pressures close to those at which charge order appears fully suppressed [102].

5.4.2 The Validity of T_0 as Gauge of the Strength of Charge Order

Another further assumption made throughout the preceding discussion is that T_0 is a useful indicator of the strength of charge order at all. The aforementioned work of LeBoeuf [103] showed that at ambient pressure both T_0 and T_{max} (the temperature at which $R_H(T, B = 35\,\mathrm{T}$ is maximal) both produce a dome peaked at $p = 1/8$. This is highly suggestive that T_0 is a valid gauge of the onset (and therefore strength) of charge order. Whether this remains true with the application of pressure is unclear from this work alone.

5.5 Concluding Statements

As is often the case, it is difficult to unambiguously disentangle a number of possible competing effects. Specifically, it is not completely clear whether an observed suppression of charge order is the result of enhanced superconductivity, effective doping or an intrinsic consequence of the tuning parameter (hydrostatic pressure) itself. The stability of charge order at $p = 0.11$ for pressures up to 2.6 GPa despite an increase in T_c of 10 K is highly suggestive that the competition is not mutual in all instances. It would require an accidental negation of competing effects for this to be observed. This scenario, however, cannot be ruled out and can in fact phenomenologically describe the evolution of T_c and T_0 at higher pressures and higher dopings.

The ambiguity is exacerbated by the presence of both two- and three-dimensional charge order. It is difficult, for example, to draw a direct comparison between the aforementioned x-ray studies [97, 98] that claim to show a total suppression of charge order at $\sim$ 1 GPa (in zero field) and the work presented here. A study of the phonon anomaly observed in these x-ray studies as it evolves in field may help reconcile the apparent contradiction between the conclusions drawn in [97, 98] and the findings reported here.

Further measurements over a wider range of dopings and at higher pressures will shed further light on the matter. Similarly, the stability of charge order and the strength of superconductivity should be studied with respect to different tuning parameters. The application of hydrostatic pressure is in principle summing the effects of uniaxial pressure derivatives. The application of uniaxial strain, for example, could disentangle the effect of different uniaxial pressure derivatives and disentangle the effect of c-axis compression which is likely to result in an effective doping through a transfer of charge and the effect of a- and b- axis strains which are likely to affect the degree of in-plane orthorhombicity.

5.6 Appendices

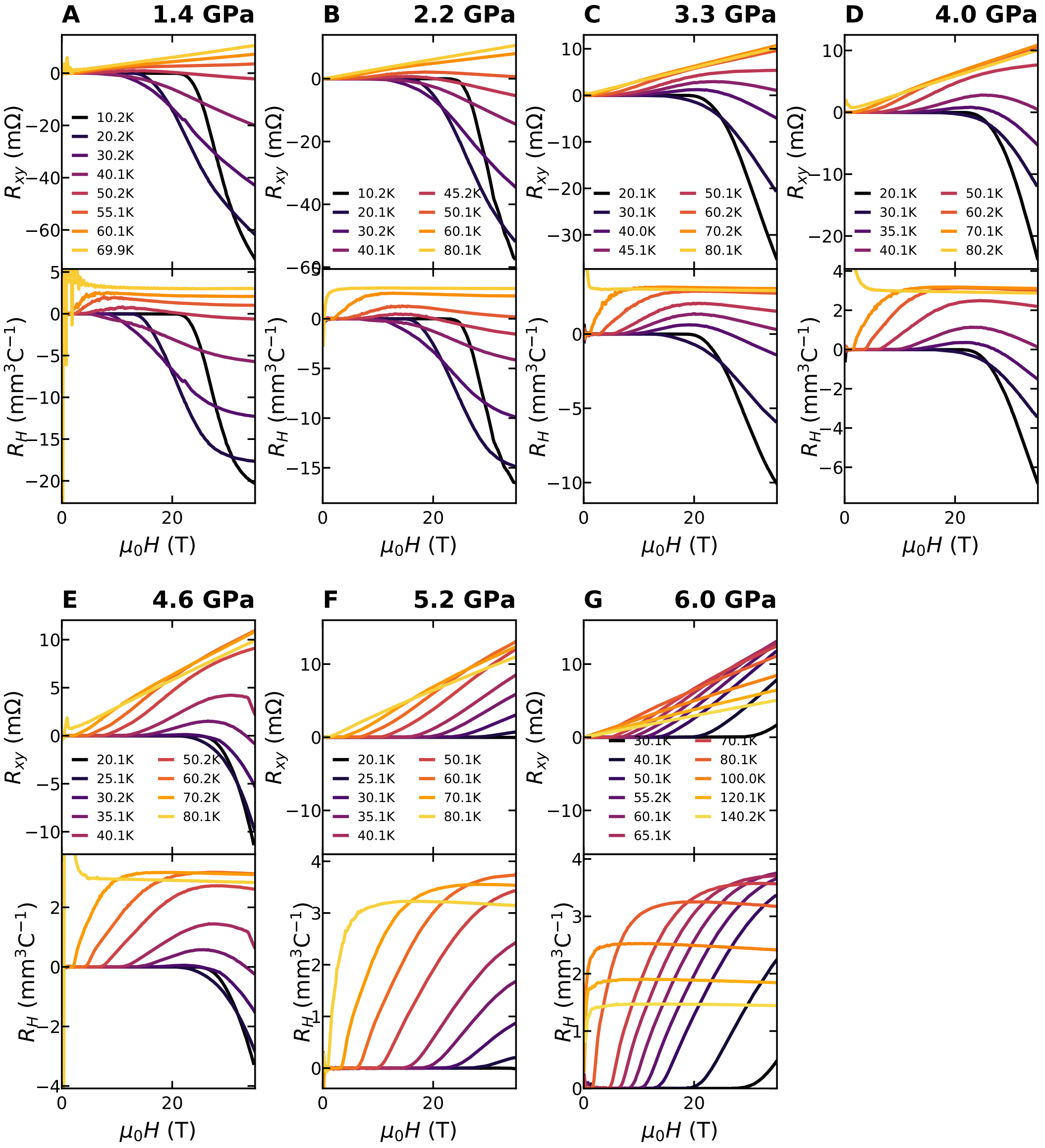

Figure 5.14: The magnetic field dependence of the Hall resistance (top of each panel) and Hall coefficient (bottom of each panel) at fixed temperatures for $p = 0.11$ (Sample C161). The data in each panel is measured at a different (indicated) hydrostatic pressure.

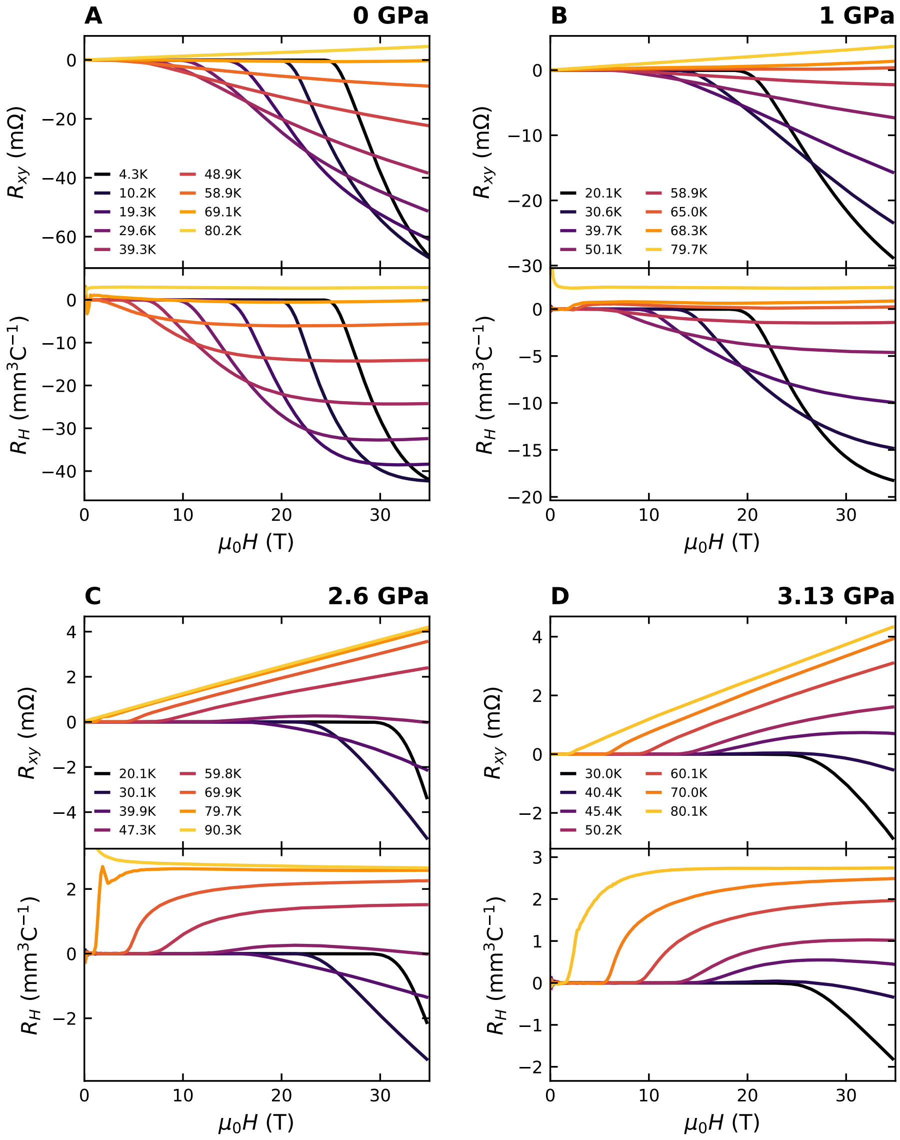

Figure 5.15: The magnetic field dependence of the Hall resistance (top of each panel) and Hall coefficient (bottom of each panel) at fixed temperatures for $p = 0.12$ (Sample CuJ2). The data in each panel is measured at a different (indicated) hydrostatic pressure.

Chapter 6

$\mathbf{FeSe}_{1-x}\mathbf{S}_x$

A comprehensive study of the high-field in-plane resistivity of $\mathrm{FeSe}_{1-x}\mathrm{S}_x$ is presented over a wide range of sulphur concentrations that span the nematic phase and with the application of hydrostatic pressure. When nematicity is suppressed with pressure, signatures of quantum criticality are revealed in the normal state akin to those that have been reported at the nematic QCP as it is suppressed with increasing sulphur concentration [19]. The application of hydrostatic pressure, however, separates the nematic QCP from a magnetic QCP such that their respective influences can be disentangled. Thus, the quantum critical phenomena observed in this work can be ascribed to a suppression of nematicity alone.

The systematic evolution of quantum critical behaviour at the QCP as it is crossed with pressure are only easily observed over a narrow range of sulphur concentrations. At some values of x, H_{c2} is enhanced such that insufficient magnetic field could be applied to reveal the normal state behaviour down to the low temperatures required. At others, magnetic order introduced additional signatures that obscure the interpretation. The dopings for which quantum critical phenomena can be observed have been identified and a follow up experiment is proposed.

The preparation of as-grown crystals and pressure cells for transport measurements was performed by the author. All of the measurements and subsequent analysis was also performed by the author.

6.1 Background

6.1.1 Iron Based Superconductivity

The discovery of superconductivity in LaOFeAs [104] marked the start of an intensive study of high-temperature superconductivity beyond the copper-based cuprates. With fluorine doping (LaFeAsO$_{1-x}$F$_x$, $x = 0.08$), T_c can be enhanced from 4 K to 26 K [105]. T_c was further enhanced to 43 K with the application of pressure [106]. The family was rapidly expanded to include compounds in which La was substituted for other lanthanides including Sm which was found to enhance T_c to 55 K [107, 108]. Thus, iron-based superconductors (FeSC) emerged as a new family of high-temperature superconductors. This came as somewhat of a surprise given that conventional wisdom of the time would have suggested that magnetic, especially ferromagnetic, elements would be highly detrimental to superconductivity.

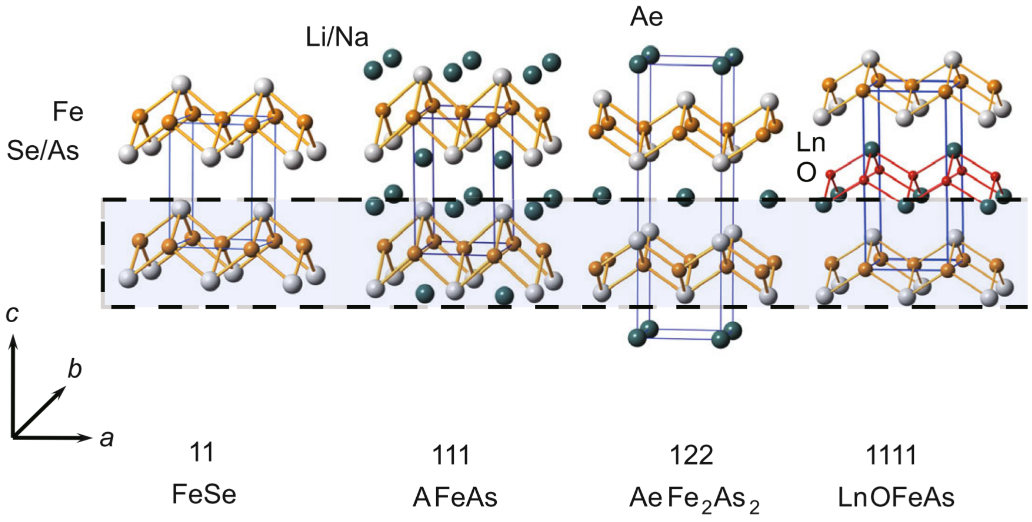

Figure 6.1: The crystal structure of a number of iron-based superconductors from [109]. A, Ae, Ln and M respectively represent alkali, alkali earth, lanthanide and transition metal atoms. The Fe-Pn/Ch trilayers that are common to this family of materials have been highlighted.

Somewhat analogous to the CuO$_2$ planes in cuprates, the common structural feature of FeSCs are a square lattice of Fe^{2+} and either pnictide (Pn) or chalcogenide (Ch) ions. These square lattices are tetragonal and form a trilayer in which Pn or Ch ions alternately sit above and below the plane. Different systems are distinguished by the choice of Pn (Pr, As) or Ch (Se, Te) and the inclusion of additional layers between the Fe-Pn/Ch trilayers. The crystal structure of a representative selection of FeSCs are shown in Figure 6.1 (from [109]). The Fe-Pn/Ch trilayers that are common to materials of this family have been highlighted. As with the cuprates in which the CuO_2-derived states are believed to be those principally responsible for superconductivity, it is the Fe-Pn/Ch trilayers that are considered essential to superconductivity in FeSCs.

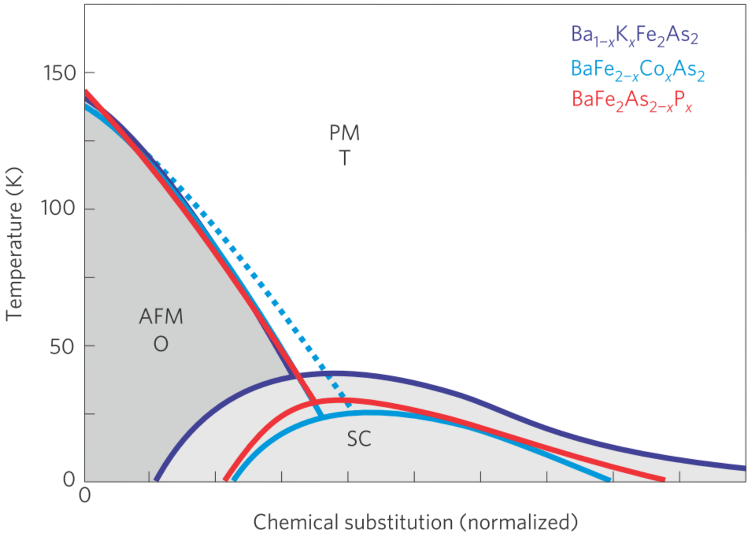

Figure 6.2: The temperature-doping phase diagrams of the Ba122 system for different dopants from [110] and references therein. The degree of chemical substitution has been normalised such that the rate of suppression of the antiferromagnetic state is the same for each system for visual clarity.

The temperature-doping phase diagram of the $BaFe_2As_2$ (Ba122) system is presented in Figure 6.2 for three different dopants. x (the amount of chemical substitution) has been normalised for each system such that the rate of suppression of the antiferromagnetic state is the same for each system for visual clarity. The features are broadly-speaking generic to all FeSCs. The parent (undoped) compound is antiferromagnetic with a Néel temperature $\sim$ 150 K above which it is paramagnetic. Unlike the cuprates in which this parent phase is (Mott) insulating, the parent phase in FeSCs is metallic. Accompanying the magnetic transition is a structural transition from tetragonal at high temperatures to orthorhombic at low temperatures. This transition can coincide with the Néel temperature or can occur at a temperature that follows but is measurably higher than the Néel temperature as indicated by the dashed line in Figure 6.2. These two phase transitions are therefore believed to be distinct. In addition to the structural transition is a nematic electronic transition. In the latter, the transition to nematic order in which in-plane symmetry is broken is driven by electronic (or orbital) degrees of freedom as opposed to phononic degrees of freedom [111, 112]. This conclusion is evidenced by the large anisotropy of the in-plane transport properties when compared with the relatively minor structural anisotropy of the system [113, 114].

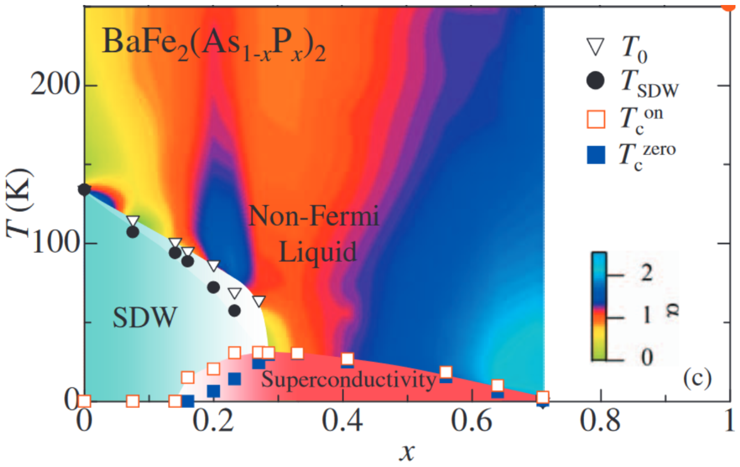

Figure 6.3: The temperature-doping phase diagram of P-Ba122 illustrating the evolution of α, the temperature exponent of the resistivity across a quantum critical point at $x = 0.30$ from [115].

At sufficiently low temperatures and at dopings at which magnetism is sufficiently suppressed, superconductivity emerges. The $T = 0$ end points of the phase boundaries delineating both the structural and nematic phases are obscured. At $x = 0.30$, a doping towards which the phase boundaries approach at low temperatures, the distinctive crossover from T^2 to T-linear behaviour of the resistivity [115, 116] (Figure 6.3), an enhancement of the effective mass [24] and anomalous critical fields [117] have indicated the presence of a quantum critical point (QCP) buried within the superconducting dome. The critical fluctuations associated with this QCP are believed to be magnetic in origin.

6.1.2 FeSe and FeSe$_{1-x}$S$_x$

FeSe was revealed to be a superconductor with $T_c \sim 8$ K [118] and is the Fe-chalcogenide with the simplest crystal structure. It is comprised only of the FeSe tetragonal trilayer sheets. It is therefore an example of an FeSC in which the parent compound is also a superconductor. Although T_c is relatively low compared with other FeSC systems, the application of hydrostatic pressure can enhance T_c to ∼40 K [119, 120] and monolayers grown on doped SrTiO$_3$ exhibit superconductivity at temperatures as high as 100 K [121]. As with other FeSCs, there is a structural transition from tetragonal to weakly orthorhombic which is found to occur at $T_s = 90$ K and this transition is found to be separated in temperature from that of the associated nematic transition [122].

The properties of FeSe can be tuned via chemical substitution as is the case in other FeSCs. A common dopant is sulphur which substitutes onto the selenium sites. With increasing x, T_s in FeSe$_{1-x}$S$_x$ is rapidly suppressed from 90 K to 0 K at $x_c \sim 0.16$ [19, 123] whilst T_c is found remain finite up to $x = 1$ (FeS) [124]. Uncharacteristically of FeSCs, the structural transition is not accompanied by the onset of long-range antiferromagnetic order [122, 125]. Thus, the strong anisotropy of electronic properties including the shape of the Fermi surface [126] and Cooper pairing [127] can be ascribed to nematicity alone and the influence of nematicity on superconductivity can be studied free from obfuscation from magnetism. Due to the absence of magnetism, the QCP at the $T = 0$ endpoint of the structural transition is in principle purely nematic in nature as well.

6.1.3 Nematic Quantum Critically in $\mathrm{FeSe}_{1-x}\mathrm{S}_x$

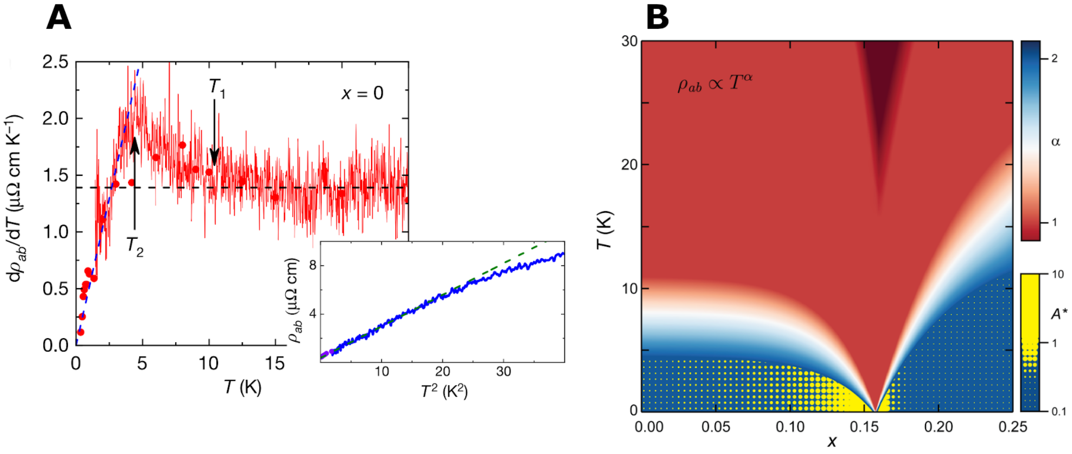

Figure 6.4: A: The temperature dependence of the high-field in-plane resistivity ($\rho_{ab}(H = 35\ \mathrm{T}, T)$) of FeSe from [19]. High-temperature linearity is found to crossover to low-temperature quadraticity. B: The evolution of the T-exponent α and T-coefficient A of the resistivity across the temperature-doping phase diagram revealing strong signatures of quantum criticality at the nematic QCP near $x = 0.16$ in $\mathrm{FeSe}_{1-x}\mathrm{S}_x$ from [23].

A recent study of the high-field in-plane resistivity of $\mathrm{FeSe}_{1-x}\mathrm{S}_x$ has revealed strong signatures of quantum criticality at the doping at which the resistive signature of T_s was found to be suppressed to zero temperature [19]. In order to measure the resistivity down to lowest temperatures a magnetic field was applied. This magnetic field was oriented $H \parallel ab$ as the MR was found to be negligible in this configuration. $\rho_{ab}(H = 35\ \mathrm{T}, T)$ is therefore expected to be representative of $\rho_{ab}(H = 0\ \mathrm{T}, T)$. The findings are summarised in Figure 6.4.

A distinct crossover from T^2 to T-linear behaviour with increasing temperature in the high-field in-plane resistivity of $\mathrm{FeSe}_{1-x}\mathrm{S}_x$ was found. This crossover could be quantified by taking the temperature at which T^2 was lost with increasing T (T_2) or the temperature at which deviation from linearity was found with decreasing temperature (T_1). T_1 and T_2 were found to be suppressed with increasing $x < x_c$ such that T-linearity was observed down to lowest temperatures at $x_c = 0.16$, the doping at which nematicity is suppressed [123]. For $x > x_c$, T^2 behaviour is recovered at increasingly high temperatures. A concurrent divergence of the T^2 coefficient A (normalised to account for the effect of a changing carrier density) was observed simultaneously at $x = x_c = 0.16$ and is reflective of a local enhancement of m^*.

Intriguingly, the same quadrature form of the MR that was found in this work in Tl2201 (Chapter 4) was observed in FeSe$_{1-x}$S$_x$ when $H \parallel c$ [23]. Distinct orbital and quadrature components of the in-plane MR could be discerned. Furthermore, the relative size of the quadrature component to the total MR was found to be maximal at $x = x_c$.

6.1.4 FeSe$_{1-x}$S$_x$ under Hydrostatic Pressure

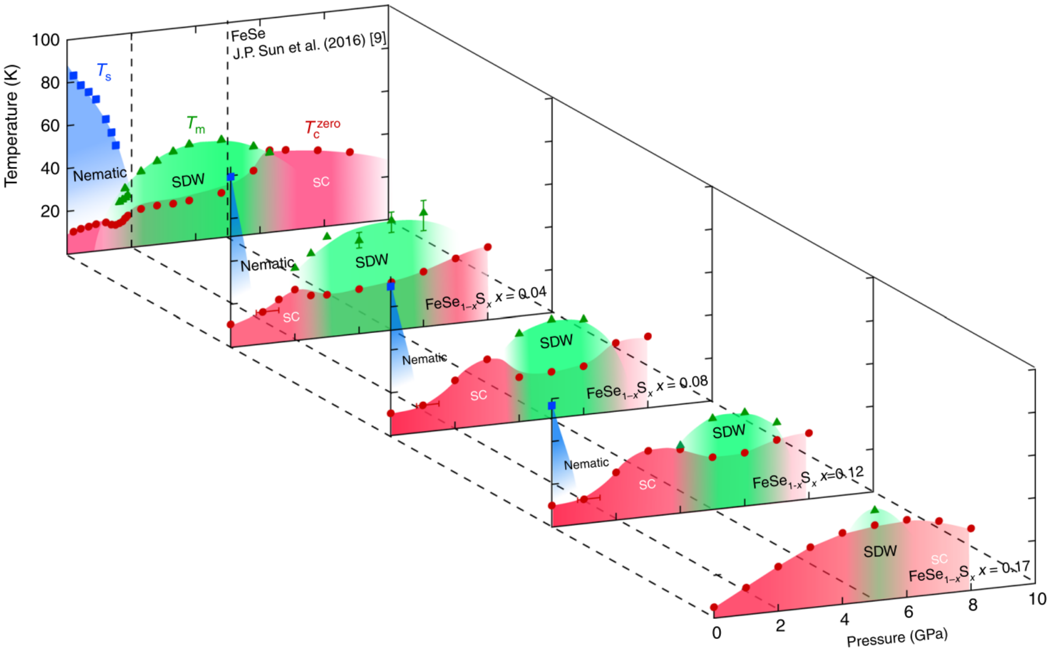

Figure 6.5: The temperature-pressure phase diagrams of FeSe$_{1-x}$S$_x$ for a number of dopings (different values of x) from [128]. Nematicity is suppressed with pressure for all dopings and a spin density wave (SDW) is stabilised.

Although long-range magnetic order has not been detected in FeSe [122], magnetic fluctuations are present but are suppressed with increasing x [129]. Proximity to a magnetic phase (SDW phase) in FeSe is revealed with the application of hydrostatic pressure [119, 125, 130]. With increasing pressure, nematicity (T_s) is suppressed and an additional magnetic phase (likely, striped antiferromagnetic order [131, 132]) is stabilised. AC magnetisation and μSR studies have shown that the superconducting volume fraction remains close to 100% whilst the magnetic volume fraction grows with increasing pressure to $\sim$ 90% at 1.4 GPa indicating a coexistence of both phases [125].

With increasing x, P_c, the pressure at which nematicity is totally suppressed, is markedly reduced. The pressure at which an SDW is stabilised is simultaneously increased [128]. Whilst there is overlap at low x, the two phases separate at high x. These findings are illustrated in Figure 6.5. The increase of P_{SDW} supports the evidence that magnetic fluctuations diminish with increasing x and indicate that the quantum critical phenomena associated with x_c are indeed of a nematic origin. It is difficult, however, to definitively rule out the possibility that the cause is not the loss of magnetic fluctuations.

The presence of magnetic fluctuations at temperatures above the magnetic transition [133] and at ambient pressure where static order is not stabilised [129] call into question how free from magnetism the system truly is at ambient pressure. The use of hydrostatic pressure as an alternative tuning parameter to doping allows for a similar study of the high-field in-plane resistivity to be performed to that which was conducted by Licciardello [19, 23]. In this case, as the nematic transition is suppressed with pressure, the magnetic phase is approached. If the electronic properties are governed by magnetism, they should evolve in the opposite manner with pressure as would be expected if nematicity is the driving mechanism. Additionally, there are values of x for which it should be possible to cross both the nematic transition and the magnetic transitions separately and at different pressures. It is therefore hoped that a study of the in-plane transport properties of FeSe$_{1-x}$S$_x$ will be able to unambiguously ascertain which of the two phases are responsible for the aforementioned quantum critical phenomena, for example.

6.2 Experimental Details

The principal purpose of the work presented in this chapter is to perform a similar study of the temperature dependence of the high-field in-plane resistivity that was performed by Licciardello (at ambient pressure) but as a function of applied hydrostatic pressure. The intent is to cross the nematic transition with pressure and see whether similar signatures of quantum critically are observed. To this end, samples of FeSe$_{1-x}$S$_x$ with sulphur concentrations between $x = 0.00$ and $x = 0.18$ were measured in high fields and with pressures up to 2 GPa using piston cylinder cells.

6.2.1 Sample Preparation and Measurement

The crystals of FeSe$_{1-x}$S$_x$ measured in this work are from the same growth batches as those that were measured by Licciardello [19, 23]. They were grown at Kyoto University by S. Kasahara using a $KCl/AlCl_3$ chemical vapour transport technique in which Fe, Se and S powders are heating in a SiO_2 tube across which a temperature gradient is applied. The dopings quoted throughout this work are nominal values provided by the crystal grower. It should however be noted that nominal sulphur concentrations are typically about $\sim 80\%$ of the concentration determined by EDX spectroscopy [123]. The nominal sulphur concentrations of the sample measured in this work were $x = 0.00$, 0.05, 0.08, 0.10, 0.13, 0.16, 0.18.

The crystals were simply cut using a knife to a rectangular shape with in-plane dimensions $\sim 800\,\mu m \times 300\,\mu m$. The thicknesses of the samples were around $\sim 50\,\mu m$. It was found that contacts made by applying silver paint directly to the sample surface would degrade from $< 1\,\Omega$ to many $k\Omega$ over the course of 24 hours. For this reason, four gold contact pads were sputtered across the width of each sample in a longitudinal configuration. Silver paint contacts subsequently applied on top of the gold were found to be low ohmic and highly stable over many days. The contact sizes are relatively large when compared with the size of each sample. It is estimated that the error in the absolute magnitude of the determined resistivities of the samples is of the order of $\sim 40\,\%$. The relative change in the resistivity as it evolves with pressure is substantially smaller.

The decision was made to use piston cylinder cells to maximise the number of samples that could be measured at the expense of limiting the maximum achievable pressure. It was possible to simultaneously mount three samples in a single pressure cell. As described in 3.3.1, samples were mounted side by side on a feed-through such that $H \parallel I \parallel ab$. Daphne 7373 was used as a pressure transmitting medium whilst a coil of Manganin was used as a pressure gauge.

As previously stated, measurements in field were all performed with $H \parallel I \parallel ab$. The primary measurement was of $\rho_{ab}(H = 35\ \mathrm{T}, T)$. Due to the large thermal mass of a pressure cell, sweeping temperature is typically performed very slowly in order to minimise the temperature difference between the thermometer which is located on the outside the pressure cell and the sample which is located inside the cell. Measurements at 35 T, however, can not be performed over such long periods of time due to the capacity of the cooling installation and the total number of magnet-hours that a project is assigned. For this reason, magnetic field sweeps were performed at fixed temperatures. Before each sweep was commenced, the stability of the temperature of both the sample and thermometer can be explicitly checked. The $\rho_{ab}(H = 35\ \mathrm{T}, \mathrm{T})$ measured as the temperature is swept at 35 T can be checked against the values of $\rho_{ab}(H = 35\ \mathrm{T})$ during these well thermalised field-sweeps. Temperature sweeps were performed down to 2.2 K, the temperature at which ^4He becomes superfluid. At the transition, an unavoidable artefact is introduced into the data.

6.2.2 Thermometer Calibration

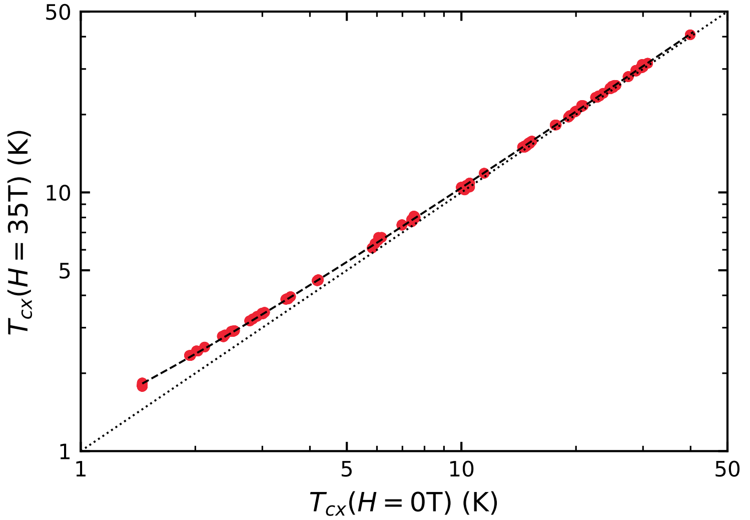

Figure 6.6: The incorrectly inferred temperature of the Cernox thermometer at 35 T against the correctly calibrated temperature measured at 0 T. The temperature dependence of the high-field resistivity of the FeSe$_{1-x}$S$_x$ crystals measured in this chapter was corrected using the calibration curve (dashed line). The dotted line indicates $T_{cx}(H = 35\text{ T}) = T_{cx}(H = 0\text{ T})$.

Whilst at fixed temperatures, it is unnecessary for the thermometer to be calibrated in field so long as the regulation of temperature is sufficiently stable. If the temperature is varied in the presence of a constant magnetic field, it is clearly necessary for the thermometer to be calibrated in field. The principle measurement in this chapter is of the temperature dependence of the in-plane MR at 35 T. Thus, calibration of the thermometer was essential.

The resistance of the Cernox resistance thermometer used to determine the temperature of the pressure cell is highly field dependent. In order to obtain a calibration curve, the resistance (and inferred temperature) of the Cernox thermometer (T_{cx}) at both 0 T and 35 T was recorded for each and every field-sweep that was performed throughout the experiment. The accuracy of each data point is then limited by the stability of the temperature throughout each field sweep. The magnitude of temperature drift can be evaluated by checking for discrepancies between the zero-field values of both the sample and thermometer resistances at the start and end of each field sweep. The affect of any random drift that occurred during a sweep is at least partially mitigated by the number of sweeps performed.

A curve mapping the incorrectly determined temperature at 35 T to the true temperature was found from a fit to data points obtained from all of the field sweeps that were performed throughout the experiment. The data (red points) and calibration curve (dashed line) are presented in Figure

6.6. This calibration curve was used to correct the measured temperature during temperature sweeps performed at 35 T. At the, lowest temperatures, the correction is as large as $\sim 30\%$ whilst it is only $\sim 1\%$ at 30 K.

6.3 Results

6.3.1 The Structural Transition at T_s

The zero-field resistivity of each sample is presented in Figure 6.7 at each pressure. An offset has been applied between subsequent increases in pressure for visual clarity. At each pressure, all of the samples show metallic behaviour at high temperatures and become superconducting below T_c. The distinctive plateau-like anomaly at T_s that is associated with the structural (tetragonal-to-orthorhombic) transition is visible in each sample at ambient pressure. With increasing pressure, T_s is visibly suppressed for all dopings. It should noted at this point that no distinction is being made here between the phononic structural transition and the electronic nematic transition. The breadth of the anomaly is wider any separation in temperature between the two transitions. The two transitions are considered to occur at the same temperature (T_s).

The evolution of T_s is more clearly seen in the derivatives of the resistivities presented in Figure 6.8. The anomaly at T_s manifests itself as a trough in $d\rho/dT$. For each sample and at each pressure, the local minimum of the anomaly (marked by an arrow in Figure 6.8) has been chosen to determine T_s. Of course, it is not possible to determine whether T_s has been completely suppressed or remains finite but is such that $T_s < T_c$. Temperature sweeps performed in the presence of a magnetic field suppressing superconductivity could allow T_s to be tracked to temperatures below T_c. This is discussed later. Similarly, the abrupt drop in the resistivity at T_c manifests itself as a sharp increase in $d\rho/dT$. As $d\rho/dT$ is positive for $T > T_c$ (ρ is metallic), a local minimum can always be found above T_c. For $x = 0.10$ at $P = 1.00$ GPa, it is apparent that the normal state resistivity features an anomaly that is highly reminiscent of that which is associated with T_s and that which is seen at higher temperatures for $P < 1$ GPa in the same sample. However, the location of the minimum is inevitably affected by the upturn in the derivative that is caused by superconductivity. This is also true for $x = 0.13$ at 1.15 GPa.

Surprisingly, it was found that $T_s(x)$ does not evolve monotonically. The apparent outlier $T_s(x = 0.08)$ is, however, highly consistent with the value found elsewhere at this doping [128]. This doping was not one which was measured by Licciardello. All other dopings have ambient pressure resistivities

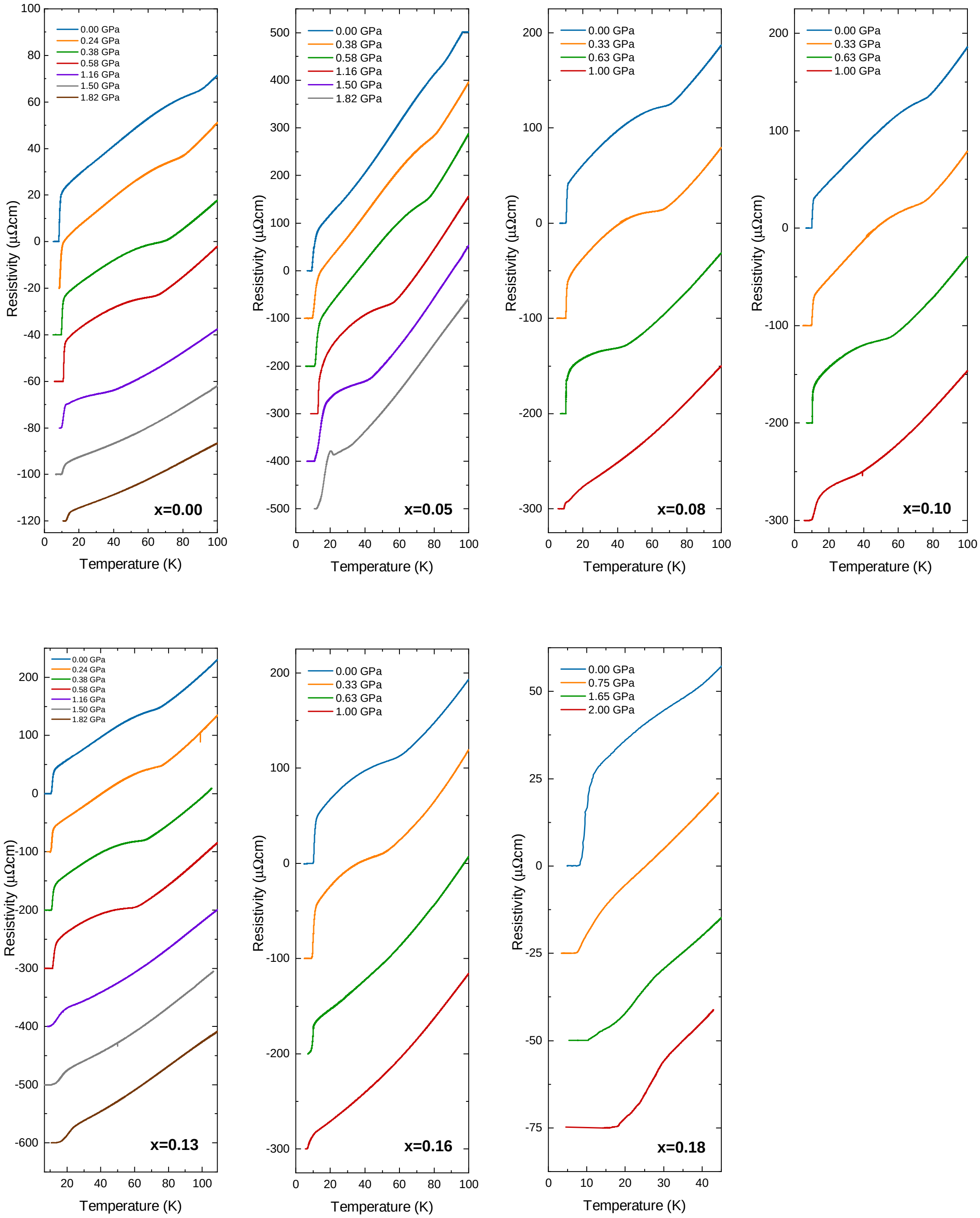

Figure 6.7: The evolution of the temperature dependence of the resistivity of all measured samples with increasing hydrostatic pressure. A clear step-like anomaly associated with the nematic phase transition can be seen to be suppressed with increasing hydrostatic pressure in each sample. For clarity, an offset has been applied with each subsequent increase in pressure of a size indicated by the major ticks of each panel.

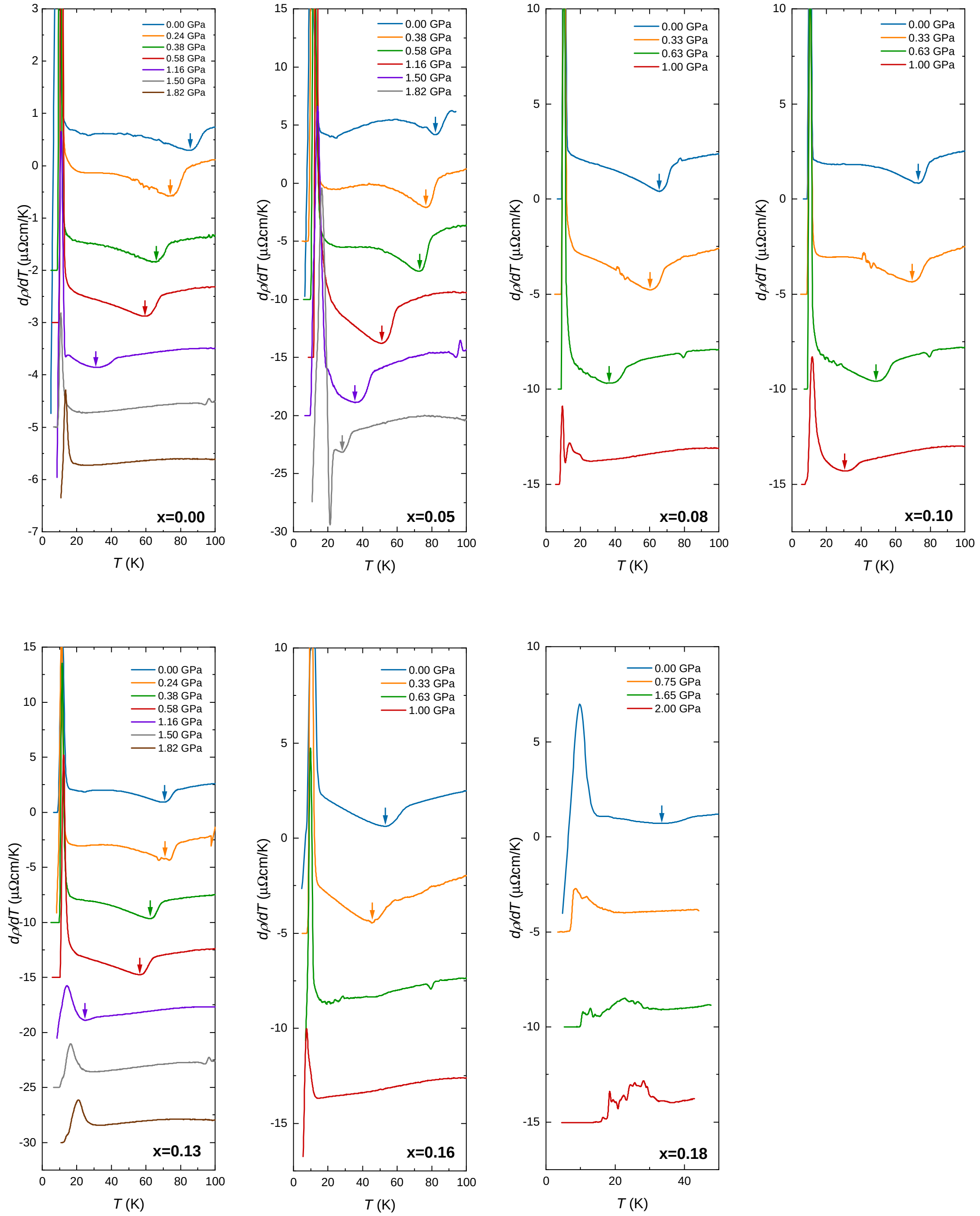

Figure 6.8: The derivatives of the temperature dependence of the resistivity of all measured samples with increasing hydrostatic pressure. The nematic transition temperature, T_s (indicated by arrows), was taken to be the local minimum of the nematic anomaly in each case. An offset has been applied with each subsequent increase in pressure of a size indicated by the major ticks of each panel for clarity.

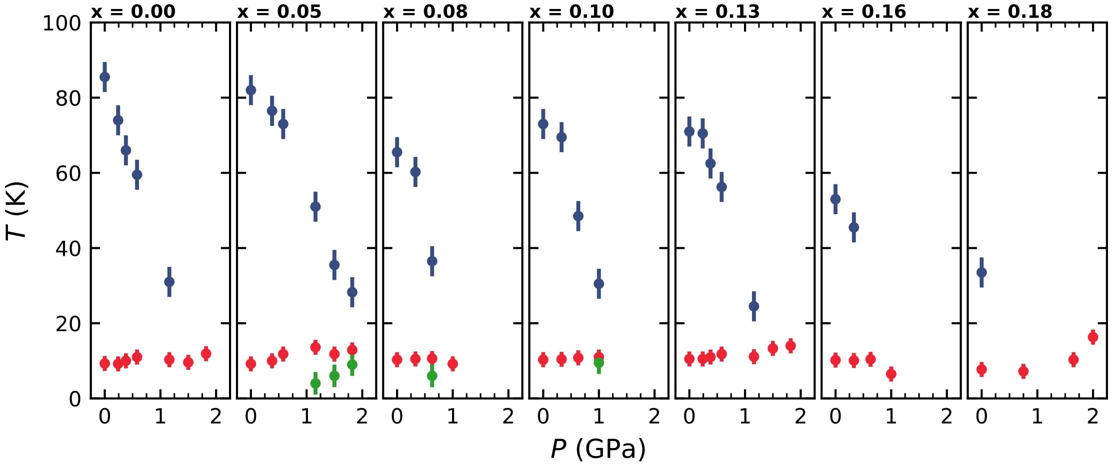

Figure 6.9: The evolution of the structural (and nematic) transition at T_s (blue) and the superconducting transition at T_c (red) with pressure for the seven samples of FeSe$_{1-x}$S$_x$ measured in this work. Also marked are the estimated onset temperatures of a magnetic phases (green) discussed in detail later.

that are highly consistent with those found by Licciardello [19]. It should be noted that although anomalies reminiscent of that at T_s at low values of x were found at $x = 0.16$ and $x = 0.18$, the authors of [19] interpreted the change of the form of the anomaly from one that appears highly asymmetric (in $d\rho/dT$) to one that is more symmetric as evidence that the structural transition had been completely suppressed at $x = 0.16$. In this work, the minimum in the anomaly at $x = 0.16$ was found to be asymmetric, hence this was taken as the value of T_s. An abrupt change from an asymmetric to symmetric anomaly at $x = 0.16$ was not observed. The presence of a minimum in the derivative at $x = 0.18$ indicates that nematicity has not been fully suppressed at this doping.

The variation in T_s and the non-monotonic behaviour of its evolution with x could imply that there is a substantial degree of random variation between the sulphur concentration of samples from the same growth. Alternatively, the nematic transition in the $x = 0.08$ sample could have been suppressed via some other sample-dependent parameter. Disorder is one possible factor, though it is noted that there is no clear increase in the absolute value of ρ_0 compared with $x = 0.05$ and $x = 0.10$ that might support this view.

T_s is suppressed in all samples with increasing pressure (Figure 6.9). The anomaly in the derivative is shifted to lower temperatures (Figure 6.8). In the simplest case, one would expect that P_c, the pressure at which T_s is suppressed to $T = 0$ K, should be proportional to, or at least decrease monotonically with, $T_s(P = 0\text{GPa})$. This is not found to be the case. At $x = 0.00$, for example, the nematic anomaly is not visible at $P = 1.50$ GPa, a pressure at which a feature is clearly seen at $x = 0.05$. In fact, the nematic anomaly was not completely suppressed at $x = 0.05$ at $P = 1.82$

GPa, the highest pressure applied at this doping. Similarly, an anomaly is seen for $x = 0.10$ at 1.00 GPa whilst an anomaly is not seen for $x = 0.08$ at 1.00 GPa. Although this would imply that P_c, is not a monotonic function of x, this is reflective of the lower value of $T_s(P = 0\text{GPa})$ at $x = 0.08$.

6.3.2 In-Plane Magnetoresistance ($\rho_{ab}(H)$)

The field dependence of the resistivity at fixed temperature is presented for three representative samples at four representative pressures in Figure 6.10. The three chosen samples ($x = 0.00, 0.05, 0.13$) were measured at the same time (side-by-side in the same pressure cell). At ambient pressure, the qualitative features of $\rho(H, T)$ are the same at all three dopings. All show a small but slightly metallic (positive) magnetoresistance at high temperatures. At low temperatures, superconducting fluctuations emerge at ~ 10 K for $x = 0.00$, a temperature at which the superconducting transition is complete at $x = 0.13$. The superconducting transition widths in field are comparably sharp at all three dopings. The evolution of $\rho(H, T)$ with hydrostatic pressure is different in all three cases.

At $x = 0.00$, there is a clear suppression of $\rho(H, T)$ with increasing hydrostatic pressure. It is difficult to determine ρ_0, but $\rho(T = 25\text{K})$ is reduced by a factor of ~ 5 between 0 GPa and 1.82 GPa. A factor ~ 2 reduction of ρ_c has been observed in FeSe at 25 K over a comparable pressure range in another study [130]. Intriguingly, however, a substantial upturn in the zero-field resistivity below 25 K was also observed at pressures greater than ~ 1 GPa in the same study. This upturn was later attributed to magnetic order emerging at ~ 1 GPa [134]. This finding is corroborated in a study of the specific heat under hydrostatic pressure [133] in which an anomaly associated with the magnetic transition was found to increase from 13 K at 0.9 GPa to 20 K at 1.5 GPa. At higher pressures, it decreased and subsequently increased again indicating the presence of two domes of magnetic order.

In contrast with $x = 0.00$, a minor enhancement of $\rho(H, T)$ is seen up to 1.16 GPa at $x = 0.05$. There is a clear enhancement of T_c, but the qualitative features of $\rho(H, T)$ remain mostly unchanged. The behaviour at 1.82 GPa is markedly different. The magnitude of $\rho(H, T = 25\text{K})$ is suppressed, the normal state field-dependence of $\rho(H, T = 20\text{K}))$ is negative at high fields and either $\rho(H)$ has become strongly field-dependent (strongly positive) or the width of the superconducting transition has dramatically increased at low temperatures. At 15 K, for example, it is difficult to establish whether superconductivity has been suppressed at the highest fields (and $H_{c2} > 35$ T) or whether the normal state response has changed dramatically such that $d\rho/dH$ is strongly positive. Between $P = 1.16$ GPa and $P = 1.82$ GPa, there is minimal change in T_c and $H_{irr}(T = 10\text{K})$ has in fact

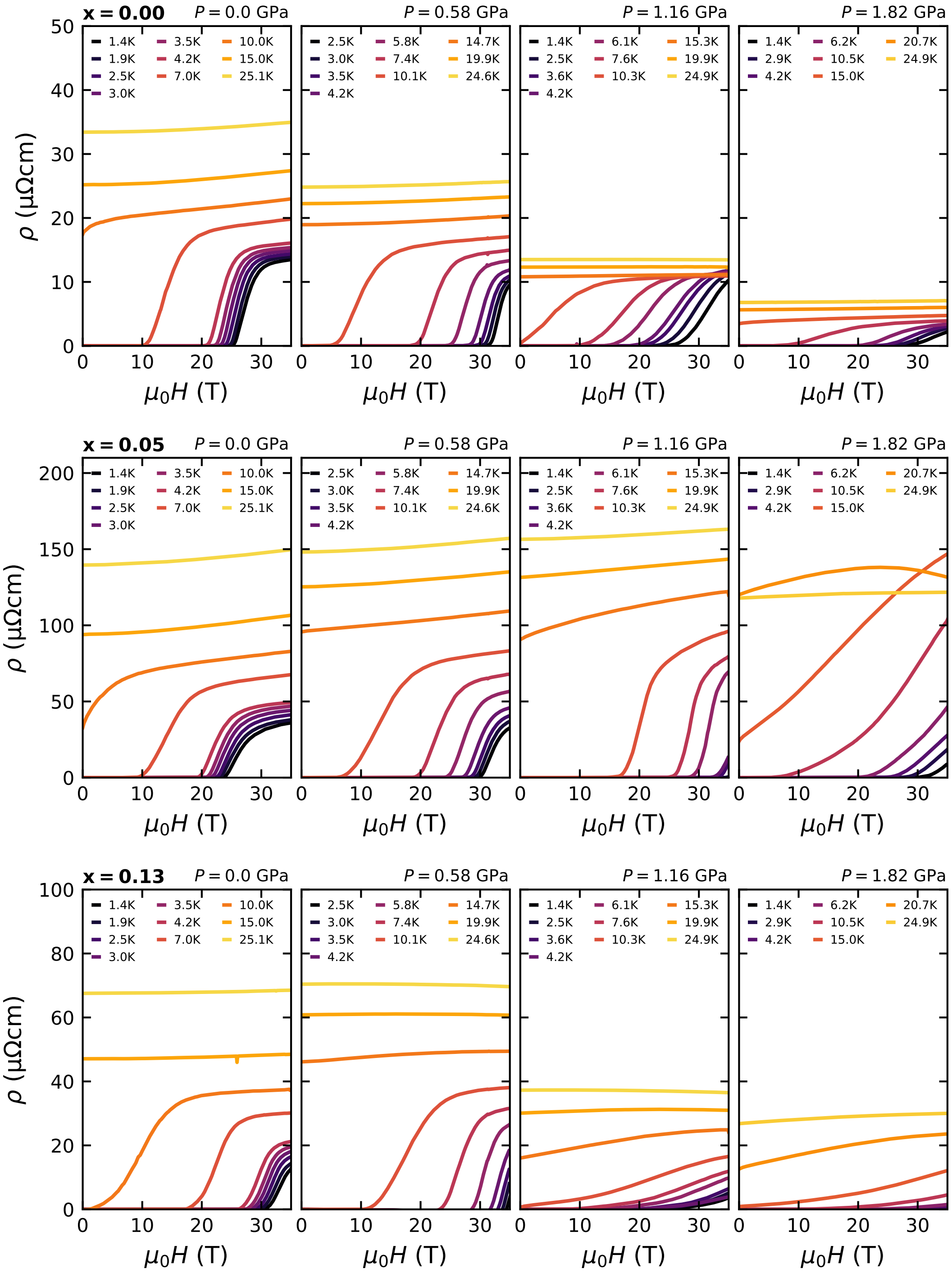

Figure 6.10: The evolution of $\rho(H, T)$ with pressure for three of the seven samples of $FeSe_{1-x}S_x$ that were measured in this thesis. Only a representative subset of the samples and pressures are shown.

decreased by a factor of ~ 2 between 1.16 and 1.82 GPa. It would therefore be surprising if H_{c2} has increased such that superconducting fluctuations persist so strongly at 35 T at the same temperature. The zero field resistivity shows an upturn just above T_c that is reminiscent of that which has been observed in $\rho_c(T)$ in FeSe at elevated pressures. In [134], a dome of magnetism was claimed to exist in the $T-P$ plane at $x = 0.043$, a doping similar to that which is being discussed here. There, however, the resistive signature of magnetic order was measured (in ρ_c) over a range of pressures between 0.6 and 1.3 GPa. It should be noted that from the evolution of T_s with pressure (Figure 6.8), P_c is found to be greater than 1.82 GPa at $x = 0.05$. Thus, the anomalous features in $\rho(H,T)$ at 1.82 GPa can not easily be ascribed to a suppression of nematic order.

A similar but less dramatic suppression of $\rho(H,T)$ with pressure is seen at $x = 0.13$ than in FeSe. Again, similarly to $x = 0.00$ and unlike $x = 0.05$, the qualitative features of $\rho(H,T)$ remain largely unchanged with increasing pressure. As with $x = 0.05$, however, the apparent width of the superconducting transition in field has dramatically increased at elevated pressures. This is somewhat reflected in the width of the transition in temperature seen in Figure 6.7.

6.3.3 The High Field Resistivity ($\rho_{ab}(T, H = 35\mathrm{T})$)

The evolution of the temperature dependence of the resistivity at 35 T with hydrostatic pressure is presented for each sample in Figure 6.11. The solid lines are $\rho(H = 35\mathrm{T}, T)$ measured as the temperature was continuously swept at high field. The temperature has been corrected for the magnetoresistance of the thermometer using the calibration curve in Figure 6.6. The solid points are $\rho(H = 35\mathrm{T}, T)$ determined from field sweeps measured at fixed temperatures. As expected if the temperature has been corrected for appropriately, the temperature sweeps pass through the points measured at fixed temperatures. Where they do not ($x = 0.18$ and $P = 0.75$ GPa, for example), the points obtained from field-sweeps performed at fixed temperature should be considered to be the more reliable of the two determinations of $\rho(H = 35\mathrm{T}, T)$.

Similarly, the dashed lines in Figure 6.11 show the evolution of the zero-field temperature dependence of the resistivity with pressure for each sample. Again, the open points show the zero-field resistivity determined from the sample field-sweeps performed at fixed temperatures. Unfortunately, there are some large discrepancies between $\rho(H = 0\mathrm{T}, T)$ determined via the two methods. The high field resistivity was always measured in a more optimal experimental configuration that minimised the possibility of temperature gradients being generated across the pressure cell. This same configuration could not always be used for the equivalent zero-field measurement due to the time

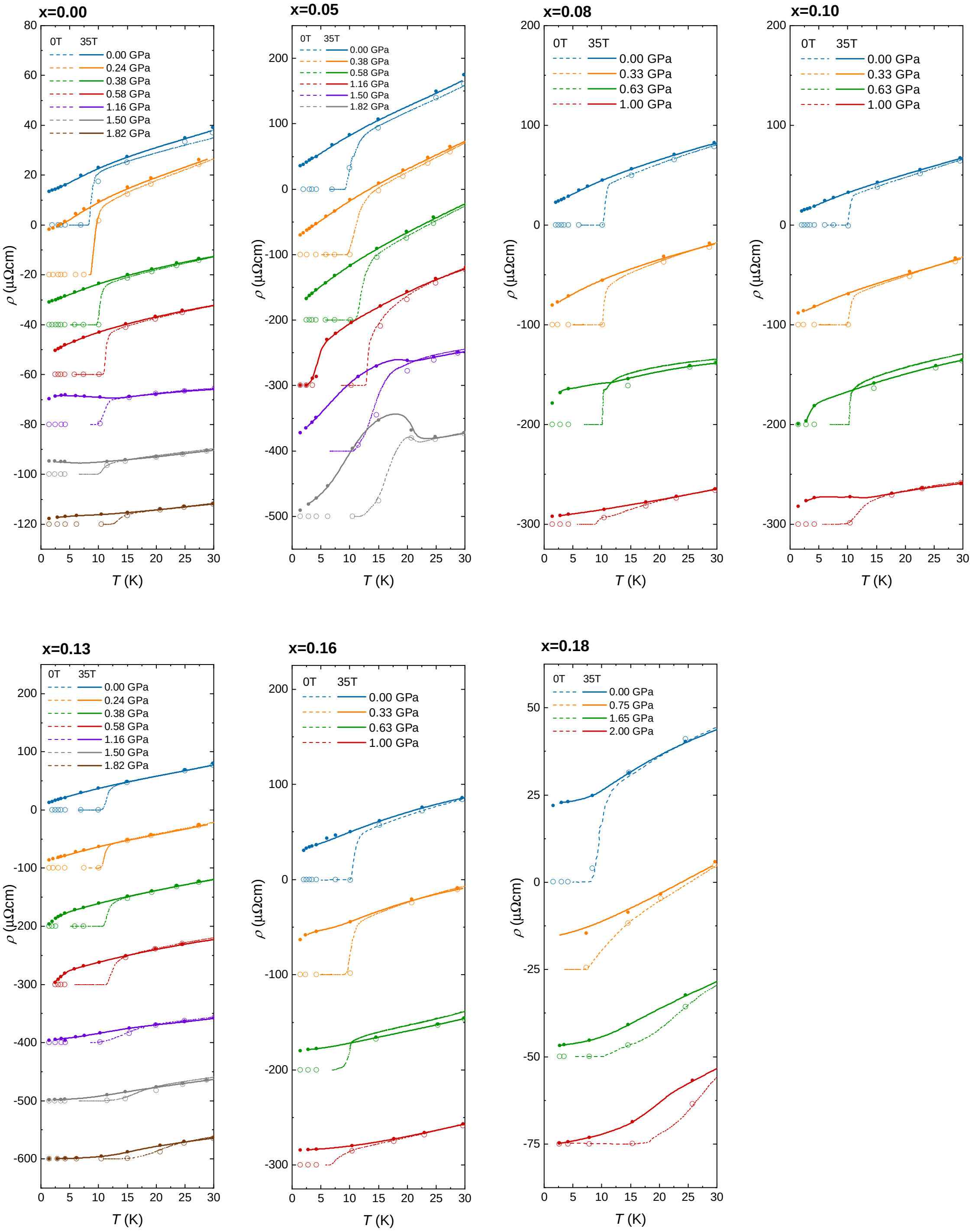

Figure 6.11: The evolution of both the zero-field resistivity (dashed lines) and the resistivity at 35 T (solid lines) of each sample with increasing hydrostatic pressure. The open points are the zero-field resistivities obtained during field sweeps performed at stabilised fixed temperatures whilst the solid points are high-field values. For clarity, an offset has been applied with each subsequent increase in pressure of a size indicated by the major ticks of each panel.

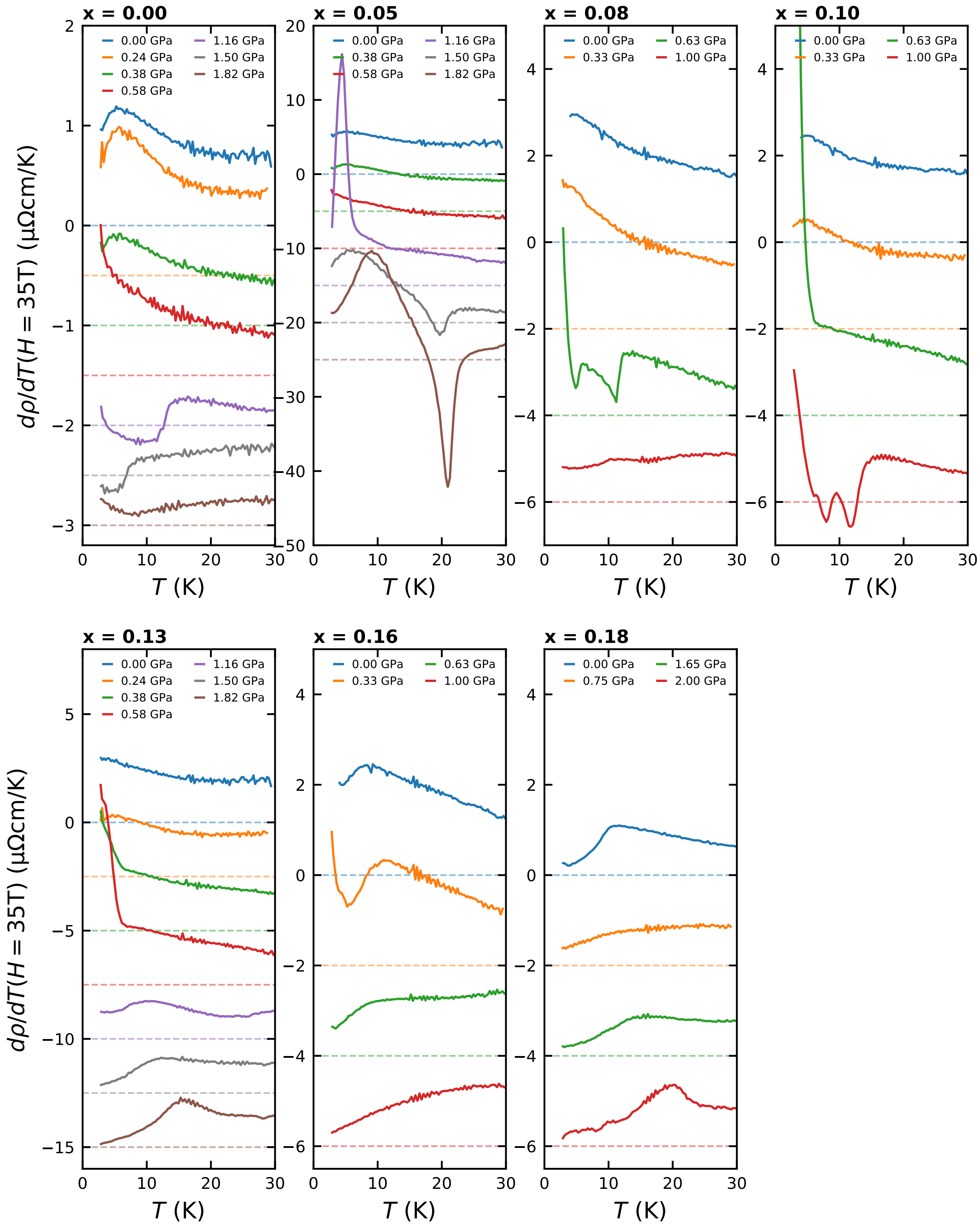

Figure 6.12: The evolution of the derivative of the high-field (35 T) resistivity of each sample with increasing hydrostatic pressure. For clarity, an offset has been applied with each subsequent increase in pressure. The coloured horizontal dashed lines denote the zero value for each pressure.

constraints and the necessity of manual intervention during the measurement. The temperature dependence was obtained by simply leaving the pressure cell to slowly warm over night in some cases with mixed results. The points determined from field-sweeps at fixed temperature should again be considered the more reliable of the two determinations of the zero field resistivity.

It is clear that at temperatures above T_c, there is little magnetoresistance for most of the pressure-doping phase space covered in this work. This is evidenced by the strong overlap of the zero-field and high-field resistivities in Figure 6.11 and the field-independence of $\rho(H)$ in Figure 6.10. At ambient pressure, $\rho(H = 35\mathrm{T}, T)$ remains metallic and is reminiscent of that reported in [19]

The evolution of derivatives of the high-field resistivity of each sample with hydrostatic pressure in presented in Figure 6.12. Offsets of the size of the major tick of each panel has been applied between each subsequent pressure. Signatures of magnetism manifest themselves more clearly in $d\rho/dT(T)$ than they do in $\rho(T)$ itself. Power law behaviour (quadraticity and/or linearity) in the normal state resistivity is also more clearly revealed in $d\rho/dT(T)$

6.4 Discussion

6.4.1 Signatures of Magnetism

In the absence of a magnetic field, there are only minor signatures in $\rho(T)$ of the magnetic order than have been reported in regions of pressure-doping phase space [119, 125, 128, 130, 133, 134]. With the application of 35 T and the consequent suppression of superconductivity, these signatures become far more apparent. In this section, the form, pressure range, and pressure dependence of the various signatures in the high-field resistivity (and $d\rho/dH$) and their broader implications with regard to the observation of nematic criticality will be discussed.

The resistive measurements reported in this work and [130, 134] are unable to ascribe features in $\rho(H, T)$ to magnetism directly. However, the authors of the authors of [130, 134] note a consistency with μSR measurements (a more direct probe of magnetism) performed under pressure [125] which claim to observe antiferromagnetism as a function of temperature and pressure. The similarity between the form of the resistive anomalies observed in [130, 134] and those observed in this work is the only evidence that the resistive features are in fact magnetic in origin.

x = 0.05

The doping at which these magnetic signatures are most apparent is $x = 0.05$. The small upturn observed in $\rho(H = 0\mathrm{T}, T)$ at 1.82 GPa (Figure 6.7) is substantially enhanced at 35 T (Figure 6.11). A similar feature can be seen in $\rho(H = 35\mathrm{T}, T)$ at 1.50 GPa with a decreased size. These anomalies are also highly apparent in $d\rho/dT(H = 35\mathrm{T}, T)$ (Figure 6.12).

It is clear from the high-field derivatives that the anomaly has similar structure at both 1.50 and 1.82 GPa. With decreasing temperature, there is a strong minimum followed by a shallow plateau and a strong maximum. All of these discernible sub-features of the anomaly occur at a higher temperature at 1.82 GPa than at 1.50 GPa. The position of the local maximum in $d\rho/dT(H = 35T)$ is marked by green points in Figure 6.9. Both the increasing temperature at which the anomaly occurs and its increasing size with increasing pressure would suggest that this is the same magnetic order reported by Matsuura [128] (and shown in the phase diagram in Figure 6.5) albeit at a lower temperature than at $x = 0.04$ (the closest doping to $x = 0.05$ that was measured in that study). This pressure dependence is opposite to the additional dome of magnetic order that has been reported to reside entirely within the nematic phase [134]. This secondary dome of magnetism emerges at $\sim$ 0.7 GPa and is entirely suppressed at $\sim$ 1.2 GPa. No signatures of this magnetic order are observed here.

In [128], the strong minimum in the derivative was found at $\sim$ 35 K at 2 GPa. There is little indication in this work that it will increase by 15 K from 20 K with the application of an additional 0.2 GPa. $T_c(P = 2\mathrm{GPa})$ (defined by $R = 0$) was found to be greater than 20 K in the aforementioned study whereas T_c is determined to be $\sim$ 12 K in this work. As with the magnetic feature, it is unlikely that the superconductivity will be enhanced to such a degree in the sample ($x = 0.05$) measured in this work at 2 GPa.

It is therefore curious that the anomaly occurs at a temperature marginally above T_c in both cases. In a scenario in which superconductivity and magnetic order compete, one would expect that the anomaly would occur at a higher temperature in the $x = 0.05$ sample measured in this work than the $x = 0.04$ sample in [128]. It could be concluded that superconductivity stabilises the magnetic order such that it the resistive anomaly always appears near to T_c. This is, however, hard to reconcile with the large differences between T_c and T_m reported in [128] and the local suppression of T_c at the pressure at which T_m is maximal at higher values of x (illustrated in Figure 6.5).

Although they are less prominent than the aforementioned features in $x = 0.05$ at $P > 1.5$ GPa, similar features are present at other sulphur concentrations. Minor kinks in the high-field resistivity that manifest themselves as local minima in their derivatives can be seen at $x = 0.00$ for $P = 1.16$, 1.50 GPa, $x = 0.08$ at 0.63 GPa and $x = 0.10$ at 1.00 GPa.

$\mathbf{x = 0.08,\ x = 0.10,\ x = 0.18}$

At both $x = 0.08$ and $x = 0.10$, similar features in the derivative of the high-field resistivity can be seen. As with $x = 0.05$, the temperatures of local maxima in $d\rho/dT(H = 35T)$ are marked in Figure 6.9. In the former, an anomaly emerges at 0.6 GPa whilst it emerges at 1.0 GPa in the latter. It is unclear whether the anomaly is present at 1.0 GPa in the $x = 0.08$ sample. There is irregular variation in the derivative that is not present, for example, at $x = 0.16$ at the same pressure which was simultaneously measured.

The progression of the anomaly in the resistivity to lower pressures is consistent with the anomaly being caused by the dome of magnetic order that resides within the nematic phase that is reported in [134]. However, this would imply that the resistive signature of this magnetic transition *is* visible in the in-plane resistivity. This begs the question why signatures of this magnetic dome are not seen at $x = 0.00$ (discussed later) and at $x = 0.05$.

At $x = 0.18$ a similar anomaly is seen at 0.0 GPa. There have been no reports of magnetic order at ambient pressure. The presence of an anomaly in this work is therefore likely the result of the nematic transition. The suggestion is then that the nematic transition has been suppressed from 30 K at 0 T to $<$ 10 K at 35 T. This is not a conclusion for which there is corroborating evidence, however.

$\mathbf{x = 0.00}$

The anomalies in the derivatives of the high-field resistivity in FeSe ($x = 0.00$) at 1.16 and 1.50 GPa (Figure 6.12 are distinct from the others in their appearance. They only manifest themselves as relatively broad minima. This is in contrast with the highly-structured form of the magnetic anomaly reported in ρ_c [130]. They are, in fact highly reminiscent of the structural anomaly associated with the structural transition. The pressure dependence is consistent with this conclusion. One would expect that the anomaly would be shifted to higher temperatures with increasing pressure if it were of a magnetic origin. One would again have to conclude, however, that the structural transition (or at least its resistive signature) is magnetic field dependent, a conclusion for which there is no corroborating experimental evidence.

Magnetic Order Inside the Nematic Phase

It is curious that the strong feature that has been reported to be associated with magnetic order in ρ_c in FeSe [130] is not seen here. Similarly, the magnetic anomalies seen in this work at $x = 0.05$ were observed over a pressure range and have a pressure dependence that is consistent with the magnetic phase reported by Matsuura [128] and are inconsistent with the secondary dome of magnetism that is reported to reside entirely within the nematic phase [134].

Both reports of a secondary dome of magnetism at low pressures were in studies of ρ_c. It is possible that there are intrinsic differences between the samples measured in this work and those measured in the aforementioned studies. Alternatively it is possible that the resistive signature is only observed in ρ_c and not in ρ_{ab}. The authors of [134] acknowledge this possibility. In the same study, no magnetic anomaly was found in ρ_{ab} in a sample with $x = 0.12$. The counter experiment, measurement of ρ_c at $x = 0.12$, was not performed. It was therefore difficult for the authors to conclude whether the secondary dome of magnetism has in fact been suppressed at $x = 0.12$ or whether a measurement of ρ_{ab} is simply insensitive to it. Similarly, the aforementioned study was performed with $H \parallel c$ whilst the field was always applied $H \parallel ab$ in this work. How this affects the underlying magnetic order and its manifestation as an anomaly in the measured resistivity remains unclear.

A definitive conclusion would require a systematic study of ρ_{ab} and ρ_c with field applied both $H \parallel c$ and $H \parallel ab$ in samples than can be ensured to be highly comparable (from the same growth, for example). The implications are perhaps highly significant. If signatures of quantum criticality are to be unambiguously attributed to nematicity, it is clearly important to be able to ascertain with certainty which regions of pressure-doping and field-temperature phase space are populated by magnetic order. The seminal study of pressure-doping-temperature phase space [128] from which the phase diagram in Figure 6.5 was taken was of ρ_{ab}, a quantity that could be insensitive to additional magnetic phases. Whether this additional magnetic phase influences the T or T^2 behaviour of the in-plane resistivity despite leaving no clear anomaly at the transition is unknown.

6.4.2 Crossover from T^2 to T Behaviour

The crossover from T-linear behaviour at high temperatures to T^2 behaviour at low temperatures that was observed by Licciardello [19] at ambient pressure is not so clearly observed in this work. For direct comparison, the derivatives of the high-field resistivity from the previous study by Licciardello are presented in Figure 6.13. In that work, two temperature, T_1 and T_2, were used to quantify the crossover from T^2 behaviour at low temperature to T-linear behaviour at high temperature. T_1 was defined as the temperature down to which a linear-in-T resistivity was observed whilst T_2 was defined as the temperature up to which a quadratic-in-T resistivity was observed. These temperatures and are labelled on the derivatives in Figure 6.13.

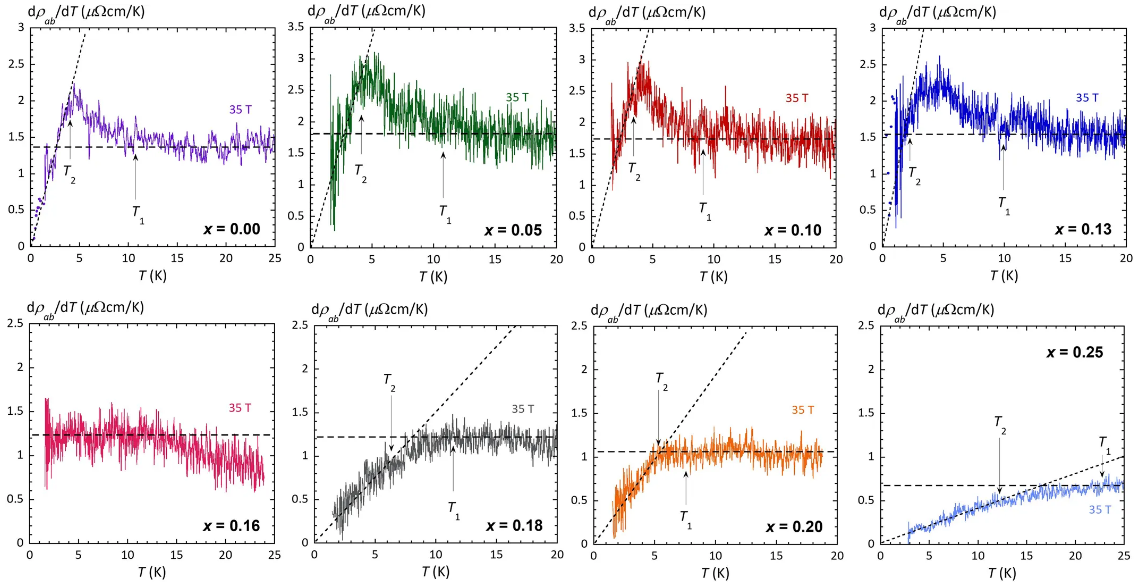

Figure 6.13: The derivatives of the high-field resistivity of $\mathrm{FeSe}_{1-x}\mathrm{S}_x$ for a range of sulphur concentrations from [19]. The samples for which data is presented in this thesis are from the same growths as those from which samples were taken in [19].

The determination of T_1 and T_2 is somewhat more difficult to make in this work even at ambient pressure. At the majority of sulphur concentrations measured in this thesis, insufficiently low temperatures could be reached to see an extended region of T^2 behaviour at low temperatures. Secondly, the extended regions of T-linearity at high temperature are simply not observed in most cases. Both of these issues become increasingly restrictive at elevated pressures. The enhancement of T_c restricts the accessible normal state behaviour to higher temperatures and the region of T-linearity at high temperatures gives way to sublinearity. In some cases, T^2 behaviour is observed with a negative coefficient.

In Figure 6.14, the evolution of T_1 is shown in three samples ($x = 0.00$, 0.05 and 0.13) over the range of pressures for which it remains possible to determine T_1. The derivatives have been normalised to their respective values at 30 K and have been plotted with an offset for clarity. In each case, the highest pressure presented is the first at which T_1 is shifted above the measured temperature range. At ambient pressure, T_1, as defined by Licciardello [19], is suppressed with increasing x in much the same way as was found previously. In stark contrast, despite the fact that nematicity is suppressed with pressure in all three cases, T_1 increases with pressure. This is contrary to expectation if the decreasing temperature down to which a linear resistivity is observed at ambient pressure is a result of increasing proximity to the nematic QCP.

There are, however, systematic changes in behaviour that occur at P_c that support the conclusion that a linear-in-temperature resistivity persists down to lowest temperatures at P_c as it was observed to at x_c (at ambient pressure). Presented in Figure 6.15 are the derivatives of the high field resistivities of three samples at the pressure immediately below P_c (as inferred from the evolution of T_s with pressure at 0 T) and pressures above P_c. For clarity, an offset has been applied between each curve and the zero axis is given by the respective coloured dashed line in each case. The three samples chosen are those at sulphur concentrations for which H_{c2} remains sufficiently low that normal state behaviour is visible down to the lowest temperatures and for which signatures of magnetic order do not obfuscate the otherwise simple temperature dependence.

At $P < P_c$, there is a negative slope in the derivative in all three cases. In all three cases, the negative slope vanishes for $P > P_c$ and a linear-in-T resistivity is restored at the highest measured temperature (horizontal dashed black lines in Figure 6.15. Similarly, at low temperatures the derivative can be closely described by a $T + T^2$-dependence at lowest temperatures. The magnitude of the T-linear term at $T = 0$ appears to decrease with increasing pressure for $P > P_c$. For $x = 0.00$, at 1.82 GPa, the low temperature behaviour is strictly quadratic. Additionally, as is clearly seen at $x = 0.16$, the temperature range up to which quadraticity extends and the temperature down to which linearity extends is enhanced to higher temperatures as pressure in increased beyond P_c. These findings are somewhat more consistent with those of Licciardello shown in Figure 6.13. The qualitative behaviour at $x > x_c$ reported by Licciardello [19] is highly reminiscent of the behaviour reported in this work at $P > P_c$.

The presence of a finite T-linear term at $T = 0$ is difficult to definitively show at the temperatures and field range presented in this work. It is possible, for instance, that superconducting fluctuations (which manifest themselves as an increase in the derivative) are responsible for the finite intercepts at $T = 0$ in Figure 6.15. The presence of a large quadratic component is unambiguous.

The conclusion is that, upon suppression of nematicity with hydrostatic pressure, the high-field resistivity is linear down to lowest temperatures at P_c. At pressures greater than P_c, there is a progressive increase in the temperature up to which a quadratic resistivity persists at low temperatures in accordance with expectation the on approach to a QCP.

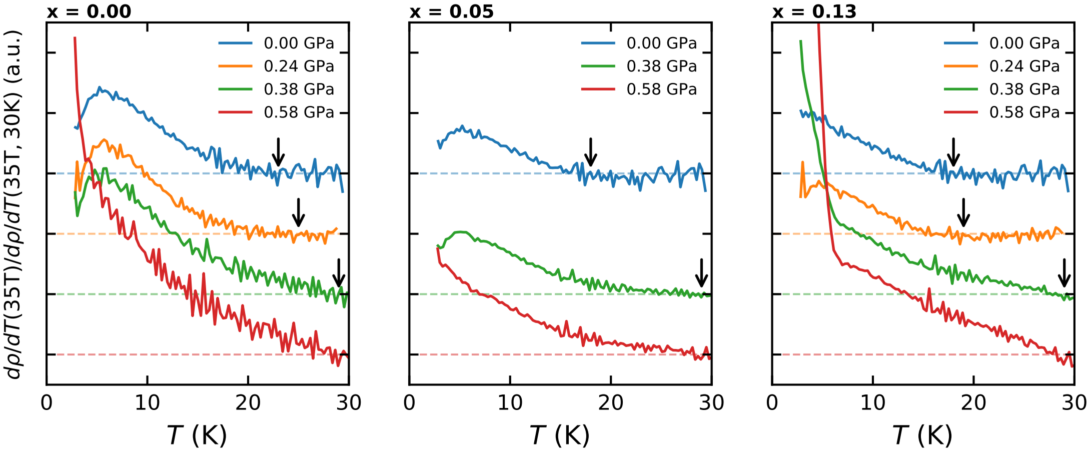

Figure 6.14: The derivative of the high field resistivity normalised to their respective values at 30 K of three selected samples ($x = 0.00$, 0.05 and 0.13). The evolution of T_1 (arrows), the temperature at which T-linear behaviour is lost with decreasing temperature, is shown.

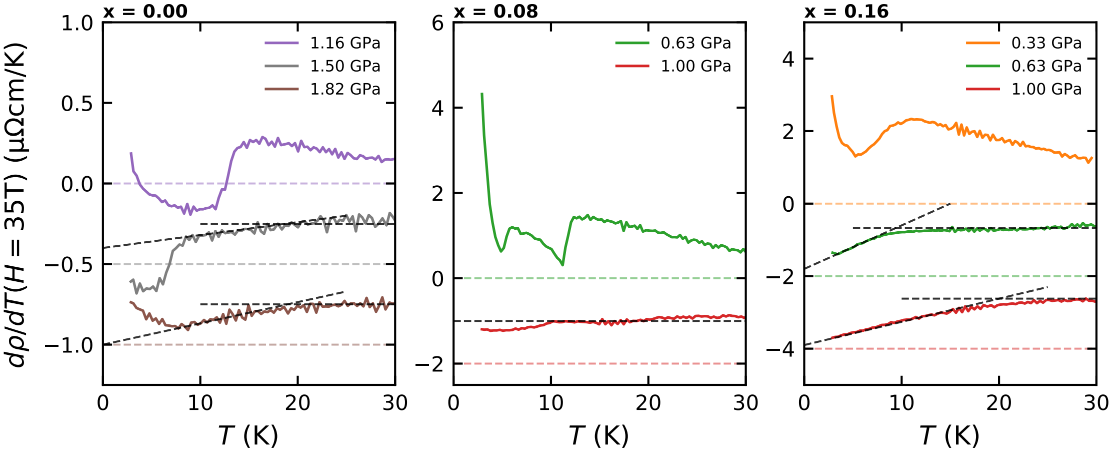

Figure 6.15: The derivative of the high-field resistivity for three samples ($x = 0.00$, 0.08 and 0.16). An offset has been applied between subsequent pressures for clarity. The zero for each curve is indicated by the coloured dashed lines. In each case, the first pressure presented is the last at which a signature of the nematic transition was observed at 0 T. For each pressure greater than the first, dashed lines have added to illustrate the return $\sim T^2$ behaviour at low temperatures and T-linear behaviour at high temperatures.

6.5 Outlook and Conclusions

In this chapter, a study of the in-plane resistivity has been presented over a wide range of sulphur concentrations in $FeSe_{1-x}S_x$. The original intent of the study was to determine whether similar signatures of quantum criticality that have been observed in the in-plane resistivity of $FeSe_{1-x}S_x$ as a function of x at the nematic QCP [19] at ambient pressure could also be observed as a function of hydrostatic pressure. Although qualitatively similar results have been found, a number of factors make an equivalent analysis somewhat difficult for $P < P_c$.

There appears to be only a very narrow range of dopings for which magnetic phases do not obscure the crossover between of T and T^2 behaviour (by introducing additional features to $\rho(H = 35\mathrm{T}, T)$) and for which the enhancement of H_{c2} with pressure is not sufficiently strong to limit access to the normal state down to the low temperatures required. Two such dopings are $x = 0.08$ and $x = 0.16$. For P close to P_c, a linear resistivity extends down to low temperatures. A linear resistivity was found at $x = 0.08$ and 1.0 GPa from 30K down to the lowest measured temperatures whilst at $x = 0.16$ and 0.63 GPa, a region of quadraticity was restored the at lowest temperatures. This low temperature region of quadratic behaviour extends to higher temperatures for $P > P_c$. These consistent with signatures of quantum critical behaviour at P_c. A repeat study of samples at these dopings is planned with the hope of revealing the quantum critical phenomena in finer detail.

Regarding magnetism in $FeSe_{1-x}S_x$, it is clear that the situation is somewhat more complex than is immediately apparent from the phase diagram in Figure 6.5. In FeSe, there is likely a single dome of magnetism [119, 130] that is detected in both ρ_{ab} and ρ_c with $H \parallel c$. At higher sulphur concentrations, it appears that this dome splits into two separate domes, one of which is observed at low pressures in ρ_c [130, 134] whilst the other is observable in ρ_c at higher pressures [119, 128] (with $H \parallel c$).

It is clear that the situation could be somewhat clarified by a systematic study of the in-plane and out-of-plane resistivity with a magnetic field oriented both $H \parallel ab$ and $H \parallel c$. It is important that samples from the same growth are used in each case to mitigate the influence of inter-sample variations. One could then at least ascertain which field and current configurations are sensitive to magnetic order over the pressure-doping phase diagram. A consistent picture could then be made with reference to previous studies in which a range of experimental configurations have been used. Further clarification could be sought using a more appropriate probe, perhaps one that is more intrinsically sensitive to magnetic order than charge transport. A systematic study of bulk magnetisation, for example, is likely to be illuminating.

Chapter 7

ZrSiS

Materials in which linear band dispersions give rise to massless fermions have become a topic of intense interest. Graphene is perhaps the archetypal example. ZrSiS is a nodal-line semimetal in which the only bands that cross the Fermi-energy are linearly dispersive and, thus, its properties are governed by Dirac quasiparticles alone. A quantum oscillation study of ZrSiS has been performed under hydrostatic pressures. The pressure dependence of the oscillatory frequencies and their associated effective masses have been analysed. Additionally, a number of highly anomalous features associated with magnetic breakdown have been revealed. The results and implications of the quantum oscillation study are presented and discussed in this chapter.

The preparation of as-grown crystals for magnetisation and transport measurements under pressure was performed by the author. All of the presented magnetisation (ambient pressure) and transport measurements (elevated pressure) and subsequent analysis was also performed by the author.

7.1 Background

7.1.1 Nodal-line semimetals

Metals can be defined as materials with a Fermi surface. That is, they are materials in which the chemical potential is crossed by electronic bands. On the contrary, insulators can be similarly defined as materials in which the chemical potential passes through a band gap. These scenarios are shown schematically in Figure 7.1A/B. An illustrative bandstructure of a semimetal is shown in 7.1C. The chemical potential is crossed by both a conduction and valence band by virtue of their overlap in energy. They are distinct from typical metals in that the density of states at the Fermi level is significantly smaller and both electrons and holes contribute to conduction.

Figure 7.1D shows the bandstructure of a Dirac semimetal, a material in which linearly dispersing bands cross at a point named the *nodal point*. Nodal-line semimetals (NLSMs) are similar to semimetals in that the Fermi energy is crossed by both a valence and conduction band. If these bands overlap in k-space (as is shown in 7.1E), a continuous line of nodal points can be defined. This continuous crossing is called a *nodal line* or *nodal loop*. It is possible for the bands that cross the chemical potential to form a nodal loop to be linearly dispersive. The Fermi surface is then defined by Dirac fermions in a material with a Fermi surface that is topologically distinct from that of a typical Dirac semimetal. ZrSiS is one such example.

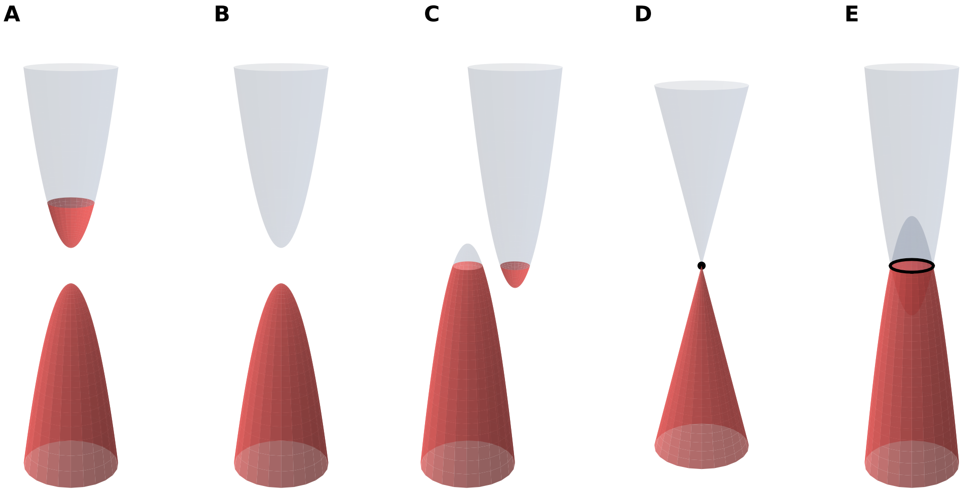

Figure 7.1: Schematic examples of two-dimensional bandstructures for metals (A), insulators (B), semimetals (C), Dirac semimetals (D) and nodal-line semimetals (E). Red and blue respectively denote occupied and unoccupied states in each case. The nodal point and nodal line in (D) and (E) are denoted by a black point and black line respectively.

7.1.2 ZrSiS

ZrSiS is a tetragonal quasi-two-dimensional material with PbFCl-type structure [135] (shown in Figure 7.2) and a member of the XSiY family of compounds where X = Zr, Hf and Y = S, Se, Te. In the *ab*-plane, buckled layers of Zr-S are found between flat, square sheets of Si. The crystallographic structure of the samples measured in this work was confirmed by x-ray diffraction (detailed later).

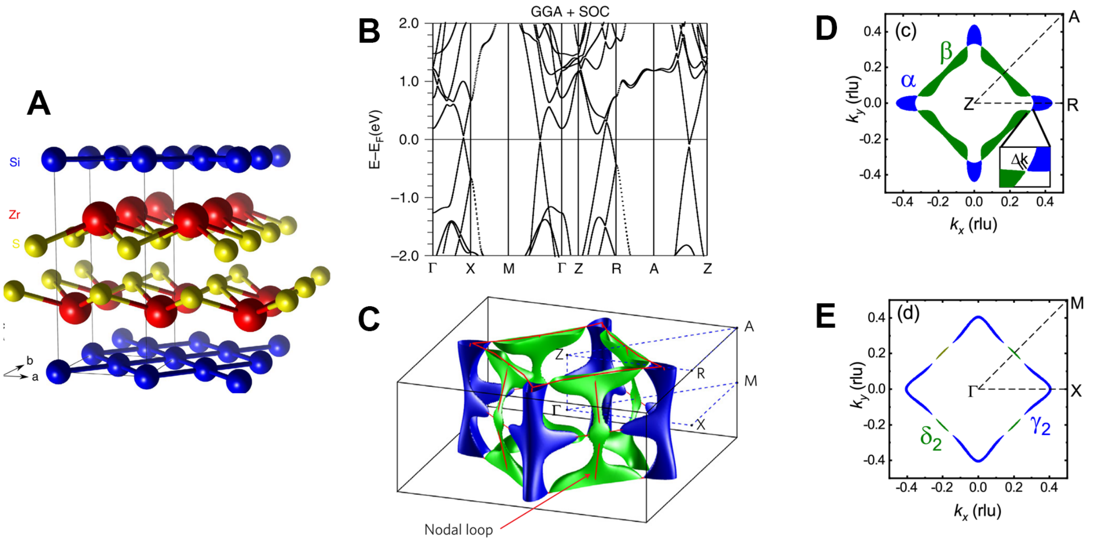

Figure 7.2: A: The crystallographic structure of ZrSiS (from [135]. B: The band structure of ZrSiS in which it can be seen that only linearly dispersive bands cross the Fermi energy (from [135]). C: The Fermi surface of ZrSiS (from [136]). The red lines denote the nodal lines. D/E: Cross-sectional slices of the Fermi surface in the ZRA (D) and ΓXM (E) planes (from [135]). Extremal orbits have been labelled using the same convention used throughout this thesis and elsewhere [135–137].

ZrSiS is an ideal example of a nodal line semimetal because the Fermi level is only crossed by the linearly dispersing nodal features in both the bulk and at the surface, a claim verified by ARPES experiments [135, 138, 139]. Additionally, the linear dispersion of the bands which cross the Fermi energy extends over an energy range as large as 2 eV above and below the Fermi level. The bandstructure is presented in Figure 7.2B whilst the resulting Fermi surface is shown in Figure 7.2C.

The study of ZrSiS with ARPES [135, 138, 139] and the measurement of quantum oscillations in particular [136, 138, 140] have revealed much about its band structure and Fermi surface. The majority of the extremal orbits that contribute frequencies to the quantum oscillation spectra reside in either the ΓXM or ZRA planes. Cross-sectional slices of the Fermi surface in both of these planes showing the principal extremal orbits and their naming convention (used elsewhere [135–137]) are presented in Figure 7.2D/E. Quantum oscillation studies have been found to be largely consistent with DFT calculations. However, due to proximity to the nodal line, many of the extremal orbits are very small and highly sensitive to small changes in E_F. Details of important discrepancies are discussed later.

Although it has been found that bandstructure calculations are in close agreement with experimental determination of the Fermi surface, there have been reports of correlation effects including tip-induced [141] and a field-enhanced effective mass [136]. This is possibly a consequence of the vanishing density of states resulting in a weakened screening of the Coulomb interaction [142], a feature of correlated electron systems more generally. With pressure, we hope to determine whether correlation effects can be enhanced, or whether addition correlation effects and exotic ordering can be generated. Signatures of such effects include an enhancement of the effective mass, for example. Equally, it might be possible to tune the system closer to the nodal line such that the quasiparticles residing at the Fermi energy are those that are topologically protected. Whether proximity to the nodal line inherently gives rise to correlation effects remains to be seen.

7.2 Experimental Details

7.2.1 Characterisation and Preparation

Two single crystal samples were sourced from the group of Leslie Schoop at Princeton University. They were grown by iodine vapour transport from stochiometric quantities of zirconium, silicon and sulphur. The details of the growth procedure can be found in Reference [137]. Samples from the same source and growth (referred to as growth 2 in Ref [137]) were analysed using both X-ray and electron diffraction as well as electron microscopy with the use of back-scattered detectors by M van Delft and co-workers [137]. They were able to confirm the crystallographic structure of the samples and did not detect any signs of inclusions.

In preparation for the transport measurements at high pressures, a magnetisation study was performed on one of the samples using a Quantum Design MPMS in magnetic fields up to 7 T. Unlike the case of SdH oscillations, magnetisation can be evaluated in absolute units. This is important because it is possible to obtain a direct estimate of the magnitude of magnetic-interaction effects which can result in the observation of additional oscillation frequencies that are reminiscent but distinct from those that are due to magnetic breakdown. This is discussed in more detail later. A small section the same crystal also underwent X-ray crystallographic analysis. The crystal structure was again confirmed.

Two samples were prepared for measurement of Shubnikov-de Haas oscillations at elevated pressures. Again, both samples were cut from the same aforementioned sample that underwent magnetisation and crystallographic analysis. The first sample, henceforth referred to as Sample 1, was prepared for measurement in a piston cylinder cell at the University of Bristol in fields up to 14 T whilst the second, Sample 2, was prepared for measurement at higher pressures in a moissanite anvil cell and at higher fields at the High Field Magnet Laboratory. The results of both will be detailed and discussed.

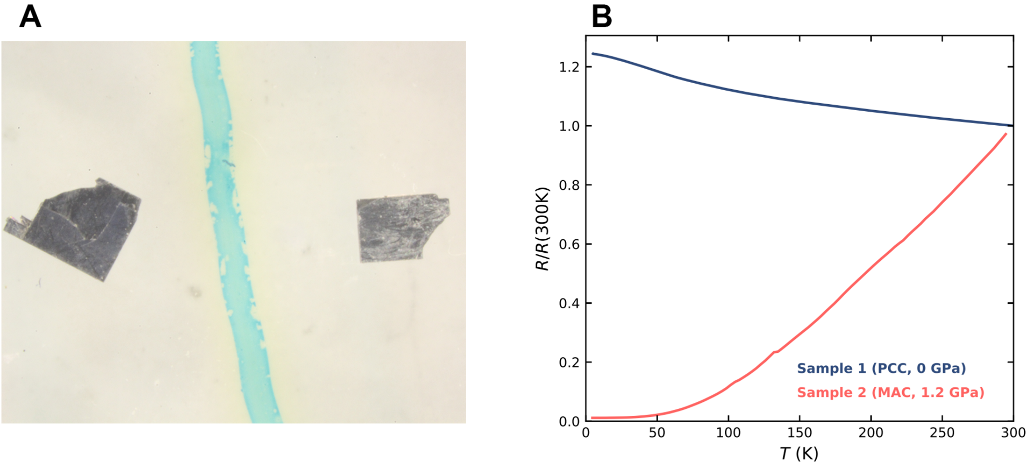

Figure 7.3: A: Photographs of as-grown samples of ZrSiS. The left-most crystal is the crystal from which all samples in this work were cut. B: The zero-field resistance of Sample 1 and Sample 2. Markedly different behaviour was observed in each. Strong Shubnikov de-Haas oscillations were observed (presented later) in both samples.

7.2.2 Sample 1

Sample 1 was cut to a rectangular shape with an aspect ratio of ~ 3 using a wire saw. Four gold contact pads were sputtered across its width in a configuration suitable for the measurement of in-plane longitudinal resistance ($I \parallel ab$). The sample was then mounted onto a card feed-through alongside a Manganin pressure gauge in an orientation such that $I \perp B$. The feed-through was inserted into a piston cylinder cell without a pressure medium for measurement at ambient pressure. It was then reloaded into the piston cylinder cell using Daphne 7373 as a pressure medium (which remains hydrostatic at room temperature up to 2.5 GPa [34]) for measurements at elevated pressures. Unfortunately, upon the initial application of pressure, contact to the sample was lost. The failed contacts were repaired in situ and the sample was successfully loaded into the cell and pressurised during the second attempt. However, because the effective current path was inevitably changed, the ambient pressure and elevated pressure data are not directly comparable. The specifics of this issue and how it affects the analysis of the data is discussed in more detail later.

Measurements on Sample 1 were primarily performed at the University of Bristol using a superconducting magnet capable of delivering magnetic fields up to 14 T. It was also extracted from the pressure cell and measured in fields up to 35 T at the High Field Magnet Laboratory where it was aligned on a rotating stage such that $H \parallel c$ at ambient pressure. The in-plane MR of ZrSiS is known to have a characteristic 'butterfly-shaped' anisotropy [143]. The MR is maximal when $H \parallel c$. The magnetic field was oriented such that the measured sample resistance was maximal in the presence of a finite field.

The normalised zero-field resistance of Sample 1 is presented in Figure 7.3B. Whilst metallic behaviour is expected [143], insulating behaviour is exhibited from the lowest temperature measured up to 300 K. It is unclear why the resistivity of Sample 1 is so highly uncharacteristic of ZrSiS. As will be reported later, the MR is similarly unreminiscent of ZrSiS based upon previous reports. The simplest explanation is that there is simply some additional material conducting in series with the sample though there is no visual evidence that this is the case. As has been stated previously, the sample was cut from the same larger sample on which a magnetisation study has been performed and the sample from which Sample 2 was also cut. One would therefore have to conclude that the additional resistance is intrinsic to the sample as opposed to originating from foreign material. It is possible that Sample 1 was cut from a region of the larger sample in which a large impurity-rich patch was present. Despite these obvious discrepancies, clear Shubnikov de-Haas oscillations were observed with the application of a magnetic field.

7.2.3 Sample 2

Sample 2 was cut to a square with sides of length ∼200 µm such that it would just fit within the hole of a gasket for mounting in a moissanite anvil cell. Six gold contacts were evaporated onto the sample as described in 3.3.2 for measurement of the in-plane resistivity. Silver paint was applied directly to the sample to make a bridge between the gold contacts and the corresponding gold tracks that are patterned on the anvil. The details of this procedure can be found in 3.3.2.

Sample 2 was then loaded into the moissanite anvil cell using glycerol as a pressure medium. This was selected due to its chemical stability, the relative ease of working with it relative to volatile pressure media and its hydrostaticity which remains good at room temperature up to around 5.5 GPa [35]. 1.2 GPa of pressure was applied to the moissanite anvil cell prior to it being taken to the High

Field Magnet Laboratory. Subsequent increases in pressure were applied at the High Field Magnet Laboratory between measurements in high magnetic fields. A maximum pressure of 5.6 GPa was applied.

The ambient pressure resistivity was not measured prior to the application of 1.2 GPa and the sample could not be salvaged from the pressure cell for this measurement to be performed afterwards. Contact to the sample was lost upon depressurisation of the pressure cell. For this reason, the normalised zero-field resistance at 1.2 GPa is presented in Figure 7.3. Unlike Sample 1, and despite being cut from the same large sample, the zero-field resistivity of Sample 2 was found to be in accordance with previous measurements [143].

7.2.4 Magnetisation

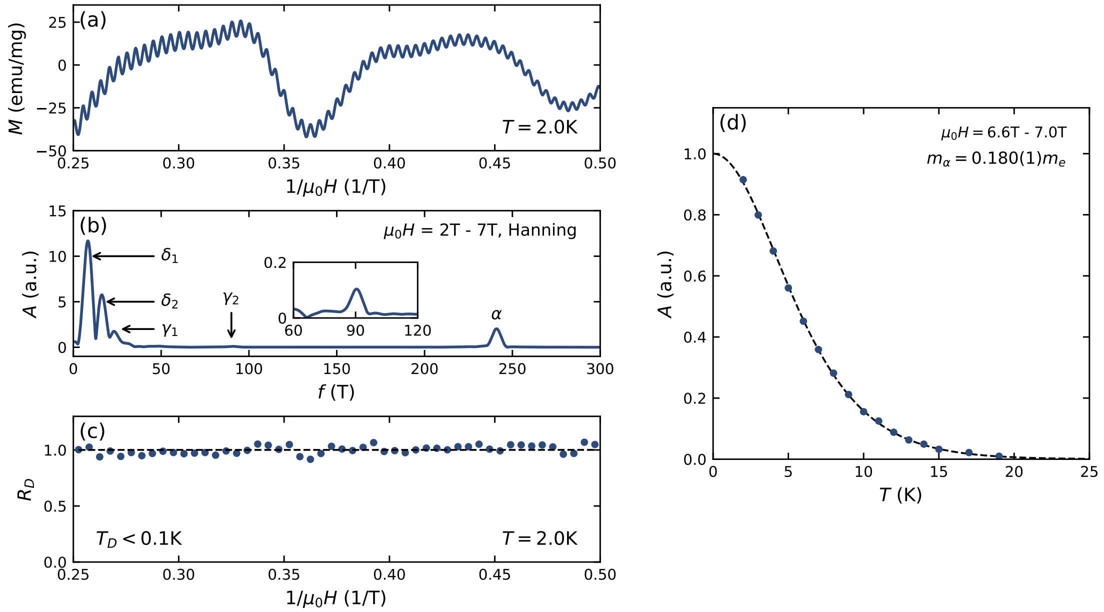

Figure 7.4: (a) The magnetisation of a 4.60 mg sample of ZrSiS between 2 T and 4 T. (b) The FFT spectrum of the oscillatory magnetisation taken between 2 T and 7 T. (c) The field-dependence of the Dingle damping term from which an upper bound of 0.1 K to the Dingle temperature is estimated. (d) The temperature dependence of the amplitude of the $\alpha = 240\,\mathrm{T}$ orbit. The dashed line is a fit to the Lifshitz-Kosevich formula from which the indicated mass was determined.

The magnetic field dependence of the magnetisation M measured at 2 K is presented in Figure 7.4a between 2 T and 4 T. No background subtraction has been made. There are clear oscillations with a frequency of 240 T superposed over lower frequency oscillations with a substantially longer period. The composite frequencies are resolved in the FFT spectrum presented in Fig 7.4b. The labelled peaks are centred at the following frequencies: $\delta_1 = 8\,\mathrm{T}$, $\delta_2 = 16\,\mathrm{T}$, $\gamma_1 = 22\,\mathrm{T}$, $\gamma_2 = 90\,\mathrm{T}$

and $\alpha = 240\,\mathrm{T}$ in close agreement with high-field torque and resistivity measurements [136, 137, 140].

As previously described in Section 2.4.3, it is possible to determine the quasiparticle mass from the temperature dependence of an oscillation amplitude. It was not possible to determine the mass of the lower frequency oscillations with sufficient accuracy due to the wide field window over which a single period extends. In this case, how to determine an 'average' magnetic field is not clear and an error in necessarily introduced. However, the mass of the α orbit could be determined. The field-dependence of M was measured in a narrow field range (between 6.6 T and 7.0 T) over which a small number of periods could be observed. Fits of a sinusoid plus a quadratic background were made at each temperature such that the amplitude of only the α frequency could be extracted. The temperature dependence is shown in Fig 7.4d and has been fitted to a curve of the Lifshitz-Kosevich form. The mass was determined to be $m_\alpha = 0.180(1)m_e$. This value is consistent with previous high field measurements [136, 140] but it believed to be more accurate due to the narrow field window over which the measurement (and analysis) was performed.

Lastly, the Dingle damping factor was evaluated by dividing the measured field dependence of M by both the temperature damping factor $R_T(m_\alpha = 0.0180)$ and $B^{1/2}$. The resultant signal was subdivided into sections each approximately $1\frac{1}{2}$ oscillation periods long and, similarly to before, fitted to a sinusoid with a linear background. The field-dependence of R_D is presented if Fig 7.4(c). There is no measurable additional attenuation of the signal. That is, R_D is unity over the measured field range. It is estimated that the Dingle temperature, T_D, has an upper bound of 0.1 K corresponding to a mean-free-path that is $> 7\,\mu\mathrm{m}$. This is more than a factor of 10 larger than values derived from SdH oscillations reported in [144].

7.2.5 Comparison with Literature

A short comparison of the ambient pressure properties of the samples measured in this work and those from other studies is made. The determined lattice parameters from the aforementioned crystallographic analysis are listed in Table 7.1 alongside literature values from Ref [145] for comparison. They were all found to be in very close agreement. All measurements presented in this thesis were performed on samples cut from the same sample from which the piece that underwent crystallographic analysis was cut. Likewise, the atomic positions are found to be in close agreement as well.

The observed frequencies of the oscillatory bulk magnetisation at ambient pressure here and

Parameter	Literature [145]	100 K	300 K
a, b	3.5440	3.5460(2)	3.5423(3)
c	8.0550	8.0530(7)	8.0487(10)
Volume	101.17	101.259(14)	100.99(2)

Table 7.1: Lattice parameters obtained via X-ray crystallography from a piece of the sample of ZrSiS from which all other samples measured in this thesis were cut.

those observed previously in both Shubnikov de-Haas and torque [140] are compared. The quoted DFT values were calculated using WIEN2k [37] and were also taken from [140].

Assigned Orbit	f_{DFT} (T)	$f_M(T)$	$f_{SdH}(T)$	[140] (T)
δ_1	7	8	6	8
δ_2	17	16	19	16
γ_1	57	23	-	22
γ_2	156	90	-	90
α	240	240	240	240
β	518	-	414	420

Table 7.2: A comparison of the frequencies assigned to fundamental orbits as determined from DFT calculations (from [140]), measurement of the bulk magnetisation (this work), resistance (SdH) (this work) and from a combination of resistance (SdH) and torque measurements also from [140]

.

There are significant discrepancies between the DFT result and those found here and in previous measurements. The assignment of those frequencies measured experimentally to those predicted by DFT is made somewhat less ambiguous when the field-angle dependence of the oscillation frequencies are compared with their calculated angle dependencies. This analysis is detailed in [140]. It has been determined thatα and β reside in the ZRA plane (Figure 7.2D), γ_2 and δ_2 reside in the ΓXM plane whilst γ_1 and δ_1 are minimal orbits around the necks of the hole-like and electron like sheets respectively (blue and green surfaces in Figure 7.2C respectively) in an intermediate plane through constant k_z. Overall, it appears that the sample from which Sample 1 and Sample 2 were cut are highly typical of ZrSiS and have the same properties as samples measured in other studies.

7.3 Sample 1 - PCC up to 2.3 GPa

The field-dependence of the resistance of Sample 1 at each measured pressure is presented in Figure 7.5. The ambient pressure measurement of R is offset from the others. This is due to the breaking and reparation of a contact in-situ between measurements as previously described. Not only is $R(T)$ highly unusual in this particular sample, $R(H)$ is not characteristic of ZrSiS. Previous measurements have shown that the MR (defined as $\Delta\rho/\rho$) is of the order of 10 000 % over the same field range [136,

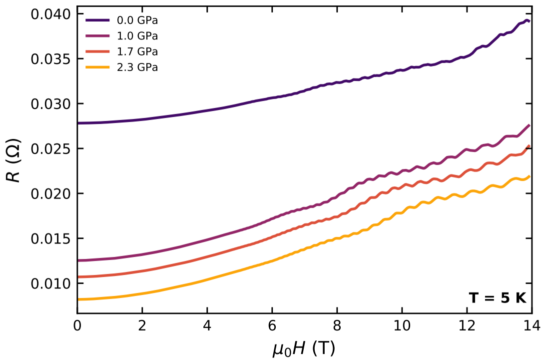

Figure 7.5: $R(H)$ of Sample 1 measured in fields up to 14 T at each of the measured pressures (including ambient).

143, 146]. The discrepancies seen in $R(T)$ and $R(H)$ are sufficiently severe to doubt whether the sample being measured is in fact ZrSiS at all. Despite this, strong quantum oscillations are seen. The oscillatory signal has been analysed and the results are presented in the following subsections.

7.3.1 Frequency Analysis

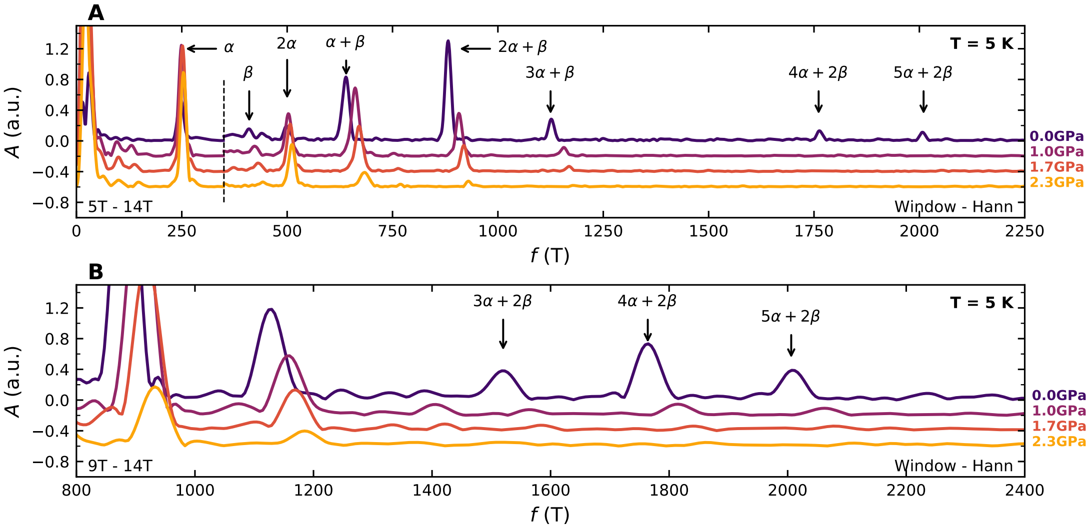

Figure 7.6: A: The FFT spectra obtained from $R(B)$ presented in Figure 7.5 between 5 T to 14 T and at 5 K. The data at frequencies higher than the dashed line has been multiplied by a factor 10 for clarity. The most prominent peaks have been labelled. B: The FFT spectra computed from the same MR data as in A but analysed over a narrower field range. An additional high frequency peak appears and is labelled.

The FFT spectra of the $R(H)$ curves of Sample 1 are shown in Figure 7.6. The spectra at elevated pressures are directly comparable as they were measured and analysed with the same experimental and analysis parameters. The amplitude of the ambient pressure curve, due to the failure and reparation of a voltage contact, can not be directly compared to the others. The ambient pressure FFT spectrum has been scaled to a comparable amplitude for clarity only. The fundamental frequency α is clearly seen with a frequency of 247 T at 0 GPa. The second harmonic of α is also clearly visible. β, the other fundamental frequency in the ΓXM-plane, is also resolved with a frequency of 410 T at 0 GPa. Between the comparable curves, there is an overall suppression of oscillation amplitude. This could be the result of the introduction of strains, through the pressure medium remains highly hydrostatic at these pressures, or an intrinsic increase in scattering.

The other prominent peaks are all found at frequencies of the form

$$f = pf_\alpha + qf_\beta \tag{7.1}$$

where p and q are integers that correspond to the number of times a quasiparticle must orbit α and β respectively. This is consistent with magnetic breakdown phenomena. What is distinctive about the breakdown frequencies observed here is that they are all additive sums of the fundamental frequencies. This is in contrast to a previous quantum oscillation study [140] in which all of the breakdown frequencies were subtractive sums of the form $pf_\alpha - qf_\beta$ or $qf_\beta - pf_\alpha$. This subtractive nature of breakdown is consistent with a picture in which one Fermi sheet is electron-like whilst the other is hole-like, as is known to be the case in ZrSiS. The hole- or electron-like nature of each pocket dictates the direction in which quasiparticles must travel around that particular portion of the Fermi surface. This provides a constraint on which frequencies should and should not be observed. To find additive sums of fundamental orbits suggest that quasiparticles are able to orbit in the same direction around each Fermi surface pocket despite the electron- or hole-like properties of either Fermi sheet. This is semiclassically forbidden.

The frequencies of those prominent peaks that remain resolved at the highest pressure measured have been tracked and the results are shown in Figure 7.7. p and q (from Equation 7.1) denote the integer multiples of α and β ascribed to the frequency in question. Dashed lines are simultaneous fits of the data to Equation 7.1. As is expected if the breakdown peaks are truly described by the additive sums of fundamental α and β, they all fall onto parallel straight lines. Whilst both α and β can be determined directly from the FFT spectra, they can also be obtained from the described fitting procedure. The results are summarised in Figure 7.8. The error associated with α_{FFT} and β_{FFT} is an estimate of the certainty with which the peak frequency can be determined. The error bars assigned to α_{fit} and β_{fit} are derived from the sensitivity of the converged fit parameters with

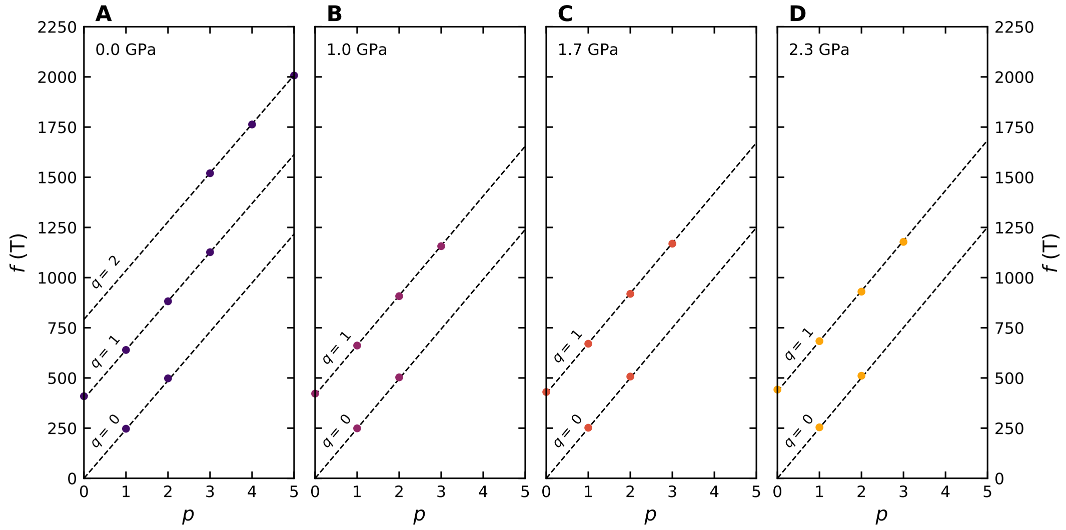

Figure 7.7: A-D: The frequencies of the prominent peaks of the FFT spectra presented in Figure 7.6 at each pressure. p and q denote the integer multiples of α and β ascribed to each frequency. Dashed lines are simultaneous fits of the data to Equation 7.1

respect to variation of α_{FFT} and β_{FFT} (the input of the fitting procedure).

Both α_{fit} and β_{fit} derived from the fitting to Equation 7.1 follow the same systematic increase with pressure as α_{FFT} and β_{FFT} but are smaller (by $\sim$ 3 T and $\sim$ 10 T respectively) in both cases. This might be due to an inherent uncertainty in their determination via either method. An alternative explanation is that the sample is misaligned to some extent. In this case, the extremal orbit associated with $\alpha+\beta$ need not be the sum of f_α and f_β. The breakdown orbit itself is required to be an extremal orbit and thus, may not necessarily lie in the same plane perpendicular to H as the fundamental orbits from which it is comprised. This is schematically illustrated in Figure 7.9. α and β are both maximal orbits. Thus, it is necessarily the case that the breakdown orbit $f_{\alpha+\beta} = f_\alpha + f_\beta$ when $H \parallel c$ and $f_{\alpha+\beta} < f_\alpha + f_\beta$ when H is slightly off-axis. Indeed, $df_\alpha/d\theta$ is positive [135]. The value of α found here is larger than in previous measurements (see Table 7.2) and larger than the value measured at ambient pressure when H was oriented with respect to the c-axis using a rotating sample stage (shown later in Figure 7.13).

At first glance, it appears that β is not the fundamental orbit based upon its small amplitude and the large amplitude of peaks assigned to $\alpha+\beta$ or $2\alpha+\beta$. If this were the case, β would be interpreted as being a breakdown orbit associated with $\beta' - \alpha$ or $\beta' - 2\alpha$. This conclusion was incorrectly drawn in a previous study [136]. However, the pressure dependence of the FFT amplitudes suggests otherwise. The amplitude of α (and 2α) barely diminishes with pressure. The amplitude of β, albeit very small even at ambient pressure, is resolvable up to 2.3 GPa. All other

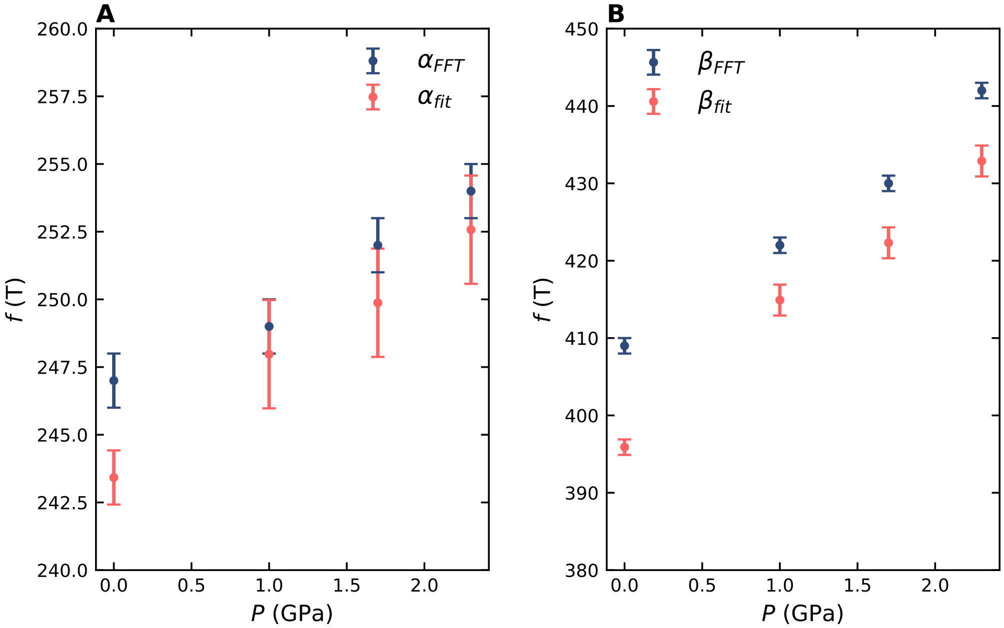

Figure 7.8: A: The pressure dependence of α as determined from the peak frequency and from fits described in the main text. B: The pressure dependence of β as determined from the peak frequency and from fits described in the main text.

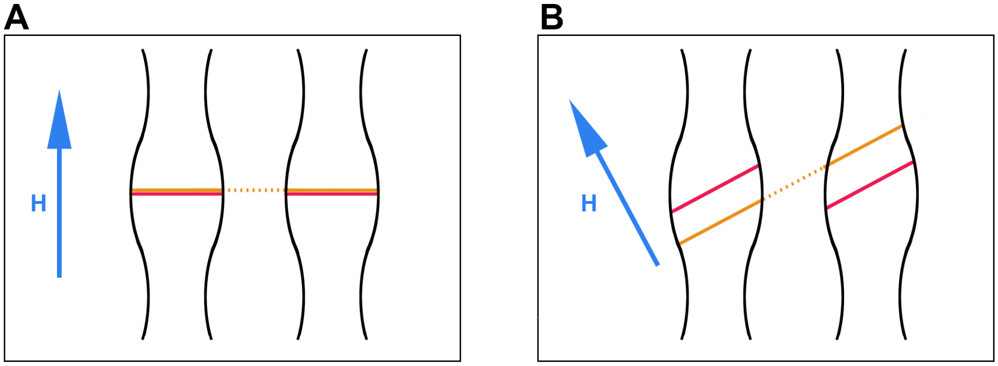

Figure 7.9: A: A schematic representation of two quasi-cylindrical Fermi sheets. When $H \parallel c$, the extremal breakdown orbit (orange) is the sum of the two fundamental orbits (red). B: The same quasi-cylindrical Fermi sheets with H oriented off-axis. The extremal breakdown orbit is no longer the sum of the two fundamental orbits.

frequencies show large attenuation with pressure. This is consistent with a pressure-induced increase of the breakdown gap.

7.3.2 Mass Analysis

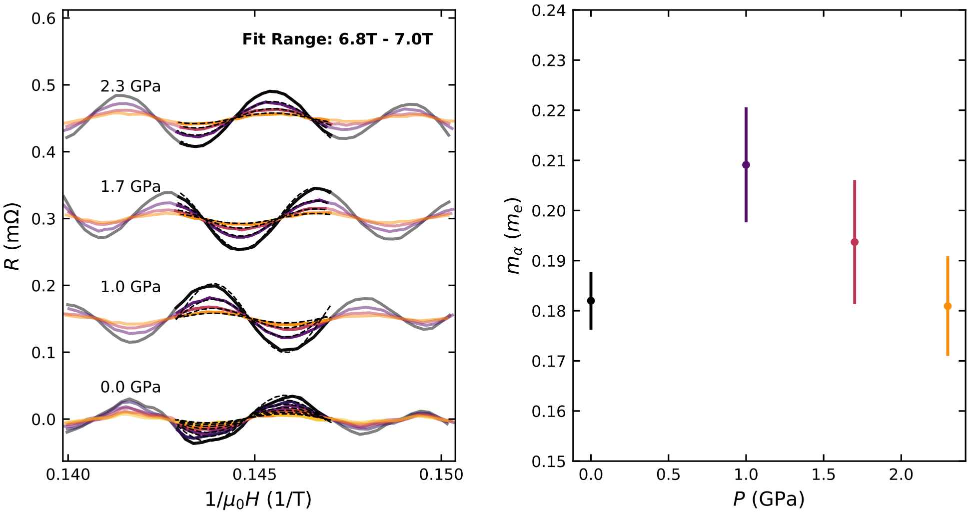

Figure 7.10: A: The oscillatory signal in a narrow field-range shown for a number of temperatures at each pressure. A polynomial background has been subtracted from each curve by fitting the entire field range shown. A 0.15 mΩ offset has been applied to each pressure for clarity. B: The pressure dependence of m_α found from direct simultaneous fits to the data presented in A. Error bars reflect the sensitivity of m_α to the field range being fitted.

There is an intermediate field range within which there is sufficient magnetic field for the oscillatory signal to have sufficient amplitude to be seen whilst being low enough that it is dominated by a small number of frequencies. In this intermediate field range, it is possible to obtain a value for the mass of the α orbit by directly fitting the raw $R(H)$ to a sinusoidal oscillation with an amplitude governed by the standard Lifshitz-Kosevich form (Equation 2.46). The principle advantage to this method is the ability to obtain a value of m_α over a narrow field range. The oscillatory MR plotted against inverse-field is presented in Figure 7.10A for a number of temperatures at each pressure. A polynomial background has been fitted and subtracted from the broader field range presented. Direct fitting has only been performed on the narrower field range. The obtained pressure dependence of m_α is shown in Figure 7.10B. The error bars are derived from analysis of the sensitivity of the obtained values of m_α to the field range being fitted to. Field ranges of the same width in the range 6 T to 7.5 T were analysed to determine this error.

The mass of the α orbit and those breakdown orbits that remain sufficiently well resolved at

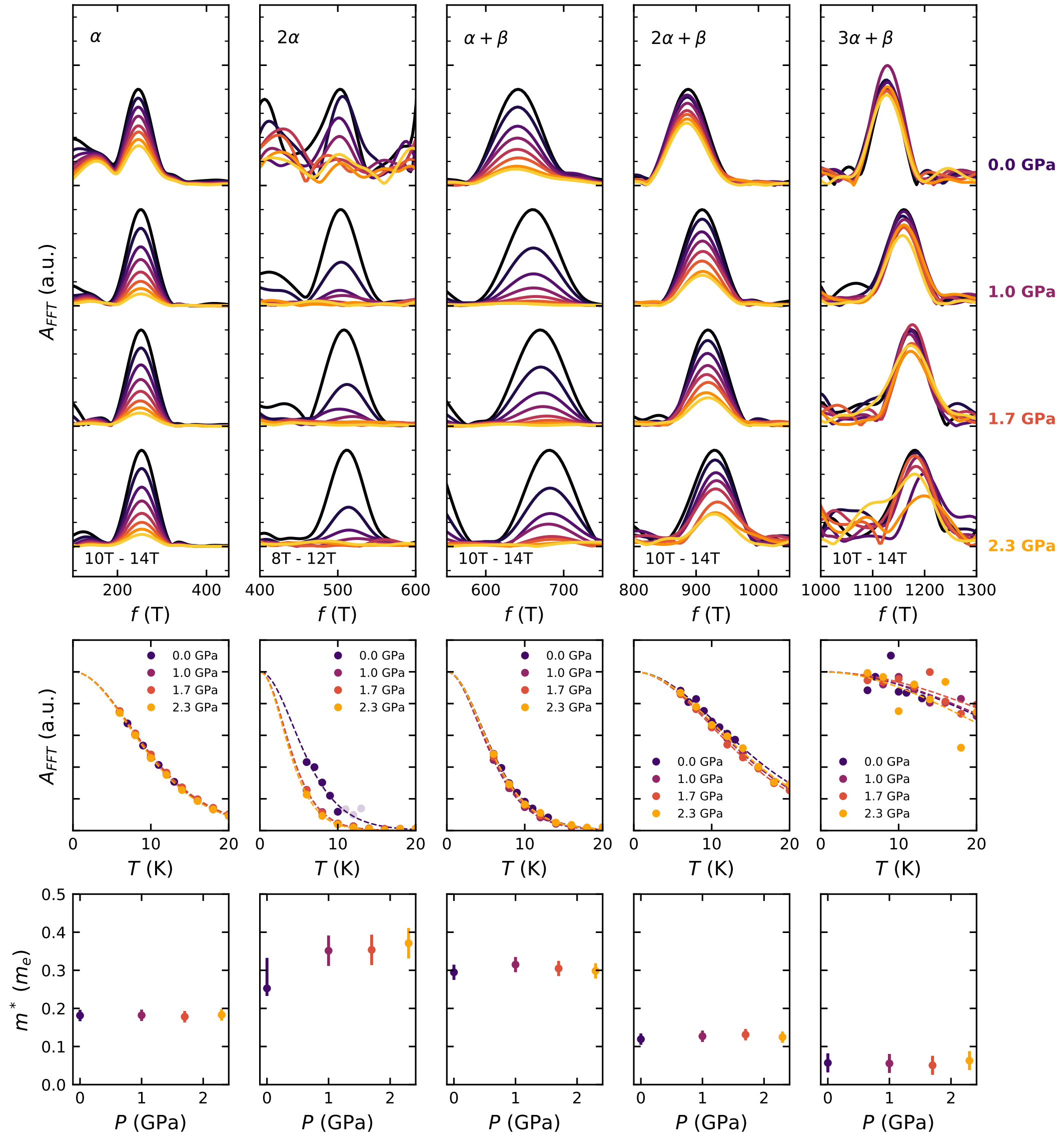

Figure 7.11: Top: Regions of the FFT spectra around the frequency-of-interest taken in a narrow field range. At each pressure, the spectra have been normalised to the lowest temperature peak for clarity. An offset has been applied to separate spectra at each pressure. Middle: The temperature dependencies of the oscillation amplitudes at each pressure. Dashed lines are fits of the data to the typical LK formula. Faded points are comparable in amplitude to the noise floor and have been excluded from the fit. Bottom: The pressure dependence of the mass of each orbit.

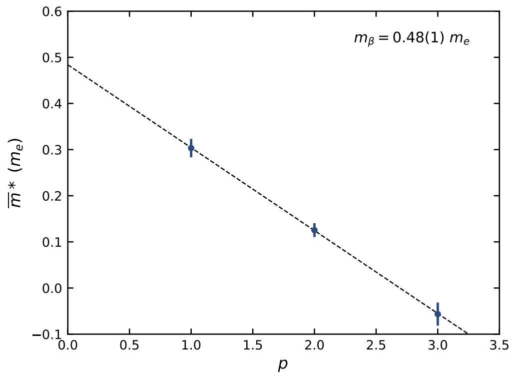

Figure 7.12: The mean mass of breakdown orbits $p\alpha + q\beta$ from which the mass of the β orbit can be inferred by extrapolating the data back to $p = 0$.

highest pressures were also evaluated by analysing the FFT spectra. To minimise the error associated with the determination of H, a narrow field-range was analysed and the peak amplitude of the frequency in question was plotted against temperature. In order for a sufficiently narrow peak to be found in the FFT spectra such that the FFT amplitude can unambiguously be attributed to the orbit-of-interest, the MR at relatively low fields needs to be analysed. The temperature-dependence of the amplitude was then fitted to the typical LK formula. The results are summarised in Figure 7.11. In the top row, the raw FFT spectra from which the peak amplitudes were extracted are shown. The maximal value of the principle peak was taken irrespective of whether there were minor deviations from the expected frequency. In the case of the 2α orbit, only temperatures less than 10 K were used for the subsequent fits (high temperatures are plotted) as the peak amplitude is of the same magnitude as the noise floor for higher temperatures. The middle row of Figure 7.11 shows the temperature dependence of the peak amplitude with fits to the usual LK temperature damping formula (dashed lines). Finally, the bottom row shows the pressure dependence of the masses associated with each orbit.

Given that the masses appear largely pressure independent, the mean values of m^* (weighted by their uncertainties) serve as a reasonable measure of the mass at any pressure. As expected of harmonics of fundamental frequencies, $\bar{m}_\alpha$ is found to be half that of $\bar{m}_{2\alpha}$. Similarly, mass of orbits described by $p\alpha + \beta$ are found to decrease with each subsequent addition of α. It may at first appear that the step size between $\bar{m}_{\alpha+\beta}$-$\bar{m}_{2\alpha+\beta}$ and $\bar{m}_{2\alpha+\beta}$-$\bar{m}_{3\alpha+\beta}$ is not uniform. The amplitude of SdH oscillations is only sensitive to the magnitude of m^*. In Figure 7.12, the mean mass of the breakdown orbits involving a single β ($q = 1$) have been plotted with $\bar{m}_{3\alpha+\beta}$ taken to be negative. It is clear that if this is done, the masses are indeed equally separated.

Although the mass of the β orbit could not be determined directly, it is possible to infer its mass by extrapolating the masses of the $p\alpha + \beta$ breakdown orbits back to $p = 0$. A linear fit has been made to $\bar{m}_{p\alpha+\beta}$ (dashed line in 7.12) and the extrapolation back to $p = 0$ reveals $\bar{m}_\beta = 0.48(1)m_e$. This is $\sim 6\,\%$ smaller than the value determined elsewhere [140].

7.3.3 Ambient Pressure

After the measurements performed in the PCC, the sample was extracted and remeasured at high fields (35 T) with the magnetic field precisely oriented $H \parallel c$. Figure 7.13A shows the field-dependence of the resistance of Sample 1 with field carefully oriented $H \parallel c$. Strong Shubnikov de-Haas oscillations are observed from $\sim 3\,$T. An expanded view of the oscillatory MR at highest magnetic fields is shown in Figure 7.13B. High frequency breakdown oscillations can be clearly seen. FFT spectra are presented in Figure 7.13C, D, and E for three different frequency ranges. The analysed field-range is also different for each panel such that the peaks are clearly resolved in each frequency range. The breakdown gap associated with the highest frequency oscillations is known to be highly angle dependent [136]. The fact that they are seen is evidence that the sample is precisely aligned with $H \parallel c$.

Surprisingly, the FFT spectrum in the range 250 T to 1000 T is very different from that which was originally measured. Not only are the peaks markedly reduced in amplitude even through the available field range is substantially higher, the frequencies themselves have changed. Perhaps the clearest breakdown peak is the one at 600 T. This was not seen previously. It was, however, a prominent feature of the FFT spectrum in other quantum oscillation studies [135, 136]. In this sense, more typical behaviour has been restored. It appears that with the application of pressure and subsequent depressurisation, the sample via some (presumably mechanical) mechanism, has been altered.

7.4 Sample 2 - MAC up to 5.6 GPa

The field-dependence of the resistance of Sample 2 at 1.4 K and in fields up to 35 T is presented in Figure 7.14 for each pressure at which it was measured. An offset has been applied between each pressure for clarity. Similar to Sample 1, the signal is comprised of high frequency oscillations with $f \sim 250 - 1000$ T superimposed over low frequency oscillations with $f \sim 0 - 30$ T. At highest fields (most clearly seen in Figure 7.14B), additional higher frequency oscillations appear. Unlike Sample 1, an MR of 15 000 % is observed at 10 T which is comparable to previous results [143]. Additionally,

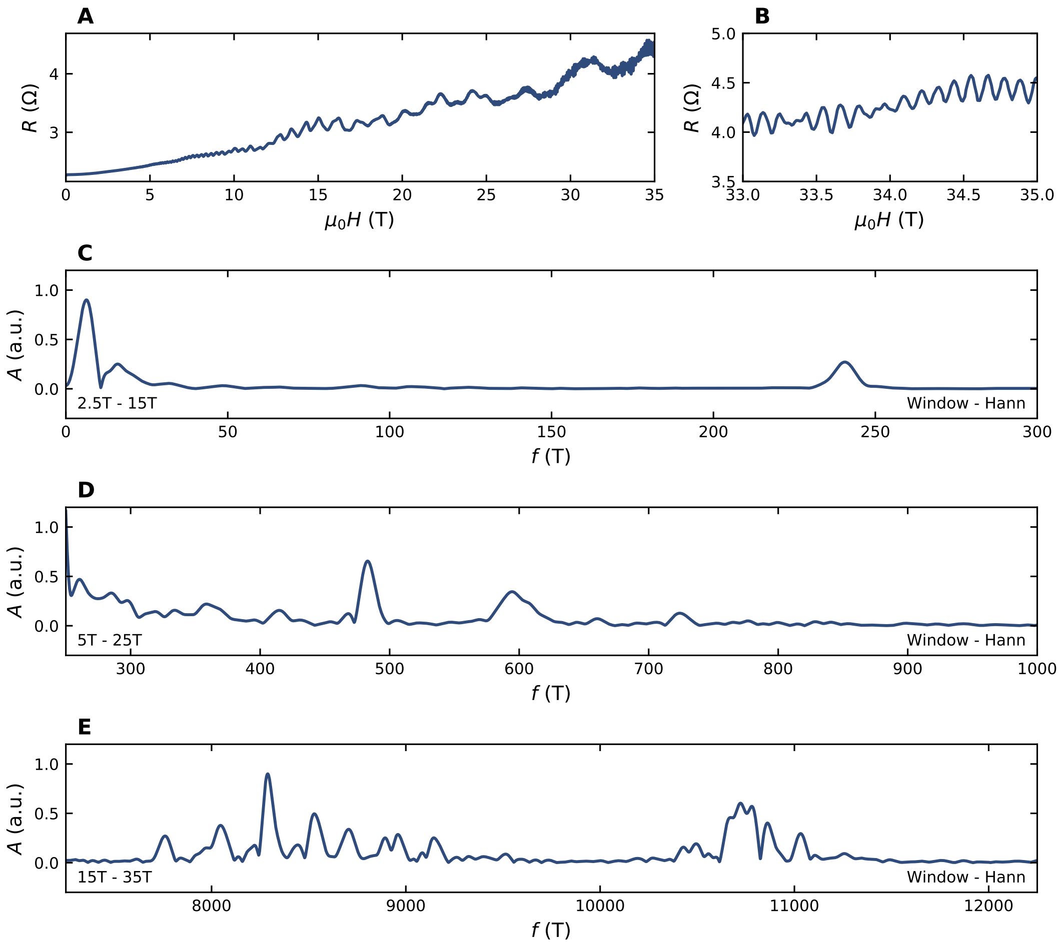

Figure 7.13: A: The magnetic field dependence of the resistance of Sample 1 showing strong Shubnikov de-Haas oscillations. B: An expanded view of the highest field data from panel A. C, D, E: The FFT spectrum for three different frequency- and field-ranges.

the zero-field resistance was found to be comparable to previous measurements as well (Figure 7.3) [137].

The complete set of FFT spectra measured at different temperatures at each pressure are presented in Figure 7.15. The measurement and analysis has been performed with the same parameters in each case such that all of the spectra are directly comparable in magnitude. The spectra have been similarly divided into three regions of frequency-space within which different field-ranges have been analysed to best illustrate the full set of peaks.

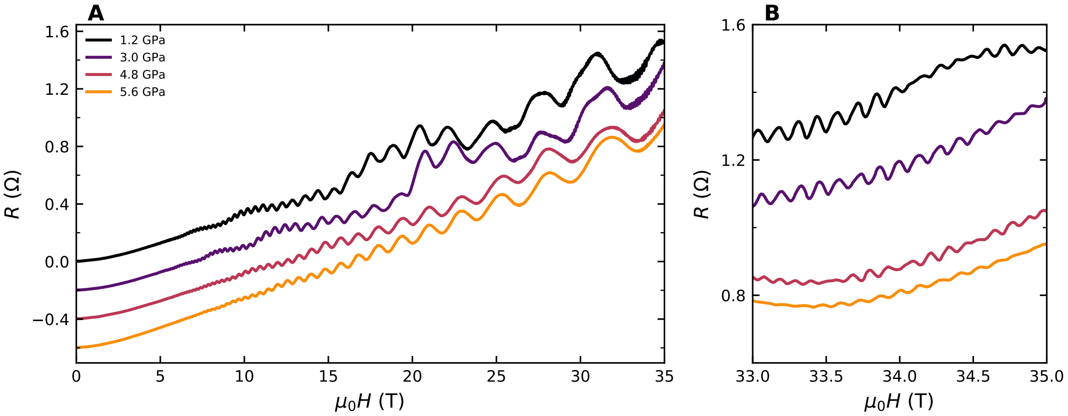

Figure 7.14: A: The field dependence of the resistance of Sample 2 at each pressure measured at 1.4 K. An offset has been applied for clarity. B: An expanded view of the highest field data from A in which high-frequency breakdown oscillations can clearly be seen.

7.4.1 Low Frequency Oscillations ($f < 1kT$)

The FFT spectra of $R(H)$ at 1.4 K (the lowest measured temperature) are presented in Figure 7.16. At frequencies less than $\sim$ 1000 T, the fundamental orbits α, β and δ_2 can be resolved in addition to a number of breakdown orbits and harmonics. These have been assigned accordingly. In the rightmost panel, additional breakdown frequencies are shown. These higher frequency oscillations can be separated into two distinct frequency ranges: those at $\sim$ 8 kT and those at $\sim$ 11 kT.

The fundamental orbits α and δ_2 can be resolved at the highest applied pressure. At 5.6 GPa, it was no longer possible to resolve the β orbit nor any of the low frequency breakdown orbits. Possible reasons for this are an increase in the breakdown gap such that there is insufficient field for tunnelling to occur, an enhancement of scattering (possibly primarily around the β orbit) or a smearing due to non-hydrostaticity of the pressure medium. The pressure dependences of those fundamental frequencies that remained resolvable up to highest pressures are presented in Figure 7.17. Both f_α and f_β are found to increase at a comparable rate to that which was found in Sample 1. The most pressure-dependent frequency that could be resolved, in both relative and absolute terms, was found to be δ_2.

Insufficient temperatures were measured at the highest pressure (5.6 GPa) for effective masses to be determined due equipment failure mid measurement. The temperature dependence of the amplitude of the FFT spectra was analysed and the using the same procedure as was used for Sample 1 (7.11). The pressure dependences of the effective masses of the α and β orbits are shown in Figure 7.18.

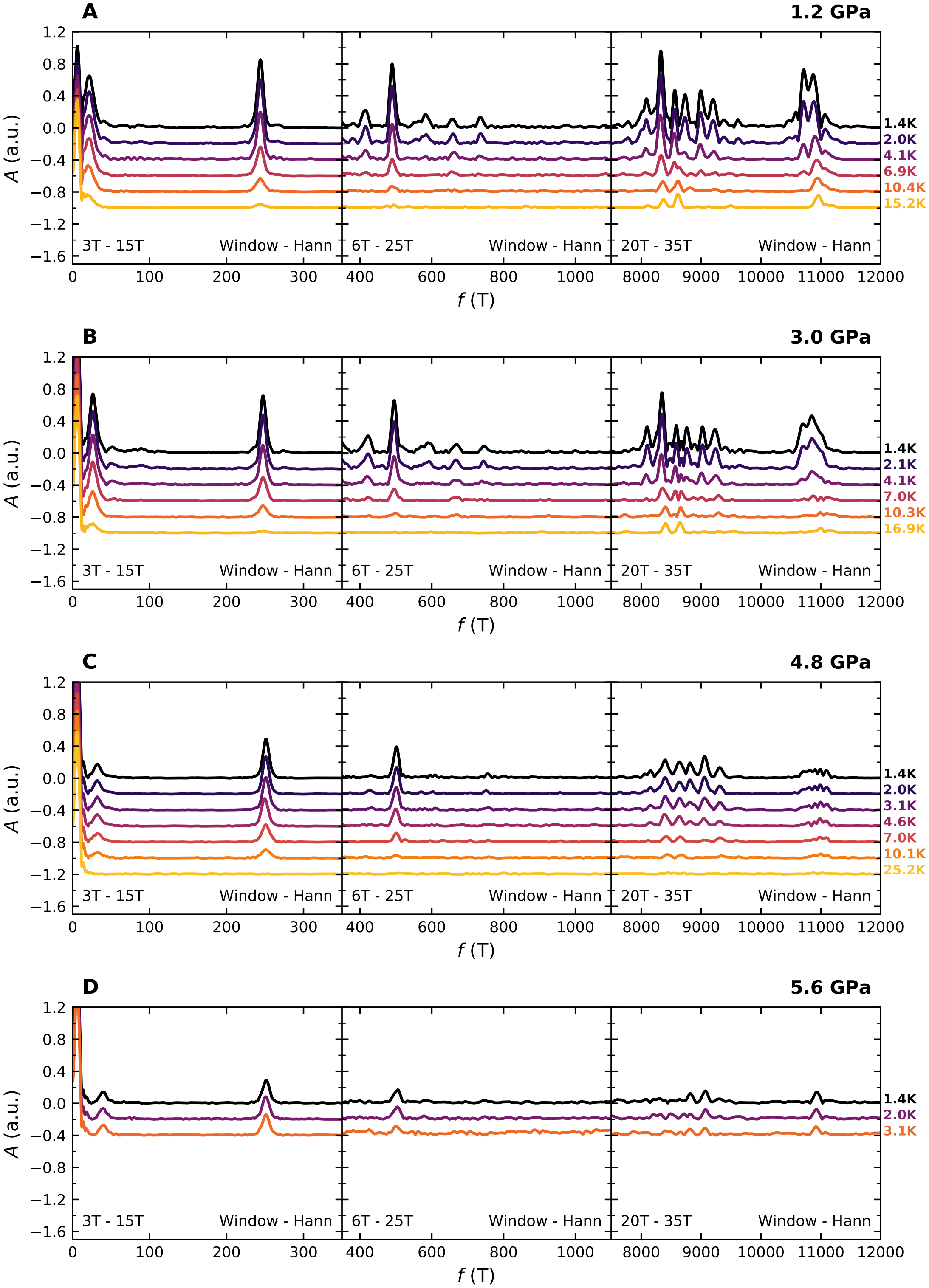

Figure 7.15: The FFT spectra taken at different temperatures for each pressure. Each panel is subdivided into three separate frequency- and field-ranges that best resolve the full spectra. Offsets have been applied between curves at different temperatures for clarity.

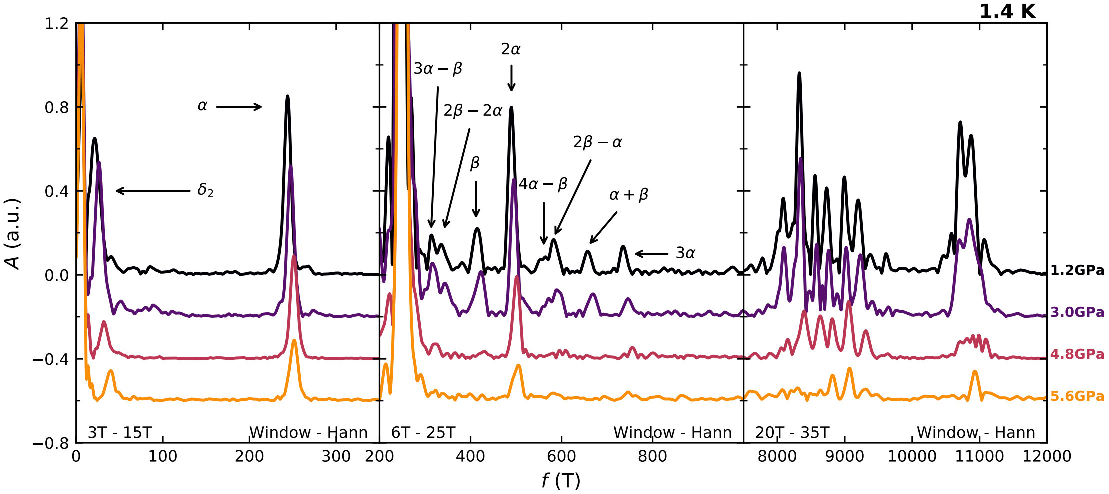

Figure 7.16: The FFT spectra of $R(H)$ at 1.4 K for pressures up to 5.6 GPa. An offset has been applied to each spectrum for clarity.

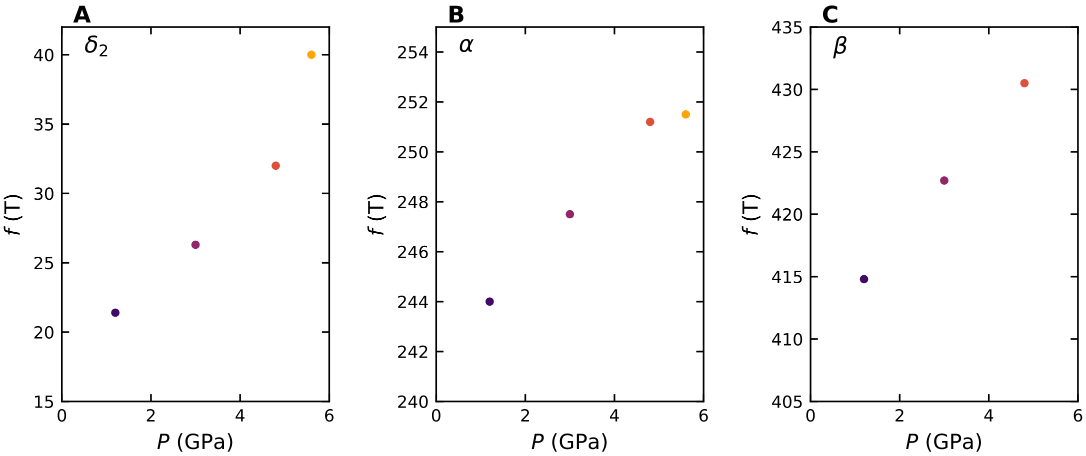

Figure 7.17: The pressure dependence of each of the fundamental frequencies which could be resolved up the highest measured pressures in a MAC up to 5.6 GPa.

7.4.2 High Frequency Oscillations (> 8 kT)

At frequencies greater than $\sim$ 7 kT, two distinct sets of breakdown orbits can be seen. At ambient pressure, the first set is between $\sim$ 8 kT and 10 kT whilst the second set is between 10.5 kT and 11.5 kT. In this work, both sets of peaks are found to be similarly prominent whilst in a previous study at ambient pressure, the second set at higher frequencies were found to be less pronounced [140]. In the same study, the peaks at $\sim$ 9 kT were attributed to breakdown in the ZRA plane resulting in orbits around the entirety of the Fermi surface that enclose a large fraction of the BZ. The assignment to each plane was made primarily by studying the spacing of the individual peaks. The spacing between adjacent peaks was found to be multiples of f_α and f_β, orbits that themselves

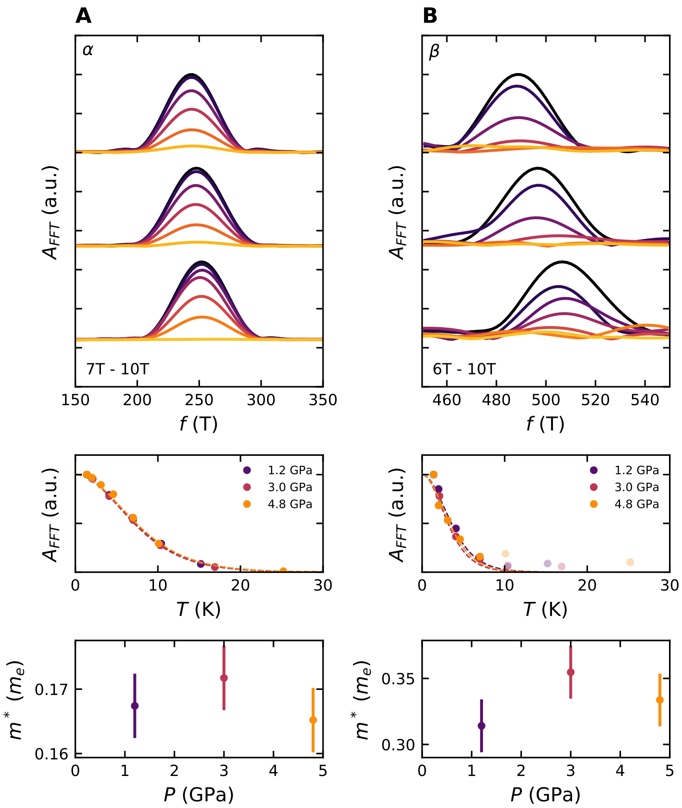

Figure 7.18: The pressure dependence of the effective mass of the α (A) and β (B) orbit up to 4.8 GPa, the highest pressure at measurements were performed at a sufficient number of temperatures. The top panels show the FFT spectra measured at different temperatures. The middle panels show the temperature dependence of the amplitude of the oscillatory signal from which fits to the LK form can be made (dashed lines). Faded points are excluded from the fitting procedure. The lower panels show the pressure dependence of the effective mass of each orbit.

resides in the ZRA plane. The area denoted A in Figure 7.19 was also found to be within $\sim 15\,\%$ of the value calculated using DFT [140]. Similarly, the breakdown frequencies at $\sim$ 11 kT were determined to be due to breakdown orbits in the ΓXM plane due to the narrower peak spacing.

The observation of breakdown frequencies that correspond to orbits around the entire nodal loop provides a further highly stringent constraint upon Fermi surface geometries that are consistent with experimental findings. Not only have the six fundamental orbits that are predicted by DFT been observed here, their figure-of-eight like breakdown frequencies have been observed and the breakdown frequencies around the entire nodal loop have been observed. These findings further confirm the cage-like structure of the Fermi surface.

Although there is sufficient separation to resolve the most prominent peaks, it is clear that in some cases there is substantial overlap between adjacent peaks. The central frequency of each peak may not be where the FFT amplitude is maxmimal. Additionally, it is clear that what appears to be

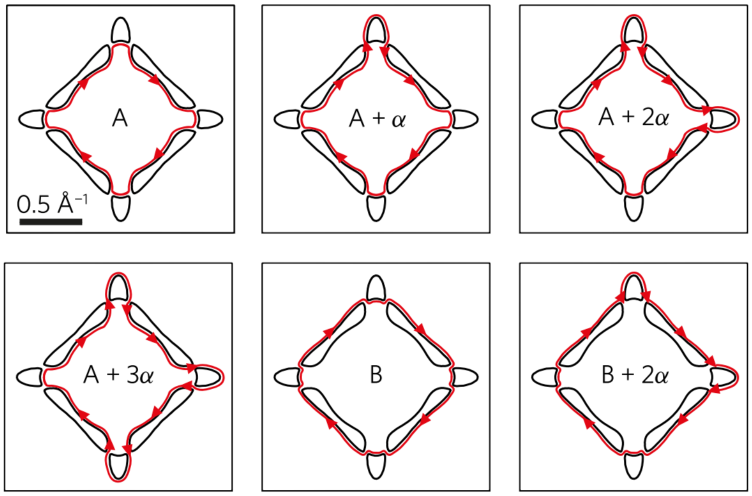

Figure 7.19: Cross-sectional slices through the Fermi surface in ZRA plane (from [136]). High frequency breakdown orbits have been labelled using the same naming convention as has been used elsewhere [136, 140].

a single peak at low temperatures is evidently two closely spaced peaks when the the FFT spectra taken at higher temperatures are examined. A clear example of this is shown in Figure 7.20. At 1.2 GPa (Figure 7.20A) and at low temperatures, only two prominent peaks are evident, one at 8550 T and the second at 8730 T. At higher temperatures, the amplitude of the 8550 T peak is substantially attenuated and a third peak centred at 8600 T is revealed.

The central panel of each sub-figure of Figure 7.20 shows the fit of the FFT spectra to three Gaussian peaks, each with their own temperature-dependent amplitudes that are governed by the usual LK formula for R_T. When their contributions are summed (black lines) the three peaks and are found to closely describe the measured FFT spectra. The right-most panel of each sub-figure shows the individual contributions of each peak (black lines) to the total FFT spectra.

Figure 7.21 shows an expanded view of the FFT spectra around the breakdown frequencies at ~ 9 kT. For all but the final pressure, the top sub-panels shows the FFT spectra. The middle sub-panels shows the FFT fitted to multiple Gaussian peaks (black lines) with their own LK temperature dependences. The lower-sub panels show the contribution to the FFT spectra from individual peaks (black lines). From these fits, both the pressure dependence of the frequencies themselves and their associated effective masses were obtained. The FFT spectra at 5.6 GPa are shown in panel D. Again, measurements were performed at an insufficient number of temperatures for effective masses to be determined. At each pressure, the FFT spectra have been normalised to the maximal amplitude of the lowest temperature FFT spectrum for clarity.

The pressure dependence of the frequencies obtained from fits to the FFT spectra in 7.21 are

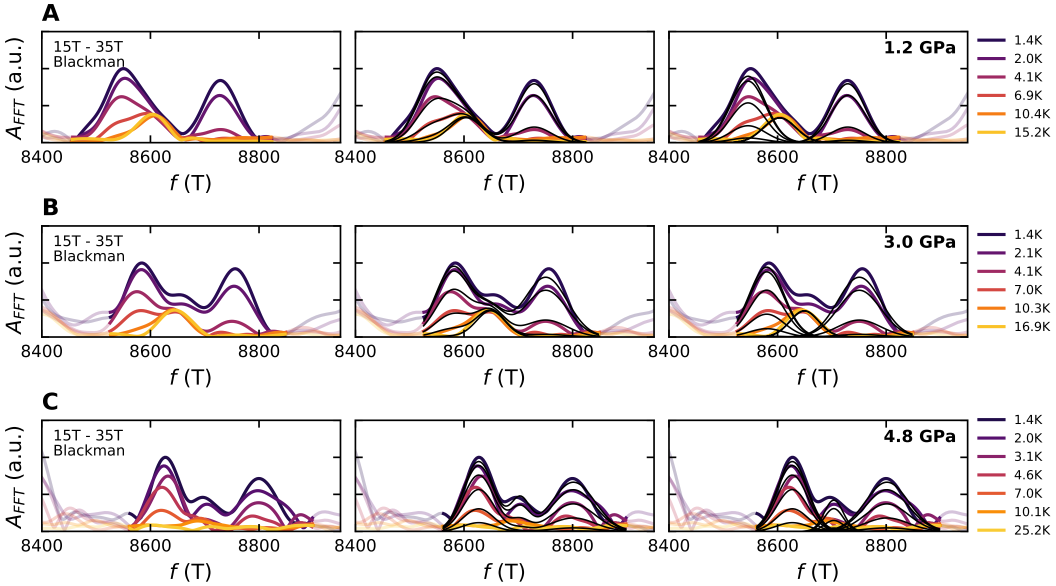

Figure 7.20: An example region of the FFT spectra in which the overlap between adjacent peaks and their relative temperature-dependent amplitudes requires that multiple peaks, each with their own temperature dependence (governed by the usual LK formula for R_T), be fitted simultaneously. The evolution of three peaks are tracked with increasing pressure.

shown in Figure 7.22A. The size of the markers are proportional to the amplitude of the peak as determined by the fitting procedure. The frequencies at 0 GPa were obtained from measurement of Sample 1. The FFT spectrum from which these frequencies were obtained is shown in Figure 7.13. The labelling convention is consistent with that used elsewhere [136, 140].

With increasing pressure, there is both a universal shift to higher frequencies and a suppression of FFT amplitude. The breakdown frequencies here have been determined to be in the ZRA plane, the same plane within which α and β reside [140]. At ambient pressure, orbits II, III and IV, were equally separated by precisely 240 T ($= f_\alpha$), a finding that is consistent with this picture. At ambient pressure, this finding is replicated in this work. At 4.8 GPa, f_α increases by more than 10 T. One would therefore expect that the breakdown peaks become increasingly separated at the same rate. This is not found to be the case. The spacing between II-IV which would be expected to increase by 20 T was found to only increase by 2 T (a value that is smaller than the error in its determination). It could be argued that a 20 T change is simply too small to resolve. The II, III and IV orbits were fitted to Gaussian curves with values of $\sigma \sim 20\,\mathrm{T}$ to $25\,\mathrm{T}$. It should be possible to resolve a change in peak separation that comparable to the width of the peaks in question.

The pressure dependence of the effective masses of the most prominent orbits are presented in Figure 7.22B. The effective masses found here are within $\sim 20\,\%$ of those obtained at ambient

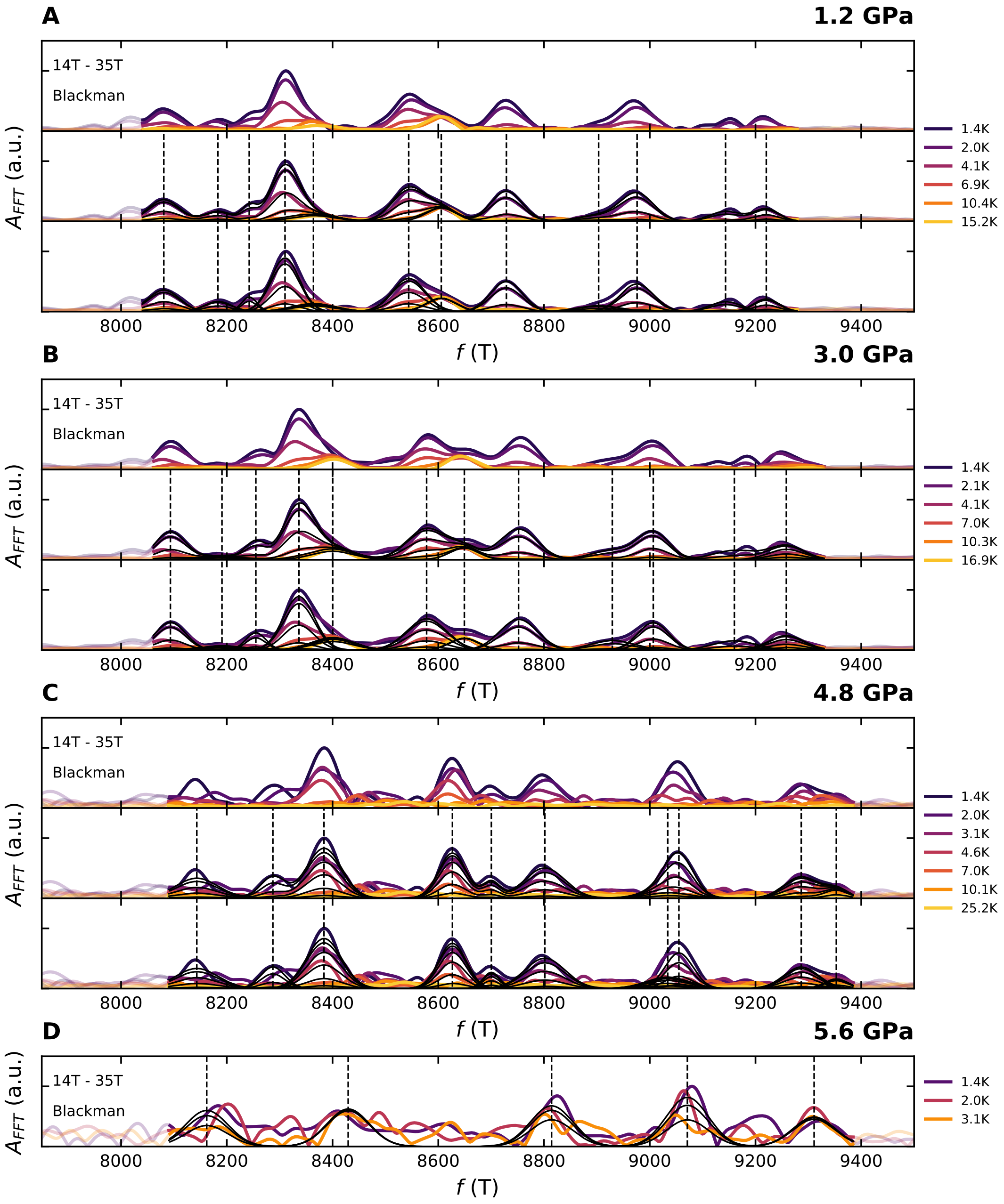

Figure 7.21: FFT spectra from the MR of Sample 2 measured at different temperatures and at elevated pressures. In A, B and C, the top sub-panels show the FFT spectra at different temperatures. The middle sub-panels show simultaneous fits of the FFT spectra (black lines) to multiple peaks each with their own LK-like temperature dependences. The bottom sub panels show the individual contributions of each temperature-dependent peak (black lines). Vertical dashed lines denote the central frequency of each fitted peak. In D, only central frequencies were obtained as measurements were performed at an insufficient number of temperatures for an effective mass of each peak to be determined. At each pressure, the spectra have been normalised to the maximal amplitude of the lowest temperature spectrum.

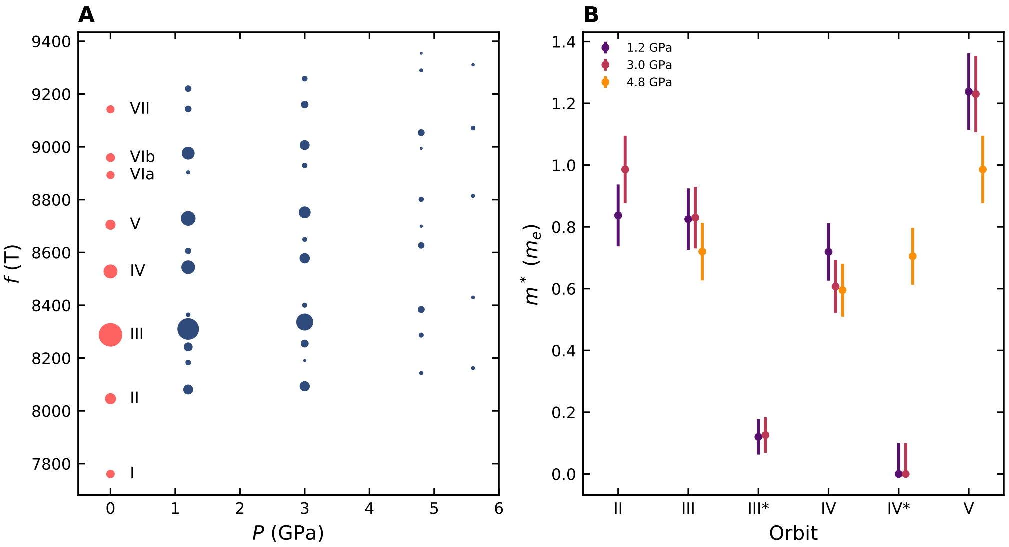

Figure 7.22: A: The pressure dependence of the frequencies obtained from fits to the FFT spectra shown in Figure 7.21. The spot sizes are proportional to the amplitude of each peak. B: The pressure dependence of the effective mass of the most prominent orbits.

pressure in a previous study [140] but are consistently lower. Two additional orbits that were not previously identified have been labelled III* and IV* that are both slightly higher in frequency than III and IV respectively. IV* is the aforementioned intermediate peak shown clearly in Figure 7.20 that emerges into view only at higher temperatures. They are substantially smaller in amplitude than both III and IV but are found to barely be attenuated over the measured temperature range for pressures up to 3 GPa. Their effective masses have therefore been found to be very small. In fact, no measurable attenuation of IV* was found at all and thus only an upper bound to its effective mass can be determined. In [140], a number of peaks were found to have anomalous temperature dependences that were not of the typical LK form. They could be approximately fitted to the sum of two oscillations that did each have a temperature-dependence of the LK form where one oscillation decays with temperature faster than the other. Notably, these frequencies were resolved at temperatures as high as 80 K. Stark interferometry was cited as the origin of these anomalously temperature-insensitive peaks. One such peak was found at 8.6 kT, the same frequency as IV*. In this work, IV and IV* are found to separate in frequency with increasing pressure. This indicates that it is likely that the anomalous form of the FFT amplitude with temperature observed in [140] can be interpreted as being due to two distinct orbits that have the same (or very similar) frequency at ambient pressure. It is interesting to note that 4.8 GPa, IV* can still be resolved but its amplitude is no longer temperature-insensitive up to 20 K as it was previously. This is reflected in the pressure dependence of m^*_{IV*} (Figure 7.22).

7.5 Discussion and Outlook

In summary, a study of SdH quantum oscillations in ZrSiS under hydrostatic pressure in which the pressure dependence of the oscillation frequencies and their associated effective masses have been presented. Hydrostatic pressure was found to increase the frequency of orbits that reside in both the ΓXM and ZRA planes. This is true of both electron- and hole-like pockets (α and β for example). This finding is incompatible with a scenario in which there is a simple pressure dependence to the Fermi energy. One would expect from the bandstructure (Figure 7.2) that either the electron- or hole-like pocket (but not both) would increase in size in this scenario. This would suggest that the nodal line is neither approached or moved away from with increasing pressure. The fact that both f_α and f_β increase suggests that pressure reduces the dispersion (slope) of the linear bands. The simple compression of lattice parameters may be sufficient to explain this effect. With decreasing real-space dimensions, the BZ should expand accordingly. This should result in a simple reduction in dE/dk assuming the overall geometry of the Fermi surface remains otherwise unchanged. However, this is at odds with the observation that the effective masses of both the α and β orbits (which are directly related to dA/dE) were not found to be pressure dependent. The effective masses of nearly all breakdown orbits were similarly pressure independent. For linearly dispersive bands, one would expect an enhancement of $m*$ in the simplest case.

A preliminary comparison with DFT calculations performed by Professor A. Carrington shows a qualitative agreement between the observed and predicted evolution of the QO frequencies with pressure. The calculations showed an increase in f_α and f_β that was very similar to that observed in this work. Further calculations and a more detailed comparison between calculation and experiment may yield further insight into the evolution of the Fermi surface with pressure. In particular, the pressure dependence of the masses of each orbit should be made. Calculations performed with a sufficiently high k-space resolution may also be able to show whether the size of the breakdown gap evolves systematically with pressure.

The only orbit for which a large change in $m*$ was observed is IV^*. The insensitivity to temperature of the amplitude of this frequency was broken at 4.8 GPa the pressure at which a finite effective mass could be determined. The apparent insensitivity of the oscillation amplitude to temperature for $T <\sim 50K$ has previously been ascribed to Stark interferometry [140]. It therefore appears that the interferometry effect is broken at this pressure.

The high frequency breakdown orbits visible in the FFT spectra obtained in Sample 2 have been studied at elevated pressures up to 5.6 GPa. The pressure dependence of the FFT frequencies and the effective masses of the associated orbits have been presented. The findings of this work are largely in accordance with previous quantum oscillation studies [136, 140].

The low frequency orbits are better resolved in oscillatory bulk magnetisation. Indeed, it was f_{δ_2} that was found to be most pressure-dependent. A study of the bulk magnetisation would be better able to resolve each of the low frequency orbits and track the evolution of both the frequencies and their associated masses with pressure.

It appears that pressure does not result in a tuning of the Fermi energy or a resultant advancement towards the nodal line. Liquid ion gating is one possible means of tuning the system closer to the nodal line by changing the carrier concentration. More similar to pressure, the effect of uniaxial strain may force a symmetry breaking that results in substantial adjustment of the bandstructure such that the nodal line lies closer to the Fermi energy. These avenues will be explored.

With regard to Sample 1, there are a number of highly peculiar results that remain unexplained. Firstly, the zero-field resistance and the low-temperature MR of the sample are highly uncharacteristic of ZrSiS. In fact, it only the presence of clear quantum oscillations that lead one to believe that the sample is in fact ZrSiS at all. The frequencies of the fundamental orbits are in very close agreement with expectation from DFT and previous results [135–137]. The breakdown frequencies, however, appear at additive combinations of fundamental frequencies which is contrary to expectation in a system where breakdown is between electron- and hole-like Fermi sheets. If the Fermi-sheets truly were both electron-like or both hole-like, a Fermi surface must have been substantially reconstructed. It is highly surprising that both α and β remain unaffected by the such a Fermi-surface reconstruction. This possibility is not believed to be responsible. Both the zero-field resistance and MR could potentially be explained by the presence of a crack or similarly major defect in the sample. This does not easily explain the observed breakdown behaviour.

Another possibility is that the sample is internally strained. It is then possible that the strain was annealed out of the sample with the application of pressure. This may explain why the forbidden breakdown frequencies were suppressed with pressure and why after returning to ambient pressure, the frequency spectrum was found to be markedly different from its as-grown state. Again, it does not simply explain the origin of the forbidden frequencies in the first place.

Whilst the additional (non-fundamental) peaks in the fourier spectra presented in this work have been attributed to magnetic breakdown in accordance with [136, 140], other mechanisms are capable of producing additional peaks as well. For example, torque interaction and magnetic interaction effects are another mechanism capable of introducing additional peaks in the FFT spectra of signals that are oscillatory in field. Furthermore, these peaks are introduced at both additive and subtractive linear combinations of fundamental frequencies. Although it is not clear whether an equivalent mechanism can generate additional peaks in SdH oscillations, the possibility should not be discounted. In the case of torque and magnetic interaction, it is not possible to introduce additional peaks with amplitudes that are larger than the fundamental orbits. The same is therefore expected of any possible effect in resistive measurements. The fact that breakdown frequencies with amplitudes that are markedly larger than those of their fundamental orbits (β in particular) would suggest that interaction effects are not the origin of the forbidden frequencies. Finally, the lack of discernible signatures of magnetic breakdown in the magnetisation measurements further evidences that the effect is not sufficient to explain the observed frequencies.

In charge-transfer salts, it was found that allowing the chemical potential to change in field allowed for the appearance of additional Fourier peaks at subtractive combinations of fundamental orbits whilst a constant chemical potential produced Fourier peaks at additive combinations [147]. Pinning of the chemical potential to Landau levels associated with a particular orbit was shown to cause energy levels associated with other orbits to cross the chemical potential at modified rates. Thus, fundamental peaks are shifted by a frequency given by that of the fundamental orbit to which the chemical potential is pinned. Whether this mechanism is relevant to ZrSiS is unclear.

Quantum interference (or Stark interferometry) is another mechanism that produces additional peaks and, indeed, has been claimed to be relevant to ZrSiS [140]. In LaB_6, quantum interference within field-induced eddy currents is believed to be responsible for a frequency with zero thermal effective mass [148]. Indeed, the principle signature that distinguishes peaks that are generated from Stark inteferometry is a temperature dependence to their amplitude that results in anomalously small thermal effective masses. Whilst the aforementioned peak at 8600 T was found to have an anomalously small effective mass in both this work and in [140], the same was not found of any other peak. Thus, Stark interferometry is not believed to be the principle mechanism behind the peaks at additive and subtractive combinations of f_α and f_β below 1 kT.

Chapter 8

Publications

1. Putzke, C. *et al.* Charge Order and Superconductivity in Underdoped $YBa_2Cu_3O_{7-\delta}$ under Pressure. *Phys. Rev. Lett.* **120,** 117002 (2018)
2. Licciardello, S. *et al.* Electrical resistivity across a nematic quantum critical point. en. *Nature* **567,** 213–217 (2019)
3. Licciardello, S. *et al.* Coexistence of orbital and quantum critical magnetoresistance in $FeSe_{1-x}S_x$. *Physical Review Research* **1,** 023011 (2019)
4. Putzke, C. *et al.* Reduced Hall carrier density in the overdoped strange metal regime of cuprate superconductors. *arXiv:1909.08102 [cond-mat].* arXiv: 1909.08102 (2019)
5. Müller, C. S. A. *et al.* Determination of the Fermi surface and field-induced quasi-particle tunneling around the Dirac nodal-loop in ZrSiS. *arXiv:2002.04379 [cond-mat].* arXiv: `2002.04379` (2020)

Bibliography

1. Anderson, P. W. More Is Different. *Science* **177,** 393–396 (1972).
2. Kamerlingh Onnes, H. Further experiments with Liquid Helium G. On the electrical resistance of Pure Metals etc. VI. On the Sudden Change in the Rate at which the Resistance of Mercury Disappears. *Koninklijke Nederlandse Akademie van Wetenschappen Proceedings Series B Physical Sciences* **14,** 818–821 (1911).
3. Bardeen, J., Cooper, L. N. & Schrieffer, J. R. Theory of Superconductivity. *Phys. Rev.* **108,** 1175–1204 (5 1957).
4. Cooper, L. N. Bound Electron Pairs in a Degenerate Fermi Gas. *Phys. Rev.* **104,** 1189–1190 (4 1956).
5. Bednorz, J. G. & Müller, K. A. Possible highTc superconductivity in the Ba-La-Cu-O system. *Zeitschrift für Physik B Condensed Matter* **64,** 189–193 (1986).
6. Tranquada, J. M., Sternlieb, B. J., Axe, J. D., Nakamura, Y. & Uchida, S. Evidence for stripe correlations of spins and holes in copper oxide superconductors. *Nature* **375,** 561–563 (1995).
7. Hashimoto, M., Vishik, I. M., He, R.-H., Devereaux, T. P. & Shen, Z.-X. Energy gaps in high-transition-temperature cuprate superconductors. *Nature Physics* **10,** 483–495 (2014).
8. Comin, R. *et al.* Charge Order Driven by Fermi-Arc Instability in $Bi_2Sr_{2-x}La_xCuO_{6+\delta}$. **343,** 4 (2014).
9. Yoshizawa, H., Mitsuda, S., Kitazawa, H. & Katsumata, K. An Incommensurate Magnetic Diffuse Scattering in Superconducting $La_{1.92}Sr_{0.08}CuO_{4-\delta}$. *Journal of the Physical Society of Japan* **57,** 3686–3689 (1988).
10. Birgeneau, R. J. *et al.* Static and dynamic spin fluctuations in superconducting $La_{2-x}Sr_xCuO_4$. *Phys. Rev. B* **39,** 2868–2871 (4 1989).
11. Landau, L. The Theory of a Fermi Liquid. *Solviet Physics JETP* **3,** 920–925 (1957).

12. L. P. Pitaevskii, E. M. L. *Physical Kinetics* (Butterworth-Heinemann, 1981).

13. Schofield, A. J. Non-Fermi liquids. *Contemporary Physics* **40,** 95–115 (1999).

14. Shoenberg, D. *Magnetic Oscillations in Metals* 1st edition (Cambridge University Press, 1984).

15. Pudalov, V. M. David Shoenberg and the beauty of quantum oscillations. *Low Temperature Physics* **37,** 8–18 (2011).

16. Priestley, M. G., Falicov, L. M. & Weisz, G. Experimental and Theoretical Study of Magnetic Breakdown in Magnesium. *Physical Review* **131,** 617–622 (1963).

17. Shibauchi, T., Carrington, A. & Matsuda, Y. A Quantum Critical Point Lying Beneath the Superconducting Dome in Iron Pnictides. *Annual Review of Condensed Matter Physics* **5,** 113–135 (2014).

18. Hussey, N. The normal state scattering rate in high-T_c cuprates. *The European Physical Journal B* **31,** 495–507 (2003).

19. Licciardello, S. *et al.* Electrical resistivity across a nematic quantum critical point. *Nature* **567,** 213–217 (2019).

20. Michon, B. *et al.* Thermodynamic signatures of quantum criticality in cuprate superconductors. *Nature* **567,** 218–222 (2019).

21. Hayes, I. M. *et al.* Scaling between magnetic field and temperature in the high-temperature superconductor $\mathrm{BaFe_2(As_{1-x}P_x)_2}$. *Nature Physics* **12,** 916–919 (2016).

22. Giraldo-Gallo, P. *et al.* Scale-invariant magnetoresistance in a cuprate superconductor. *Science* **361,** 479–481 (2018).

23. Licciardello, S. *et al.* Coexistence of orbital and quantum critical magnetoresistance in $\mathrm{FeSe_{1-x}S_x}$. *Physical Review Research* **1,** 023011 (2019).

24. Walmsley, P. *et al.* Quasiparticle Mass Enhancement Close to the Quantum Critical Point in BaFe2(As1-xPx)2. *Physical Review Letters* **110,** 257002 (2013).

25. Hashimoto, K. *et al.* A Sharp Peak of the Zero-Temperature Penetration Depth at Optimal Composition in $\mathrm{BaFe_2(As_{1-x}P_x)_2}$. *Science* **336,** 1554–1557 (2012).

26. Eremets, M. I. *High Pressure Experimental Methods* 1st edition (Oxford University Press, 1996).

27. Zeto, R. J. & Vanfleet, H. B. Pressure Calibration to 60 kbar Based on the Resistance Change of a Manganin Coil under Hydrostatic Pressure. *Journal of Applied Physics* **40,** 2227–2231 (1969).

28. Drozdov, A. P., Eremets, M. I., Troyan, I. A., Ksenofontov, V. & Shylin, S. I. Conventional superconductivity at 203 kelvin at high pressures in the sulfur hydride system. *Nature* **525,** 73 (2015).

29. Drozdov, A. P. *et al.* Superconductivity at 250 K in lanthanum hydride under high pressures. *Nature* **569,** 528–531 (2019).

30. Mao, H. K., Xu, J. & Bell, P. M. Calibration of the ruby pressure gauge to 800 kbar under quasi-hydrostatic conditions. *Journal of Geophysical Research: Solid Earth* **91,** 4673–4676 (1986).

31. Dewaele, A., Loubeyre, P. & Mezouar, M. Equations of state of six metals above 94 GPa. *Physical Review B* **70,** 094112 (2004).

32. Dewaele, A., Torrent, M., Loubeyre, P. & Mezouar, M. Compression curves of transition metals in the Mbar range: Experiments and projector augmented-wave calculations. *Physical Review B* **78,** 104102 (2008).

33. Klotz, S., Chervin, J.-C., Munsch, P. & Marchand, G. L. Hydrostatic limits of 11 pressure transmitting media. *Journal of Physics D: Applied Physics* **42,** 075413 (2009).

34. Yokogawa, K., Murata, K., Yoshino, H. & Aoyama, S. Solidification of High-Pressure Medium Daphne 7373. *Japanese Journal of Applied Physics* **46,** 3636–3639 (2007).

35. Klotz, S., Takemura, K., Strässle, T. & Hansen, T. Freezing of glycerol–water mixtures under pressure. *Journal of Physics: Condensed Matter* **24,** 325103 (2012).

36. Nikolo, M. Superconductivity: A guide to alternating current susceptibility measurements and alternating current susceptometer design. *American Journal of Physics* **63,** 57–65 (1995).

37. Blaha, P. *et al. WIEN2k, An Augmented Plane Wave + Local Orbitals Program for Calculating Crystal Properties* 1st edition (Karlheinz Schwarz, Techn. Universität Wien, Austria, 2018).

38. Sheng, Z. Z. & Hermann, A. M. Bulk superconductivity at 120 K in the Tl-Ca/Ba-Cu-O system. *Nature* **332,** 138–139 (1988).

39. Momma, K. & Izumi, F. VESTA 3 for three-dimensional visualization of crystal, volumetric and morphology data. *Journal of Applied Crystallography* **44,** 1272–1276 (2011).

40. Pederzolli, D. R., Wltschek, G. M., Attfield, J. P. & Fuess, H. Phase transitions in the $Tl_2Ba_2CuO_{6+\delta}$ superconductor. *Phys. Rev. B* **58,** 5226–5229 (9 1998).

41. Shimakawa, Y., Kubo, Y., Manako, T. & Igarashi, H. Variation in T_c and carrier concentration in Tl-based superconductors. *Phys. Rev. B* **40,** 11400–11402 (16 1989).

42. Shimakawa, Y. *et al.* Neutron-diffraction study of $Tl_2Ba_2CuO_{6+\delta}$ with various T_c's from 0 to 73 K. *Phys. Rev. B* **42,** 10165–10171 (16 1990).

43. Peets, D. C. *et al.* $Tl_2Ba_2CuO_{6+\delta}$ brings spectroscopic probes deep into the overdoped regime of the high-T_c cuprates. *New Journal of Physics* **9,** 28–28 (2007).

44. Vignolle, B. *et al.* Quantum oscillations in an overdoped high-Tc superconductor. *Nature* **455,** 952 (2008).

45. Rourke, P. M. C. *et al.* A detailed de Haas–van Alphen effect study of the overdoped cuprate $Tl_2Ba_2CuO_{6+\delta}$. *New Journal of Physics* **12,** 105009 (2010).

46. French, M. M. J., Analytis, J. G., Carrington, A., Balicas, L. & Hussey, N. E. Tracking anisotropic scattering in overdoped $Tl_2Ba_2CuO_{6+\delta}$ above 100 K. *New Journal of Physics* **11,** 055057 (2009).

47. Abdel-Jawad, M. *et al.* Anisotropic scattering and anomalous normal-state transport in a high-temperature superconductor. *Nature Physics* **2,** 821–825 (2006).

48. Platé, M. *et al.* Fermi Surface and Quasiparticle Excitations of Overdoped $Tl_2Ba_2CuO_{6+\delta}$. *Phys. Rev. Lett.* **95,** 077001 (7 2005).

49. French, M. M. J. *Angle Dependent Magnetoresistance in* $Tl_2Ba_2CuO_{6+\delta}$ PhD thesis (University of Bristol, 1997).

50. Tyler, A. W. *An Investigation into the Magnetotransport Properties of Layered Superconducting Perovskites.* PhD thesis (University of Cambridge, 1997).

51. Hussey, N. E. *et al.* Angular Dependence of the *c*-axis Normal State Magnetoresistance in Single Crystal $Tl_2Ba_2CuO_6$. *Phys. Rev. Lett.* **76,** 122–125 (1 1996).

52. Abdel-Jawad, M. *et al.* Correlation between the Superconducting Transition Temperature and Anisotropic Quasiparticle Scattering in $Tl_2Ba_2CuO_{6+\delta}$. *Phys. Rev. Lett.* **99,** 107002 (10 2007).

53. Klehe, A.-K. *et al.* Pressure-induced oxygen ordering phenomena in high-Tc superconductors. *Physica C: Superconductivity and its Applications* **257,** 105–116 (1996).

54. Looney, C., Schilling, J., Doyle, S. & Hermann, A. Possibility for oxygen relaxation below 15 K in superconducting Tl2Ba2CuO6 + x. *Physica C: Superconductivity* **289,** 203–210 (1997).

55. Looney, C., Kline, J., Mascarenhas, F., Schilling, J. & Hermann, A. Influence of oxygen content on the activation energy for oxygen ordering in Tl2Ba2CuO$_{6+\delta}$. *Physica C: Superconductivity* **351,** 215–226 (2001).

56. Sadewasser, S., Schilling, J. S., Paulikas, A. P. & Veal, B. W. Pressure dependence of ${T}_{c}$ to 17 GPa with and without relaxation effects in superconducting ${\mathrm{YBa}}_{2}{\mathrm{Cu}}_{3}{\mathr
Physical Review B* **61,** 741–749 (2000).

57. Takahashi, H. *et al.* Anomalous behavior of the pressure dependence of lattice constants in $Tl_2Ba_2CuO_{6+x}$. *Physica C: Superconductivity* **191,** 248–254 (1992).

58. Ono, S. & Ando, Y. Evolution of the resistivity anisotropy in $Bi_2Sr_{2-x}La_xCuO_{6+\delta}$ single crystals for a wide range of hole doping. *Physical Review B* **67,** 104512 (2003).

59. Kubo, Y., Shimakawa, Y., Manako, T. & Igarashi, H. Transport and magnetic properties of $Tl_2Ba_2CuO_{6+\delta}$ showing a δ-dependent gradual transition from an 85-K superconductor to a nonsuperconducting metal. *Phys. Rev. B* **43,** 7875–7882 (10 1991).

60. Manako, T., Kubo, Y. & Shimakawa, Y. Transport and structural study of $Tl_2Ba_2CuO_{6+\delta}$ single crystals prepared by the KCl flux method. *Phys. Rev. B* **46,** 11019–11024 (17 1992).

61. Mackenzie, A. P., Julian, S. R., Sinclair, D. C. & Lin, C. T. Normal-state magnetotransport in superconducting $Tl_2Ba_2CuO_{6+\delta}$ to millikelvin temperatures, 8 (1996).

62. Hussey, N. E., Gordon-Moys, H., Kokalj, J. & McKenzie, R. H. Generic strange-metal behaviour of overdoped cuprates. *Journal of Physics: Conference Series* **449,** 012004 (2013).

63. Hussey, N. E., Abdel-Jawad, M., Carrington, A., Mackenzie, A. P. & Balicas, L. A coherent three-dimensional Fermi surface in a high-transition-temperature superconductor. *Nature* **425,** 814–817 (2003).

64. Bangura, A. F. *et al.* Small Fermi Surface Pockets in Underdoped High Temperature Superconductors: Observation of Shubnikov–de Haas Oscillations in $YBa_2Cu_4O_8$. *Phys. Rev. Lett.* **100,** 047004 (4 2008).

65. Putzke, C. *et al.* Reduced Hall carrier density in the overdoped strange metal regime of cuprate superconductors. *arXiv:1909.08102 [cond-mat].* arXiv: 1909.08102 (2019).

66. Tinkham, M. *Introduction to Superconductivity* 2nd edition (McGraw-Hill, Inc., 1996).

67. Ayres, J. *et al.* Incoherent Transport in the Strange Metal Regime of HIghly Overdoped Cuprates. *Science (Submitted)* (2020).

68. Badoux, S. *et al.* Change of carrier density at the pseudogap critical point of a cuprate superconductor. *Nature* **531,** 210–214 (2016).

69. Legros, A. *et al.* Universal T-linear resistivity and Planckian dissipation in overdoped cuprates. *Nature Physics* **15,** 142–147 (2019).

70. Cooper, R. A. *et al.* Anomalous criticality in the electrical resistivity of $La_{2-x}Sr_xCuO_4$. *Science* **323,** 603–607 (2009).

71. Marel, D. v. d. *et al.* Quantum critical behaviour in a high-Tc superconductor. *Nature* **425,** 271–274 (2003).

72. Zaanen, J. Why the temperature is high. *Nature* **430,** 512–513 (2004).

73. Bangura, A. F. *et al.* Fermi surface and electronic homogeneity of the overdoped cuprate superconductor $Tl_2Ba_2CuO_{6+\delta}$ as revealed by quantum oscillations. *Physical Review B* **82,** 140501 (2010).

74. Hashimoto, M., Vishik, I. M., He, R.-H., Devereaux, T. P. & Shen, Z.-X. Energy gaps in high-transition-temperature cuprate superconductors. *Nature Physics* **10,** 483–495 (2014).

75. Chen, S.-D. *et al.* Incoherent strange metal sharply bounded by a critical doping in Bi2212. *Science* **366,** 1099–1102 (2019).

76. Bruls, G. J. C. L., Bass, J., van Gelder, A. P., van Kempen, H. & Wyder, P. Linear Magnetoresistance Caused by Sample Thickness Variations. *Phys. Rev. Lett.* **46.** Publisher: American Physical Society, 553–555 (1981).

77. Ramakrishnan, N., Lai, Y. T., Lara, S., Parish, M. M. & Adam, S. Equivalence of effective medium and random resistor network models for disorder-induced unsaturating linear magnetoresistance. *Phys. Rev. B* **96.** Publisher: American Physical Society, 224203 (2017).

78. Singleton, J. A simple transport model for the temperature-dependent linear magnetoresistance of high-temperature superconductors. *arXiv:1810.01998 [cond-mat].* arXiv: 1810.01998 (2018).

79. Boyd, C. & Phillips, P. W. Single-parameter scaling in the magnetoresistance of optimally doped La_{2-x} Sr_x CuO_4. *Physical Review B* **100,** 155139 (2019).

80. Wu, T. *et al.* Incipient charge order observed by NMR in the normal state of YBa2Cu3Oy. *Nature Communications* **6.** Article, 6438 (2015).

81. Cheong, S.-W. *et al.* Incommensurate magnetic fluctuations in $La_{2-x}Sr_xCuO_4$. *Phys. Rev. Lett.* **67,** 1791–1794 (13 1991).

82. Wu, T. *et al.* Magnetic-field-induced charge-stripe order in the high-temperature superconductor YBa2Cu3Oy. *Nature* **477,** 191 (2011).

83. Ghiringhelli, G. *et al.* Long-Range Incommensurate Charge Fluctuations in (Y,Nd)Ba2Cu3O6+x. *Science* **337,** 821–825 (2012).

84. Chang, J. *et al.* Direct observation of competition between superconductivity and charge density wave order in $YBa_2Cu_3O_{6.67}$. *Nature Physics* **8,** 871 (2012).

85. Chang, J. *et al.* Magnetic field controlled charge density wave coupling in underdoped YBa 2 Cu 3 O 6+x. *Nature Communications* **7,** 1–7 (2016).

86. Hücker, M. *et al.* Competing charge, spin, and superconducting orders in underdoped $YBa_2Cu_3O_y$. *Phys. Rev. B* **90,** 054514 (5 2014).

87. Blanco-Canosa, S. *et al.* Resonant x-ray scattering study of charge-density wave correlations in $YBa_2Cu_3O_{6+x}$. *Phys. Rev. B* **90,** 054513 (5 2014).

88. Liang, R., Bonn, D. A. & Hardy, W. N. Evaluation of CuO 2 plane hole doping in YBa 2 Cu 3 O 6 + x single crystals. *Physical Review B* **73,** 180505 (2006).

89. LeBoeuf, D. *et al.* Lifshitz critical point in the cuprate superconductor $YBa_2Cu_3O_y$ from high-field Hall effect measurements. *Phys. Rev. B* **83,** 054506 (5 2011).

90. Doiron-Leyraud, N. *et al.* Quantum oscillations and the Fermi surface in an underdoped high-Tc superconductor. *Nature* **447,** 565 (2007).

91. Jaudet, C. *et al.* de Haas–van Alphen Oscillations in the Underdoped High-Temperature Superconductor $YBa_2Cu_3O_{6.5}$. *Phys. Rev. Lett.* **100,** 187005 (18 2008).

92. Allais, A., Chowdhury, D. & Sachdev, S. Connecting high-field quantum oscillations to zero-field electron spectral functions in the underdoped cuprates. *Nature Communications* **5,** 5771 (2014).

93. Doiron-Leyraud, N. *et al.* Evidence for a small hole pocket in the Fermi surface of underdoped YBa2Cu3Oy. *Nature Communications* **6,** 6034 (2015).

94. Grissonnanche, G. *et al.* Direct measurement of the upper critical field in cuprate superconductors. *Nature Communications* **5,** 3280 (2014).

95. E. Stupp, D. M. G. in *Physical Properties of High Temperature Superconductors III* (ed Ginsberg, D. M.) (World Scientific, Singapore, 1992).

96. Segawa, K. & Ando, Y. Intrinsic Hall response of the ${\mathrm{CuO}}_{2}$ planes in a chain-plane composite system of ${\mathrm{YBa}}_{2}{\mathrm{Cu}}_{3}{\mathrm{O}}_{y}$. *Physical Review B* **69,** 104521 (2004).

97. Souliou, S. M. *et al.* Rapid suppression of the charge density wave in YBa 2 Cu 3 O 6.6 under hydrostatic pressure. *Physical Review B* **97,** 020503 (2018).

98. Huang, H. *et al.* Modification of structural disorder by hydrostatic pressure in the superconducting cuprate $YBa_2Cu_3O_{6.73}$. *Phys. Rev. B* **97,** 174508 (17 2018).

99. Gerber, S. *et al.* Three-dimensional charge density wave order in YBa2Cu3O6.67 at high magnetic fields. *Science* **350,** 949–952 (2015).

100. Vinograd, I. *et al.* Nuclear magnetic resonance study of charge density waves under hydrostatic pressure in YBa 2 Cu 3 O y. *Physical Review B* **100,** 094502 (2019).

101. Reichardt, S. *et al.* Bulk Charge Ordering in the CuO2 Plane of the Cuprate Superconductor YBa2Cu3O6.9 by High-Pressure NMR. *Condensed Matter* **3,** 23 (2018).

102. Putzke, C. *et al.* Inverse correlation between quasiparticle mass and Tc in a cuprate high-Tc superconductor. *Science Advances* **2,** e1501657 (2016).

103. LeBoeuf, D. *et al.* Electron pockets in the Fermi surface of hole-doped high-Tc superconductors. *Nature* **450,** 533 (2007).

104. Kamihara, Y. *et al.* Iron-Based Layered Superconductor: LaOFeP. *Journal of the American Chemical Society* **128,** 10012–10013 (2006).

105. Kamihara, Y., Watanabe, T., Hirano, M. & Hosono, H. Iron-Based Layered Superconductor La[O1-xFx]FeAs (x = 0.05-0.12) with Tc = 26 K. *Journal of the American Chemical Society* **130,** 3296–3297 (2008).

106. Superconductivity at 43 K in an iron-based layered compound $LaO_{1-x}F_xFeAs$.

107. Chen, X. H. *et al.* Superconductivity at 43 K in SmFeAsO1-xF x. *Nature* **453,** 761–762 (2008).

108. Zhi-An, R., Wei, L., Jie, Y., Wei, Y. & Xiao-Li, S. Superconductivity at 55 K in Iron-Based F-Doped Layered Quaternary Compound Sm[O1-xFx]FeAs, 3.

109. Luo, X. & Chen, X. Crystal structure and phase diagrams of iron-based superconductors. *Science China Materials* **58,** 77–89 (2015).

110. Paglione, J. & Greene, R. L. High-temperature superconductivity in iron-based materials. *Nature Physics* **6,** 645–658 (2010).

111. Fernandes, R. M., Chubukov, A. V., Knolle, J., Eremin, I. & Schmalian, J. Preemptive nematic order, pseudogap, and orbital order in the iron pnictides. *Physical Review B* **85,** 024534 (2012).

112. Fernandes, R. M. & Schmalian, J. Manifestations of nematic degrees of freedom in the magnetic, elastic, and superconducting properties of the iron pnictides. *Superconductor Science and Technology* **25,** 084005 (2012).

113. Tanatar, M. A. *et al.* Uniaxial-strain mechanical detwinning of CaFe 2 As 2 and BaFe 2 As 2 crystals: Optical and transport study. *Physical Review B* **81,** 184508 (2010).

114. Chu, J.-H. *et al.* In-Plane Resistivity Anisotropy in an Underdoped Iron Arsenide Superconductor. *Science* **329,** 824–826 (2010).

115. Kasahara, S. *et al.* Evolution from non-Fermi- to Fermi-liquid transport via isovalent doping in $BaFe_2(As_{1-x}P_x)_2$ superconductors. *Physical Review B* **81,** 184519 (2010).

116. Analytis, J. G. *et al.* Transport near a quantum critical point in $BaFe_2(As_{1-x}P_x)_2$. *Nature Physics* **10,** 194–197 (2014).

117. Putzke, C. *et al.* Anomalous critical fields in quantum critical superconductors. *Nature Communications* **5,** 5679 (2014).

118. Hsu, F.-C. *et al.* Superconductivity in the PbO-type structure α-FeSe. *Proceedings of the National Academy of Sciences* **105,** 14262–14264 (2008).

119. Sun, J. P. *et al.* High-T_c Superconductivity in FeSe at High Pressure: Dominant Hole Carriers and Enhanced Spin Fluctuations. *Physical Review Letters* **118,** 147004 (2017).

120. Medvedev, S. *et al.* Electronic and magnetic phase diagram of β-$Fe_{1.01}Se$ with superconductivity at 36.7 K under pressure. *Nature Materials* **8,** 630–633 (2009).

121. Ge, J.-F. *et al.* Superconductivity above 100 K in single-layer FeSe films on doped SrTiO3. *Nature Materials* **14,** 285–289 (2015).

122. McQueen, T. M. *et al.* Tetragonal-to-Orthorhombic Structural Phase Transition at 90 K in the Superconductor $Fe_{1.01}Se$. *Phys. Rev. Lett.* **103,** 057002 (5 2009).

123. Hosoi, S. *et al.* Nematic quantum critical point without magnetism in $FeSeS_{1-x}S_x$ superconductors. *Proceedings of the National Academy of Sciences* **113,** 8139–8143 (2016).

124. Reiss, P. *et al.* Suppression of electronic correlations by chemical pressure from FeSe to FeS. *Physical Review B* **96,** 121103 (2017).

125. Bendele, M. *et al.* Pressure Induced Static Magnetic Order in Superconducting FeSe 1 - x. *Physical Review Letters* **104,** 087003 (2010).

126. Watson, M. D. *et al.* Emergence of the nematic electronic state in FeSe. *Physical Review B* **91,** 155106 (2015).

127. Sprau, P. O. *et al.* Discovery of orbital-selective Cooper pairing in FeSe. *Science* **357,** 75–80 (2017).

128. Matsuura, K. *et al.* Maximizing Tc by tuning nematicity and magnetism in $\mathrm{FeSe}_{1-x}\mathrm{S}_x$ superconductors. *Nature Communications* **8,** 1143 (2017).

129. Wiecki, P. *et al.* Persistent correlation between superconductivity and antiferromagnetic fluctuations near a nematic quantum critical point in $\mathrm{FeSe}_{1-x}\mathrm{S}_x$. *Physical Review B* **98,** 020507 (2018).

130. Kaluarachchi, U. S. *et al.* Nonmonotonic pressure evolution of the upper critical field in superconducting FeSe. *Physical Review B* **93,** 064503 (2016).

131. Khasanov, R. *et al.* Pressure-induced magnetic order in FeSe: A muon spin rotation study. *Physical Review B* **95,** 180504 (2017).

132. Kothapalli, K. *et al.* Strong cooperative coupling of pressure-induced magnetic order and nematicity in FeSe. *Nature Communications* **7,** 12728 (2016).

133. Gati, E., Böhmer, A. E., Bud'ko, S. L. & Canfield, P. C. Bulk Superconductivity and Role of Fluctuations in the Iron-Based Superconductor FeSe at High Pressures. *Physical Review Letters* **123,** 167002 (2019).

134. Xiang, L. *et al.* Dome of magnetic order inside the nematic phase of sulfur-substituted FeSe under pressure. *Physical Review B* **96,** 024511 (2017).

135. Schoop, L. M. *et al.* Dirac cone protected by non-symmorphic symmetry and three-dimensional Dirac line node in ZrSiS. *Nature Communications* **7,** 1–7 (2016).

136. Pezzini, S. *et al.* Unconventional mass enhancement around the Dirac nodal loop in ZrSiS. *Nature Physics* **14,** 178–183 (2018).

137. Van Delft, M. *Emergent phenomena in Weyl, nodal line and one-dimensional semimetals* PhD thesis (Radboud University, 2019).

138. Wang, X. *et al.* Evidence of Both Surface and Bulk Dirac Bands and Anisotropic Nonsaturating Magnetoresistance in ZrSiS. *Advanced Electronic Materials* **2,** 1600228 (2016).

139. Fu, B.-B. *et al.* Dirac nodal surfaces and nodal lines in ZrSiS. *Science Advances* **5,** eaau6459 (2019).

140. Müller, C. S. A. *et al.* Determination of the Fermi surface and field-induced quasi-particle tunneling around the Dirac nodal-loop in ZrSiS. *arXiv:2002.04379 [cond-mat]* (2020).

141. Aggarwal, L. *et al.* Tip-induced superconductivity coexisting with preserved topological properties in line-nodal semimetal ZrSiS. *Journal of Physics: Condensed Matter* **31,** 485707 (2019).

142. Huh, Y., Moon, E.-G. & Kim, Y. B. Long-range Coulomb interaction in nodal-ring semimetals. *Physical Review B* **93,** 035138 (2016).

143. Novak, M. *et al.* Highly anisotropic interlayer magnetoresitance in ZrSiS nodal-line Dirac semimetal. *Physical Review B* **100,** 085137 (2019).

144. Singha, R., Pariari, A. K., Satpati, B. & Mandal, P. Large nonsaturating magnetoresistance and signature of nondegenerate Dirac nodes in ZrSiS. *Proceedings of the National Academy of Sciences* **114,** 2468–2473 (2017).

145. Sankar, R. *et al.* Crystal growth of Dirac semimetal ZrSiS with high magnetoresistance and mobility. *Scientific Reports* **7,** 40603 (2017).

146. VanGennep, D. *et al.* Possible pressure-induced topological quantum phase transition in the nodal line semimetal ZrSiS. *Physical Review B* **99,** 085204 (2019).

147. Harrison, N. *et al.* Magnetic breakdown and quantum interference in the quasi-two-dimensional superconductor in high magnetic fields. *Journal of Physics: Condensed Matter* **8.** Publisher: IOP Publishing, 5415–5435 (1996).

148. Harrison, N., Goodrich, R. G., Vuillemin, J. J., Fisk, Z. & Rickel, D. G. Quantum Interference in LaB_6. *Phys. Rev. Lett.* **80.** Publisher: American Physical Society, 4498–4501 (1998).

149. Putzke, C. *et al.* Charge Order and Superconductivity in Underdoped $YBa_2Cu_3O_{7-\delta}$ under Pressure. *Phys. Rev. Lett.* **120,** 117002 (2018).